University of Basel

Swiss Nanoscience Institute

Swiss Nanoscience Institute
Center of Excellence supported by the University of Basel and the Canton of Aargau

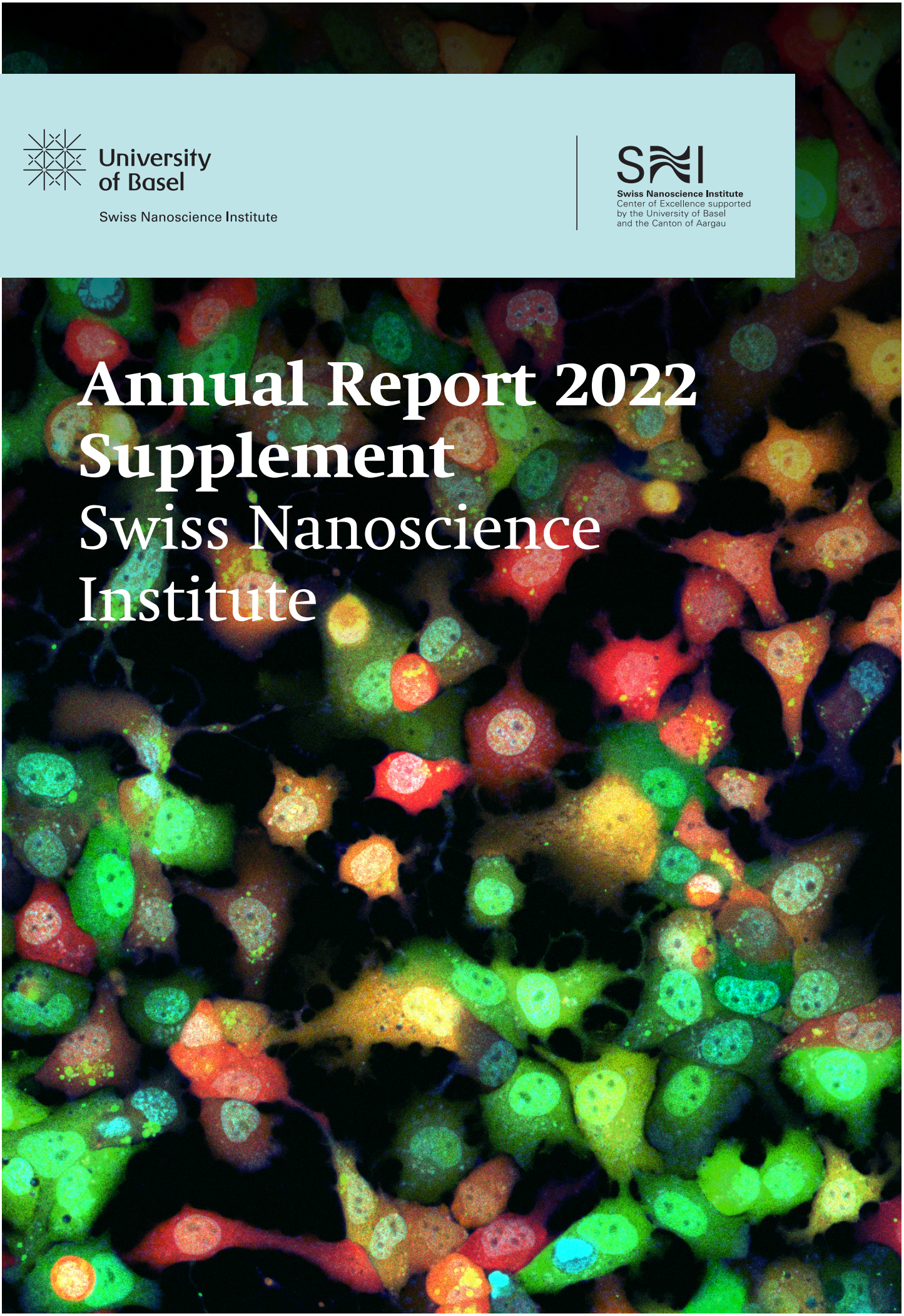

Annual Report 2022 Supplement

Swiss Nanoscience Institute

Cover image:
Analysis of human cells expressing a red fluorescent transgene by confocal microscopy. Cells were transfected using a lipid-nanoparticle (LNP) based gene delivery system.
Bright green signal: endosomal escape, green signal: Galectin3-GFP, red signal: transgene RFP,-cyan signal: cell nuclei, blue signal: LNP
(Image: Claudio Alter, Department of Pharmaceutical Sciences, University of Basel)

Contents

Magnetic Frustration in an on-surface Kagome Network

Project P1602: Self-assembly and magnetic order of 2D spin lattices on surfaces
Project Leader: T. A. Jung and J. Dreiser
Collaborators: M. Heydari (SNI PhD Student), M. Brunthaler, M. Hua, N. Lin

Magnetic frustration1 may occur in antiferromagnetic (AFM) systems if spin centers are, for example, arranged within a trigonal network. If spins are aligned in AFM order i.e. if spins on neighboring atoms point in opposite (180 degree) direction along two of the three bonds in any of the triangular units, the spins linked by the third bond are pointing in parallel direction and violate the AFM ordering of the network. Among the different magnetic systems which show geometrical frustration, Kagome antiferromagnets (KAFM) are promising candidates to probe frustration for their small coordination number compared to e.g. triangular systems. KAFMs have been intensely studied in theoretical work and in some experimental efforts, predominantly of 3D materials and their surfaces. Magnetically frustrated systems in general provide fundamentally interesting materials for the large fraction of the spins that can re-orient with a very low activation energy. Such materials may form spin-liquids for the high volatility of their local spin order. Also unique order-to-disorder transitions may occur as they are well suited to compare experiments and theory on the level of fundamental spin ordering mechanisms. Due to their spin-frustration such materials lack long range order. On the basis of calculations, it has been discussed that degeneracy can be lifted and some ordering may emerge if larger spin values and/or long-range interactions beyond the nearest neighbor are taken into account [2]. Ground states of magnetically frustrated materials are still controversially discussed as they depend on the dimensionality of the lattice (and the presence / absence of defects), the material anisotropy, spin quantum number, and more. This provides another motivation to investigate quasi-classical and classical KAFMs in particular at low and variable temperatures. Planar 'on-surface' spin architectures provide a uniquely suited material enabling a new scientific approach. Here ordering phenomena can be investigated by spectro-microscopy correlation using statistically averaging non-local spectroscopies and local probes with down to single atom / spin resolution.

In this work we used on-surface coordination chemistry to form a Kagome lattice of Fe(II) ions on Au(111) surfaces while benzene-1,2,3,4,5,6-hexaol (BHO) molecules act as the ligands. After characterizing the sample by X-ray photoelectron spectroscopy and scanning tunneling microscopy, we investigated its electronic configuration and magnetic properties by means of X-ray absorption spectroscopy and X-ray magnetic circular dichroism.

Scanning Tunneling Microscopy (STM) data (Fig. 1a shows the supra-molecular islands of self-assembled Fe and benzene-1,2,3,4,5,6-hexaol (BHO) linkers after optimized sample preparation by sublimation of the two components onto atomically clean Au(111) substrates. The island distribution is homogeneous across the sample and corresponds to ~16% surface coverage in the case of this specific sample. The inset shows a zoom view with four network patches showing the distortion of the herringbone structure caused by the network-substrate interactions. Figure 1b resolves the molecules at high resolution. As a guide to the viewer, the positions of the atoms coordinating the molecules have been superimposed onto the STM micrograph together with the chemical structure of the linker molecule after its dehydrogenation upon network formation. In the areas where the atoms have not been marked the atoms can be recognized in the high resolution micrographs.

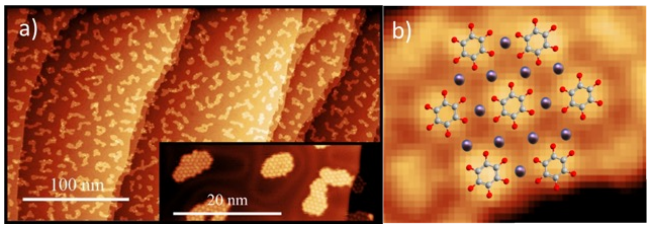

Fig. 1: a) Morphology of the Fe-benzenehexol containing Kagome network. STM micrograph (T = 300 K) of the coordination network. (Ubias = -1.0 V , I_t = 10 pA, T = 300 K) b) high-resolution STM data resolving the molecules and adatoms. The adatom positions are indicated. (Ubias = -1.0 V , I_t = 20 pA, T = 300 K)

X-ray absorption spectroscopy has been performed to identify the chemical and magnetic structure of the network. Figure 2a and b top shows the normalized X-ray absorption spectra (XAS) taken with circularly (+/-) polarized light at T = 2.5 K and B = 6.8 T for Fe L2,3 edges. Both Fe absorption spectra (+/-) exhibit two absorption peaks at the Fe L3 edge with an energy difference of about 0.7 eV at 706.1 eV and 706.8 eV. Assigning the peaks to the specific transitions/oxidation states of the ions requires proper simulations, as spin-orbit and electron-electron interactions are of the same order of magnitude as the ligand field effects and XAS spectra are highly dependent on changes in the ligand field.

The x-ray magnetic circular dichroism (XMCD) has been plotted in figure 2 (a,b)-bottom. The very similar absorption behavior of the system for the two different polarizations leads to a very weak XMCD signal. This indicates a weak magnetic response of the system in contrast to the high-spin state of Fe(II) (total spin moment of S = 2 and magnetic moment of 3.6 μ_B) obtained from spin polarized DFT analysis [3]. The total magnetic moment and the contributions from spin/orbital moment has been approximated by analyzing the sum rules. The very low magnitude of the XMCD signal compared to these calculations suggests a significantly smaller value for the net total magnetic moment per Fe atom in the coordinated network. This can be quantitatively estimated to about a fraction of a Bohr magneton.

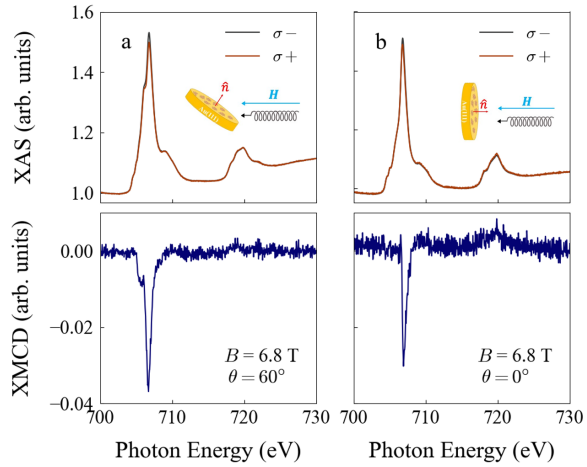

Fig. 2: a, b) Normalized circularly polarised x-ray absorption (top) and x-ray magnetic circular dichroism spectra (bottom) recorded at the Fe L2,3 edges and B = 6.8 T for grazing (θ=60°) and normal incidence (θ=0°), respectively.

To obtain further insight into the magnetic properties of the system, we measured element-specific magnetization curves at T = 2.5 K for normal and grazing incident angles (Fig. 3a). In both cases, the magnetization of the sample linearly changed with increasing magnetic field and no saturation is visible, even at B = 6.8 T. At normal incidence, the linear change of the magnetization curve can be explained by the magnetic anisotropy of the system. Such anisotropy in conjunction with magnetic hard-axis behavior has already been evidenced by sum rule calculations and DFT calculations. At grazing incidence simulations suggest an easy plane magnetic anisotropy for the network, which was not visible in the experimental magnetization data. All these observations are consistent with the presence of a strong AFM coupling (persistent to high magnetic fields) of the Fe atoms via coordination ligands and the absence of a global alignment of the magnetic moments and therefore frustration.

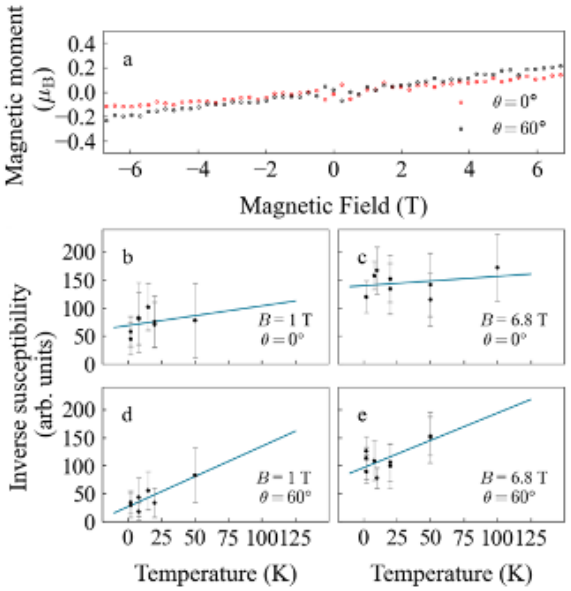

Fig. 3 : a) Low temperature (T = 2.5 K) field dependent magnetization of Fe atoms at normal (θ=0°) and grazing (θ=60°) incidence angle. (b-e) Temperature dependence of the inverse susceptibility (scattered dots) and fitted Curie-Weiss law (blue lines) at 1 T and at 6.8 T for normal and grazing incidence. Extracted Weiss temperatures are shown in Table 2.

Temperature dependent inverse Magnetic susceptibility plots, for high (6.8 T) and low (1 T) magnetic field and both normal and grazing incident angles have been extracted from XMCD experiments as plotted in figure 3 b-e. Also a Curie-Weiss plot has been fitted to the inverse susceptibility data towards their improved discussion. The extracted Weiss temperature and effective magnetic moment is shown in table 1 with the approximated experimental error. At normal incidence, for both high field and low field measurements, there is no significant change in the inverse susceptibility at all temperatures. This suggests a high Weiss temperature possibly related to the high magnetic anisotropy and the hard-axis perpendicular to the surface. In case of grazing incidence, the inverse susceptibility is lower at lower temperatures. The negative Weiss temperature w suggests that the system is dominated by antiferromagnetic interactions between iron ions. Considering the geometry of the network this implicitly confirms, again, the magnetic frustration of the system.

Table.1 : Weiss temperatures extracted by fitting of the Curie-Weiss law to χ^{-1} as shown in figure 3.

Magnetic Field	Incident angle	θ_w [K]
1.0 T	0°	-196 ± 50
6.8 T	0°	-842 ± 70
1.0 T	60°	-24 ± 15
6.8 T	60°	-98 ± 30

References

[1] R. Moessner, A. P. Ramirez, Geometrical frustration, Phys. Today 59, 24 (2007)

[2] D. J. J. Farnell, Emergence of magnetic order in kagomé antiferromagnets, Front. Phys. 14, 23302 (2019)

[3] P. Müller, A. Zander, J. Richter, Thermodynamics of the kagome-lattice Heisenberg antiferromagnet with arbitrary spin, Phys. Rev. B 98, 024414 (2018)

Visualizing molecular dynamics of the nuclear pore complex permeability barrier

Project P1603: A mechano-optical microscope for studying force transduction in living cells
Project Leader: R. H. Y. Lim and E. Meyer
Collaborator: T. Kozai (SNI PhD Student)

Introduction

The nuclear pore complex (NPC) is a huge biological nanopore that acts as the sole gateway between the cytoplasm and nucleus in eukaryotic cells. The central channel of each NPC possesses numerous intrinsically disordered proteins termed FG nucleoporins (or FG Nups) that function as a permeability barrier to facilitate biomolecular exchange. Nevertheless, structural characterization of the NPC interior has remained challenging. Here, we have resolved the dynamic behavior of the permeability barrier inside the central channel of isolated S. cerevisiae NPCs at millisecond timescales by high-speed atomic force microscopy (HS-AFM), which captures dynamic behavior with 2-3 nm lateral and 0.15 nm vertical spatial resolution [1].

Nanoscale characterization of individual isolated yeast NPCs

HS-AFM is a technique using a small cantilever with a nanometer sharp probe tip, which enables direct imaging of proteins in action with the high spatial resolution (Fig. 1a). In collaboration with Prof. Mike Rout (Rockefeller University), we have used HS-AFM to study isolated yeast NPCs. The HS-AFM images revealed isolated NPCs without and with cargoes "caught" in transit (known as central plugs, or CP) [2] (Fig. 1b). Both NPCs without CP (-CP) and with CP (+CP) show eight distinct sub-complexes (or "spokes") that enclose a central channel. Further analysis (Fig. 1c-d) shows that the size of the NPCs is consistent with previous studies [3, 4] whereby the diameter of the isolated NPC does not vary significantly between -CP and +CP NPCs (Fig. 1d). Indeed, the pore depth of -CP NPC is deeper than +CP NPC, indicating that the central channel is obstructed by CP (Fig. 1e).

Dynamic behavior of the permeability barrier within -CP NPC

Although the structure of the yeast S. cerevisiae NPC has been determined at sub-nanometre precision [2, 3], the nanoscopic behavior of its permeability barrier remains elusive. By HS-AFM, we observed the FG Nups to dynamically and repeatedly extend into and retract from the pore interior in -CP NPCs (Fig. 2a). Nevertheless, the FG Nups were occasionally intermingling with each other. Since they are dynamically fluctuating within the central channel, it is difficult to track and analyze individual FG Nup behaviors. In order to collectively quantify FG Nup dynamics within the central channel, we computed radial kymographs that represent a spatial position over time and using an autocorrelation function (ACF) to estimate a decay time. Figure 2b is a plot of average decay times as a function of the distance from the pore center. FG Nup dynamics is most rapid within the central region of the pore and slower near the periphery.

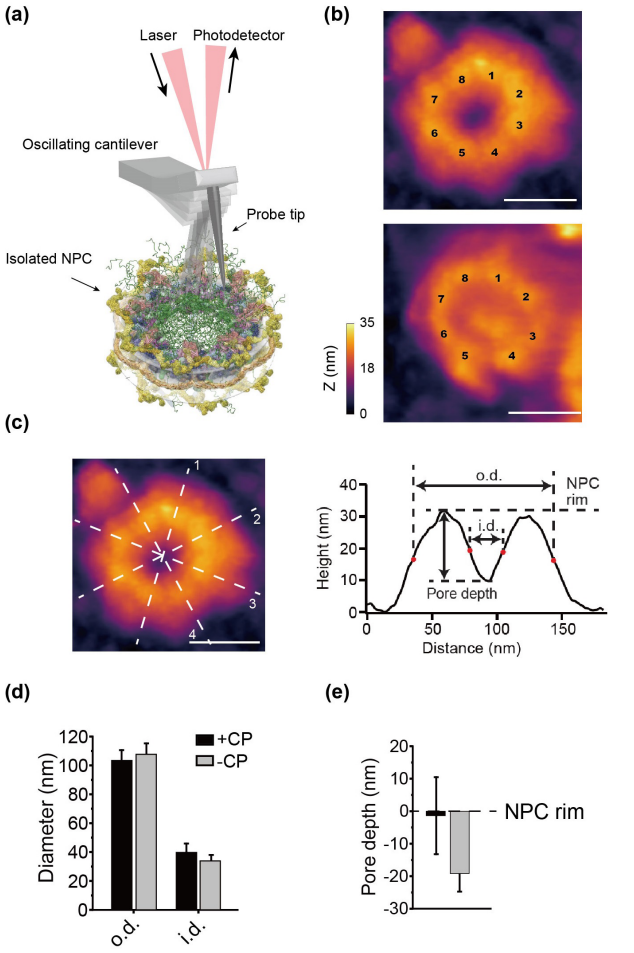

Fig. 1: a) Schematic of HS-AFM. The laser monitors the cantilever position in Z, which is deviated by the shape of a protein under the probe tip. The structure of the isolated NPC is adapted from Kim et al. [3] b) Representative HS-AFM images of isolated -CP (top) and +CP (bottom) NPCs. Eight spokes (numbered) can be resolved from the corresponding cross-sectional profiles (black lines). Scale bars, 50 nm. c-e) NPC diameter was calculated by averaging over 4 different rotations. Outer and inner diameters are given by o.d. and i.d., respectively. Pore depth was measured from the NPC rim. These parameters correspond to the cross-sectional profile shown in c. d and e) Dimensional analysis summary.

Dynamic behavior of the permeability barrier within +CP NPC

Furthermore, we explored the dynamic behavior of the permeability barrier within +CP NPCs. FG Nups can be resolved in the gaps between the CP and the NPC walls (Fig. 3a). In-

terestingly, the FG Nups show to interact with the CP dynamically and intermittently. As in figure 2b, the tau plot represents the decay times averaged over the 10 +CP NPC pores and indicates that the dynamics is faster in the central region and slower at the periphery (Fig. 3b).

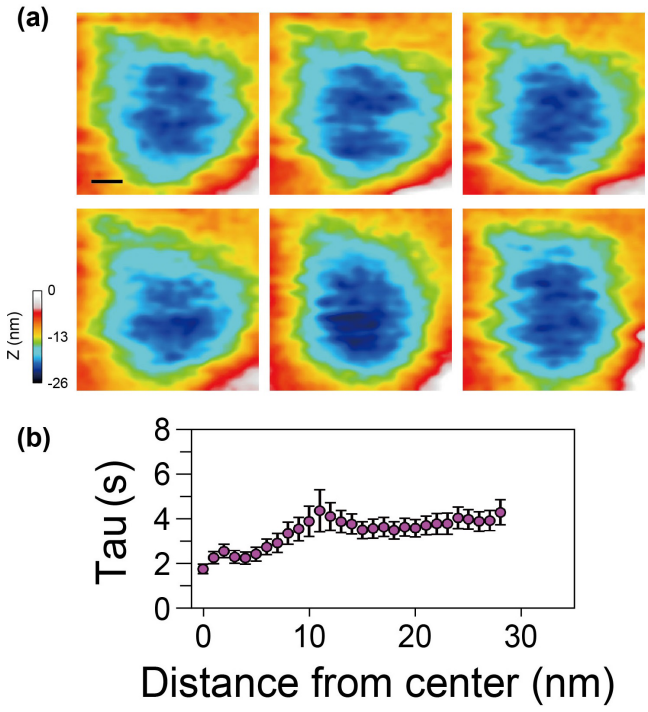

Fig. 2: a) Representative zoom-in HS-AFM images of FG Nup dynamics within a -CP NPC. Scale bar, 5 nm. b) Average tau plot (19 NPCs) as a function of the distance from the pore center. Data are mean ± s.e.m.

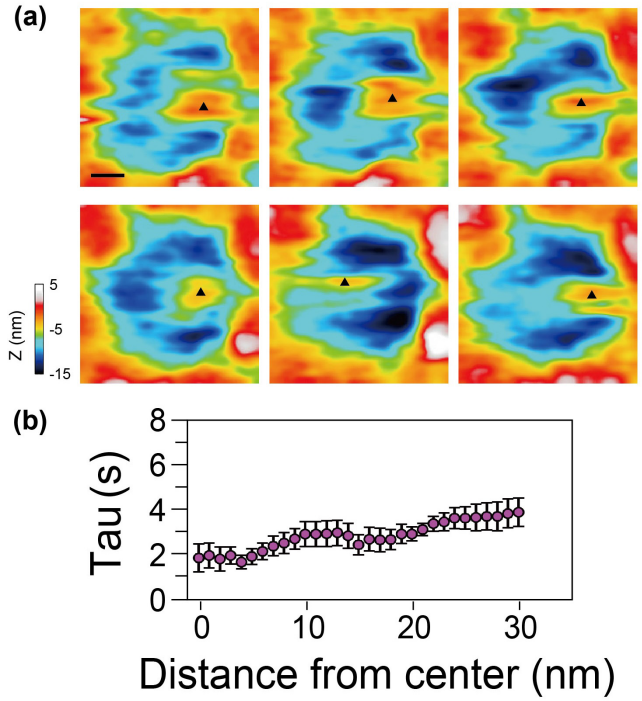

Fig. 3: a) Representative zoom-in HS-AFM images of CP and FG Nup dynamics within a +CP NPC. The black triangles indicate the CP. Scale bar, 10 nm. b) Average tau plot (10 NPCs) as a function of the distance from the pore center. Data are mean ± s.e.m.

Summary

We have used HS-AFM to investigate the dynamic behavior of FG Nups within isolated yeast NPCs to reveal the molecular basis of the NPC permeability barrier. These findings have been further substantiated by HS-AFM analysis of NPCs isolated from mutant strains and Brownian dynamics (BD) simulations of the FG Nup dynamics in collaboration with Prof. Andrej Sali (UCSF) (data not shown). Additionally, certain FG repeats may undergo phase separation in vitro (e.g., hydrogels) [5]. Therefore, we are also trying to resolve the dynamic behavior in hydrogels formed by FG repeats to compare their in vitro dynamics to that in native NPCs.

References

[1] Y. Sakiyama, A. Mazur, L. E. Kapinos, R. Y. H. Lim, Spatiotemporal dynamics of the nuclear pore complex transport barrier resolved by high-speed atomic force microscopy, Nature Nano, 11, 719-724 (2016)

[2] D. Stoffler, K. N. Goldie, B. Feja, U. Aebi, Calcium-mediated structural changes of native nuclear pore complexes monitored by time-lapse atomic force microscopy, J. Mol. Biol. 287, 741–752 (1999)

[3] S. J. Kim, et al., Integrative structure and functional anatomy of a nuclear pore complex, Nature 555, 475–482 (2018)

[4] C. W. Akey, et al., Comprehensive structure and functional adaptations of the yeast nuclear pore complex, Cell 185, 361–378 (2022)

[5] H. B. Schmidt, D. Görlich, Nup98 FG domains from diverse species spontaneously phase-separate into particles with nuclear pore-like permselectivity, eLife 4, e04251 (2015)

Development of a nanofluidic particle size sorter and its biomedical applications

Project P1702: Single organelle size sorting by a nanofluidic device
Project Leader: Y. Ekinci and R. H. Y. Lim
Collaborators: T. Mortelmans (SNI PhD Student), X. Li, T. Braun, P. M. Kristiansen

Research context

Immunoassays are techniques used to detect specific molecules in (bio)fluids such as cell lysate, serum, or urine [1, 2]. These methods are highly specific and sensitive, but traditional immunoassay techniques have lengthy operational protocols, high reagent consumption, and require centralized laboratories. To address these limitations, micro- and nanofluidic devices have gained interest in biomedical research because they can process samples quickly with precise fluid control and low-volume requirements. These devices can also be miniaturized for "lab-on-a-chip" applications. Typically, such devices are two-dimensional, meaning that the height of the channel remains constant, but by varying the height, more complex functions can be achieved. Traditional micro- and nanofluidic devices often require additional infrastructure like syringes or pressure pumps, which limits their portability and use in resource-limited settings [3, 4].

In this project, we developed micro- and nanofluidic devices with channels that vary in all three dimensions to overcome the limitations of traditional immunoassays and active fluidic systems. A thermoplastic device with a vertically tapered channel was developed for size-dependent separation and immobilization of bio-functionalized particles, which were then used for on-chip fluorescent immunosorbent assays. The device is passively operated, using surface tension and specialized capillary constructs to provide a steady, homogeneous flow. A key component of the device is its nano functionality in the vertical axis, which allows for low aspect ratio patterning, reduces resolution requirements, and simplifies downstream fabrication processes. These nanofluidic devices were used for various biomedical applications, including multiplexed antibody detection of SARS-CoV-2 and Influenza A. This was further extended by performing similar assays in diluted whole blood to provide quantifiable insights into patient immune levels, and in doing so overcoming major drawbacks of current point-of-care diagnostics, such as lateral flow assays.

Overall, the use of 3D micro- and nanofluidic devices with channel variations in all three dimensions represents a significant advancement in immunoassay techniques, providing a viable alternative to traditional methods with reduced operational requirements and improved portability.

Results and discussion

The first step in the device fabrication process involved using so-called grayscale electron beam lithography (g-EBL). This is a technique used to fabricate structures with tunable control of resist topography. However, typically, the height of these structures is in the submicron range. This poses a significant drawback for patterning fluidic structures. Therefore, an extensive experimental characterization of the post-exposure behavior of poly(methyl methacrylate) (PMMA) for grayscale structuring with several micrometers in height was performed. The results provided a model that enabled us controlled and reproducible 3D micrometer structuring via g-EBL [5]. However, as g-EBL method is a direct writing technique, it does not allow for the cost-effective fabrication of nanofluidic devices. To overcome this, we replicated the fluidic pattern into a commercial UV-curable material. This negative copy was used to hot emboss the fluidic design into PMMA. This copy contains all the features present in the original g-EBL exposure and facilitates easy upscaling for rapid prototype generation and testing. It was shown that this replicated thermoplastic copy could easily and passively separate five different sizes of nanoparticles from a single 4 µl droplet of a multi-particle mixture (Fig. 1).

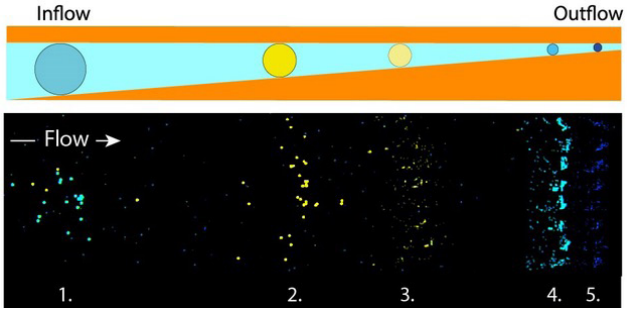

Fig. 1: Top:Schematic of the cross-sectional view of the device. Bottom: Top-down fluorescence microscopy image showing size-dependent particle trapping of polystyrene beads in a capillary-driven 3D nanofluidic device.

To show the potential of this type of thermoplastic nanofluidic devices, it was used for multiplexed on-chip immunoassays for COVID-19 (Fig. 2) reaching nanomolar sensitivities. This technology was further extended to perform multiplexed testing for short and long-term antibodies against both Influenza A and COVID-19 [6]. This was possible in a single microscopic field-of-view, using less than 10 µl of sample volumes and provided a quantifiable insight into patient antibody levels with a nanomolar sensitivity.

To pave the way for potential device commercialization, an alternate thermoplastic patterning method was investigated, namely injection molding, as this is compatible with conventional large-scale nanofoundries. In doing so, high volume and cost-effective device fabrication could be achieved. This was done in close collaboration with the Fachhochschule Nord-West Schweiz (FHNW; Fig. 3) [7].

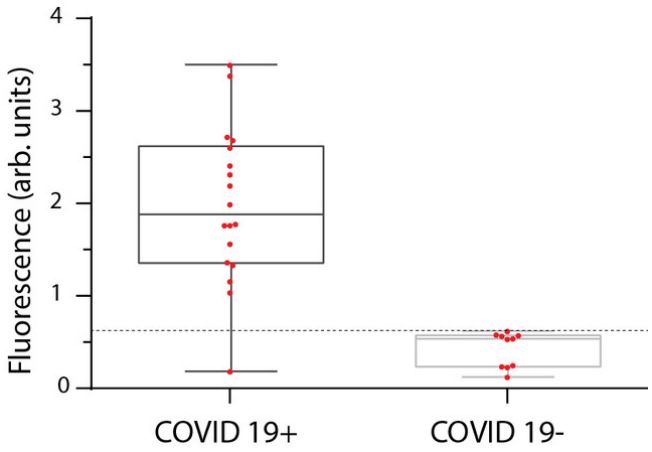

Fig. 2: COVID-19 patient serum test validation. The box plot has whiskers from the minimum to the maximum value, whereas the dashed line graphically indicates the cut-off value separating negative from positive values.

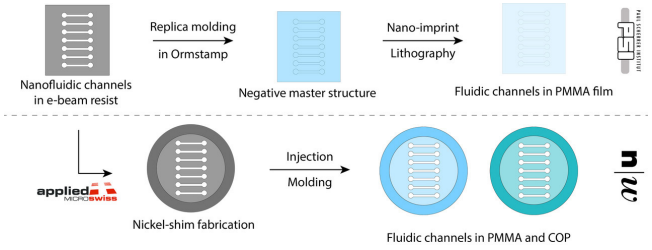

Fig. 3: A schematic illustrating the two investigated fabrication routes for 3D nanofluidic thermoplastic devices: nano-imprint lithography (top) and injection molding (bottom).

Furthermore, we extended the study by employing pre-trapped particles to serve as the support for on-particle fluoresce-linked immunosorbent assays, which reach nanomolar sensitivities without filtering or incubation and washing steps, thereby substantially simplifying the preparation of the immunoassays. Moreover, by leveraging the shallow device dimensions of the device, we demonstrated that sample loading to read-out is possible in less than 10 min and does not require washing steps due to the small detection volume inside the nanofluidic channels. The height profile of the device was further optimized to allow red blood cells to flow through easily, enabling whole-blood immunoassays, without the need for sample pretreatment steps. The presence of red blood cells has no detrimental effect on the sensitivity of the assay.

In conclusion, the research presented in this report showed the in-depth development and optimization of grayscale e-beam lithography to fabricate a master mold with structures containing all the relevant nanoscale topography variations. These master structures enabled cost-effective upscaling of nanofluidic device fabrication using thermoplastic patterning methods such as hot embossing and injection molding. The final thermoplastic devices were used to perform highly sensitive on-chip immunoassays for COVID-19 and Influenza A in a single channel. The devices also allow rapid and sensitive testing of bodily fluids without any need for preparation, filtering, incubation, or washing. Future work will involve the development of a multiplexed immunoassay for the detection of, for example, 15 different biomarkers, antigens, and antibodies in a single field-of-view with channel parallelization (Fig. 4) in addition to size-dependent multiplexing.

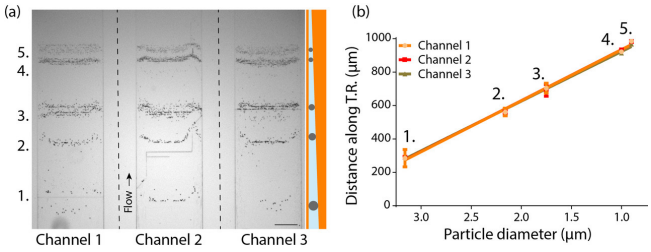

Fig. 4: Size-dependent trapping of 15 calibration-grade nanoparticles. a) bright-field microscope image b) quantified trapping position.

References

[1] A. H. C. Ng, U. Uddayasankar, A. R. Wheeler, Immunoassays in microfluidic systems. Anal. Bioanal. Chem. 397, 991–1007 (2010)

[2] X. Wang, L. Cohen, J. Wang, D. R. Walt, Competitive Immunoassays for the Detection of Small Molecules Using Single Molecule Arrays. J. Am. Chem. Soc. 140, 18132–18139 (2018)

[3] L. Gervais & E. Delamarche, Toward one-step point-of-care immunodiagnostics using capillary-driven microfluidics and PDMS substrates. Lab Chip 9, 3330–3337 (2009)

[4] S. K. Sia & L. J. Kricka, Microfluidics and point-of-care testing. Lab Chip 8, 1982–1983 (2008)

[5] T. Mortelmans, et al. Grayscale e-beam lithography: Effects of a delayed development for well-controlled 3D patterning. Microelectron Eng 225, 111272 (2020)

[6] T. Mortelmans, D. Kazazis, C. Padeste, P. Berger, X. Li, and Y. Ekinci*, Poly(methyl methacrylate)-Based Nanofluidic Device for Rapid and Multiplexed Serological Antibody Detection of SARS-CoV-2, ACS Appl. Nano Mater. 5, 517–526 (2022)

[7] T. Mortelmans, D. Kazazis, J. Werder, P. M. Kristiansen, Y. Ekinci, Injection Molding of Thermoplastics for Low-Cost Nanofluidic Devices. ACS Appl. Nano Mater. 5, 12, 17758–17766 (2022)

Engineering novel binding activity into mechanostable protein scaffolds

Project P1704: Evolving protease enzymes with new sequence specificity using peptide-hydrogel cell encapsulation
Project Leader: M. Nash and S. Reddy
Collaborator: J. López Morales (SNI PhD Student)

Rational design of proteins coupled to artificial directed evolution can adjust the course of natural evolution to obtain the desired properties in a protein. Binding to targets of clinical interest is one of the most needed properties. In this project, we selected a cell receptor called programmed death ligand 1 (PDL1 or CD274) as the bait to the engineered binder. This receptor is overexpressed in cells from different types of cancer and helps them to evade the immune system from eliminating spreading cancer cells [1]. PDL1 is an essential target for immunotherapy against aggressive cancers. The most important binders to PDL1 in such therapy are anti PDL1 antibodies. These, however, can suffer from induced dissociation from metastatic cancer cells if subjected to mechanical stresses in the bloodstream. Currently, there is no antibody or scaffold that can alleviate this need.

Therefore, we are studying the evolvability of an alternative scaffold to develop mechanostable antibody mimics that bind to PDL1 under shear stress. These antibody mimics are based on a single protein domain highly resistant to chemical, thermal and mechanical denaturing forces. We are rationally engineering the scaffold by a bioinformatic- and biophysics-guided approach to select and engineer loops amenable to random mutagenesis for a synthetic library with potential binding to PDL1. To preserve the mechanical properties of the scaffold, only exposed positions were considered and their modification showed no negative effect either on thermal stability or the mechanical stability.

To design a scaffold library, degenerated codons were employed with different amino acid content and to introduce bias towards residues that play a strong role in binding interactions. The mutant gene library was then constructed by isothermal assembly using a BioXP microfluidic-liquid handler robot. Full length genes were chemically co-transformed with a linearized plasmid into EBY100 yeast cells for homologous gap repair and in vivo assembly. A library with a diversity of $1x10^8$ unique variants was chosen, displayed on the surface of yeast cells [2] (Fig. 1a) and challenged against soluble PDL1. Fluorescence activated cell sorting was employed to evaluate the interaction between the displayed scaffold and PDL1 and to isolate binders at decreasing concentrations of antigen. This allowed to reduce the complexity of the library while enriching for the best binders (Fig. 1b). After six cycles of enrichment, ten single clones from three different rounds were isolated on plates, cultured independently, and treated for plasmid extraction. Sanger sequencing and sequence alignment analysis showed that there was a reduction in the diversity of the observed mutations in the randomized loops as a function of the decreasing concentration of PDL1. These results indicate that binders of higher affinity have been progressively enriched.

A deeper analysis on the group of binders isolated at 50 nM PDL1 was performed to observe the apparent dissociation constant of the best binders. On-yeast titration of PDL1 revealed that the best binder isolated during the selection stage of the campaign was the mutant scaffold J, which showed a K_D=0.78 µM PDL1 (Fig. 1c). Taking into account the non-existing binding activity of the template domain to PDL1, (no binding observed at 9.3 µM PDL1) the newly acquired capacity of sub-micromolar PDL1 binding indicates a 12-fold improvement.

Current efforts are focused on characterizing the full sequence repertoire after a binding round at 10 nM PDL1 (Fig. 1d) by Next-Generation-Sequencing. Here, deep sequencing will identify the truly enriched motif that confers PDL1 binding. New rounds of affinity maturation will follow and imply creating a new library using the identified motif as the new starting template and accumulate mutations as rounds of enrichment progress. Final characterization of the mechanical resistance to unfolding due to shear stress[3] will be performed to corroborate that the starting mechanostability of the domain was preserved.

We envision that the outcome of this project will constitute a novel type of binding function, engineered into a scaffold that already showed resistance to chemical, thermal and mechanical stimuli. Moreover, our methodology will ease the development of diagnostic and therapeutic solutions for cancer malignancies, and an efficient platform for directed evolution of proteins within the rising field of mechanobiology.

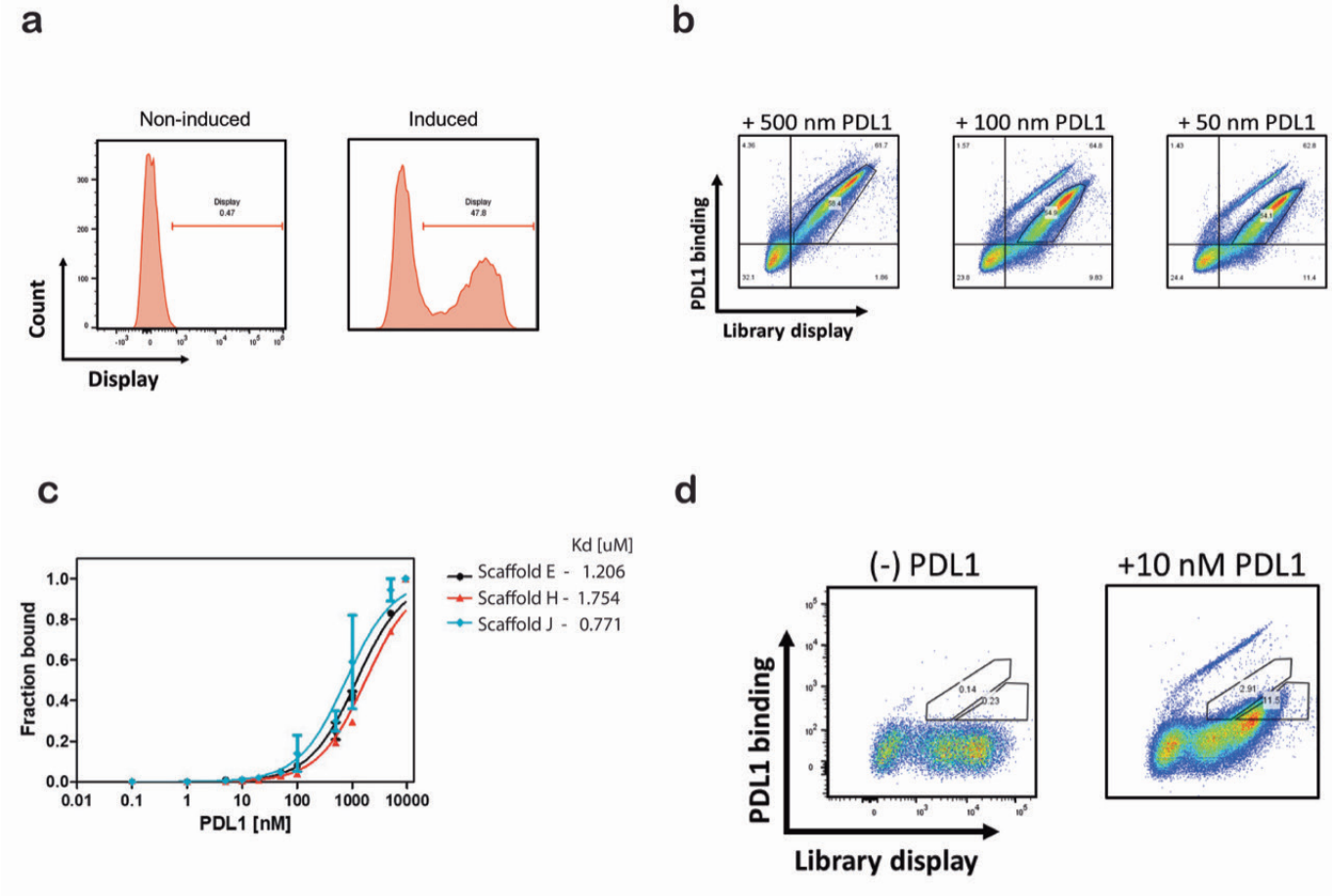

Fig. 1: Strategy for engineering mechanical properties of scaffold domains. a) Displaying fraction of a scaffold library on the surface of yeast cells measured by flow cytometry. b) Fluorescence activated cell sorting cycles of enrichment at decreasing concentration of PDL1 to enrich binders. c) On-yeast titration curves of PDL1 from the best three hits obtained at a sorting experiment using 50 nM PDL1. The best binder, scaffold J was successfully isolated (K_D=0.77 μM PDL1). d) Sorting and isolation of binders at 10 nM PDL1. The shown gates indicate high and low affinity clustering that will undergo deep sequencing.

References

[1] J. M. Chemnitz, R. V. Parry, K. E. Nichols, C. H. June, J. L. Riley, SHP-1 and SHP-2 associate with immunoreceptor tyrosine-based switch motif of programmed death 1 upon primary human T cell stimulation, but only receptor ligation prevents T cell activation. J. Immunol., 173, 945–54 (2004)

[2] E. T. Boder & K. D. Wittrup, Yeast surface display for screening combinatorial polypeptide libraries, Nat. Biotechnol. 15, 553–557 (1997)

[3] M. S. Santos, H. Liu, V. Schittny, R. Vanella, M. A. Nash, Correlating Single-Molecule Rupture Mechanics with Cell Population Adhesion by Yeast Display. Biophysical Reports, 2(1) (2022)

Towards label-free HTS in enzyme engineering

Project P1705: Genetic selection of nanocatalysts
Project Leader: S. Panke, P. S. Dittrich, and T. R. Ward
Collaborator: E. Rousounelou (SNI PhD Student)

Introduction

Directed evolution represents a powerful tool for developing biocatalysts for synthetic organic chemistry and homogeneous catalysis, including new-to-nature transformations [1, 2]. A successful directed evolution experiment depends on two factors: genetic diversity and high throughput screening/selection methods. Thanks to the substantial advances in our ability to generate genetic diversity and large variant libraries, the main limitation of each directed evolution experiment is the efficiency of screening methods for the identification of desired variants [3]. Conventional screening methods rely mostly on optical (fluorescent) readouts, which often have a defined and limited reaction scope, since an optical readout is usually not easily related to the outcome of a biotechnologically relevant chemical reaction [4]. While methods employing mass spectrometry (MS) are label-free (and therefore quite general) and can directly analyze products of useful chemical reactions, they are currently slow and destructive. Consequently, they require elaborate workflows to separately store the genetic information than can be retrieved in case of success.

To overcome these fundamental problems, we are developing a novel high-throughput screening (HTS) methods that [i] addresses the speed issue by coupling microfluidics with MALDI MS and [ii] compensates the destructiveness of MS analysis by co-analyzing the product or side-products of the reaction with unique peptide barcodes that maintain the genotype-phenotype linkage. In figure 1, an overview of the method is illustrated. Firstly, a library of unique DNA and peptide barcode combinations is generated, which is identified via next generation sequencing. The enzyme variant library is then cloned into the barcoded vectors so that every variant is associated with a unique combination of a DNA and a peptide barcode. The barcoded enzyme library is transformed into E. coli competent cells, followed by single cell spotting onto a picolitre array and cell lysis (see Fig. 1.1). After enzyme/peptide barcode expression, each sample is incubated with candidate substrate(s) and cofactor(s) (see Fig. 1.1) and the reaction is analyzed by MALDI-TOF MS. The mass spectrum of each sample delivers information about the product amount or distribution, but also its unique identity via the peptide barcode (see Fig. 1.2). The latter is uniquely linked to the variant, but also to a DNA barcode and thus, after designing DNA primers specific to the DNA barcode, the desired variant can be retrieved by PCR, from a large pool of variants, and the genotype can be determined by sequencing (see Fig. 1.3).

Intervention-free production and release of peptide barcode and enzyme variant in E. coli

The proposed method depends on the detection of the peptide barcode and the reaction product(s) during MALDI-MS analysis. Consequently, we need to ensure that both the peptide barcode and the enzyme variant are expressed sufficiently.

For that reason, each clone is transformed with two plasmids. The first plasmid, which is the "barcoded" plasmid, carries an enzyme variant under the control of an inducible promoter (P$_{T7}$). Moreover, each variant is flanked with a unique set of DNA barcodes and a unique peptide barcode. The second plasmid, which is called the "lysis" plasmid, carries the gene template of protein E under the influence of promoter σ^S. This protein is a coliphage protein that forms pores perforating the cell membrane and wall of E. coli lead-

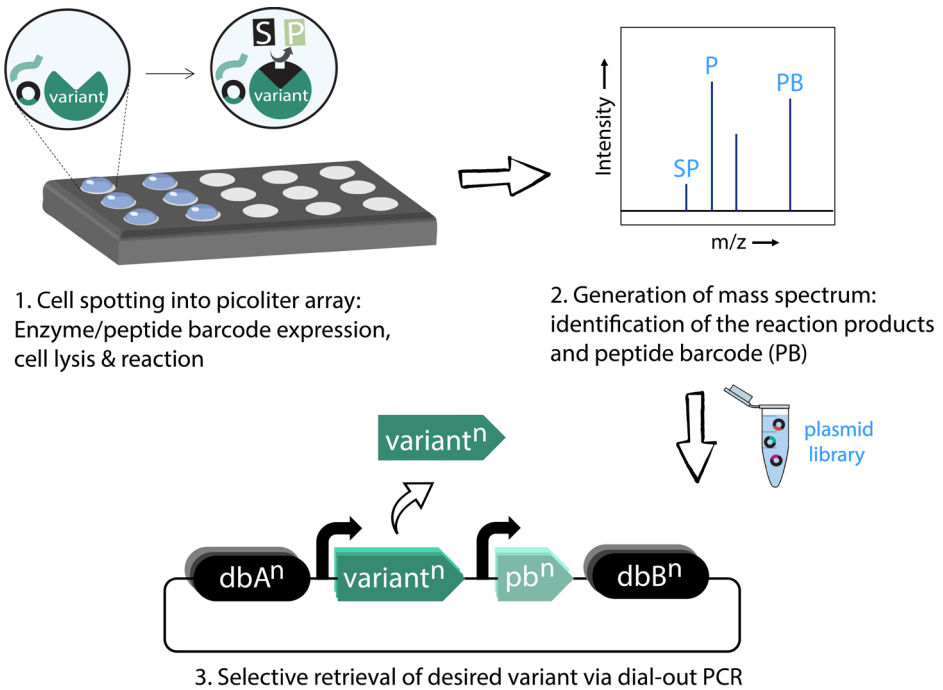

Fig. 1: Simplified overview of the proposed HTS method. For further information, refer to text. SP: side-product ; P: product ; PB: peptide barcode ; db: DNA barcode ; pb: peptide barcode gene template

ing to a release of cytosolic proteins and eventually complete cell lysis in the late exponential to stationary growth phase. In autoinduction medium the two plasmids lead to an autonomous protein production and release system. The autoinduction medium that is used is ZYM-50525. The principle behind that medium is based on carbon sources present in the medium that are metabolized differentially to promote high density cell growth and automatically induce protein expression driven by lac promoters.

Picoliter well array for bacterial growth, protein production and reaction analysis

To address the speed issue, a picoliter well array (PWA) was designed and manufactured by Dr Todd Duncombe, from the Dittrich lab. Each well has a 50 µm diameter and a volume of approximately 39 pl.

After bulk disposition of the cell solution on top of the PWA, single cells are trapped inside the wells and let grown to a high-density culture. During cell growth, enzyme expression is induced via the autoinduction medium ZYM-5052. When enough target enzyme variants and peptide barcodes are produced and nutrients become scarce, protein E is expressed leading to cell lysis and release of the enzyme variant and the peptide barcode into the extracellular space. Subsequently, the PWA is cooled down and placed under vacuum to deposit the matrix on top of the array via sublimation [6] and each well is analysed in MALDI-MS.

Unique identification of enzyme variant via MALDI-MS analysis of its peptide barcode

The peptide barcodes are encoded on the same plasmid that encodes the enzyme variant and they serve as the unique identifiers of the variant they are associated with during MALDI-MS analysis. For that reason, each barcode is composed of genetically encoded peptide sequences designed to produce a unique and detectable MS signal.

The peptide barcode library was initially designed in silico using a python script. Subsequently, 50 peptides from the library were randomly selected, synthesized and analyzed in MALDI-MS. All the peptides showed high ionization efficiency and were detectable even at low concentrations (0.006 µM).

Although recombinant protein synthesis in E. coli is a standard method of genetic engineering, the synthesis of short peptides is not. One of the central reasons for that might be that short peptides are an important nutrient source in E. coli and therefore might be difficult to accumulate in the cytoplasm. This problem will be tackled by ensuring that peptide production is as efficient as possible and by combining 3 peptides through protease recognition sites that together will compose one bigger peptide barcode. Each peptide barcode will be enzymatically digested right before MS analysis, producing a characteristic peptide fingerprint during MALDI-MS.

Selective retrieval of desired variant by dial out PCR

Although we can uniquely identify each clone during MALDI-MS analysis based on the MS signal of each peptide barcode, the sample and with it the enzyme variant is still destroyed in the process due to the destructive nature of ionization. To keep the genotype-phenotype linkage and retrieve the sequence of the enzyme, we need to map the peptide barcode information back to the specific plasmid from which it originated, and which is still available from a duplicate of the plasmid library. This mapping is achieved via barcoded plasmids that are “tagged” with a unique peptide barcode sequence and a unique set of semi-degenerate DNA barcode sequences that flank each enzyme variant present in the pool (see Fig. 1.3). The unique set of DNA barcodes can then be used to design PCR primers and selectively retrieve the gene in question from the duplicate library.

References

[1] U. T. Bornscheuer et al. Engineering the third wave of biocatalysis, Nature 485, 185-194 (2012)

[2] M. Jeschek, S. Panke, T. R. Ward, Artificial Metalloenzymes on the Verge of New-to-Nature Metabolism, Trends Biotechnol 36, 60-72 (2018)

[3] C. Zeymer, D. Hilvert, Directed Evolution of Protein Catalysts, Annu Rev Biochem 87, 131-157 (2018)

[4] M. Wojcik, A. Telzerow, W. J. Quax, Y. L. Boersma, High-Throughput Screening in Protein Engineering: Recent Advances and Future Perspectives, Int J Mol Sci 16, 24918-24945 (2015)

[5] F. W. Studier, Protein production by auto-induction in high density shaking cultures, Protein Expr Purif 41, 207-234 (2005)

[6] J. A. Hankin, R. M. Barkley, R. C. Murphy, Sublimation as a method of matrix application for mass spectrometric imaging, J Am Soc Mass Spectrom 18, 1646-1652 (2007)

Fiber-based cavity optomechanics

Project P1706: Ultrasensitive force microscopy and cavity optomechanics using nanowire cantilevers
Project Leader: M. Poggio and F. Braakman
Collaborator: D. Jaeger (SNI PhD Student)

Introduction

Nanoscale mechanical resonators such as thin membranes or nanowire crystals have the potential to uniquely enrich the capabilities of force microscopy. Currently, force microscopy techniques rely heavily on micron-sized cantilevers as force transducing elements, such as silicon beams or quartz tuning forks. In recent years, a new direction has emerged that replaces these conventional cantilevers with bottom-up grown nanoscale structures, such as carbon nanotubes or nanowires. Their small size and nearly defect-free crystal structures leads to potentially record force sensitivities, low mechanical losses and high operation frequencies. Several experiments have recently demonstrated the potential and versatility of this approach. In our own lab, we have demonstrated a new type of force microscopy using nanowires, in which we have shown sensitivity not only to the magnitude of forces, but also their direction [1].

Furthermore, nanomechanical resonators enable fundamental studies into the hybridization of different physical quantities, such as light and mechanical motion. Such hybrid systems form a promising platform to implement measurements operating at the limits imposed by quantum uncertainty and quantum non-demolition measurements. They may also allow investigation of quantum decoherence mechanisms, entanglement, and ultimately the transition from quantum to classical physics. We focus on two types of hybrid structures: nanowire heterostructures and 2D membranes with defects. Both systems combine excellent mechanical properties with the possibility of hosting optically active qubits in the form of embedded quantum dots or crystal defects. These qubits themselves already form interesting objects of study, as they can be used to sensitively measure electric and strain fields [2]. Moreover, when coupled to a mechanical degree of freedom, qubits can – through their nonlinear character – generate a large enhancement of the radiation pressure interaction between light and matter, as well as boost optical cooling of the mechanical resonator [3].

Our aim is to enable operation of such hybrid systems in regimes dominated by quantum effects, by improving optical excitation and detection of the mechanical resonator and embedded quantum emitters. To reach this goal, we will:
1: Integrate such hybrid systems into high-finesse optical cavities. Read-out of both the mechanical motion and of the photons emitted by embedded quantum emitters can be much improved by placing the system inside an optical cavity. Moreover, such a cavity allows to strongly couple the motion as well as quantum emitters to the cavity light field. In particular, this provides a straightforward path to the realization of a tri-partite hybrid system [3]. Such a tri-partite system allows to significantly enhance optical cooling and will allow the observation and utilization of quantum states of motion.
2: Implement resonant excitation of quantum emitters in a force microscopy setup. This will significantly reduce the optical linewidth of the qubits and should allow for mechanical displacement sensitivity reaching the Heisenberg uncertainty limit.

Optical Setup and Cavity

We have constructed a Fiber Fabry-Perot cavity (FFPC) for membrane in the middle optomechanics at cryogenic temperatures. The cavity can be measured through reflection or transmission and can be stabilized using a Pound-Drever-Hall scheme. This will enable optomechanical experiments, such as optical cooling of a mechanical oscillator, as well as cavity QED experiments, allowing the measurement of a tri-partite hybrid system.

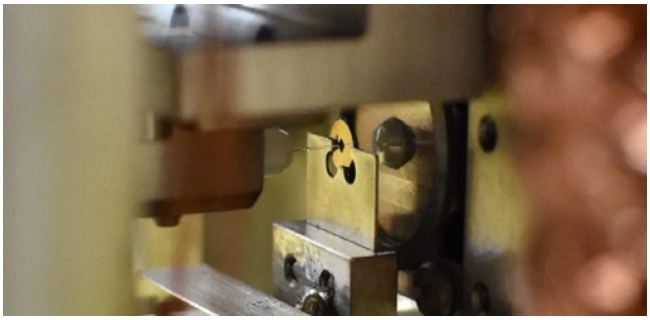

Fig. 1: The FFPC mounted in a probe operating in vacuum and low temperature (4 K).

We achieved a stable lock of the cavity length within a few percent of the cavity linewidth (Fig. 2) both at room temperature and at 4 K. Until now this was only possible with FFPC's that were severely limited in finesse or tunability, we reported our findings in [4].

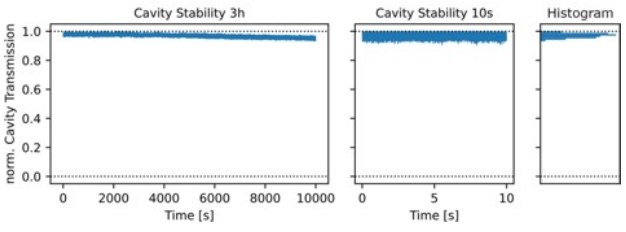

Fig. 2: Normalized cavity transmission signal as a function of time, showing long term stability.

hBN drum resonators

As a first step towards creating a tri-partite system, we focus on drums of hexagonal boron-nitride (hBN). hBN is a host for crystal defects which can serve as quantum emitters. These emitters are ultra-bright, highly stable and can be

observed at room temperature [5]. In addition, hBN drums are mechanical oscillators with favorable frequencies (MHz regime), low mass, and small mode volume.

We have successfully used high temperature annealing recipes to create emitters located at edges of hBN flakes, and we were able to observe several such emitters in spectroscopy measurements.

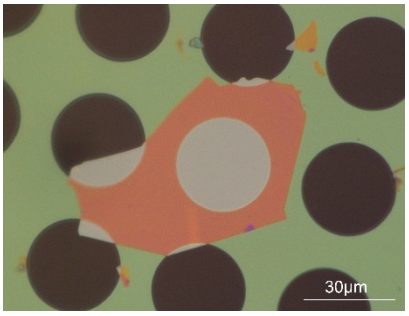

Fig. 3: Optical microscope image of an hBN drum resonator on a Norcada SiN membrane.

To use these flakes as mechanical resonators that can be positioned inside our cavity, we have developed a wet transfer technique that allows us to place them on top of a silicon nitride (SiN) hole grid membrane, resulting in hBN drum resonators (Fig. 3).

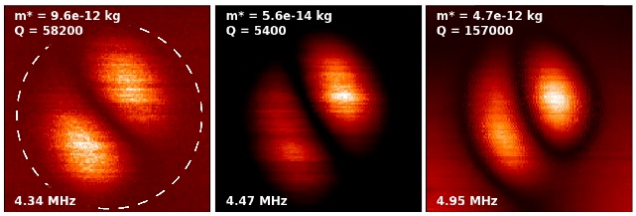

Fig. 4: Mode images of several hybridized modes, m and Q extracted from thermal spectra. The white dashed circle indicates the edge of the hBN drum.*

We have characterized both the spectral and spatial dependence of the drum's mechanical modes, revealing hybridization between the SiN membrane and the hBN drum. The SiN membrane lends its high Quality factor (Q) to the hBN drum modes, while also increasing the effective mass (m*), depending on the degree of hybridization (Fig. 4 and Fig. 5).

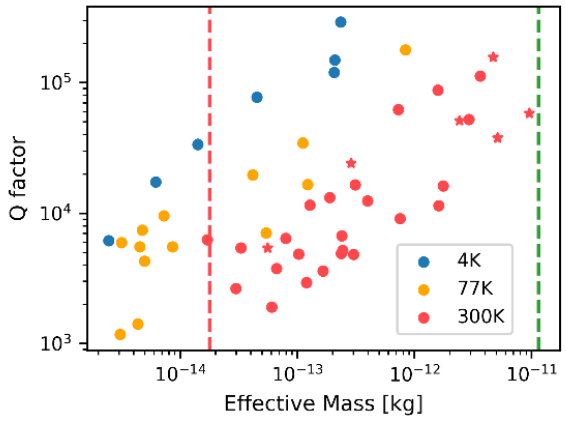

Fig. 5: m vs. Q of the hBN modes at different temperatures. Higher values indicate more influence of the SiN membrane. Dashed vertical lines represent the expected m* of the hBN drum (red) and the SiN membrane (green) at room temperature.*

This effect could be exploited to engineer hybrid drum/membrane modes that combine the unique properties of 2D materials with the high Q of SiN membranes for optomechanical or sensing applications. We are currently preparing a manuscript about these findings. Finally, we have integrated the drums into our FFPC to characterize the optomechanical interaction. As a first step, we were able to measure the coupling strength by displacing the hBN drum along the cavity axis.

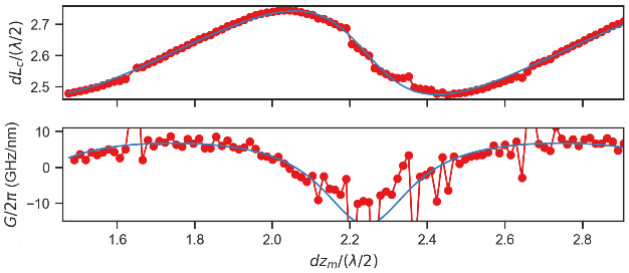

Fig. 6: Cavity resonance length modulated by the position of the hBN drum along the cavity axis (top), extracted dispersive coupling G (bottom).

The measured dispersive coupling of 10 GHz/nm compares favorably to state-of-the-art systems [6] and underlines the potential of our setup.

Outlook

We plan to further explore the optomechanical interaction by performing optomechanically induced transparency experiments. In parallel, we are working on a way to deterministically position quantum emitters within hBN flakes, paving the way towards a fully coupled tripartite system. Moreover, we want to use our highly versatile experimental platform to investigate the interaction of other samples with our cavity, such as nanowires, carbon nanotubes or 2D magnets.

References

[1] N. Rossi, F. R. Braakman, D. Cadeddu, D. Vasyukov, G. Tütüncüoglu, A. Fontcuberta i Morral, and M. Poggio, Vectorial scanning force microscopy using a nanowire sensor, Nat. Nanotechnol. 12, 150 (2017)

[2] M. Montinaro, G. Wüst, M. Munsch, Y. Fontana, E. Russo-Averchi, M. Heiss, A. Fontcuberta i Morral, R. J. Warburton, and M. Poggio, Quantum dot opto-mechanics in a fully self-assembled nanowire, Nano Lett. 14, 4454 (2014)

[3] J. Restrepo, C. Ciuti, and I. Favero, Single-Polariton Optomechanics, Phys. Rev. Lett. 112, 013601 (2014)

[4] T. Ruelle, D. Jaeger, F. Fogliano, B. Braakman and M. Poggio, A tunable fiber Fabry–Perot cavity for hybrid optomechanics stabilized at 4K, Rev. Sci. Instrum. 93 095003 (2022)

[5] T. Tran, K. Bray, M. Ford et al., Quantum emission from hexagonal boron nitride, Nat. Nanotechnol. 11, 37–41 (2016)

[6] F. Rochau, I. Sanchez Arribas, A. Brieussel, SS. tapfner, D. Hunger, E. M. Weig, Dynamical Backaction in an Ultrahigh-Finesse Fiber-Based Microcavity, Phys. Rev. Applied 16, 014013 (2021)

Origin of moiré excitons in a $WSe_2/MoSe_2$ bilayer

Project P1707: Nano-photonics with van der Waals heterostructures
Project Leader: R. J. Warburton and I. Zardo
Collaborators: L. Sponfeldner (SNI PhD Student) and N. Leisgang

Exciting an electron across the band gap of a semiconductor leaves behind a hole in the valence band. An exciton is a bound electron-hole pair. Excitons in two-dimensional semiconductors, MoS_2 for instance, have very large binding energies, hundreds of meV, such that they are stable even at room temperature. The electron and hole are tightly bound on account of the strong confinement in the vertical direction, the large effective mass of both electron and hole, and the modest permittivity of both MoS_2 and the encapsulation material, h-BN. On the one hand, excitons are a robust sensor of spin: they can be injected into a valley with a particular spin, simply by choosing the polarisation of light [1,2]. On the other hand, excitons in monolayer MoS_2 cannot be tuned with electrical fields [3]. This restricts possibilities: it is difficult to transport an exciton across a device with an electric field; it is likewise difficult to create a single-exciton trap electrically in order to create an array of single-photon emitters. These drawbacks can be potentially overcome with a bilayer system, bilayer MoS_2 [2, 4] or $MoSe_2/WSe_2$. In the latter case, the electron is trapped in one layer, the hole in the other. The physical separation between electron and hole equips the exciton with a dipole moment such that the exciton responds strongly to an applied electric field. Furthermore, by introducing a twist between the two layers, a moiré potential is created – an array of potential minima, each of which may act as an exciton trap. The moiré pattern is sketched in figure 1. In practice, implementation of the bilayer concept has led to a range of apparently contradictory results, in particular on introducing a twist. The simple picture is inadequate and even the most basic properties of the excitons are contested.

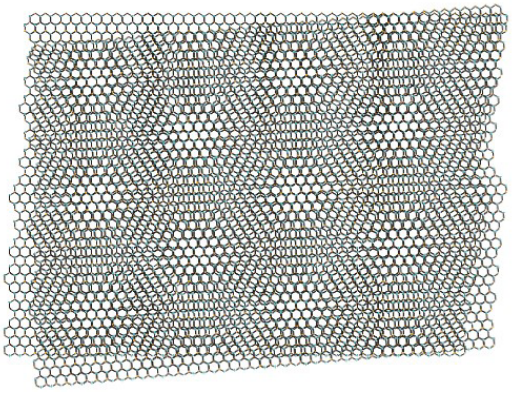

Fig. 1: Moiré superlattice formed when stacking two monolayers at an angle on top of each other.

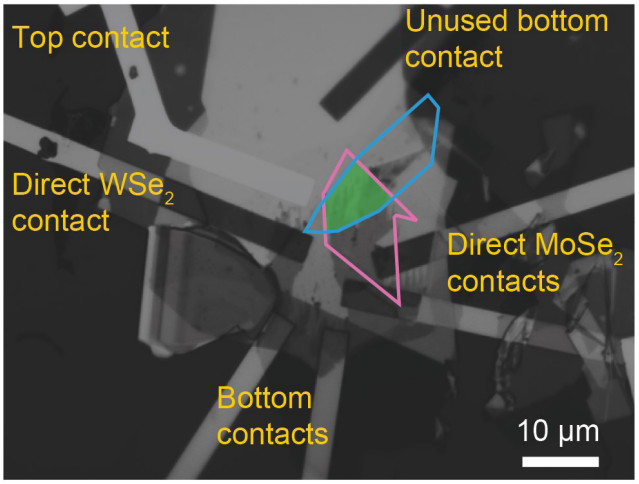

Fig. 2: Optical microscope image of the gated device with marked electrical contacts. The $MoSe_2$ (WSe_2) monolayer is highlighted by the pink (blue) shape. The bilayer region is shaded in green.

Our approach to resolving the nature of the lowest-energy excitons in bilayer $MoSe_2/WSe_2$ is, first, to construct a high-quality, gated device. Figure 2 shows an optical microscope image of the studied device. The bilayer twist angle is about 3 degrees, so-called R-stacking. (H-stacking has a twist with angles close to 60 degrees.) The two monolayers were aligned by using optical second-harmonic generation to determine the axes of the two crystals before fabricating the device [5]. The gates give independent control of the electron concentration in the layers and the applied electric fields. Second, we perform a hyperspectral analysis at cryogenic temperatures.

At low excitation powers, the photoluminescence (PL) shows a double-peak structure (see Fig. 3a). This is in itself revealing: the simplest model of an interlayer exciton predicts a single-peak. Both peaks exhibit a strong shift in energy with applied electric field: this demonstrates that both excitons have an interlayer character. However, on increasing the laser power as shown in figure 3b, the upper peak increases in intensity more rapidly than the lower peak such that at the highest power, the upper peak dominates the spectrum, a striking and unusual feature. The power dependence is clear evidence that the peaks arise from processes which are different in at least one key respect. This difference was resolved in the hyperspectral analysis.

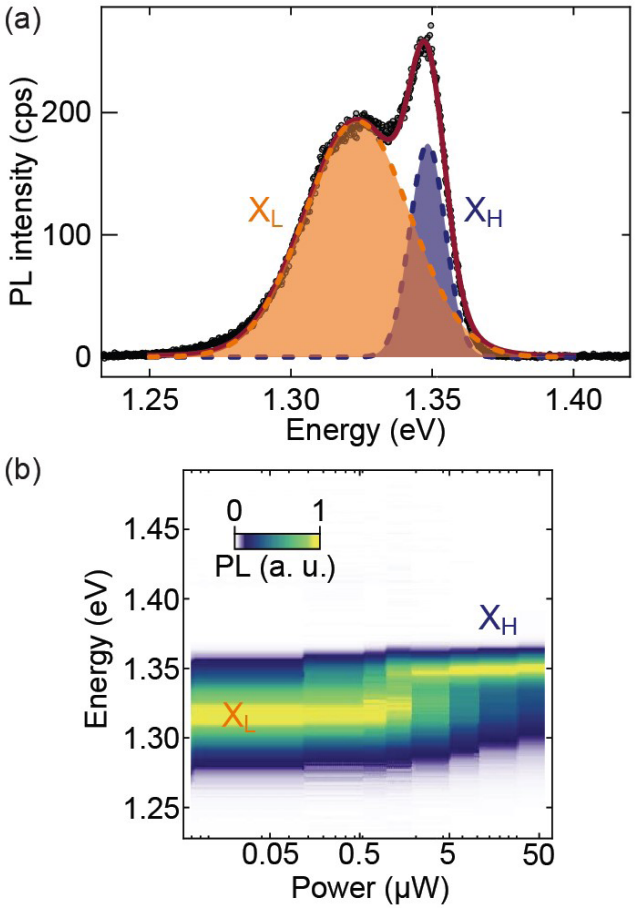

Fig. 3: a) Low-temperature photoluminescence (PL) spectrum of interlayer excitons in a $MoSe_2/WSe_2$ bilayer exhibiting a double-peak structure consisting of a lower peak XL and an upper peak XH. b) Normalised PL spectra as a function of laser power. On increasing the power, the upper peak XH gains in importance and at the highest power dominates the spectrum.

We are led to the conclusion that the lower-energy peak arises from a momentum-indirect transition and that the higher-energy peak arises from a momentum-direct transition. While the momentum space origin is different for the two excitons, the real space origin of both excitons corresponds to the minimum of the moiré potential. The experiments reveal that the R-stacked twisted bilayer has an indirect bandgap. This has been proposed also for the H-stacked twisted bilayer [6, 7]. The experiments demonstrate the importance of the moiré potential. This can be exploited in the future to create close-to-flat bands in which electron-electron correlations become profound.

References

[1] J. G. Roch, G. Froehlicher, N. Leisgang, P. Makk, K. Watanabe, T. Taniguchi, R. J. Warburton, Spin-polarized electrons in monolayer MoS_2. Nat. Nanotechnol. 14, 432-436 (2019)

[2] L. Sponfeldner, N. Leisgang, S. Shree, I. Paradisnos, K. Watanabe et al., Capacitively and inductively coupled excitons in bilayer MoS_2. Phys. Rev. Lett. 129, 107401 (2022)

[3] J. G. Roch, N. Leisgang, G. Froehlicher, P. Makk, K. Watanabe, T. Taniguchi, C. Schönenberger, R. J. Richard, Quantum-Confined Stark Effect in a MoS_2 Monolayer van der Waals Heterostructure. Nano Lett. 18, 1070-1074 (2018)

[4] N. Leisgang, S. Shree, I. Paradisanos, L. Sponfeldner, et al. Giant Stark splitting of an exciton in bilayer MoS_2. Nat. Nanotechnol. 15, 901-907 (2020)

[5] N. Leisgang, J. G. Roch, G. Froehlicher, et al. Optical second harmonic generation in encapsulated single-layer InSe. AIP Advances 8, 105120 (2018)

[6] B. Miller, A. Steinhoff, B. Pano, J. Klein, F. Jahnke, A. Holleitner, U. Wurstbauer, Long-lived direct and indirect interlayer excitons in van der Waals heterostructures. Nano Lett. 17, 5229-5237 (2017)

[7] E. Barré, O. Karni, E. Liu, A.L. O'Beirne, X. Chen et al. Optical absorption of interlayer excitons in transition-metal dichalcogenide heterostructures. Science 376, 406-410 (2022)

Extremely efficient preparation of plasma membrane vesicles as an addition to existing EVs

Project P1801: Bioinspired nanoscale drug delivery systems for efficient targeting and safe in vivo application
Project Leader: J. Huwyler and C. Palivan
Collaborator: C. Alter (SNI PhD Student)

Introduction

Extracellular vesicles (EV) are extremely important for the new era of bio-pharmaceutical engineering due to their potential for therapeutic applications [1]. EVs are cell derived membranous vesicles which carry cell specific lipids, proteins (i.e., enzymes, cell adhesion molecules, cluster of differentiation proteins (CD)), nucleic acids (i.e., various RNA and DNA), metabolites, organelles, and even viruses [2,3]. EVs are classified into two main categories based on their biogenesis: exosomes and ectosomes. Exosomes are small EVs (40 to 150 nm diameter), originate from the endosomal compartment of the cell, and are continuously released to the surrounding by prokaryotic and eukaryotic cells through exocytosis of multivesicular bodies and amphisomes [3]. Ectosomes, on the other hand, form by direct budding/blebbing of the plasma membrane and are a large group of different types of vesicles including microvesicles, apoptotic bodies (ApoBDs) and vesicles (ApoEVs), and large oncosomes with sizes ranging from 50 to >1000 nm [3]. Therapeutic nucleic acids, proteins, or small molecular weight drugs were loaded exogenously into EVs and successfully delivered to cells in vitro and in vivo, but only few EV technologies have progressed into clinical trials. Indubitably, one of the major drawbacks for clinical translation is the EV production [4]. Typical EV secretion rates range between 60–170 exosomes/cell/hour, depending on the cell line [5].
To overcome this hurdle, we developed a valuable alternative to the standard EV preparation protocol, which can be applied to nearly all cell lines and even primary cells. It is based on the generation of chemically induced giant plasma membrane vesicles (GPMVs), which are harvested and processed by size homogenization into nano-sized plasma membrane vesicles (nPMVs). Further, we evaluated the cellular interaction of nPMVs with in vitro cell cultures and zebra fish embryo (ZFE) and compared them to exosomes.

Material and methods

Chemical vesiculation agents (paraformaldehyde and dithiothreitol) were used to induce cellular injury and membrane blebbing in Huh7 and HEK293 cells. The vesiculation started a few minutes after incubation (37°C and 5% CO_2) and the produced GPMVs (ApoBDs) were harvested from donor cells after 6 h.

Then, GPMVs were stained with 1 µM of a lipophilic dye (DiI) and homogenized through filter extrusion in order to produce nPMVs (ApoEVs). Exosomes were produced as previously described [6] and labeled with 1 µM DiI. DiI labeled DOPC and DOPC:PS liposomal formulations, serving as negative and positive controls, were produced by thin-film hydration method [7]. Cell viability was assessed using MTS assay [8]. In vitro uptake studies were performed with flow cytometry. ZFE experiments were conducted as previously described [9].

Results and discussion

First, we compared the production rate of our newly developed nPMVs preparation protocol with an existing exosome preparation protocol and found production rates of 1100-1400 particles/cell/hour for the nPMV and 5-7 particles/cell/hour for the exosome preparation protocol, respectively. Indicating that our nPMV preparation protocol is at least an order of magnitude more efficient. Next, we incubated HEK293/Huh7 nPMVs and exosomes, DOPC:PS, and DOPC liposomes with Huh7 cells for 24 h and analyzed the cell viability. Cell viability was not significantly changed by nanoparticles (Fig. 1a). Uptake of these nanoparticles were measured by flow cytometry after incubation for 15 min, 1, 4, and 24 h (Fig. 1b). We observed a time-dependent uptake (normalized relative fluorescence unit (RFU)) in Huh7 cells for all particles. The uptake was fast in the first 4 hours, then started to saturate and reached the highest value after 24 hours. Huh7/HEK293 nPMVs and the respective exosomes showed comparable uptake, which was slightly higher than the uptake of DOPC:PS liposomes. Negligible uptake of DOPC liposomes was measured.

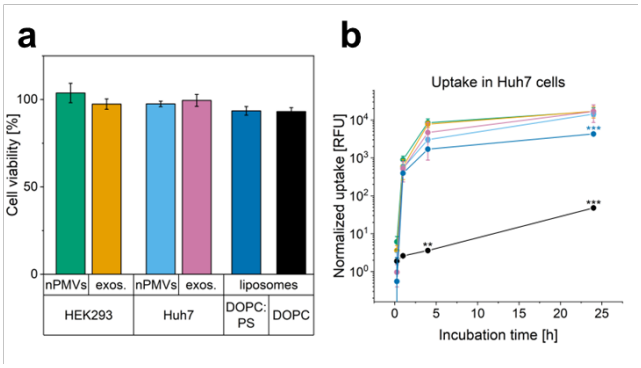

*Fig. 1: Cell viability of Huh7 cells and interaction of various nanoparticles with Huh7 cells. a: Huh7 cell viability after 24 h incubation with HEK293/Huh7 nPMVs and exosomes, DOPC:PS, and DOPC liposomes measured by MTS assay. b: Flow cytometry based cellular uptake quantification of DiI labeled HEK293 nPMVs (green), HEK293 exosomes (orange), Huh7 nPMVs (blue), Huh7 exosomes (pink), DOPC:PS (dark blue), and DOPC liposomes (black) by Huh7 cells after indicated time points. Values are means ± SD. Levels of significance: *: $p \leq 0.05$, **: $p \leq 0.01$, ***: $p \leq 0.001$.*

We further injected DiI labeled HEK293/Huh7 nPMVs or exosomes or DOPC:PS/DOPC liposomes in 48 h post fertilization old transgenic (Kdrl:EGFP) ZFE, expressing EGFP in their vasculature. Four and 24 h after injection, we observed that HEK293/Huh7 nPMVs and exosomes were mainly sequestered

by scavenger endothelial cells in the caudal vein plexus possibly through scavenger receptors (i.e., stabilin) [10] and dynamin-dependent endocytosis [11] but also to a lesser extent in tissue resident/patrolling macrophages. Representative image for these nanoparticles is shown in figure 2a. The fast clearance of nPMVs and exosomes was moreover supported by the low circulation and extravasation factors, which describe the circulation and extravasation behavior of nanoparticles in the zebrafish (REF), as determined by semi-quantitative image analysis. It is interesting to note that identical interactions and observations were previously described for other exosomes [11–13]. Liposomal formulations on the other hand showed significantly higher circulation and extravasation times being indicative for a lower cell interaction behavior (Fig. 2b).

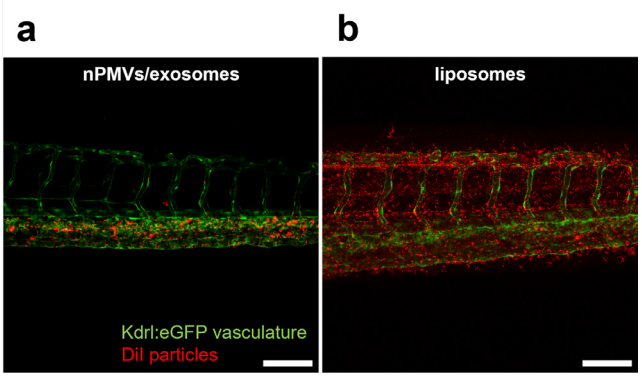

Fig. 2: Biodistribution of nPMVs/exosomes and liposomes (red signal) in the vasculature of transgenic (Kdrl:EGFP) zebrafish embryos (green signal) 24 h after injection. Representative image for the biodistribution of HEK293/Huh7 nPMVs/exosomes (a) and DOPC:PS/DOPC liposomes (b). Scale bar: 100 µm.

Conclusion

We were able to produce high yields of nPMVs from various cell lines with our optimized preparation method, which exceeds the production rate of existing exosome preparation protocols by at least an order of magnitude. Furthermore, we observed a fast and efficient uptake of nPMVs and exosomes in vitro and in vivo. These results suggest that nPVMs can serve as a valuable addition to existing EVs and offer new perspectives for the design of EV based therapeutic systems.

References

[1] D. E. Murphy, O. G. de Jong, M. Brouwer, M. J. Wood, G. Lavieu, R. M. Schiffelers, P. Vader, Extracellular vesicle-based therapeutics: natural versus engineered targeting and trafficking. Exp. Mol. Med. 51, 1–12 (2019)

[2] G. van Niel, G. D'Angelo, G. Raposo, Shedding light on the cell biology of extracellular vesicles. Nat. Rev. Mol. Cell Biol. 19, 213–228 (2018)

[3] E. I. Buzas, The roles of extracellular vesicles in the immune system. Nat. Rev. Immunol. 1–15 (2022)

[4] S. G. Antimisiaris, S. Mourtas, A. Marazioti, Exosomes and Exosome-Inspired Vesicles for Targeted Drug Delivery. Pharmaceutics 10, 218 (2018)

[5] Y.-J. Chiu, W. Cai, Y.-R. V. Shih, I. Lian, Y.-H. Lo, A Single-Cell Assay for Time Lapse Studies of Exosome Secretion and Cell Behaviors. Small 12, 3658–3666 (2016)

[6] W. Heusermann, et al. Exosomes surf on filopodia to enter cells at endocytic hot spots, traffic within endosomes, and are targeted to the ER. J. Cell Biol. 213, 173–184 (2016)

[7] H. Zhang, Thin-Film Hydration Followed by Extrusion Method for Liposome Preparation. in Liposomes 17–22 (Humana Press, New York, NY, 2017)

[8] MTS Assay Kit (Cell Proliferation) (Colorimetric). 4.

[9] S. Sieber, P. Grossen, P. Detampel, S. Siegfried, D. Witzigmann, J. Huwyler, Zebrafish as an early stage screening tool to study the systemic circulation of nanoparticulate drug delivery systems in vivo. J. Controlled Release 264, 180–191 (2017)

[10] G. Arias-Alpizar, B. Koch, N. M. Hamelmann, M. A. Neustrup, J. M. J. Paulusse, W. Jiskoot, A. Kros, J. Bussmann, Stabilin-1 is required for the endothelial clearance of small anionic nanoparticles. Nanomedicine Nanotechnol. Biol. Med. 34, 102395 (2021)

[11] F. J. Verweij, et al. Live Tracking of Inter-organ Communication by Endogenous Exosomes In Vivo. Dev. Cell 48, 573-589.e4 (2019)

[12] F. J. Verweij, V. Hyenne, G. V. Niel, J. G. Goetz, Extracellular Vesicles: Catching the Light in Zebrafish. Trends Cell Biol. 29, 770–776 (2019)

[13] V. Hyenne, et al. Studying the Fate of Tumor Extracellular Vesicles at High Spatiotemporal Resolution Using the Zebrafish Embryo. Dev. Cell 48, 554-572.e7 (2019)

Deep learning enhanced directed evolution

Project P1802: From Schrödinger's equation to biology: Unsupervised quantum machine learning for directed evolution of anti-adhesive peptides
Project Leader: M. Nash and A. von Lilienfeld
Collaborator: V. Doffini (SNI PhD Student)

Introduction

The Covid-19 pandemic showed us that our deeply interconnected world is extremely vulnerable to highly contagious pathogens. In this context, viruses are not the only threat we might face in future epidemic scenarios. Specifically, bacteria that show antibiotic resistance characteristics are an enormous hazard to humanity, and this topic has garnered increased interest from across the biomedical research community in recent years. It is crucial to explore new strategies to fight against antibiotic resistant pathogens and develop new pharmacological treatments.

In our project, we focus on a specific class of microbes which use specialized surface proteins called adhesins to bind human tissue and spread the infection inside the host. The detailed structure and mechanism behind many such bacterial binding adhesin domains are known, while for others no structural information is available. Such adhesins typically bind short peptide sequences located on abundant blood or cell-surface proteins of the intended host (Fig. 1). The goal of our project is to identify novel peptide candidates which bind strongly to the bacterial adhesin of the pathogen agent, inhibiting it from attaching to the host's cells.

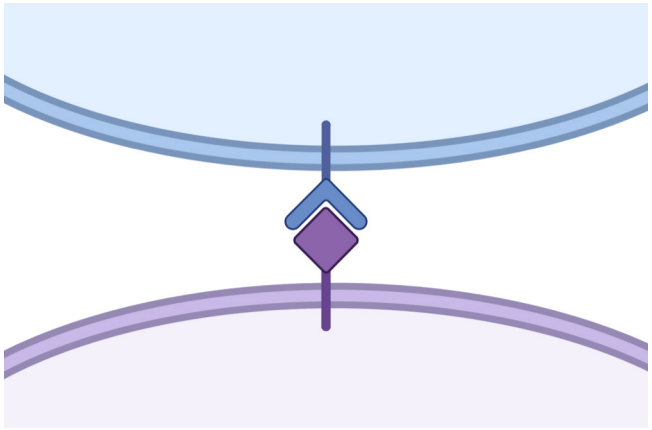

Fig. 1: Schematic representation of the binding between the pathogen (in blue) and the human cell (violet). The binding protein of the microorganism is shown in blue as well, while the attach site of the human cell is the violet square.

By using state of the art technologies like deep mutational scanning and next generation sequencing, it is already possible to generate data for hundreds of thousand different peptide variants in a relative short amount of time. Despite the fact that this might sound like a lot of data, they cover just a minimal fraction of the enormous space of possible amino acid combinations, even for small chains. For example, even for a peptide of a couple dozen amino acids, the number of total possible combinations are many orders of magnitude greater than the stars in the whole universe. Practically, this problem usually leads to a repetitive approach, called directed evolution, where mutations are screened and ranked based on a fitness function. In our case, the fitness function would be a measure of the binding strength between the adhesin protein and the peptide. After this first screening, the best mutations are selected, fixed and millions of new variants are produced changing the amino acids on the other positions. Afterwards, the new variants are screened and ranked again and the procedure is repeated for many iterations until an optimum is reached. Unfortunately, such protocol is not exempt from criticism; firstly, by exploring just single point mutations it is likely to get stuck on a local optimum instead of finding the global one; and secondly, since the presented protocol needs to be repeated multiple times, the burden of experiments needed is still high and it impacts negatively the time, resources and costs involved.

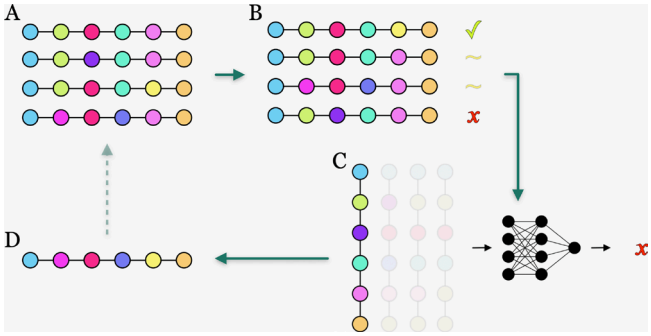

Fig. 2: Schematic representation of deep learning enhanced direct evolution. Starting from upper left, a library containing many mutants is synthesized (A). Then, the different variants are sequenced and sorted by a chosen output (B). After that, a neural network is trained in order to connect the specific sequences to the fitness variable (C). Finally, the model is used to perform in-silico screening of new variants. The best candidates are synthesized in the lab (D) and, eventually, added to the library for a new iteration.

In order to increase the efficiency as well as the accuracy of directed evolution, we propose a deep learning assisted approach (see Fig. 2). Such a methodology is still based on screening and ranking peptides, but in this case a deep neural network is fitted to connect the specific amino acid residues to the corresponding fitness function value. If successful, the deep neural network can be used to screen in-silico many more variants than are available experimentally, giving the possibility to efficiently find a new maximum of the fitness function without the need of many iterations as in the "classical" directed evolution approach. Moreover, since we are not anymore constrained by fixing the single best mutations found in the previous screening, the fitness

maximum we reach using metaheuristic techniques will be theoretically better than the previous one.

Material and methods

During the initial phase of the project, we focused on the synthesis and fluorescent labeling of one of the binding proteins of a pathogenic organism as well as the production of an E. Coli library. This library contains millions of bacteria, where each of the individual cells displays on its surface a specific peptide of defined length. The number of mutations in the library follows a binomial distribution with an 80% wild-type (WT) probability. Such library was cloned via HiFi assembly from fragments produced by Twist Bioscience. It was then screened using the bacterial adhesin labelled with a fluorescent dye molecule (Fig. 3). Peptides that strongly bind the adhesin will retain the fluorescent label after washing. The fluorescent intensity is detected by flow cytometry analysis and the cells are sorted, isolated and enriched for positive binders.

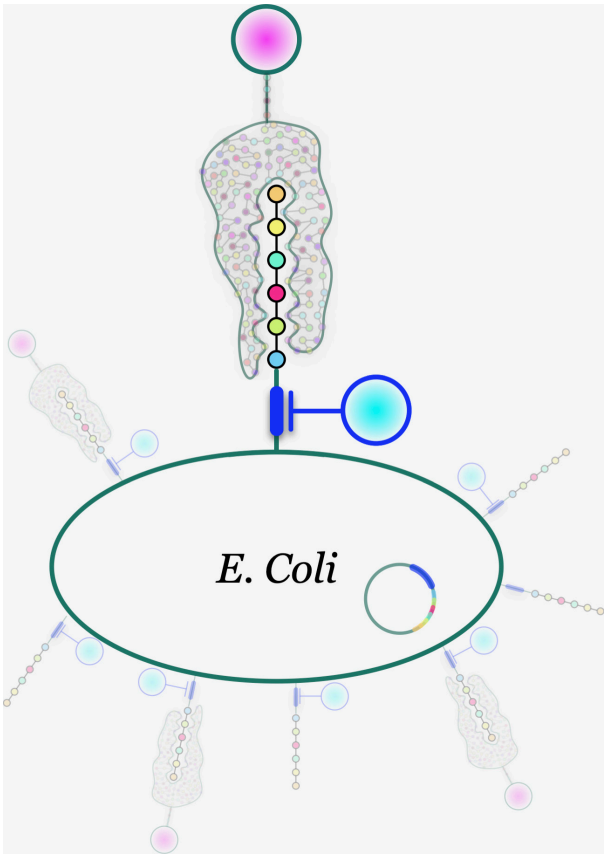

Fig. 3: Schematic representation of the binding between the protein of the pathogenic organism and one of the randomized peptides displayed on the cell surface of an E. Coli. The fluorescent label is shown in pink.

Results and discussion

Here we present the screening of the produced library and the WT (Fig. 4). Flowcytometry analysis of the full library clearly showed a good binding of a consistent part of it. One additional sign of the binding activity was the correlation trend shown in the plot. In fact, if the expression level of a surface displayed peptide variant that binds to the label protein increases, one should expect a higher signal coming from the adhesin. This was also confirmed by repeating the flowcytometry analysis with only the wild type (Fig. 4, bottom part). In addition, by considering the position of the WT population, one could deduct that such variant is among the strongest binders.

Outlook

In the next stage of the project, we will sort the bacteria in the library by setting gates along the estimated direction of the binding energy (as shown in figure 4 with green arrows). The plasmids containing the genetic information for the various variants will then be sequenced, enabling us to construct an affinity ranking. This ranking will be utilized to train a machine learning model to identify new candidates with higher binding energies. However, a potential limitation to this final step may occur if we find that the wild-type peptide is the strongest binder within the library. In this case, the machine learning algorithm may have difficulty finding superior candidates.

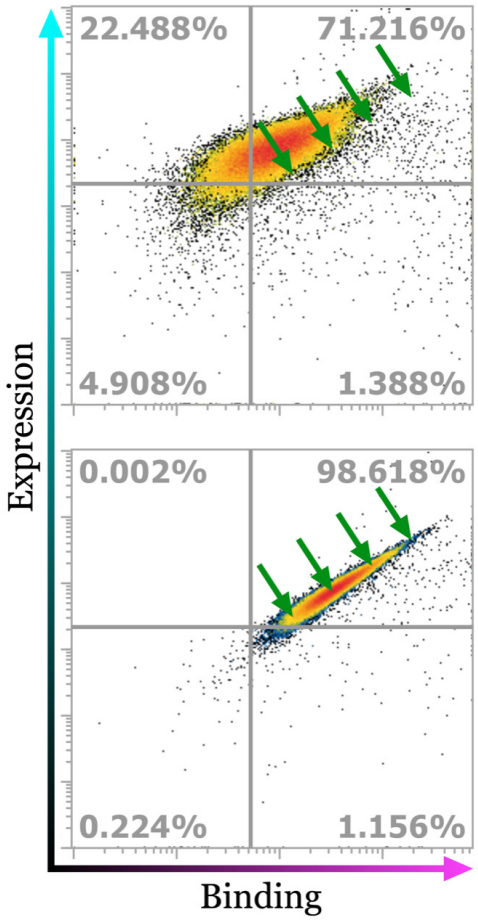

Fig. 4: On top, screening plot of the binding between the peptide library and the labelled protein of the pathogenic organism. Each point corresponds to one distinct peptide. On bottom screening of only the wild-type. On the abscissa is shown the binding while on the ordinate is the expression level or, in other words, how many peptides are displayed on the cell surface of the E. Coli. The four green arrows shown the direction of the binding energy (heads correspond to higher affinity).

References

[1] R. Vanella, D. Tien Ta and M. A. Nash, Enzyme-mediated hydrogel encapsulation of single cells for high-throughput screening and directed evolution of oxidoreductases, Biotechnology and Bioengineering, 116(8), 1878–1886 (2019)

[2] K. Yang, Z. Wu and F. Arnold, Machine-learning-guided directed evolution for protein engineering, Nat Methods 16(8), 687-694 (2019)

Magnetic phase transition in MoS_2 detected with AFM

Project P1803: Nanoscale mechanical energy dissipation in quantum systems and 2D-materials
Project Leader: E. Meyer and M. Poggio
Collaborator: A. Ollier (SNI PhD Student)

Introduction

Monolayer molybdenum disulfate (MoS_2) is a 2D semiconductor in the transition-metal dichalcogenides family that appear to be a very good candidate to be a 2D magnetic material. Indeed, its strong spin-orbit coupling induces a spin degeneracy of its valence and conductance bands, with one band that is spin up and the other spin down polarized. Recent experiments showed that a doping driven magnetic phase transition is expected from a ferromagnetic (FMP) to a paramagnetic (PMP) phase. The phase transition is a band structure changes (Fig. 1B). In the low doping region, the gap between the two polarized conductance bands is large hence the electrons only lie in the lower band that is spin polarized [1]. The system is in a strongly correlated states and ferromagnetism can arise. At a certain doping, the band structure changes drastically and the gap between the two degenerated bands shrink [1, 2]. The electrons can lie in both bands and suppress the polarization inducing paramagnetism. Here we employ the pendulum atomic force microscope (p-AFM), which uses very soft cantilevers to measure dissipative effects. In this configuration, the cantilever is positioned perpendicularly to the sample surface to avoid the tip snapping into contact. That way, p-AFM is few orders of magnitude more sensitive to the acting forces than conventional AFM . The measurements are operating with a home-made magnetic tip where a cobalt samarium ($CoSm_5$) particle was glued at the end of a tipless ARROW-TL cantilever. The characterization of the cantilever reveals a coercive field of ΔB=0.4 T allowing a large magnetic range of operation and a magnetic moment of $m=2.5\times10^{-14}A.m^2$. The measurements were performed under ultra-high vacuum conditions at low temperatures (T=5 K and T=77 K).

Magnetic phase transition

Figure 1 shows the typical frequency-shift and dissipation spectra under external magnetic field (B_{ext}-field) over MoS_2 monolayer. The parabolic background is due to the capacitive coupling of the oscillating tip and the underlying surface. In addition to the parabolic background a peak is visible at a doping $n=3\times10^{12}cm^{-2}$ (arrows and dash line) in both spectra. Interestingly, sweeping the doping from low to high (FWD) and high to low (BWD) shows different trend (see inset in Fig. 1A) indicating that the peak observed in the FWD spectra is not due to capacitive effects. The external B_{ext}-field highlight the different nature of the two regions. The low doping region is B_{ext}-field independent with a very low noise level. This is consistent with a strongly correlated state where all the spins are polarized, and the oscillating tip cannot disturb the system even under B_{ext}-field as expected for FMP. On the other side of the peak, the noise level is more prominent. The dissipation and the frequency shift increase linearly with B_{ext}-field. This behavior is indicating a drastic change of the nature of MoS_2 where the electrons are free to have the spin orientation they want and can move freely characteristic to PMP.

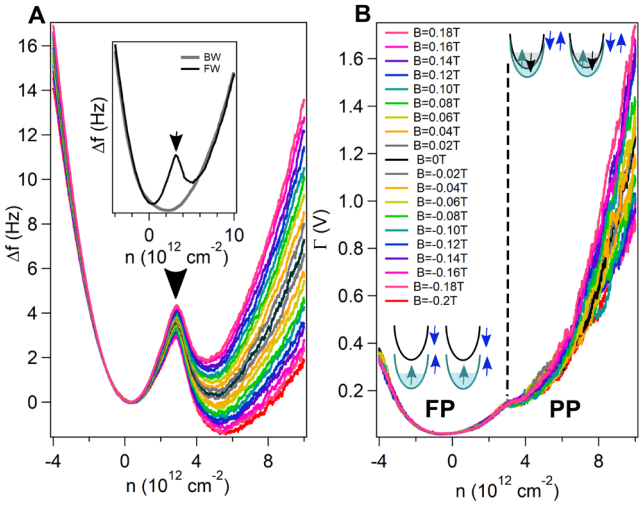

Fig. 1: A) frequency-shift versus doping under different B_{ext}-field. The inset shows the FWD and the BWD sweeps for B_{ext}=0 T.
B) corresponding dissipation spectra. The insets are schematizing the band structure in each phase.

Pauli paramagnetic spin susceptibility

To access the Pauli spin susceptibility, the frequency shift is converted into force/magnetic force (F) using [3, 4]:

$$F = \frac{2}{3}\frac{b_0 L k}{b_1 \omega_0}\Delta\omega = qH_{samp}$$

where bi are constants, L, k, ω_0 and $\Delta\omega$ are the cantilever length, spring constant, resonance frequency and frequency-shift, q is the magnetic point charge and H_{samp} the magnetic strength of the sample. Figure 2A shows F versus B_{ext} for different doping cuts. The trend is linear, and F can be approximated with this equation:

$$F(B_{ext}) = s \times B_{ext} + c$$

where c is a constant and $s=dF/dB_{ext}$. Pauli paramagnetic spin susceptibility is defined as:

$$\chi = \frac{dM_s}{dH} = -\frac{\mu_0}{w_{eff}B_{tip}} \cdot s$$

where M_s is the saturation magnetization of the cantilever, $H=H_{tip}+H_{samp}$ the total magnetic strength of the system, μ_0

the vacuum permittivity and w_{eff} the effective width of the cantilever shadow on the sample surface. The determination of χ using the extracted s from the experimental data is presented in figure 2B. The behavior of χ indicates a strongly correlated electron system due to the discontinuous character of the susceptibility [5].

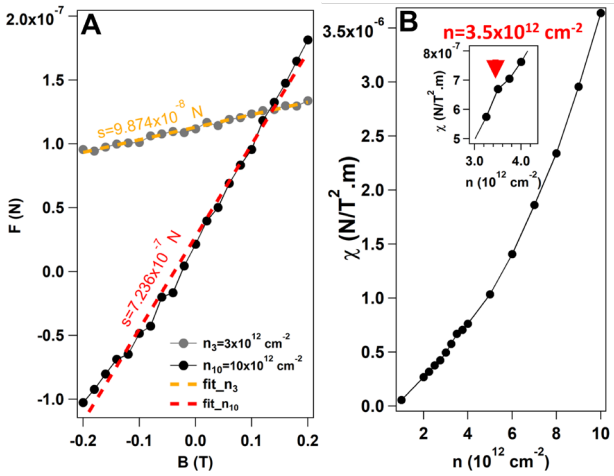

Fig. 2: A) force versus B_{ext} for $n=3x10^{12}cm^{-2}$ and $n=10x10^{12}cm^{-2}$ in gray and black respectively. The dash lines are the corresponding linear fit where the s in given for each curve. B) extracted χ for each doping. The inset is a zoom-in the transition region where a slight protuberance is observed marking the delimitation of each phase.

First-order phase transition

This linear behavior is a strong hint for a first-order phase transition as mentioned by theoretical [3] and photoluminescent [2] experiments. A first-order phase transition is characterized by a latent energy (El) where during the phase transition a fixed amount of energy is released or dissipated. The transition can occur only after its total release or dissipation, in the meantime the system stays in a constant state (here doping). The latent energy is often achieved with the applications of an external force (temperature, doping, mechanical vibration, etc.). To address the hysteresis observed (inset Fig. 1A) a doping depletion experiment was performed by changing the starting doping of sweeping (V_{BG}^{S}). Figure 3 shows the corresponding FWD curves. A distinct change of the transition peak intensity and position is observed. This figure shows that the phase transition is only possible if the bands are fully emptied before starting the filling of the conduction bands. This is indicating that the process cannot occur of the bands partially filled. The minimal depletion density to enable the transition to occur is V_{BG}^{S}=-0.5 V (inset Fig. 3). This behavior is another hint for a first-order phase transition scenario.

Conclusion

In conclusion, our measurements on a monolayer MoS_2 exhibit clear sign of a doping driven magnetic phase transition. The magnetic phase seems to come from a ferromagnetic to a paramagnetic phase. The phase transition appeared to be a first-order phase transition indicated by the hysteresis observed between the FW and the BW sweeps and the depletion effect observed. The extracted Pauli spin susceptibility show a strongly correlated electron system.

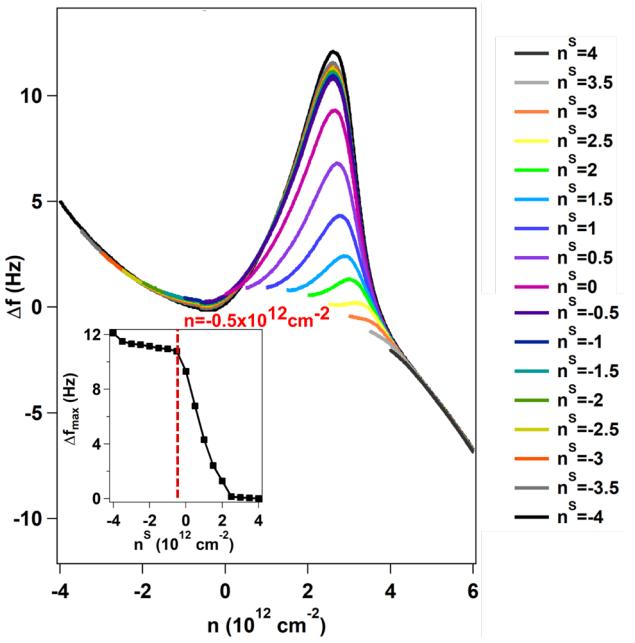

Fig. 3: Frequency-shift versus doping where the starting doping n^s was changed with a step of $0.5x10^{12}cm^{-2}$. The inset shows the evolution of the intensity of the transition peak and the dash line shows n_m.

References

[1] J. G. Roch, D. Miserev, G. Froehlicher, N. Leisgang, L. Sponfeldner, K. Watanabe, T. Taniguchi, J. Klinovaja, D. Loss, R. J. Warburton, First-order magnetic phase transition of mobile electrons in monolayer MoS2, PRL 124, 187602 (2020)

[2] D. Miserev, J. Klinovaja, D. Loss, Exchange intervalley scattering and magnetic phase diagram of transition metal dichalcogenide monolayers, PRL B 100, 014428 (2019)

[3] U. Gysin, S. Rast, A. Aste, T. Speliotis, C. Werle, E. Meyer, Magnetic properties of nanomagnetic and biomagnetic systems analysed using cantilever magnetometry, Nanotechnology 22, 285715 (2011)

[4] H. J. Hug, B. Stiefel, P. J. A. van Schendel, A. Moser, R. Hofer, S. Martin, H. -J. Güntherodt, Quantitative magnetic force microscopy on perpendicularly magnetized samples, JAP Physics 83, 5609 (1998)

[5] A. Shashkin, S. Anissimova, M. R. Sakr, S. V. Kravchenko, V.T. Dolgopolov, T. M. Klapwijk, Pauli susceptibility of a strongly correlated two-dimensional electron liquid, PRL 96, 036403(2006)

Quantifying bacterial responses to antibiotics at the single-cell level

Project P1805: High-throughput multiplexed microfluidics for antimicrobial drug discovery
Project Leader: E. van Nimwegen and V. Guzenko
Collaborator: M.-E. Alaball Pujol (SNI PhD Student)

Introduction

Without effective antimicrobials, the success of modern medicine would be at risk for treating infections including during major surgery and cancer chemotherapy. Misuse and overuse of antimicrobials are the main drivers in the development of resistant pathogens; however, it has also become clear in the last decades that the sensitivity to treatment varies from cell to cell, even in an isogenic population. In particular, some cells are in physiological states that allow them to survive antibiotic treatment without any resistance mutations [1]. Slow growing cells have been reported to be more tolerant to antibiotics, and this increased tolerance can facilitate the subsequent fixation of resistance mutations [2]. Yet, most in vitro assays that are used to discover and study antimicrobial compounds are based on liquid cultures in which bacterial cells grow exponentially so that slow-growing bacteria are quickly outcompeted, making it impossible to assess the effects of the compounds on slow growing cells. Consequently, the determinants of sensitivity to antibiotics are only poorly understood at the single-cell level due to the lack of quantitative data.

In recent years, powerful methods have been developed to quantitatively measure behaviour and responses in single bacterial cells. By combining microfluidics with time-lapse microscopy, it is possible to track growth, gene expression, division, and death within lineages of single cells. An especially attractive microfluidic design is the so-called Mother Machine, where bacteria grow within narrow growth channels that are perpendicularly connected to a main flow channel, which supplies nutrients and washes away cells growing out of the growth channels. In this field, our lab has developed an integrated microfluidic and computational setup to study the response of single bacteria to controlled environmental changes [3]: the dual-input Mother Machine (DIMM) allows arbitrary time-varying mixtures of two input media, such that cells can be exposed to a precisely controlled set of varying external conditions. The companion image analysis software MoMA segments and tracks cell lineages from phase-contrast images with high-throughput and high accuracy.

In the present project we use this integrated setup to quantify how the response of individual bacteria to treatment with antibiotics depends on their physiological state at the time the treatment commences. For this, we focus on treating Escherichia coli (E. coli) with a variety of clinically relevant antibiotics at clinically relevant concentrations. Moreover, we aim to develop new microfluidic designs that enable the study of multiple antibiotics and strains in parallel. Our long-term aim is to use this approach to identify compounds that specifically target non-growing subpopulations of pathogenic bacteria.

Designing microfluidic devices to study bacterial responses to complex treatments at the single-cell level

Designing microfluidic chips that enable to multiplex the testing of different strains and media requires improving two aspects of current designs: the multiplexing of the media reservoirs and the loading of the cells into the device.
For the former, a multiplexed version of the classic DIMM was already designed in our lab, with eight inlets and outlets (Fig. 1A). Furthermore, working together with the mechanical workshop of Biozentrum we developed a prototype pressurized box to multiplex the reservoirs for the input media.

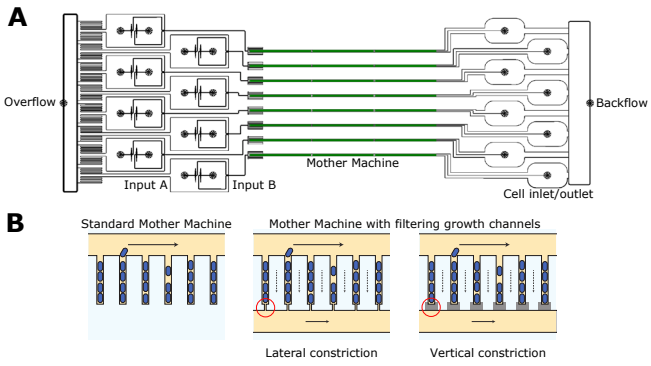

Fig. 1: Design of the microfluidic chips. A) Multiplexed DIMM. B) Different filter constriction designs.

To address the cell loading, we wanted to design a modified version of the standard Mother Machine where the closed end of growth channels is replaced by constrictions that act as filters. These filter structures are shallower and/or narrower than the growth channels, connected to the main flow channel, but also connected to a backflow channel so that media can flow through, but not the cells. This allows loading of the growth channels by simply `filtering' a diluted bacterial culture through the chip. In addition, with these filters, there is no nutrient gradient inside the channels and the addition or the removal of chemicals of interest is immediate. Lastly, the flow through the growth channels can help retaining motile cells by mechanically pushing them toward the filter end. These filter channels have already been produced using a lateral constriction [4]. Because of the small size of these structures, they are very challenging to manufacture, and require e-beam lithography which is not widely available.

To establish the production of the filter channels we have pursued two strategies (Fig. 1B). On the one hand, together with Dr. Vitaliy Guzenko at PSI we used the e-beam lithography system Raith EBPG 5000Plus to microfabricate lateral

constrictions. With this strategy the design consists of two layers of different thicknesses, one for the main flow channels (20 µm wide and 10 µm deep), connected to the narrow (<1 µm) and shallow (900 nm deep) growth channels. The lateral constriction reduces the width of the channels to 250 nm. So far, these constrictions turned out not to be stable enough, but we are working on new designs, that will be tested soon.

The alternative strategy led by Dr. Thomas Julou is based on a 3-layer design, where the third layer is shallow enough to produce a vertical constriction, reducing the channel height by 250 nm. The vertical constriction consists of a reservoir-like structure surrounding the growth channel. This design has been tested and has already been successfully used for some experiments.

Mother Machine experiments to characterize bacterial responses to antibiotic treatment

We focused on 3 clinically relevant antibiotics for Urinary Tract Infection (UTI) treatment: Ciprofloxacin (CIP), Ceftriaxone (CEF), and Gentamicin (GEN). The experiments consisted of treating cells of E. coli strain MG1655 with different concentrations of each antibiotic, ranging from the maximum concentration measured in serum during clinical treatment, to sub-Minimal Inhibitory Concentration (MIC) values. The experimental timeline consisted of 6 hours of exponential growth in M9 minimal media supplemented with 0.2% glucose, followed by the antibiotic treatment that lasted 2 hours, after which the survival was assessed by exposing the bacteria to fresh media for 16 hours.

We calculated the survival rates for all the conditions by tracking the `mother' cells (ie. cells at the bottom of the growth channels) across the treatment and counting the cells that produced viable progeny after the treatment. We found that, although the fraction of surviving cells drops with concentration for each antibiotic, the concentration range over which survival rates fall is very between antibiotics (Fig. 2A).

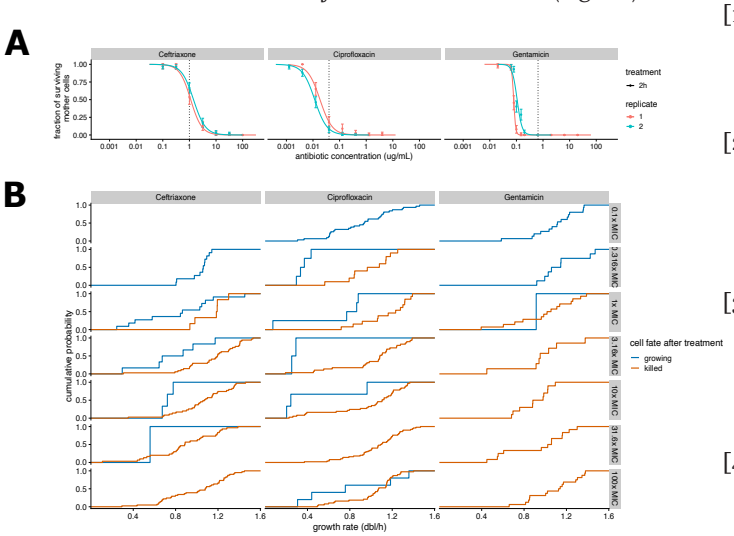

Fig. 2: A) Survival rates of mother cells at different antibiotic concentrations. The coloured dots show the fractions of surviving cells for each replicate, with standard deviation error bars. The lines show Hill function curves fitted to the data of each antibiotic and replicate. Vertical dashed lines show MIC values measured in bulk. Error bars show ±2 standard deviations. B) Cumulative distributions of growth rates of cells just before the treatment stratified by cells that survived (blue) and died (red). Each column corresponds to an antibiotic and each row to a treatment concentration. Note that only a single distribution is shown when there were only surviving or only dying cells.

We obtained quantitative data from the experiments using the DeepMoMA software, a new version of the MoMA (Mother Machine Analyser) software, that integrates the U-Net convolutional neural network architecture, developed by Dr. Michael Mell in our group. DeepMoMA allows quantifying single-cell response to antibiotic treatment, and it has been adapted to different cell morphologies that result from the treatment with antibiotics. These morphologies include lysis, filamentation and loss of phase contrast, which are observed at different rates across the different antibiotics and treatment concentrations.

Using this new image analysis allowed us to reconstruct cell lineages across the first set of the 2-hour treatment replicates, and we quantified various single-cell variables, including instantaneous growth rates. We then analyzed how the growth rate of the cells just before the treatment affected their subsequent survival. As shown in Figure 2B, surviving cells generally were growing more slowly just before the treatment than cells that died.

These results were obtained with a lab strain in minimal synthetic media. For future work, we aim to compare these results with results from a more clinically relevant context. For that, we have already established the workflow to work with the uropathogenic E. coli (UPEC) strain CFT073, and we have started to test how it grows in the new Mother Machine designs in urine-like media. We use the previously defined Synthetic Human Urine [5], to have a media that is closer to real urine than laboratory-defined media. We will thus explore single-cell responses of the CFT073 strain to antibiotics while growing in this synthetic urine media. We also plan on continuing the analysis of the MG1655 experiments, as well as testing new experimental designs that will include exposing cells to different treatment times, as well changing growth media so as to alter the distribution of single cell growth rates before the treatment.

References

[1] D. Hughes and D. I. Andersson, Environmental and genetic modulation of the phenotypic expression of antibiotic resistance, FEMS microbiology reviews 41 (2017)

[2] E. Rotem, A. Loinger, I. Ronin, I. Levin-Reisman, C. Gabay, et al., Regulation of phenotypic variability by a threshold-based mechanism underlies bacterial persistence, PNAS 107 (2010)

[3] M. Kaiser, F. Jug, T. Julou, S. Deshpande, T. Pfohl, et al., Monitoring single-cell gene regulation under dynamically controllable conditions with integrated microfluidics and software , Nat. Commun. 9 (2018)

[4] Ö. Baltekin, A. Boucharin, E. Tano, D. I. Andersson, J. and Elf, Antibiotic susceptibility testing in less than 30 min using direct single-cell imaging, PNAS 114 (2017)

[5] D. S. Ipe and G. C. Ulett, Evaluation of the in vitro growth of urinary tract infection-causing gram-negative and gram-positive bacteria in a proposed synthetic human urine (SHU) medium, J. Microbiol. Methods 127 (2016)

Image the twist!

Project P1806: Image the twist!
Project Leader: V. Scagnoli and P. Maletinsky
Collaborators: S. Treves (SNI PhD Student), J. White, V. Ukleev

Introduction and motivation
The aim of this project is to determine the formation mechanism of skyrmions, a topologically protected magnetic structure [1]. Currently it is not fully understood what drives the formation and annihilation events in skyrmion hosting materials; such knowledge is particularly important if skyrmions are to be implemented into improved technological applications in the future [2]. Observations of skyrmion formation and annihilation events require the use of 3D tomographic techniques in bulk 'extended' samples, which host room temperature skyrmions. For magnetic materials, where one needs to reconstruct a vector field, the most appropriate measurement technique is a variation of tomography called laminography [3], where the condition that the tomographic rotation angle is perpendicular to the beam direction is relaxed.

A system of recent interest for hosting room temperature skyrmions even in the absence of applied magnetic fields is $NdMn_2Ge_2$, a rare-earth based centrosymmetric material. The bulk of this material is known to host different metastable magnetic textures stabilized by high- and low- magnetic field cooling protocols. Metastable skyrmions have been nucleated with a field cooling procedure and then observed using topological Hall effect measurements [4, 5] and Lorentz transmission electron microscopy (LTEM) [6]. The shortfall of LTEM is that it is only sensitive to the in plane (IP) component of magnetisation (unless tilted). This does not allow for the true identification of the topological charge [7], i.e. the distinction between skyrmion (with non-zero topological charge) and twisted magnetic arrangement with zero topological charge. Using a combination of scanning transmission x-ray microscopy with the x-ray magnetic dichroism (XMCD) effect would allow for measurements to be made on extended samples in 3D, allowing for a distinction between topologies to be made.

Last year we demonstrated that a metastable skyrmion lattice could be created and imaged using 2D scanning transmission x-ray microscopy XMCD measurements. We then explored the robustness of these magnetic textures with an exploration of parameter space. Initially we heated the sample with a skyrmion lattice from room temperature to the Curie temperature (T_c) of 330 K, observing that the lattice remains unchanged up until this temperature. We then applied several magnetic field procedures, the most interesting of which showed that we can deform and recover the skyrmion lattice. This involved cycling an out of plane magnetic field from 0 T to -140 mT and then back up to 140 mT.

In the third year of this project, we have built upon the experimental results gained in the previous year. To obtain a 3D dataset of the skyrmion lattice the imaging technique known as laminography was used; the experiment was performed at the POLLUX beamline at the Swiss Light Source (SLS) [3].

Key experimental results:
The third year of this project built upon the new pathways discovered last year. This paved the way for the first major milestone to be achieved, namely to obtain a 3D dataset of a metastable skyrmion lattice. This exciting result came from measuring a lamella cut from a single crystal of $NdMn_2Ge_2$ and the use of laminography. The measurements involved taking 2D magnetic images via XMCD projections of the sample, tilted at 30 degrees using scanning transmission x-ray microscopy. Each projection was separated from the previous by 7.7 ° of rotation about the sample's vertical axis. Projections were taken until we had made one full rotation of the sample.

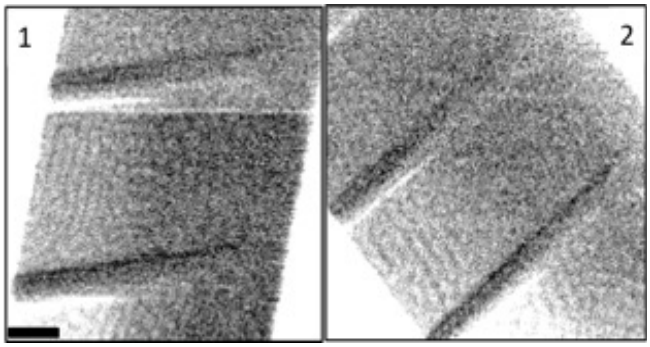

Fig. 1: XMCD projections of the $NdMn_2Ge_2$ lamella which show the skyrmion lattice and helical domains. 1) The starting position of the lamella, 0 °. 2) at 43.3 °. Scale bar 1 μm.

Initially the metastable skyrmion lattice was established in a 2D imaging configuration. This allowed for a field cool to be performed from 330 K (T_c) to room temperature (RT) whilst a small out of plane magnetic field of 50 mT was applied. The field was then switched off upon reaching RT and was followed up with further measurements. These confirmed that the lattice was metastable and the sample was switched to the laminography stage. This stage tilts the sample by 30° from the x-ray axis. Tilting the sample allows for all three of the magnetic components to be recovered with minimal loss of information.

Once in the laminography stage further measurements were made. These confirmed that the skyrmion lattice was still present and helped identify an area with the most interesting magnetic features. XMCD projections were then taken at regular angular intervals of rotation about the sample axis until a full rotation had been made. Two projections can be

seen in (Fig. 1) and show the skyrmion lattice mixed with a helical phase.

The dataset containing all of these projections then underwent analysis. This involved removing bad frames and aligning the projections to one another, allowing for a reconstruction of the sample shape and electron density ("non-magnetic") to be made. Once this model was created, the data was processed by a magnetic reconstruction code. This normalizes the magnetic signals for all frames, and subtracts the positive circularly polarized contribution from that of its negative counterpart. The difference signal, proportional to so-called XMCD effect, is proportional to the magnetization direction parallel to the beam and is used to create, by combining all the projections, a 3D model of the magnetic structures within the sample

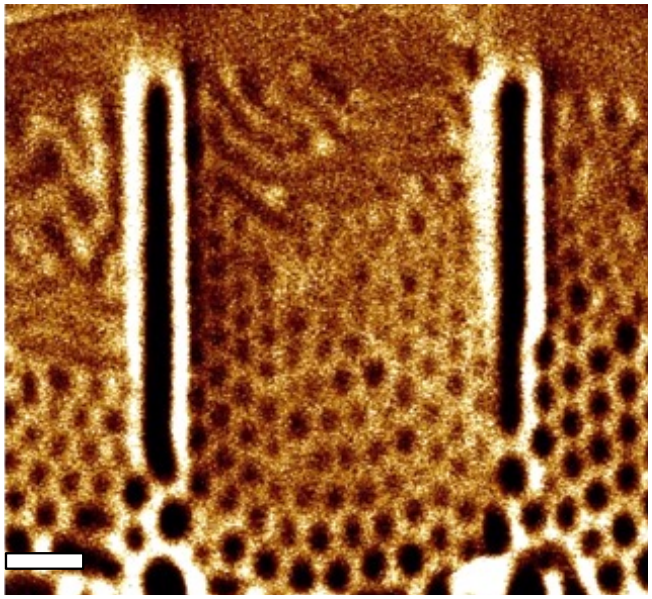

Fig. 2: An MFM image taken a month after the beamtime at POLLUX, orientation is 90 ° clockwise from the scanning transmission x-ray microscopy 0 ° image. The skyrmion lattice along with the helical phase can still be seen, which demonstrates the metastability of these magnetic textures in $NdMn_2Ge_2$. Scale bar represents 1 µm.

The analysis and reconstruction of the dataset is currently still underway. Due to the unfavorable shape of the sample, it can be difficult for the reconstruction algorithm to correctly align and process the frames. This results in the electronic (structural) reconstruction being close to reality, but the magnetic reconstruction to fail in modeling the system. The code is being optimized to remedy this issue and a final result is expected to follow in the coming months.

In order to confirm the metastability of the skyrmion lattice over an extended amount of time, we have performed further magnetic force microscopy (MFM) images, several weeks after the initial study. A low moment tip was used so that the stray fields of the sample could be measured without influencing the magnetic structures. The resulting image showed that the skyrmion lattice was still present along with the helical phase (Fig. 2). This demonstrates that the skyrmion lattice in $NdMn_2Ge_2$ is metastable and can persist for weeks after it has been established.

Outlook

The reconstructed data set from this beamtime will help to explain how a skyrmion phase can transition into a helical phase on the fundamental level. Due to the metastability of the lattice further measurements will be made using nitrogen vacancy (NV) magnetometry to provide more quantitative information on the system, such as the strengths and directions of the stray fields. These NV measurements could also be used to study dynamics of the system such as breathing modes of the skyrmions, or their transitions into the helical phase when applying a magnetic field or temperature change. A comparison could then be made between these observations and simulations to help complete the understanding of the system and the influences that external mechanisms have on it.

References

[1] T. H. R. Skyrme, A unified field theory of mesons and baryons, Nucl. Phys. 31, 556 (1962)

[2] S. S. P. Parkin, H. Masamitsu, L. Thomas, Magnetic Domain-Wall Racetrack Memory, Science, 320, 190 (2008)

[3] C. Donnelly, M. Guizar-Sicairos, V. Scagnoli, S. Gliga, M. Holler, J. Raabe, L. J. Heyderman, Three-dimensional magnetization structures revealed with X-ray vector nanotomography, Nature, 547, 328 (2017)

[4] S. Wang, Q. Zeng, D. Liu, H. Zhang, L. Ma, et al., Giant Topological Hall Effect and Superstable Spontaneous Skyrmions below 330 K in a Centrosymmetric Complex Noncollinear Ferromagnet NdMn2Ge2, ACS Appl. Mater., 12, 24125 (2020)

[5]. X. Zheng, X. Zhao, J. Qi, X. Luo, S. Ma, et al., Giant topological hall effect around room temperature in noncollinear ferromagnet NdMn2Ge2 single crystal, Appl. Phys. Letters 118, 072402 (2021)

Strong coupling between a single photon and a singlet-triplet qubit

Project P1807: Andreev Spin Qubit (ASQ) in Ge/Si Nanowires
Project Leader: C. Schönenberger, F. Braakman, I. Zardo, and D. Zumbühl
Collaborators: J. H. Ungerer (SNI PhD Student), A. Pally, A. Kononov, J. Ridderbos, S. Lehmann, C. Thelander, K. A. Dick, P. Scarlino, A. Baumgartner, C. Schönenberger

Hybrid circuit QED architecture

It has been predicted that a successful implementation of a quantum computer promises enormous advantages as compared to classical computers. For realizing a useful quantum computer, a physical implementation of its building blocks, the quantum bits (qubits), is needed. One approach relies on spin qubits. Spin qubits in semiconductors are promising contenders for realizing scalable quantum computers because of their small footprint, long coherence times and fast gate operations [1].

A disadvantage of current spin qubits lies in the short-range interaction that is used for entangling gates between several spin qubits. Superconducting circuits can solve this issue and attempts towards realizing a distant entangling gate, based on superconducting circuits, resulted in strong coupling between a spin-qubit and a microwave photon in a superconducting resonator [2-4] as well as distant spin-spin interactions [5, 6]. However, these attempts rely on a complicated gate architecture and on micromagnets and resulted in relatively weak coupling strengths. These obstacles complicate have so far inhibited the successful realization of distant entangling gates.

Here, we address these challenges by implementing a hybrid architecture based on a high impedance resonator and a semiconductor nanowire: A superconducting resonator (figure 1a) hosts single microwave photons. The resonator is structured into a thin film of NbTiN and features a large impedance kΩ. The magnetic-field resilience enables operation of a spin qubit and the coupling between the resonator and spin qubit is enhanced by the large impedance [7].

The qubit is defined by an even number of electrons confined in a double quantum dot (DQD) in a crystal-phase engineered InAs nanowire (NW) [8, 9], shown in figure 1b. In these NWs, the conduction band offset between wurtzite and zincblende crystal phase gives rise to a sharp confinement potential defining the DQD. This material platform offers two striking advantages: Firstly, the confinement of the electrons does not require any gate electrodes, hence remarkably reducing the device complexity compared to QDs defined by depletion or accumulation gate electrodes. Secondly, the electrons are located within the zincblende InAs segments yielding a large intrinsic spin-orbit interaction (SOI) [10]. The large SOI renders the implementation of micromagnets unnecessary. Furthermore, the large intrinsic SOI results in an enhanced spin-qubit photon coupling strength compared to previous demonstrations [2-4].

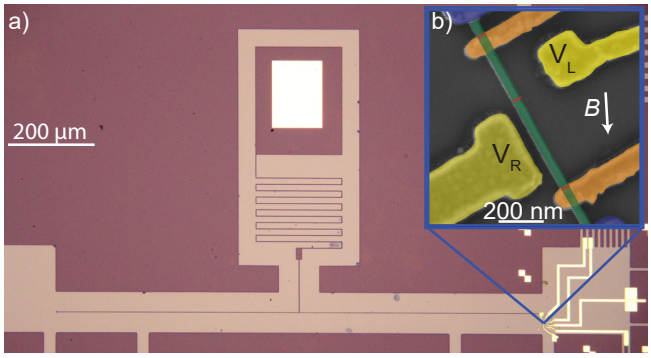

Fig. 1: The device. a) microscope image of the high-impedance, magnetic-field resilient NbTiN resonator. The NbTiN appears purple. b) False-colored scanning electron micrograph of crystal-phase nanowire device. The zincblende nanowire segments are colored green while the wurtzite barriers are colored red. Gate electrodes (yellow) are biased by the gate voltages V_R and V_L as indicated. The resonator is connected to the gate labelled with V_R. An in-plane magnetic field B is applied in the indicated direction.

Dipolar interactions between DQD and resonator

We explore the device by measuring the response of the resonator at its resonance frequency as a function of the gate voltages applied to the DQD. This measurement results in a characteristic honeycomb pattern, shown in figure 2. Whenever the electrochemical energies of the two dots are degenerate with each other or the leads, a change in the resonator response is observed. The formation of the characteristic honeycomb pattern therefore is a signature of the dipolar coupling between the resonator and the DQD [11].

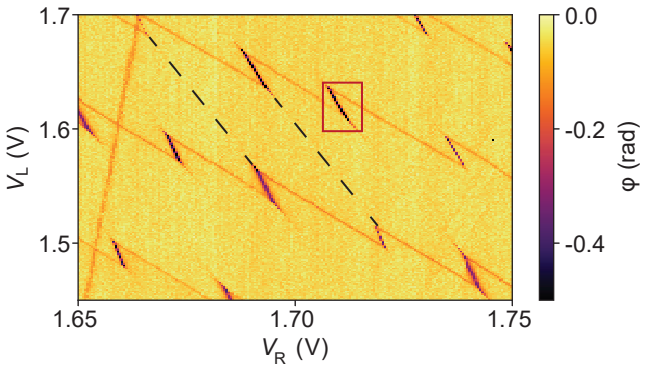

Fig. 2: Charge-stability diagram. Resonator phase response φ as function of gate voltages. The data exhibits the characteristic charge-stability diagram of a DQD.

Coupling between a single photon and a singlet-triplet qubit

After having demonstrated the dipolar interaction at zero magnetic field, B=0, as a next step, we define a spin qubit in the DQD by applying a magnetic field. At a finite magnetic field strength, the two lowest energy levels of the DQD have a singlet and a triplet character which are split by the SOI. This two-level system forms a spin qubit where the two spin states own a different charge distribution in the DQD. This results in a spin electric-dipole moment, hence mediating a coupling to the resonator. This coupling gives rise to an avoided crossing between the photonic resonator excitation and the spin if the two uncoupled transition frequencies are resonant with each other.

Because of the spin-orbit character of the spin qubit, the spin transition frequency can be tuned by both, the electrostatic dot-dot detuning ϵ and by the magnetic field strength B, allowing us to bring the spin transition frequency into resonance with the resonator excitation frequency as shown in figure 3. When the two systems are brought in resonance with each other, we observe an avoided crossing which is a signature of a coherent spin-photon coupling. By fitting a Jaynes-Cummings Hamiltonian, we determine the electron spin-photon coupling strength of $g/2\pi$=114±9 MHz. Together with the qubit linewidth $\gamma/2\pi$=190±24 MHz and resonator decay rate $\varkappa/2\pi$=34.1±0.3, this puts us in the strong coupling regime, $2g/(\gamma+\varkappa/2) \geq 1$, in which a single photon coherently hybridizes with the spin qubit.

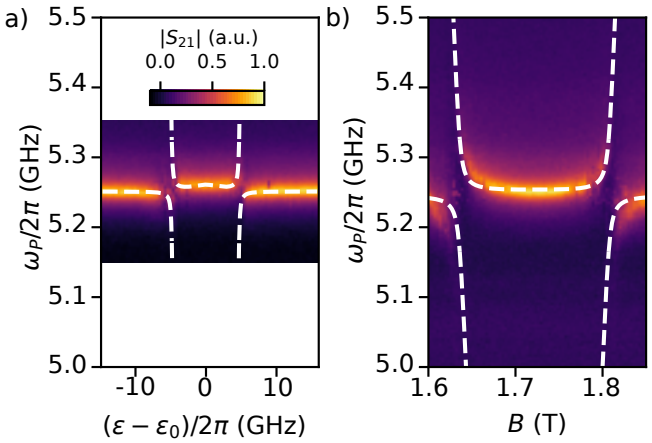

Fig. 3: Avoided crossings a) Transmission amplitude $|S_{21}|$ as function of probe frequency ω_p and dot detuning ϵ at a magnetic field strength of B=1.67 T exhibiting an avoided crossing. b) $|S_{21}|$ as function of probe frequency and B showing an avoided crossing at DQD detuning $\epsilon \approx \epsilon_0$. The avoided crossings are a signature of a coherent interaction between a single microwave photon in the resonator and a singlet-triplet qubit that has both spin and charge character. The white, dashed lines are fits to a Jaynes-Cummings Hamiltonian.

Summary and Outlook

The presented results are a proof-of-principle of an electron spin-photon interface based on intrinsic spin-orbit interaction. Together with the crystal-phase defined barriers, this approach drastically simplifies the geometry needed for realizing a spin-photon interface by eliminating the micromagnets and depletion/accumulation gates. Moreover, the measured electron spin-photon coupling strength exceeds the one of previous experiments [2-6] by an order of magnitude, hence setting a new world record.

We anticipate that the simplifications in the device architecture might enable scalability of the spin qubit system. Furthermore, the large spin-photon coupling strength might permit the successful realization of entangling gates between distant spin qubits. Therefore, these results can substantially contribute to realizing a useful, spin-based quantum computer.

References

[1] D. D. Awschalom, L. E. Bassett, A. D. Dzurak, E. L. Hu, J. R. Petta, Quantum spintronics: engineering and manipulating atom-like spins in semiconductors , Science 339(6124) (2013)

[2] X. Mi, M. Benito, S. Putz, D. M. Zajac, J. M. Taylor, G. Burkard, J. R. Petta, A coherent spin–photon interface in silicon, Nature 555(7698) (2018)

[3] N. Samkharadze, G. Zheng, N. Kalhor, D. Brousse, A. Sammak, U. C. Mendes, A. Blais, G. Scappucci, L. M. K. Vandersypen, Strong spin-photon coupling in silicon, Science 359(6380) (2018)

[4] A. J. Landig, J. V. Koski, P. Scarlino, U. C. Mendes, A. Blais, C. Reichl, W. Wegscheider, A. Wallraff, K. Ensslin, T. Ihn, Coherent spin–photon coupling using a resonant exchange qubit, Nature 560(7717) (2018)

[5] F. Borjans, X. G. Croot, X. Mi, M. J. Gullans, J. R. Petta, Resonant microwave-mediated interactions between distant electron spins, Nature 577(7789) (2020)

[6] P. Harvey-Collard, J. Dijkema, G. Zheng, A. Sammak, G. Scappucci, L. M. K. Vandersypen, Coherent spin-spin coupling mediated by virtual microwave photons, Physical Review X 12(2) (2022)

[7] N. Samkharadze, A. Bruno, P. Scarlino, G. Zheng, D. P. Di Vincenzo, L. DiCarlo, L. M. K. Vandersypen, High-kinetic-inductance superconducting nanowire resonators for circuit QED in a magnetic field, Phys Rev Appl 5(4) (2016)

[8] S. Lehmann, J. Wallentin, D. Jacobsson, K. Deppert, K. A. Dick, A general approach for sharp crystal phase switching in InAs, GaAs, InP, and GaP nanowires using only group V flow, Nano Letters 13(9) (2013)

[9] D. Barkera, S. Lehmann, L. Namazi, M. Nilsson, C. Thelander, K. A. Dick, V. F. Maisi, Individually addressable double quantum dots formed with nanowire polytypes and identified by epitaxial markers, Appl. Phys. Letter 114(18), 183502 (2019)

[10] M. Nilsson, F. V. Boström, S. Lehmann, K. A. Dick, M. Leijnse, C. Thelander, Tuning the two-electron hybridization and spin states in parallel-coupled InAs quantum dots, PRL 121(15) (2018)

[11] T. Frey, P. J. Leek, M. Beck, A. Blais, T. Ihn, K. Ensslin, A. Wallraff, Dipole coupling of a double quantum dot to a microwave resonator, PRL 108(4) (2012)

Dynamics of a coupled ion-nanowire hybrid system

Project P1808: Quantum dynamics of an ultracold ion coupled to an nanomechanical oscillator
Project Leader: S. Willitsch and M. Poggio
Collaborator: M. Weegen (SNI PhD Student)

Introduction

Ultracold trapped ions in linear radiofrequency traps are well-established and highly controllable quantum systems with a variety of applications in fields such as precision spectroscopy, cold chemistry, quantum information and optical clocks [1]. Nanomechanical oscillators are highly sensitive objects for the development and implementation of technologies in miniaturized devices. Their nanoscopic size makes them excellent candidates for the study of physics on the border of classical and quantum physics and highly susceptible to very weak forces. This property makes nanomechanical oscillators excellent measuring probes with high sensitivities that enabled the development of devices such as the atomic force microscopes [2].

This project is aimed at the implementation of an ion-nanowire hybrid system to explore new methods of quantum state preparation, manipulation and readout via the mutual interaction of its constituents. A charged Ag_2Ga nanowire is positioned in close proximity to the trapped ions such that they experience a strong mutual Coulomb interaction. By mechanically driving the nanowire at its resonance frequency and matching it to a trapped ion's axial frequency, an efficient energy transfer from the mechanical nanowire motion to the ion motion is expected. Theoretical descriptions of the ion-nanowire resonant drive have shown an increase in the kinetic energy of the ions in a classical description, as well as the creation of highly excited coherent states in a quantum mechanical description in which the ion is initially prepared in its motional ground state [3].

Since the charged conducting nanowire effectively acts as an additional electrode to the trap geometry, the effective trapping potential gets altered by the presence of the nanowire. This makes the matching of both frequencies additionally challenging, as the ion's eigenfrequencies experience a shift depending on parameters such as the distance of the ion to the nanowire and the effective charge of the nanowire. Close proximity of the nanowire to the trapping region in the center of the trap leads to more invasive distortions of the fields, undermining the harmonic potentials desired in linear radiofrequency traps. While these distortions introduce challenges, they may also offer opportunities for the study and shaping of anharmonic trapping potentials for the creation of Schrödinger-cat type states.

Here, we report the progress and recent developments of the experimental setup, including the implementation of a new technique for the demonstration of the resonant ion-nanowire drive on a classical level.

Experimental Setup

The core feature of the experimental setup is the combination of a miniaturized linear radiofrequency wafer trap with a conducting nanowire as shown in figure 1.

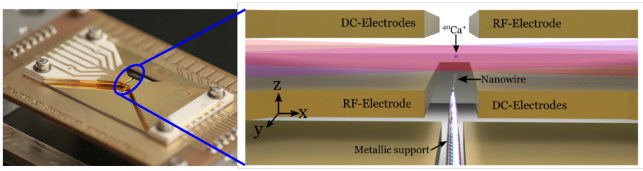

Fig. 1: Photograph of gold-coated wafer radiofrequency trap (left), schematic side view of the trap electrodes with the nanowire positioned close to the ions (right) [3].

The nanowire is positioned on the conic tip of a metallic Tungsten holder and can be positioned in all spatial directions with attocube nanopositioners.

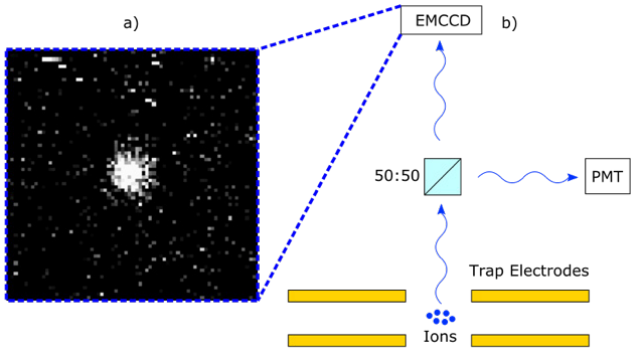

Fig. 2: EMCCD camera image of a single trapped ion (a) and a simplified schematic of the optical detection setup for the ion fluorescence (b).

Neutral ^{40}Ca ions are ejected into the trap by evaporation from a calcium source and subsequently singly ionized in two steps with 423 nm and 375 nm lasers. The resulting $^{40}Ca^+$ ions are a typically used species of trapped ions, as they offer a simple Doppler cooling scheme due to their single valence electron, requiring a 397 nm cooling and 866nm repumping laser, which are easily accessible laser wavelengths.
The trapped ions are monitored by an optical setup with an EMCCD camera on top of the experimental chamber. For efficiently cooled ions, this setup allows the distinction of individual ions on the image of the camera (see Fig. 2).
In addition to the EMCCD camera, a 50:50 beam splitter and a PMT have recently been added to the setup (see Fig. 2). This allows the detection of single 397 nm photons scattered by the ions due to their fluorescence generated by Doppler laser cooling. This addition of a PMT vastly improved the detec-

tion capabilities and sensitivity of the setup as the fluorescence detected by the EMCCD camera alone proved to not be a sufficiently sensitive detector.

Photon-Correlation Method

Recently, a photon-correlation method for the sensitive detection of ion motion has been implemented and tested in the experimental setup [4].

The method can be used to detect periodic motion of trapped ions with sufficiently high velocities, such that the resulting Doppler shift due to the ion motion leads to a measurable change in the ion fluorescence. Typically, this method is used for the detection and minimization of undesired excess micromotion in radiofrequency traps, but here the intention is to generalize this method to measure the induced ion motion at a resonant ion-nanowire drive.

In the photon-correlation method, the fluorescence of the ions measured by a PMT is correlated with the applied RF frequency of the trap. Since the micromotion of the ions is exactly periodic at the RF frequency, the resulting fluorescence shows a periodic time profile when the ion micromotion Doppler-shifts the laser scattering from the 397 nm resonance.

This method can be extended to measure the driven motion of the ions at their secular (trapping) frequencies. This has recently been observed in our trap for an electrical drive from an applied AC field of low amplitudes on the order of a few ten mV.

Figure 3 shows an example measurement of the photon-correlation method for driven secular motion of trapped ions at the nanowire resonance frequency, as well as a fit of the theoretical description of the ion fluorescence rate given by:

$$K(t) = K_0 \frac{(\frac{\Gamma}{2})^2}{((\frac{\Gamma}{2})^2 + (\delta - k v_{max} \cos(\omega - \varphi))^2)} \quad (1) \qquad [4]$$

Here, Γ is the inverse of the 397 nm transition life time of $^{40}Ca^{+}$, δ is the detuning from the 397 nm laser to the resonance, k is the laser's wave vector, vmax the velocity amplitude of the observed motion at frequency ω and ϕ is a phase. K_0 is the unshifted fluorescence rate of the ions at velocity v = 0. Low ion velocities appear as approximately sinusoidal distributions, as is the case shown in figure 3.

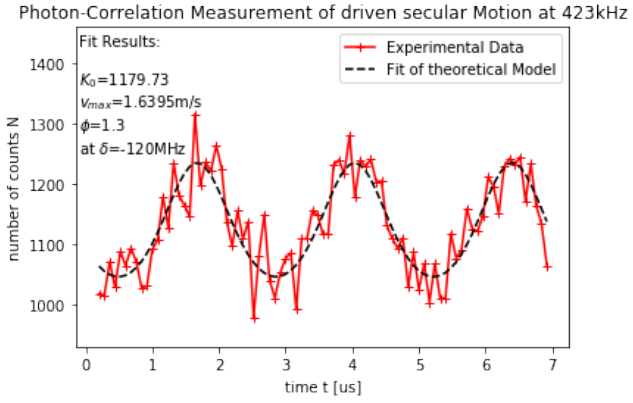

Fig. 3: Observation of driven secular motion with the photon-correlation method over three oscillation periods. The experimental data are well described by the fit of the theoretical model given by equation (1).

The goal is now to further extend this method to the observation of mechanically driven motion by the ion-nanowire interaction.

Summary & Outlook

The experiment has been extended by the addition of a PMT to the optical detection setup and the implementation of the photon-correlation method, allowing more sensitive measurements of periodic ion motion by detecting their change in fluorescence.

The functionality of the photon-correlation method in the setup has been demonstrated for the detection of ion micromotion as well as ion secular motion driven by electric AC field.

The next goal for the project is the extension of the photon-correlation method for the detection of periodic ion motion driven by the mechanical oscillation of the nanowire, demonstrating the resonant energy-transfer from the nanowire to the ion in the classical regime.

References

[1] S. Willitsch, Coulomb-crystallised molecular ions in traps: methods, applications, prospects, Int. Rev. Phys. Chem., 31 (2), 175 (2012)

[2] F. J. Giessibl, Advances in Atomic Force Microscopy, RMP 75, 3 (2003)

[3] P. N. Fountas, M. Poggio, S. Willitsch, Classical and quantum dynamics of a trapped ion coupled to a charged nanowire, New J. Phys. 21(1), 013030 (2019)

[4] D. J. Berkeland, J. D. Miller, J. C. Bergquist, W. M. Itano, D. J. Wineland, Minimization of ion micromotion in a Paul trap, J. Appl. Phys. 83, 5025 (1998)

Blotting-free whole cell and organelle vitrification for in situ cryo-EM

Project P1901: Microfluidics to Study Huntington's Disease by Visual Proteomics
Project Leader: T. Braun and E. Pecho-Vrieseling
Collaborator: A. Fränkl (SNI PhD Student), I. Takashi, N. Zimmermann, B. Engel, W. Wietrzynski

Introduction
Understanding high-resolution structural information is essential to interpret a cell's working mechanisms. In the last decade, cryogenic electron microscopy (cryo-EM) has become a compelling method to determine macromolecules' architecture at atomic resolution. However, cryo-EM is still rapidly developing; specific research focuses are improved sample preparation methods, strategies to investigate cellular ultrastructures, and expanding the application of EM as an analytical tool.
In recent years, we have developed a system of microfluidic modules for cryo-EM sample preparation. The different modules can be combined in various configurations for an experiment. Typical examples are (i) the microfluidic isolation, cryo-EM preparation, and building of an atomic model from less than 1 µL cell lysate [1] or (ii) the single-cell analysis by visual proteomics by combining microfluidic cell-lysis and EM sample preparation [2, 3]. The latter allows the proteome-wide detection of the structural rearrangement of protein complexes of single cells by a method we call "differential visual proteomics." Unfortunately, this method does not allow for investigating the social context of proteins in the cell or how cells interact with each other. Therefore, new protocols are being developed, allowing us to "mill" a lamella into the cell, which is thin enough to investigate the proteins at high resolution by cryo-EM tomography. This allows the in-situ investigation of the proteins in a small part of the cell. Unfortunately, classical preparation methods for whole-cell vitrification use extensive filter paper blotting or are prolonged, disturbing thin cellular structures and exhibiting significant intra-cellular stress (Fig. 2A).

Here we aim to develop a series of new preparation protocols for the vitrification of adherent and free-floating eukaryotic cells and organisms. These methods avoid filter-paper blotting entirely and can be performed in less than half a minute. Furthermore, the cell's environment is controlled throughout the preparation. Finally, the thin sample layer can be optically monitored immediately before vitrification (under development).

Functional Cryo-EM sample preparation for cellular bodies
Eukaryotic flagella axonemes are long and fragile structures. Therefore, the preparation for cryo-EM is delicate; in particular, the paper blotting step used in classical preparation methods disturbs, flattens, or disrupts the ultra-structure. Therefore, we used the cryoWriter system for the cilia preparation and optimized the protocol for sample thickness and usable area for tomography.

To prepare larger areas of the sample, we first applied a larger sample volume (17 nl) and recovered most of the sample afterward. For cilia-axoneme preparation, the withdrawal rate was the crucial factor for controlling the thickness of the ice (Fig. 1A). We got preliminary results for activated flagella in good quality and thickness vitrified ice with visible structures (Fig. 2D).

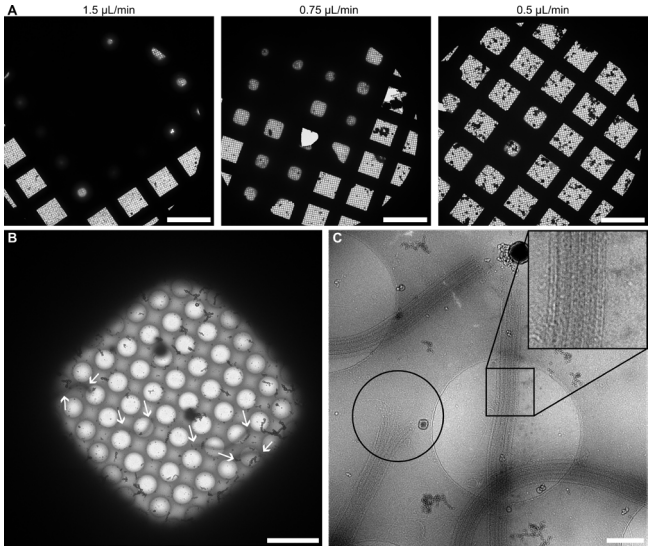

Fig. 1: Preparation of isolated cilia axonemes for cryo-EM. A) Sample withdrawal rate is a crucial factor. We obtained areas of usable thickness with a sample withdrawal rate of 0.75 µl/min. B) Overview of cilia preparation (arrows). Scale-bar: 10 µm. C) Higher magnification of prepared cilia. Intact protein bundles are visible inside the higher magnification visible in the inset). Although the preparation of the cilia is a harsh process, as visible at the ripped-off ends of the cilia (black circle). Scale bar: 500 nm.

The optimized axoneme preparations are an excellent test sample to perform in situ activity tests in the sample layer immediately before vitrification for cryo-EM. To do this, we are implementing an additional cryoWriter module, which allows imaging of the thin sample layer immediately before vitrification by fluorescence and dark-field light microscopy (see project A17.3 FuncEM).

Printing organisms for lamella milling
We are developing new protocols for the vitrification of complete eukaryotic adherent or detached cells. Here we show a new method to position algae cells on the cryo-EM grid for subsequent Focused Ion Beam Scanning Electron Microscopy (FIB-SEM). This technology allows the milling of thin lamella through individual cells. Cryo-electron tomography will enable us to characterize the ultrastructure of the proteins and lipids inside the lamella. Current techniques for depositing the cells on a grid result in a random distribution (Fig.

3A); however, the cells must be placed in the middle of the grid for FIB milling. The cryoWriter's microfluidic capillary allows us to "print" the organism or structure in a specific location on an EM grid. This allows for a much more precise deposition pattern (Fig. 3B).

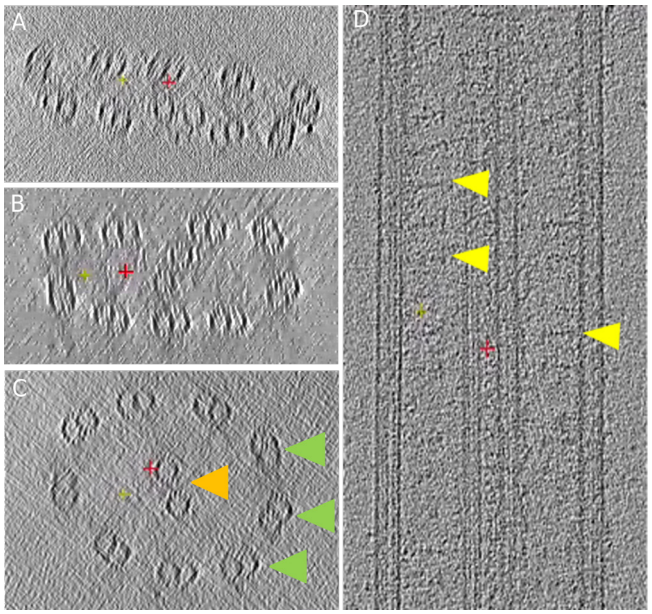

Fig. 2: Electron tomograms showing de-membraned Chlamydomonas flagella (axoneme) in various ice thicknesses. A) Chlamydomonas flagella in too thin ice resulting in a crushed structure. B) Chlamydomonas flagella in thicker layer of ice but still being warped by the ice being too thin C) Chlamydomonas flagella in an ideal amount of ice with both the central pair and outer doublets clearly visible. Green arrows indicate microtubule doublets. Orange arrow indicated central pair. D) A top side tomogram of the Chlamydomonas flagella assembly clearly showing the microtubule doublets and the central pair. Yellow arrows indicate radial spokes.

Outlook

We use the cryoWriter system to optimize the preparation of delicate organelles and complete tiny organisms in a blotting-free manner. These biological structures are subsequently characterized by cryo-electron tomography. In parallel, we develop new optical systems to describe the thin sample layers immediately before vitrification, enabling functional assays in the future.

References

[1] C. Schmidli, S. Albiez, L. Rima, R. Righetto, I. Mohammed, P. Oliva, L. Kovacik, H. Stahlberg, T. Braun, Microfluidic protein isolation and sample preparation for high-resolution cryo-EM. PNAS U.S.A. 116 (30) (2019)

[2] S. A. Arnold, S. Albiez, N. Opara, M. Chami, C. Schmidli, A. Bieri, C. Padeste, H. Stahlberg, T. Braun, Total sample conditioning and preparation of nanoliter volumes for electron microscopy. ACS Nano, 10, 4981-4988 (2016)

[3] A. Syntychaki, L. Rima, C. Schmidli, T. Stohler, A. Bieri, R. Sütterlin, H. Stahlberg, D. Castaño-Diez, T. Braun, Differential visual proteomics: Enabling the proteome-wide comparison of protein structures of single-cells. J. Proteome Res. 18 (9) (2019)

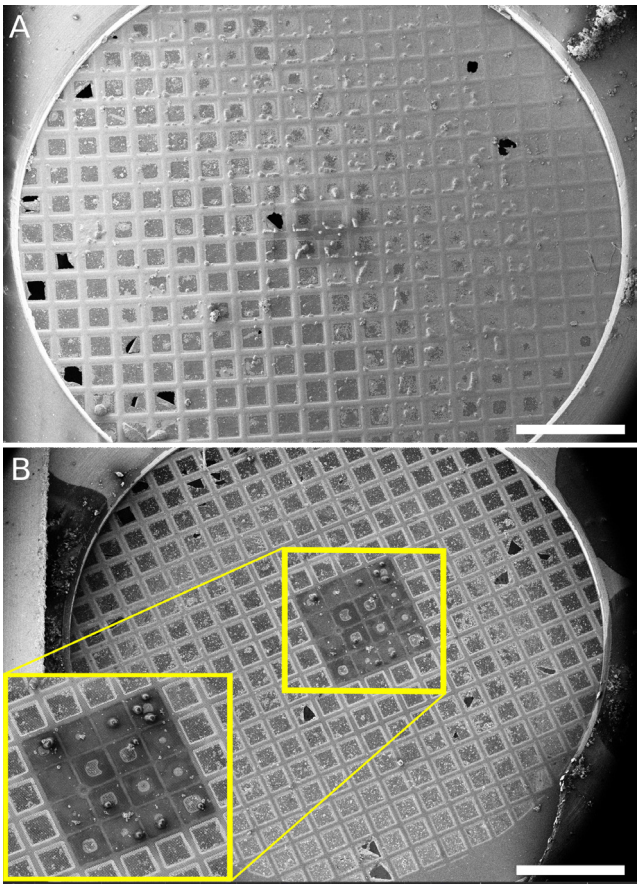

Fig. 3: Preparation and deposition of Chlamydomonas on EM grids via A) the classic Vitrobot approach with 3 µl sample and excess fluid removal by extensive filter-paper blotting, and, B) precise microfluidic deposition onto a targeted area using the cryoWriter. Scale bar: 500 µm.

Dual scale approach towards cardiac replacement engineering

Project P1902: Directional 3D nanofiber network to mimic in-vivo myocardial syncytium towards guiding contraction patterns in in-vitro heart models
Project Leader: M. Gullo, M. Poggio, and A. Marsano
Collaborator: F. Züger (SNI PhD Student)

Introduction

Cardiovascular diseases are one of the most common causes of hospitalization or death in the industrialized world and are becoming a leading global threat of the 21st century. An impairment of heart functionality, after a myocardial infarction combined with a low intrinsic regenerative capability of cardiomyocytes (CMs) leads to a loss of cardiac tissue. Replacing affected tissue urges the need for novel biofabrication methods to counter this challenge [1, 2].

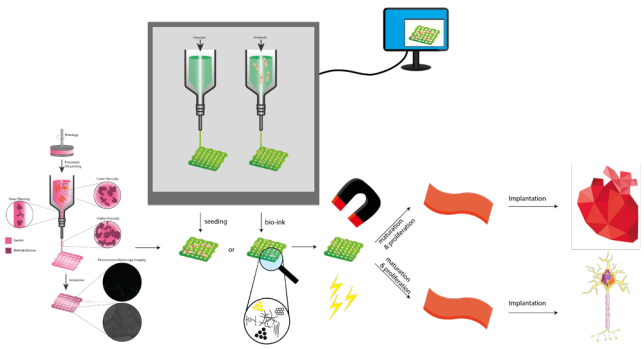

Fig. 1: Schematic representation of a typical workflow of a biofabrication process to produce cardiac or neural constructs using a cost effective bioink.

Using biofabrication techniques to mimic and replicate natural tissue as well as cell environment is a very capable way to achieve physiologically relevant conditions. Especially in electrophysiological human tissue like cardiac tissue, proper signal transduction is of paramount importance for appropriate function and cell maturation as well as differentiation. Precisely, these conductive properties are challenging to engineer. In human cardiac tissue the conductance within the whole myocardium is provided by specialized cells (Purkinje fibers) with a high conductivity, capable to propagate timely the electrical signal. These cells forming the so-called syncytium [3]. To rebuild these natural properties current research tries to exploit the intrinsic characteristics of conductive nanocomposites, like metal nanocomposites (NPs), carbon nanotube (CNTs) or graphene and integrate them into non-conductive hydrogels. In our project conductive nanofibers are being biofabricated to mimic this conductive system and make electrical stimulation possible. Moreover, a novel cost effective and versatile bioink has been developed, which, due to its rheological properties and tunable stiffness, has the potential to be implemented in a dual scale approach. This dual scale approach in which 3D-printed micrometer scale and electrospun nanometer scale structures are combined, electrophysiological conditions should be possible to achieve [4]. This approach to mimic the cardiac conductive system by means of conductive nanofibers has the potential to be a promising implementation in 3D-biofabricated human tissue substitutes and regenerative medical applications.

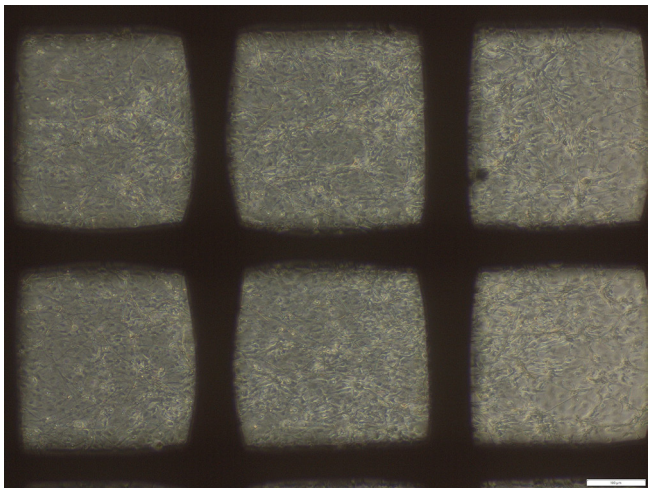

Fig. 2: LM image of beating CMs cultivated for 7 d on the electrically conductive PCL-CNT dual scale construct, scale bar = 100 µm.

Conductive scaffold

Increasing the resemblance of our biofabricated construct to extracellular matrix (ECM), in which the cardiac cells are embedded, is a key factor in tissue engineering. Therefore, during the last year our dual scale approach, combining electrospun PCL nanofiber with a 3D-printed PCL microstructure was extended to electrically conductive PCL-CNT nanofibers. A novel electrospinning solution had to be developed and the fabrication method had to be refined. The produced scaffold was subsequently seeded with CMs to study its influence on the cardiac cells. To avoid rupture of the fragile fiber constructs a tailored plasma activation, and cell seeding method was devised. This cell culture experiment indicates alignment of cells along the desired directionality of the conductive PCL-CNT nanofibers. Moreover, the obtained data implies an enhancement in cell maturation, since beating tissue could already be observed after 7 d in culture (Fig. 2).

Bioink

Conversely to the previously described method of a 3D-printed PCL microscale construct, where the cells are seeded after successful additive manufacturing, a bioink was developed, which can directly be loaded with cells and printed. This hydrogel could work as an alternative to the PCL microstructure of the aforementioned dual scale construct. Therefore, a novel approach of blending gelatin (15% w/v gelatin) and methylcellulose (MC, 8% w/w) in a 2:1 ratio

was optimized, and its rheological properties were measured. The bioink properties were successfully optimized to present three different temperature regimes: low viscosity for eased cell suspension and printing with minimal shear stress, form fidelity directly after printing and long term structural stability during incubation. Additionally, the bioink's printability was characterized by measuring printing uniformity (U), pore factor (Pr) and shape fidelity (I). Elastic modulus alterations were examined, and the ink was loaded with cells for 3D-bioprinitng and multiday cell experiments (Fig. 3).

Outlook

Conductive materials within the implantable construct are of paramount importance for better cell maturation and signal transduction. Experimental data indicates favorable CM maturation and alignment along the designed direction. To better understand this process, cell viability and contraction must be quantified, as well as the maturity of cells. Furthermore, electrical stimulation for further maturation improvement can be applied to the dual scale construct. After the developed bioink is being optimized for CM culture and 3D-printing, the combination of this bioink with conductive electrospun NF within a dual scale construct will be investigated.

References

[1] N. Freemantle, J. Cleland, P. Young, J. Mason, J. Harrison, Beta Blockade after myocardial infarction: systematic review and meta regression analysis. BMJ 318, 1730–1737 (1999)

[2] F. Züger, A. Marsano, M. Poggio, M. R. Gullo, Nanocomposites in 3D Bioprinting for Engineering Conductive and Stimuli-Responsive Constructs Mimicking Electrically Sensitive Tissue, Advanced NanoBiomed Research 2, 2100108 (2022)

[3] R. E. Ideker, W. Kong, S. Pogwizd, Purkinje Fibers and Arrhythmias. Pacing Clin Electrophysiol 32, 283–285 (2009)

[4] D. Baruffaldi, G. Palmara, C. Pirri, F. Frascella, 3D Cell Culture: Recent Development in Materials with Tunable Stiffness. ACS Appl. Bio Mater. 4, 2233–2250 (2021)

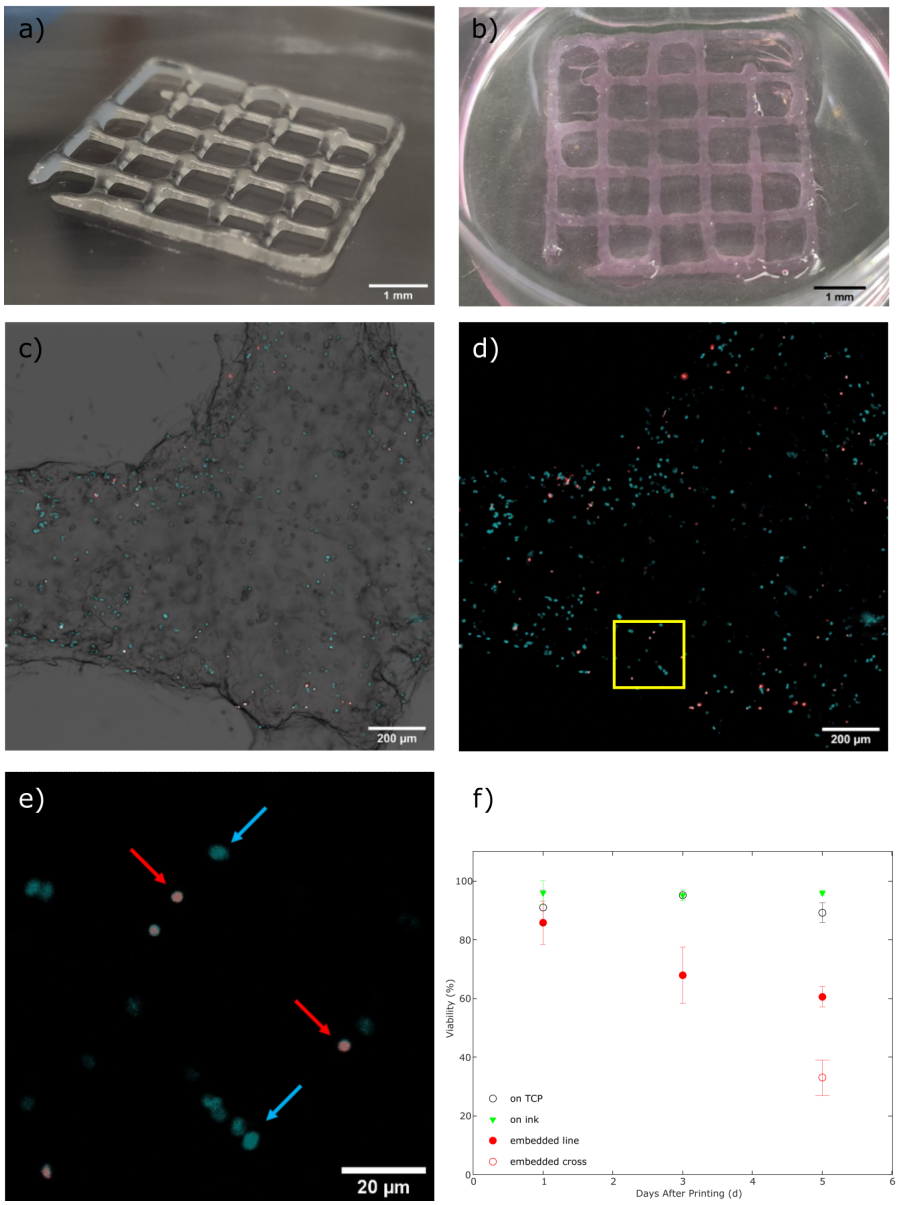

Fig. 3: a) Photograph of a 3D-bioprinted construct directly after printing and submersion for 5 min in a corresponding TG crosslinking solution. Ink contains NIH 3T3 cells. A photograph of a non-crosslinked construct directly after printing can be found in the supplementary data (figure S1a, scale bar = 1 mm; b) Photograph of a 3D-bioprinted construct five days after printing and incubation at 37°C, ink contains NIH 3T3 cells, scale bar = 1mm; c) Fluorescence microscopy image of 1d postprint construct stained with Hoechst 33342 (blue) and PI (red), stacking of BF, Hoechst and PI channel, scale bar = 200 µm; d) Fluorescence microscopy image of 1d postprint construct, stacking of Hoechst and PI channel only, scale bar = 200 µm; e) Zoom into fluorescence microscopy image of 1d postprint construct. Blue arrows indicate Hoechst 33342 staining of cell nucleus (alive cell), while red arrows indicate PI staining of cell nucleus (necrotic cell), scale bar = 20 µm (f) Graphic cell viability illustration of cells seeded on tissue culture plate (TCP, control I, empty black circle), of cells seeded onto previously 3D-printed constructs (control II, green triangle) and cells 3D-bioprinted within the bioink (red circles). Additionally on day 5, the viability is split into viability in crossing structures (empty red circle) and viability in 'line' structures (full red circle). All with corresponding error bars.

Sensitivity enhancement of nano-sensors for fuel cells

Project P1903: Neutron nanomediators for non-invasive temperature mapping of fuel cells
Project Leader: M. Kenzelmann and P. Boillat
Collaborator: A. Ruffo (SNI PhD Student), M. Strobl

Introduction

Fully non-invasive measurement of the temperature inside operating polymer electrolyte fuel cells (PEFC) is of high interest, because the water balance as well as the degradation processes are strongly influenced by the temperature. In our approach, magnetic nanoparticles are integrated in fuel cell structures in order to depolarize a neutron beam. As the magnetic moments are reduced with increasing temperature, these particles can effectively be used as contactless sensors. In this report, we compare the neutron beam depolarization calculated for measured parameters of our materials (such as the crystallite size and the saturation magnetization) to the depolarization effectively measured by neutron imaging. Furthermore, we show how magnetizing the material in a direction perpendicular to the beam polarization can greatly enhance the sensitivity for temperature measurements.

Sensitivity for non-magnetized materials

The sensitivity for our application is defined as the change of measured polarization as a function of temperatures. A good sensitivity requires that the used nanoparticles both have a high depolarization coefficient, and a high dependence of this coefficient on temperature. When a ferromagnetic material is not magnetized, the magnetic domains are randomly oriented. In these conditions, the depolarization coefficient η of a neutron beam transmitted through this material can be evaluated by the following formula [1]:

$$\eta = \frac{\gamma^2 \cdot B^2 \cdot d}{3v^2} \qquad (1)$$

Where γ is the neutron gyrometric ratio (a physical constant), B is the local magnetic flux density, d is the magnetic domain size and v is the neutron velocity. As seen from equation (1), the depolarization coefficient is proportional to the domain size (or to the particle size in the case of single domain nanoparticles), meaning that, even if the local B field is the same, smaller particles result in a lower depolarization which is detrimental for our sensitivity. In addition to this, due to the random orientation of spins near the surface of nanoparticles [2], the average magnetization of nanoparticles is lower than that of the corresponding bulk material. This is illustrated in the comparison of magnetization curves for Ni powders with different sizes (see Fig. 1), where the saturation magnetization (value at 10 kOe, called "M_s" hereafter) is clearly lower for smaller particles.

Using magnetization curves, the expected neutron depolarization coefficient was calculated from equation (1). Under the assumption that the materials are always locally saturated, and the magnetization merely reorients the spin of all domains, the value of the local magnetic flux density B can be obtained from M_s (which was measured at several different temperatures). The value of d is obtained from the crystallite size measured by XRD and the neutron velocity v is approximated using a constant wavelength of 5 Å.

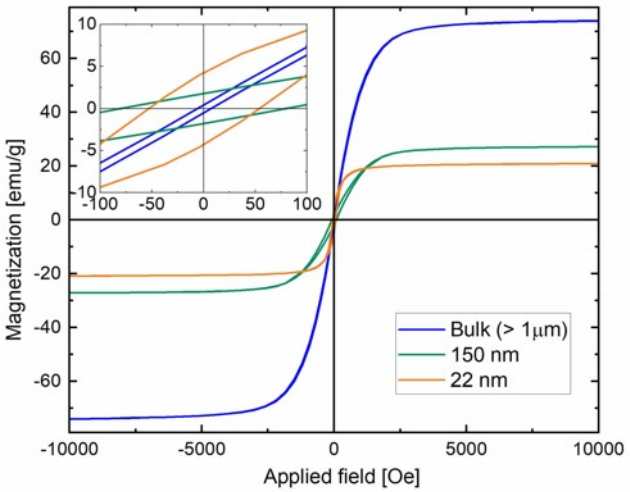

Fig. 1: Magnetization curves measured at room temperature (300 K) for Ni powders with different sizes.

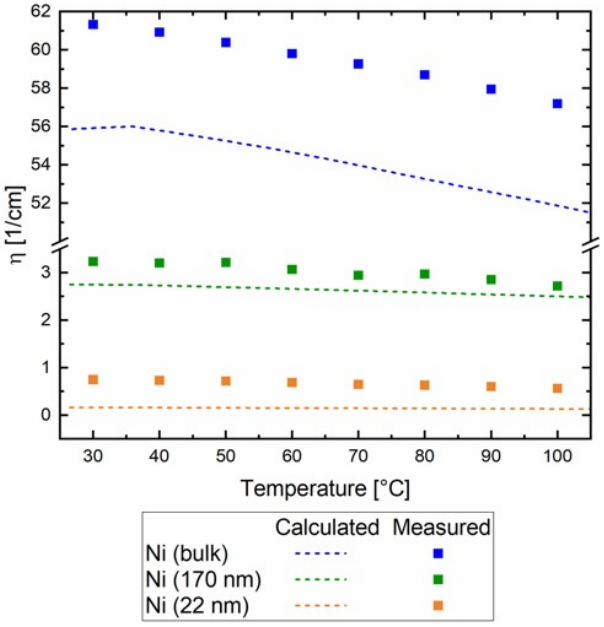

Fig. 2: Depolarization coefficient measured using depolarization neutron imaging (DNI) compared to the calculated values based on equation (1).

The comparison of these calculated values with the ones measured experimentally (see Fig. 2) shows that the simple representation based on equation (1) reasonably approximates (within 20%) the experimental depolarization coefficients of bulk and 170 nm Ni particles as well as their dependence on temperature. For the 22 nm particle, the relative error is much larger, and the reasons for such a discrepancy are still to be clarified.

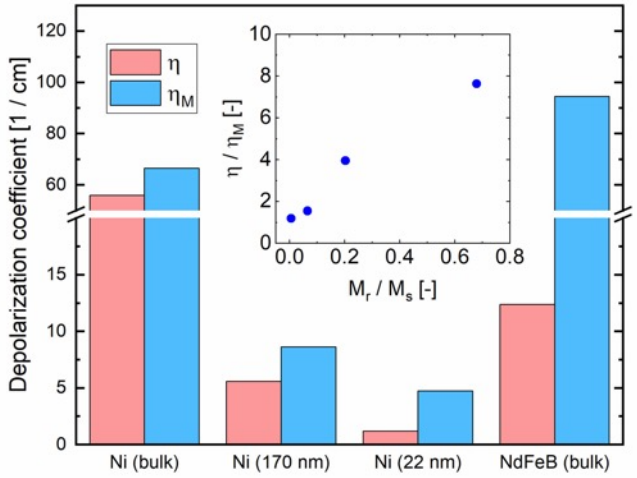

Fig. 3: Enhancement of the depolarization by magnetizing the sample in a direction perpendicular to the polarization. In the insert, the enhancement ratio (η/η_M) is compared to the remanence fraction (M_r/M_s)

Enhancing the sensitivity with magnetization

The depolarization coefficient of non-magnetized materials is determined by the precession of the neutron spin going through magnetic domains of random orientation. After a material has been magnetized in a direction perpendicular to the neutron beam polarization, the average precession angle is larger because the domains are preferentially oriented in a direction making a large angle with the neutron spin. As a result, an enhancement of the beam depolarization is expected. This expectation is confirmed by measurements (see Fig. 3) showing that the depolarization coefficient can be as much as eight times larger for the magnetized material when compared to the pristine materials. AS could be expected, materials with a high remanence fraction (defined as the ratio of remanent to saturation magnetization) show the highest increase of depolarization coefficient when magnetized.

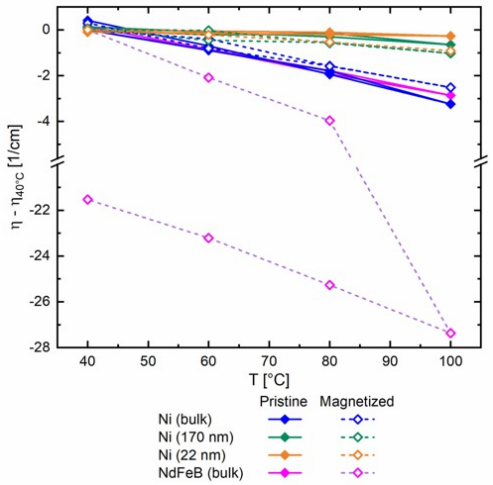

Fig. 4: Absolute change of depolarization coefficient as a function of temperature for pristine and magnetized materials.

The sensitivity for temperature measurements is defined by the change of depolarization coefficient as a function of temperature. As seen in figure 4, when not magnetized, the highest sensitivity is observed for bulk Ni and NdFeB and is in the range of 0.05 cm^{-1}/K. As expected, magnetization does not improve the sensitivity of the bulk Ni material, but results in doubling the sensitivity of the NdFeB material to 0.1 cm^{-1}/K. Moreover, between 80°C and 100°C a much higher slope is observed (1.2 cm^{-1}/K). As shown by the hysteresis, this rapid change as a function of temperature is irreversible, meaning that is can probably be attributed to demagnetization of the material (reorientation of the domains towards a more isotropic distribution). While adding complexity, this also opens opportunities: It would be possible to apply the magnetization to the material in the fuel cell before operation, and keep this demagnetization as a memory of the highest reached temperature for each location. This would allow to measure this recorded temperature in situations where the fuel cell is not operation, for example to avoid disturbance due to the distribution of liquid water. In summary, the bulk NdFeB material, when magnetized, offers the best perspectives for temperature measurements.

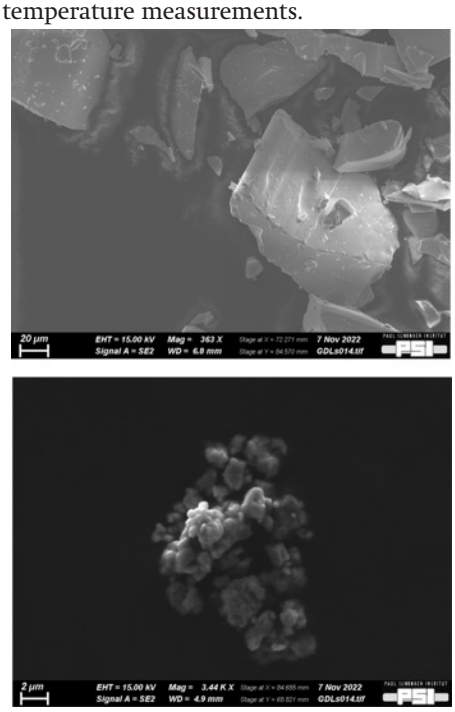

Fig. 5: SEM images of the NdFeB powder as received (top) and after 6 hours of ball milling (bottom).

However, the particles size still need to be reduced to sizes about 1 µm or below in order to integrate them in fuel cell structures. The chosen approach is to use the bulk material and reduce the particles size by ball milling (see Fig. 5). Further investigations will identify whether the excellent temperature sensitivity of the bulk NdFeB powder can be kept when using smaller particles.

References

[1] M. Strobl, H. Heimonen, S. Schmidt, M. Sales, N. Kardjilov, A. Hilger, I. Manke, T. Shinohara, and J. Valsecchi, Polarization measurements in neutron imaging, J Phys D: Applied Physics 52, 123001 (2019)

[2] T. Kim and M. Shima, Reduced magnetization in magnetic oxide nanoparticles, J Appl Phys 101, 09M516 (2007)

Carbon black and red lights: Key ingredients for time-resolved protein crystallography

Project P1904: Revealing protein binding dynamics using time-resolved diffraction experiments at SwissFEL
Project Leader: C. Padeste and T. Ward
Collaborators: M. Carrillo (SNI PhD Student), J. H. Beale

Time-resolved diffraction experiments at X-ray free electron lasers (XFELs) enable new insights into the function of proteins [1]. Sequential delivery of large numbers of protein microcrystals at high rates is essential to conduct such experiments. This is achieved either using liquid or viscous jets, or using fixed targets, on which the samples are deposited and rastered in-step with the pulsed XFEL beam [2, 3]. We are developing microstructured polymer-based fixed targets (MISP-chips) for specific applications at the Cristallina station at SwissFEL/ARAMIS.

Fabrication of microstructured polymer chips

The central part of the MISP-chip is a micro-structured membrane made from thermoplastic polymers such as cyclo-olefin polymer (COP) and cyclo-olefin copolymer (COC). The membrane is manufactured using silicon microfabrication, micro¬molding and hot embossing techniques (Fig. 1).

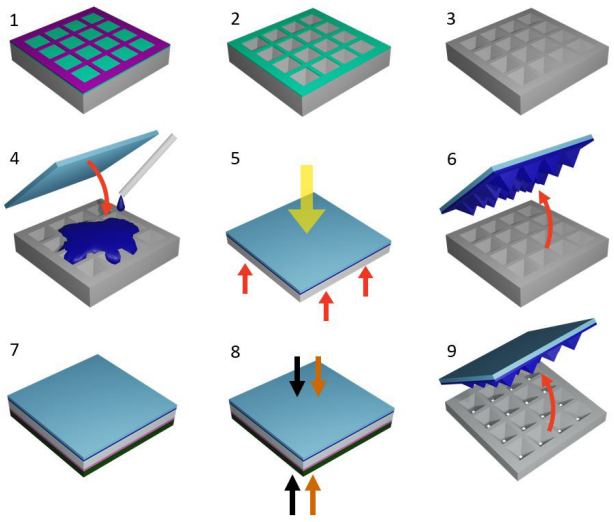

Fig. 1: Fabrication of polymer membranes for the MISP-chips. Laser lithography is used to define the structure on a nitride-coated silicon <100> wafer (1). Using reactive ion and KOH etching the master mold with arrays of pyramid-shaped cavities is produced (2, 3). A stamp is formed by pouring OrmoStamp® onto the master, covering it with a glass slide (4), crosslinking by exposure to UV and heat (5) and separating from the master (6). The OrmoStamp copy is placed on the COC or COP foil, backed with polyimide and Teflon (7) and imprinted in a hot press (8). This results in the membrane with inverted pyramid shaped cavities with openings at the bottom (9).

We are taking advantage of high-precision silicon microfabrication methods to create a master mold with arrays of pyramidal shaped cavities. Anisotropic KOH etching yields inverted pyramid structures following exactly the Si111-planes in the crystalline silicon wafer. An imprint stamp is then molded using UV-curable OrmoStamp® material, and hot-embossed into a thermoplastic polymer film. This film needs to be thinner than the pyramid height, leading to puncturing of the film by the tips of the pyramids. A 3D printed frame is finally glued onto the structured polymer film (Fig. 2).

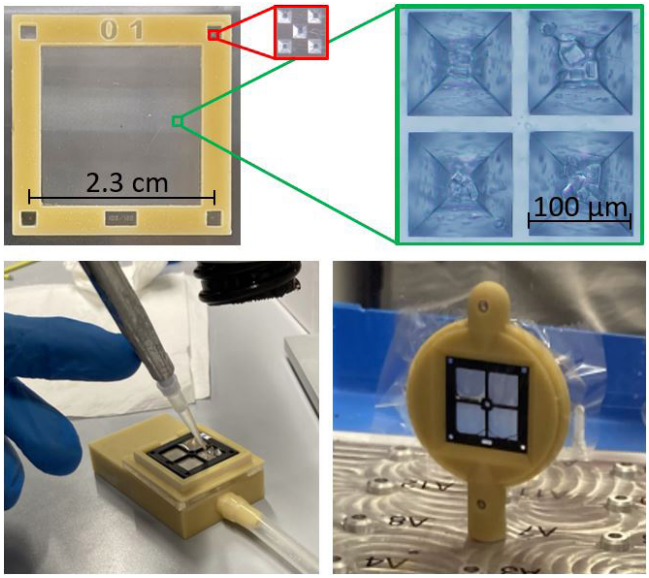

Fig. 2, top row: image of an assembled MISP chip, with details of the fiducials used for alignment and of the membrane area with deposited microcrystals. Bottom row: deposition of the crystal slurry and removing of the liquid through a vacuum line; chip protected with mylar foils assembled in the chip holder.

Sample deposition and data acquisition

The function of the MISP-chip is shown in figure 2. The microcrystal-containing solution is pipetted onto the chip and the liquid is drained off through under-pressure, in order to funnel the crystals into the pyramidal shaped cavities of the membrane. This leads to a preferential arrangement of the crystals in the centers of the cavities. The process is dependent on crystal sizes, concentrations and the membrane parameters.

The loaded chips are enclosed in a thin polymer foil, fixed to a sample holder and aligned to the beam using the fiducials at the corners. The assembled fixed targets are then precisely scanned through the beam at a speed matching the 100 Hz repetition rate of the XFEL pulses. Initial measurements at SwissFEL showed that the pyramidal apertures can be easily filled with a range of different crystal sizes.

Black supports

The transparency of the MISP-chips proved to be beneficial for sample deposition, as microcrystals are well visible in optical microscopes, allowing for easy optimization of the loading procedure. However, light propagates over wide distances through the film (Fig. 3, left). This causes problems for time-resolved experiments, where individual wells are illuminatied by an optical laser, triggering a reaction inside the protein crystal, before being probed by a subsequent X-ray pulse.

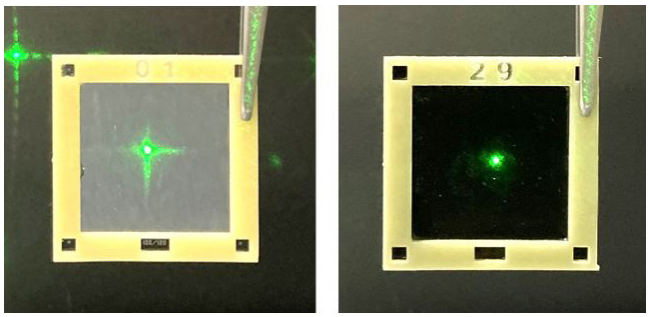

Fig. 3: Light propagation in MISP-chips with transparent membranes (left) and with black membranes (right). Chips were illuminated from the front using an unfocused green laser. On the black chips the light is mostly confined to the directly exposed area.

As light-absorbing polymer films with suitable thickness and thermal properties for the developed fabrication process are not commercially available, we started producing black COC films by solvent casting, using a mixture of acetylene-derived carbon black and COC dissolved in toluene (Fig. 4). By casting 500 µm thick layers using a 500-µm slit applicator and adjusting the COC concentration in a range of about 20 wt%, 50 µm thick films were obtained after solvent evaporation. Membranes produced from these films showed significantly reduced light propagation (Fig. 3, right).

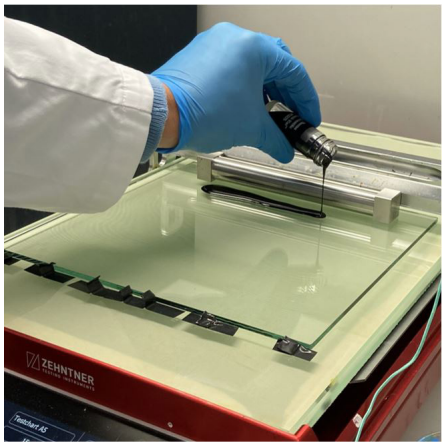

Fig. 4: Fabrication of black COC films by solvent casting, using a solution of COC and carbon black in toluene.

Experiments under red-light conditions

During a commissioning of optical pump/X-ray probe experiments using a light sensitive protein, only red lights were allowed in the entire experimental station (Fig. 5). This prevented light activation of the protein crystals before the experiment.

Structural changes of a light-sensitive protein (a LOV domain) upon photo-activation have been determined earlier using synchrotron and XFEL experiments [4]. We used these LOV-domain crystals for the initial tests of the MISP-chips for time-resolved measurements. While the clear chips were very useful for optimization of deposition parameters and to measure the initial "dark" state of the protein, it turned out that light-propagation indeed inhibited the acquisition of useful data of light-activated states. However, the black chips provided enough light absorption to allow the individual addressing of single wells using a focused optical laser pulse.

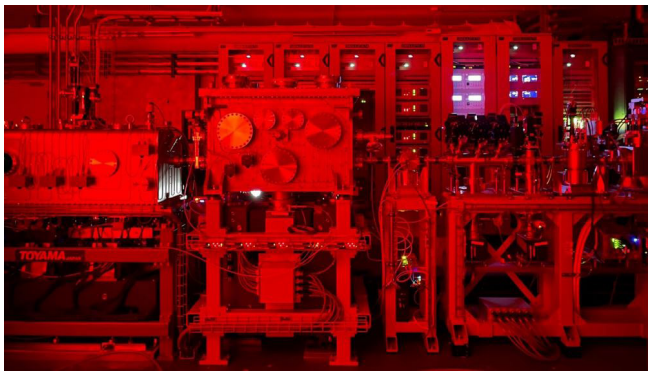

Fig. 5: View inside the cristallina hutch at SwissFEL during the first optical pump/X-ray probe crystallography experiments using the fixed-target approach. To avoid light contamination of the optically sensitive protein crystals, only red lights were allowed.

In summary, we developed stable, reliable supports for serial crystallography, in both, clear and black version. These allow to considerably increase the versatility an efficiency of time-resolved crystallography at SwissFEL and other latest generation X-ray sources.

References

[1] A. Aquila et al., Time-resolved nano¬crystallo-graphy using an X-ray free-electron laser, Optics Express 20, 2706 (2012)

[2] F. Z. Zhao, B. Zhang , E.-K. Yan, B. Sun, Z.-J. Wang, J.-H. He, D.-Ch. Yin, A guide to sample delivery systems for serial crystallography, The FEBS journal 286, 22 (2019)

[3] I. Martiel, H. M. Müller-Werkmeister and A. F. Cohen, Strategies for sample delivery for femtosecond crystallography, Acta Crys. D75, 160, (2019)

[4] S. Aumonier, G. Santoni, G. Gotthard, D. von Stetten, G. A. Leonard, A. Royant, Millisecond time-resolved serial oscillation crystallography of a blue-light photoreceptor at a synchrotron, IUCrJ, 7, 728 (2020)

Applying nanowire MFM to 2D materials

Project P1905: Magnetic force microscopy with nanowire transducers
Project Leader: M. Poggio and E. Meyer
Collaborator: L. Schneider (SNI PhD Student)

Introduction

Recent years have seen rapid progress in nanometer-scale magnetic imaging technology, with scanning probe microscopy driving remarkable improvements in both sensitivity and resolution. Among the most successful tools are magnetic force microscopy (MFM), spin-polarized scanning tunneling microscopy, as well as scanning magnetometers based on nitrogen-vacancy centers in diamond, Hall-bars, and superconducting quantum interference devices. Over the past 3 years, we have been using nanowire (NW) force sensors as ultra-sensitive MFM probes. Using NWs functionalized with magnetic tips, we strive to map magnetic fields and dissipation with enhanced sensitivity and resolution compared to the state of the art and to apply these new capabilities to study magnetization in 2D materials.

The key component of a force microscope is the force sensor, which consists of a mechanical transducer, used to convert force into displacement, and an optical or electrical displacement detector. In MFM, "top-down" Si cantilevers with sharp tips coated by a magnetic material have been the standard transducer for years. Under ideal conditions, state-of-the-art MFM can reach spatial resolutions down to 10 nm, although more typically around 100 nm. These cantilevers are well-suited for the measurement of the large forces and force gradients produced by strongly magnetized samples. The advent of NWs and carbon nanotubes grown by "bottom-up" techniques now gives researchers access to much smaller force transducers than ever before. This reduction in size implies both a better force sensitivity and potentially a finer spatial resolution. Sensitivity to small forces provides the ability to detect weak magnetic fields and therefore to image subtle magnetic patterns; tiny concentrated magnetic tips have the potential to achieve nanometer-scale spatial resolution, while also reducing the invasiveness of the tip on the sample under investigation. Such improvements are crucial for imaging nanometer-scale magnetization textures in 2D systems.

Recent efforts have demonstrated the use of single NWs as sensitive scanning force sensors [1]. When clamped on one end and arranged in the pendulum geometry, i.e. with their long axes perpendicular to the sample surface to prevent snapping into contact, they probe both the size and direction of weak tip-sample interactions. NWs have been demonstrated to maintain excellent force sensitivities around 1 aN/Hz½ near sample surfaces (<100 nm), due to extremely low noncontact friction. As a result, NW sensors have been used as transducers in force-detected nanometer-scale magnetic resonance imaging and in the measurement of tiny optical and electrical forces. In a proof-of-principle microscopy experiment in the Poggio lab, we showed that a magnet-tipped NW can be sensitive to magnetic field gradients of just a few mT/(m Hz^{½}), equivalent to the gradient produced by a few tens of Bohr magnetons or a few nA of flowing current at a distance of a few hundred nanometers [2]. Such sensitivity compares favorably to that of other magnetic microscopies, including scanning Hall microscopy, scanning SQUID microscopy, and scanning nitrogen-vacancy magnetometry [3].

Goals

Despite these promising features, until now, only proof-of-principle NW MFM experiments have been carried out on the well-known magnetic field profile of a current-carrying wire [2, 4]. We intend to move past this demonstration stage by:

1. optimizing the magnet-tipped NW transducers to achieve the highest possible sensitivity and resolution;

2. using the new scanning probes to image magnetism in 2D vdW systems.

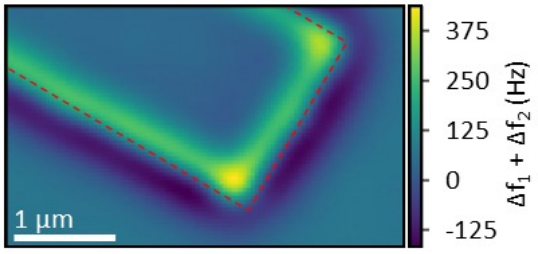

Fig. 1: NW MFM of a corner of a rectangular shaped bilayer of $EuGe_2$ (dashed line) covered with SiOx. Measured at 8 T and 4.7 K with a 200-nm tip-sample spacing.

Results

In the third year of work, we can report progress on both the NW MFM itself and on imaging experiments on 2D magnets. Because we are convinced that our unique nanometer-scale magnetic field imaging technique has much to reveal about the behavior of newly discovered 2D magnets, we are working on producing 2D magnets that we can image with our NW MFM. This effort consists mostly of exfoliating few or single layer 2D magnetic materials near the edge of a Si chip, where the flakes are accessible to our scanning NW microscope (the microscope works only within ~100 of micrometers from an edge due to the constraints imposed by the optical detection of the NW motion). We initially studied samples of layered $PtSe_2$, which can be purchased from HQ Graphene and is stable in air [5]. This material is particularly interesting to study, since it displays a layer-dependent magnetism, which – unlike previously studied 2D magnets – is

induced by defects. Despite producing mono- and few-layer samples of sufficient lateral size (several micrometers on a side) and imaging them with our NW MFM, we did not yet see clear evidence of magnetism. We will make further attempts on this sample, since we cannot yet be certain that technical limitations in the experiments did not prevent us from measuring magnetic effects. We have also started a campaign of 2D magnet fabrication, making use of the glove-boxes available in the department. We anticipate to soon have other samples from the long list of interesting 2D magnets, including Fe_3GeTe_2, $Cr_2Ge_2Te_6$, $MnPS_3$, CrI_3, CrB_3, $CrCl_3$, VI_3, $FeCl_3$, MnI_2, CoI_2, NiI_2, and $NiBr_2$.

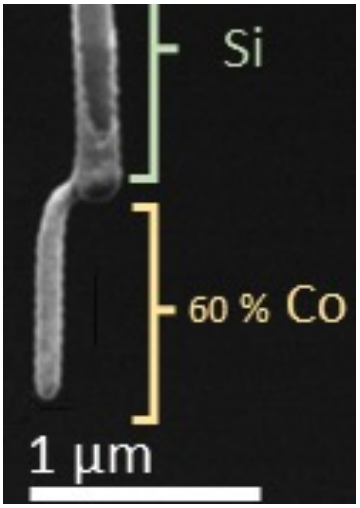

Fig. 2: Scanning electron micrograph of a Co tip deposited by FEBID (at the SNI Nano Imaging Lab) on the free end of a Si NW. The Si NW (length: 20 µm) was grown by the Budakian group (Waterloo).

In the meantime, we have begun collaborating with the Maletinsky group, who is studying the 2D magnet $EuGe_2$ using scanning nitrogen-vacancy (NV) microscopy (SNVM). We have scanned bilayer samples of $EuGe_2$ [6], as shown in figure 1, and will make similar images of monolayer samples. The NW MFM images are complementary to the SNVM images, because they provide different contrast, i.e. field gradients and magnetic dissipation, and can function under much higher magnetic fields. Measurements on bilayer $EuGe_2$ have already provided important insight into the magnetism of this sample, showing a clear saturation behavior as a function of out-of-plane field, evidence of antiferromagnetic coupling between layers, domain formation, and a strong signature in the dissipation corresponding to a magnetic phase transition as a function of decreasing temperature. Measurements are ongoing, but it is already clear that the combined high spatial resolution and high sensitivity of NW MFM provides a new window in the magnetism of the 2D material.

We have also dedicated a significant effort this year to improving the NW MFM technique. First of all, we have implemented an optical drive, via an auxiliary laser, to excite the NW. This method replaces the piezoelectric drive, which was formerly used and provides a significant improvement, because it drives the NW modes via a photothermal effect. In contrast, the piezoelectric element excited a number of mechanical modes in the holder and the probe itself in addition to the NW modes. These modes often caused problems for the phase-locked-loop, which is tasked with keeping track of the NW frequency. As a result, measuring the NW frequency and making MFM images has become significantly faster and more robust. Second, we have installed a heater and thermometer stage near the sample in order to be able to make measurements between 4.7 and 50 K. Third, and finally, we have started functionalizing NWs with magnetic tips ourselves here in Basel, using focused electron beam induced deposition (FEBID) carried out in the Nano Imaging Lab of the SNI. We grow Co tips on the free ends of Si NWs provided by our collaborator Prof. Raffi Budakian (Waterloo, Canada). With this new control over the process, we have achieved NWs combining the sharpest and highest magnetization tips made so far with NWs having high mechanical quality factors. This combination should allow us to do NW MFM with higher sensitivity and spatial resolution than before and will be crucial in measurements of the subtle magnetic field patterns produced by 2D magnets.

References

[1] N. Rossi, F. R. Braakman, D. Cadeddu, D. Vasyukov, G. Tütüncüoglu, A. Fontcuberta i Morral, and M. Poggio, Vectorial scanning force microscopy using a nanowire sensor, Nat. Nanotechnol. 12, 150 (2017)

[2] N. Rossi, B. Gross, F. Dirnberger, D. Bougeard, and M. Poggio, Magnetic Force Sensing Using a Self-Assembled Nanowire, Nano Lett. 19, 930 (2019)

[3] E. Marchiori, L. Ceccarelli, N. Rossi, L. Lorenzelli, C. L. Degen, and M. Poggio, Nanoscale magnetic field imaging for 2D materials, Nat. Rev. Phys. 4, 49 (2022)

[4] H. Mattiat, N. Rossi, B. Gross, J. P. Navarro, C. Magén, R. Badea, J. Berezovsky, J. M. De Teresa , and M. Poggio, Nanowire Magnetic Force Sensors Fabricated by Focused-Electron-Beam-Induced Deposition, Phys. Rev. Appl. 13, 044043 (2020)

[5] A. Avsar, A. Ciarrocchi, M. Pizzochero, D. Unuchek, O. V. Yazyev, and A. Kis, Defect Induced, Layer-Modulated Magnetism in Ultrathin Metallic PtSe2, Nat. Nanotechnol. 14, 674 (2019)

[6] A. M. Tokmachev, D. V. Averyanov, A. N. Taldenkov, O. E. Parfenov, I. A. Karateev, I. S. Sokolov, and V. G. Storchak, Lanthanide f7 metalloxenes – a class of intrinci 2D ferromagnets, Mater. Horizons 6, 1488 (2019)

Heteromeric nm-sized assembly characterisation and machine learning

Project P1906: Machine learning assisted design of heteromeric self-assembled molecular capsules
Project Leader: K. Tiefenbacher and A. von Lilienfeld
Collaborator: I. Martyn (SNI PhD Student)

Introduction

Self-assembled supramolecular capsules display biomimetic catalytic properties, due to their rigid internal cavity modeling the active site of an enzyme. These nm-sized molecular containers can encapsulate guest molecules and stabilise reactive intermediates by means of non-covalent interactions, catalyzing reactions such as terpene cyclisation [1]. However, most known hydrogen-bonded capsules are homomeric (self-assembled from only one building block). Due to the high symmetry of their internal cavity, homomeric capsules are limited in their ability to impose specific conformations on the encapsulated substrate, resulting in limited product selectivity [2]. Our screening results revealed a strong preference for thermodynamic self-sorting, except where the homomeric assembly of a building block was disfavoured by solubility effects.

Assembly characterization

A molecular model of the discovered heteromeric assembly was proposed, based on bonding motifs derived from existing crystal structures. The hexameric structure was found to be stable during structural optimization (Spartan '20, Wavefunction, equilibrium geometry calculation). The predicted structure does not incorporate water into the hydrogen bonding network, such as in the resorcin[4]arene $[RS]_6[H_2O]_8$ assembly. This structural prediction is consistent with DOSY-water titration and experimentally observed self-assembly below 1 equivalent of water per equivalent of hexamer. The exact ratio of building blocks in the assembly was also confirmed by means of quantitative NMR, using triethylsilane as an internal standard. The experimental 2D NMR data is consistent with the predicted binding motifs of the model, however, the signal broadening of phenolic hydroxide peaks prevents unambiguous structural assignment. Further NMR studies are in progress, with the hope that variable-temperature NMR will cause these environments to become visible and permit full structural elucidation.

The heteromeric assembly underwent extensive guest uptake screening, where it was found that the dynamic nature of the hydrogen-bonded assembly plays a role in the stability of the heteromeric host in the presence of guest molecules. Should the guest molecule exhibit a higher affinity for one building block over the other, the heteromeric assembly will dissociate to favor guest uptake by the homomeric assembly of one of the component building blocks. This behavior illustrates the complexity of heteromeric molecular assembly design: the assembly, if it is to act as a catalyst, must not only be stable under reaction conditions, but also capable of substrate encapsulation without re-equilibration to another assembly. In this case, the only suitable guest molecule was found to be C_{60}-fullerene. The fact that larger fullerenes and malonate derivatives exhibit no guest uptake behavior imply a definite size limitation for this system.

Crystallization of this system poses several challenges, as the large internal cavity is filled with solvent molecules in the absence of a suitable guest, which are a source of significant disorder in the crystallographic data. Therefore, crystallization of such species are conducted in the presence of guest. Single crystals suitable for X-ray diffraction analysis were obtained by slow vapor diffusion of diisopropyl ether into the solution of the assembly and C60 guest in chloroform. However, potentially due to the low solubility of guest in organic solvents, a crystal structure of the heteromeric assembly has not yet been obtained. In the solid phase, the only species observed are those of the homomeric assemblies of the constituent building blocks.

Finally, characterisation of the heteromeric assembly was investigated by mass spectrometry (MS). As the structure is assembled by non-covalent hydrogen bonding, typical MS methods such as electrospray ionization were found to destroy the assembly during the ionization process. Matrix-assisted desorption/ionisation-time of flight-mass spectrometry (MALDI-TOF MS) provides a softer ionization method, with the drawback that the analyte must be co-crystallised with an acidic matrix solution. The heteromeric assembly shows some resilience to acids such as TFA, but not at the concentration required to conduct MALDI-TOF MS. Screening of a wide range of matrix solutions was carried out, in conjunction with C_{60} guest and Ag^+ labelling to generate charged species in a nondestructive manner. The first-shot phenomenon was also employed, in case multiple laser pulses degraded the hexameric assembly. This method gave a MALDI peak corresponding to the doubly Ag^+-labelled heteromeric assembly.

Open assembly

During the investigation of the heteromeric assembly, it was found that one of the two constituent building blocks, previously not known to assemble in apolar solvents due to its low solubility, does indeed self-assemble in chloroform at low concentrations. Molecular modelling indicated a belt-like tetrameric structure, with free phenol groups not involved in the hydrogen bonding network.

Further study of this building block revealed that these free phenolic groups could be saturated by the addition of methanol, drastically increasing the solubility of the assembly. The open nature of this tetramer, featuring two windows of approximately 12 Å diameter, could lead to catalytic properties of interest, as the guest need not be completely encapsulated by the assembly. However, due to the lack of incorporated water molecules, this tetramer was unable to carry out glycosylation or furanosylation by the "proton wire" mechanism [3].

Supramolecular Toolkit

The manual screening of a chemical space consisting of supramolecular building blocks did not yield a large number of new heteromeric assemblies, due to a marked preference for thermodynamic self-sorting behavior. This lack of data on persistent, characterizable heteromeric assemblies hindered the development of a machine learning model to predict self-sorting molecular properties.

To address this, it was decided to investigate the use of Supramolecular Toolkit (STK), a Python library which automates the construction of supramolecular structures from molecular building blocks. This software makes use of an evolutionary algorithm for the discovery of new supramolecular assemblies with user-defined properties [4]. As this method was developed primarily for the design of covalently-bonded or metal-ligand species, significant modification was required to make STK capable of representing non-covalent assemblies. For example, non-integer bond numbers and variable atomic valencies were not supported.

After some modification, the structures of non-covalent molecular containers could be represented within such a system, although the STK assembly protocol generates species with long bonds which require further optimization (Fig. 1). However, the scope of possible mutation operations (rotation, replacement of building blocks) was not broad enough to automatically generate the desired structural diversity of heteromeric assemblies. In order to produce adequately diverse mutated structures, with features such as varied amounts of water incorporated into the bonding network and varied bond order of hydrogen bonding functional groups, a more flexible mutation protocol is required.

Outlook

In the next stage of the project, two material discovery machine learning methods – a Monte Carlo molecular docking simulation technique, and a functional group mutation algorithm – will be combined to generate mutated heteromeric assemblies from an input of 3D structures of literature-known homomeric assemblies. The population will be evaluated following each mutation step to find the most suitable candidates for stable heteromeric assemblies.

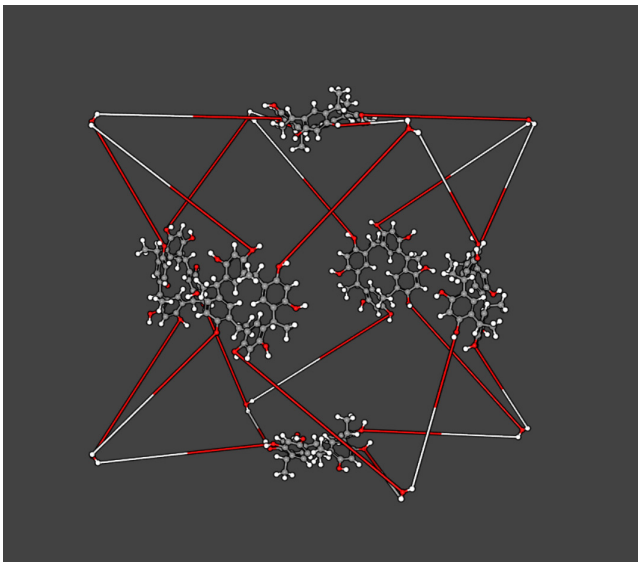

Fig. 1: Resorcin[4]arene hexameric assembly with 8 incorporated water molecules, generated by STK.

Prediction of the binding energy of a guest is a method drawn from the field of drug design. For this project, the method to be used is a Monte Carlo simulation technique, which performs geometry- and energy-based docking to search for a binding mode with an energy minimum for both guest and host [5]. In this phase of the project, a rigid guest will be used to ensure that the internal cavity motif is persistent throughout the mutation process, disfavoring the creation of energetically stable collapsed structures.

With such a technique, it should be possible to explore the energy landscape of heteromeric supramolecular assemblies. A first benchmark will be to rediscover the heteromeric assembly from the manual screening experiments by the ML method.

References

[1] Q. Zhang, L. Catti, K. Tiefenbacher, Catalysis inside the Hexameric Resorcinarene Capsule, Acc. Chem. Res. 51, 2107-2114 (2018)

[2] I. Némethová, L. Syntrivanis, K. Tiefenbacher, Molecular Capsule Catalysis: Ready to Address Current Challenges in Synthetic Organic Chemistry?, Chimia 74, 561-568 (2020)

[3] T-R. Li, F. Huck, G. M. Piccini, K. Tiefenbacher, Mimicry of the proton wire mechanism of enzymes inside a supramolecular capsule enables β-selective O-glycosylations, Nat. Chem. 14, 985-994 (2022)

[4] L. Turcani, A. Tarzia, F. Szczypiński, K. Jelfs, stk: An extendable Python framework for automated molecular and supramolecular structure assembly and discovery, J. Chem. Phys. 154, 214102-214113 (2021)

[5] M. Liu, S. Wang, MCDOCK: A Monte Carlo simulation approach to the molecular docking problem, J. Comput. Aided Mol. Des. 13, 435-451 (1999)

Towards quantum coherent coupling between a nanomechanical membrane and an atomic ensemble

Project P1907: Spin-opto-nanomechanics
Project Leader: P. Treutlein and P. Maletinsky
Collaborators: G.-L. Schmid (SNI PhD Student), M. Ernzer, M. Bosch Aguilera

Engineering quantum mechanical interactions between a mechanical oscillator and atomic spins is interesting for fundamental quantum science as well as promising for applications in quantum sensing. In previous experiments we used light to generate strong coupling over a large distance between a mechanical oscillator and an ensemble of atomic spins [1]. This strong coupling was subsequently used to demonstrate coherent feedback cooling of the mechanical oscillator with the atomic spins [2]. In coherent feedback, a quantum system is controlled through its interaction with another one, in such a way that quantum coherence is preserved. In contrast to measurement-based feedback, coherent feedback does not rely on measurements, thus avoiding the associated quantum backaction. Coherent feedback can outperform measurement-based feedback in certain tasks such as cooling of a nanomechanical oscillator. Using the atomic spins as a controller, we demonstrated coherent feedback cooling of a nanomechanical membrane to 216 mK in a room temperature environment [2].

In future experiments, we will use the light-mediated coupling to create quantum entanglement between the spin ensemble and the mechanical oscillator. To reach this goal, we have to engineer quantum coherent coupling between the two systems. While in the so-called "strong coupling" regime, the coupling rate g is larger than the average decay rate of the systems, $g>\gamma_s+\gamma_m$, for "quantum coherent coupling" the coupling rate must exceed the average decoherence rates, $g>\gamma + \gamma_m \cdot (2n_{th}+1)$. This is a much stricter condition, since the thermal decoherence rate is the decay rate multiplied with the number of phonons in the environment. While the atomic spins are coupled by light to an environment at near zero temperature, the membrane is mounted in a support at finite temperature and n_{th} is a large number. To reach the quantum coherent coupling regime, we have to optimize and characterize both individual systems.

Hybrid setup

Our hybrid system consists of a mechanical oscillator and a collective atomic spin coupled by laser light over a distance of one meter in a looped geometry (Fig. 1). A coupling laser interacts first with the spin, then with the membrane and once again with the spin as sketched in figure 1 and detailed in [2].

The collective spin is realized with an ensemble of 1.3×10^7 ultracold ^{87}Rb atoms confined in an optical dipole trap. The atoms are optically pumped into the hyperfine ground state $|F=2,m_F=-2\rangle$ in a static magnetic field. The spin interacts with the light by the off-resonant Faraday interaction.

The mechanical oscillator is placed in a single-sided optical cavity which enhances the optomechanical coupling to the light field. The membrane can be driven by a modulation of the amplitude of the ingoing light. The position of the membrane is imprinted on the phase of the outgoing light.

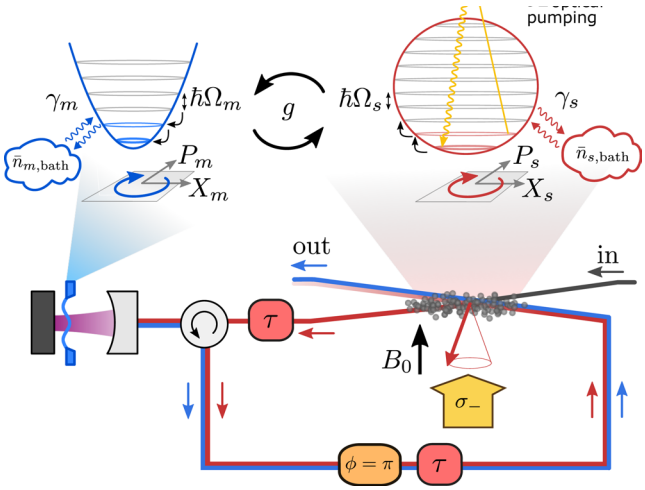

Fig. 1: Sketch of the light-mediated spin-membrane coupling. Light interacts first with the spin, then with the membrane, and then again with the spin. On the way back from the membrane to the spin, a π-phase is imprinted on the light, rendering the spin-membrane interaction effectively Hamiltonian for zero-delay $\tau=0$. The systems can be approximated by harmonic oscillators of frequencies Ω_m and Ω_s with damping rates γ_m and γ_s coupling them to a bath with $\bar{n}_{(m,bath)}$ and $\bar{n}_{(s,bath)}$ phonons, respectively. The oscillators are coupled at a rate g.

By coupling both the spin and the membrane in a looped geometry to the light, we can create an effective Hamiltonian coupling between the two systems [1].

Soft-clamed membranes

In our previous work [1, 2] we used the 22-mode of a 100 nm thick SiN square membrane. The membrane was embedded in a phononic crystal which creates a bandgap around the resonance frequency of the 22-mode. The high stress of the SiN and the shielding from the environment result in a Q-factor of 2×10^6.
The main source of loss for these kinds of square membranes is the bending loss at the edge between membrane and support structure [3]. Bending losses can be reduced by patterning the membrane itself instead of the support structure of the membrane. The periodic structure on the membrane, which creates a bandgap, has a defect in the middle where the mode of interest is localized. Figure 2 shows the fundamental vibrational mode of the defect in such a membrane, which was fabricated by our collaborators in the Gröblacher group at TU Delft.

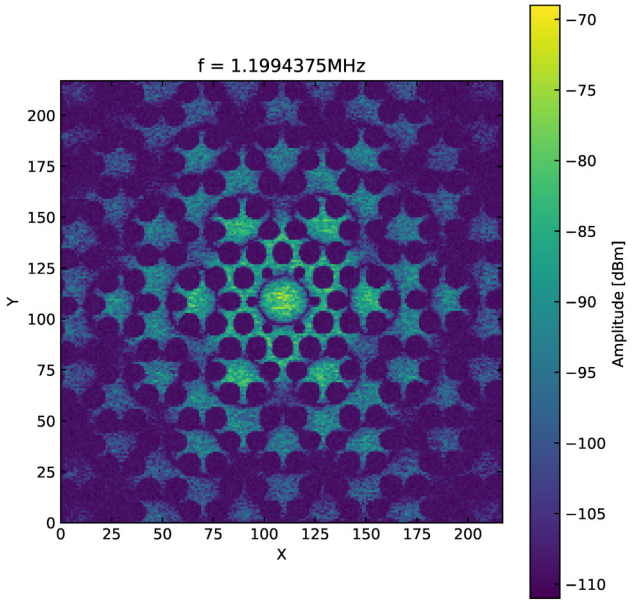

Fig. 2: Fundamental mode of the defect of a soft-clamped membrane. For this image, a laser was scanned over the membrane and at each point the thermal noise was measured by detecting the phase of the reflected light.

The vibrational mode shown in figure 2 has a Q-factor of 7.6 x 10^7. Introducing the new, soft-clamped membrane into the hybrid system will allow us to reach the mechanical ground-state when the membrane is cooled by the spin.

Characterization of spin ensemble

The atomic spins interact with the light through the off-resonant Faraday interaction. In contrast to the membrane, the spins are not coupled to a thermal bath. Still, to interface the spin with the light in a quantum-noise-limited way, we have to understand the spin-light interaction precisely. In particular, the inhomogeneity of the light intensity over the atomic cloud can have a significant impact on expected mean values and quantum noise amplitudes.

For a homogeneous coupling between the spins and the light, the Hamiltonian reads $H=\hbar\alpha_1 S_z F_z$ where α_1 is the vector polarizability constant, S_z is the circularly polarized Stokes-vector component and F_z a collective spin component, where the collective spin is the sum of all individual atomic spins $F_z=\sum_i f_z^{(i)}$.

In our experiment, the waist of the laser and the waist of the atomic cloud are of similar size such that atoms at different positions in the cloud experience different light intensities. In this inhomogeneous regime we can write the Hamiltonian as $H=\hbar\alpha_1 S_z \sum_i \eta_i f_z^{(i)}$ where each spin is multiplied with a constant η_i which is proportional to the local intensity. From the Hamiltonian, we can calculate the angle by which the light polarization is rotated due to the interaction with the atomic spins. This Faraday angle is given by

$$\theta = S_y^{(out)}/2S_x = \alpha_1 F_z \langle\eta\rangle/2$$

where $\langle\eta\rangle$ is the mean η_i. From absorption imaging of the atomic cloud, we get an estimate for F_z. The vector polarizability α_1 is calculated from theory, thus we can calibrate $\langle\eta\rangle$ for our experiment (see Fig. 3).

From a realistic value of $\langle\eta\rangle$ the quantum limits of the spin-light interface can be inferred.

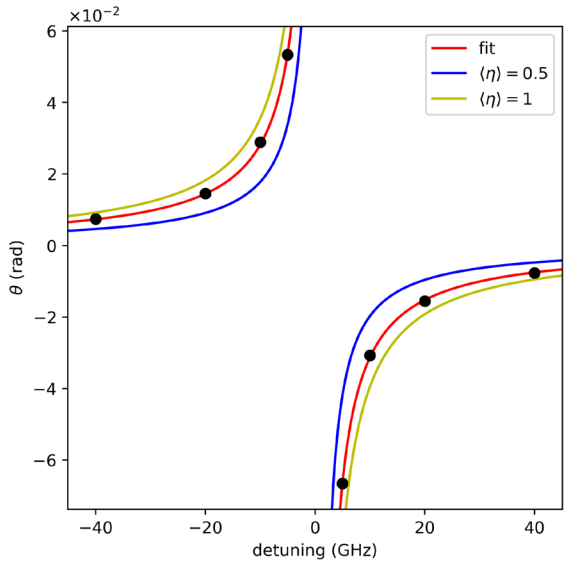

Fig. 3: Faraday angle as function of the detuning from the D2-tansition. The blue and yellow lines show the theory for the limiting cases where the atoms are homogeneously distributed over the beam (⟨η⟩=0.5, blue) or all atoms are at the focus of the beam (⟨η⟩=1, yellow). A fit to the measured data gives ⟨η⟩=0.79 (red).

Outlook

Membranes with higher Q-factors and a better understanding of the spin-light interface will allow us to perform spin-membrane coupling experiments in the quantum coherent regime. If each of the systems is limited by quantum backaction noise, this will allow us to perform a variety of quantum information tasks such as quantum state swaps or the creation of entangled states by two-mode squeezing.

References

[1] T. M. Karg, B. Gouraud, C. T. Ngai, G.-L. Schmid, K. Hammerer, and P. Treutlein, Light-mediated strong coupling between a mechanical oscillator and atomic spins 1 meter apart, Science 369, 174 (2020)

[2] G.-L. Schmid, C. T. Ngai, M. Ernzer, M. Bosch Aguilera, T. Karg, and P. Treutlein, Coherent feedback cooling of a nanomechanical membrane with a spin, Phys. Rev. X, 12, 011020 (2022)

[3] Y. Tsaturyan, A. Barg, E.S. Polzik, A. Schliesser, Ultracoherent nanomechanical resonators via soft clamping and dissipation dilution, Nat. nanotech. 12, 776-783 (2017)

Luminescent Pt(II) complexes aggregate towards functional nanowires

Project P1908: Chiral Recognition in Molecular Nanowires from Square-Planar Platinum(II) Complexes
Project Leader: O. Wenger and C. Sparr
Collaborator: A. Huber (SNI PhD Student)

In the context of chiral recognition, we designed new nanostructured "chiral nose"-type materials to selectively sense chiral volatile organic compounds (VOCs)[1, 2]. Controlled helical superstructures composed of stacked square planar platinum (II) complexes are of key interest to us. In theory, interactions of small chiral molecules with the crystal lattice can provoke changes in photoluminescence, vapochromism [3], or electrical conductance, thus leading to sensing behavior.

Ideally, stereoisomers of specific VOC analytes could interact with the nanowire crystal lattice by intercalation, or through π-π interactions directly at the atropisomeric moieties of the complexes.

The tendency of square planar Pt(II) complexes to form stacked aggregates arises from weak metal-metal interactions between the $5d_{z2}$ orbitals upon close contact (<3.5 Å)[4].

Stereogenic Pt(II) isocyanide complexes

Taking advantage of the Sparr group`s expertise on atroposelective oligo-naphthylene synthesis [5, 6], the selective formation of (R_a)- or (S_a)- di-naphthylenes was achieved. The iterative addition of building block (BB in Scheme 1a) to aromatic aldehydes was followed by an enantioselective arene-forming aldol-condensation [6]. The atropisomeric scaffold will then be transformed into isocyanide ligands, following methods developed in the Wenger group (Scheme 1a)[7].

The sterically demanding monodentate ligand was introduced to perturb the intermolecular stacking in order to induce a helical supramolecular arrangement. On the other hand, the metal-metal interactions are meant to stabilize the oligomeric nanowire structures [3, 4].

Recently, we prepared two reference Pt(II) complexes without the atropisomeric moiety (Scheme 1b) to study their luminescence and assembly behavior. The reference complexes should reveal the envisaged core structure`s steric and electronic properties towards close Pt-Pt distances upon aggregation.

Aggregation, luminescence and crystal analysis of reference complexes (1) and (2)

With the reference complexes (1) and (2) in hand, we studied the absorption and emission in solution.

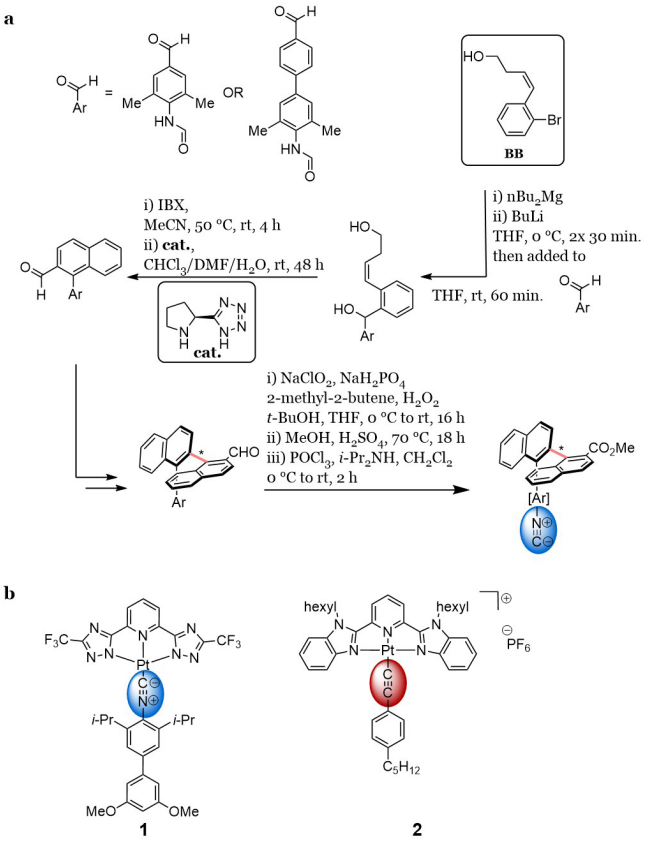

Scheme 1: a) Synthetic strategy towards monodentate atropisomeric isocyanide ligands (blue). b) Prepared reference complexes with isocyanide- (1) and alkynyl (red) ligand (2).

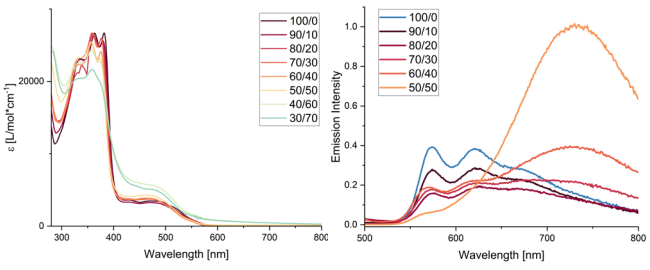

Fig. 1: UV-vis absorption (left) and emission (right) spectra of (2) in the given ratios of CH_2Cl_2/cyclohexane, x/y.

Figure 1 shows the UV-vis absorption (left) and emission (right) spectra of (2) in different dichloromethane/cyclohex-

ane solvent mixtures. The UV-vis absorption spectra show a metal to ligand charge transfer band at 490 nm, which increased in apolar solvent (green bands), indicating additional charge transfer through close metal-metal contacts. Especially the emission maximum and intensity changed drastically in a more apolar solvent (orange trace), indicating the emission of aggregates, which is different to the more structured monomer emission (blue trace).

Next, we successfully crystallized the Pt(II) complex (1) by slow evaporation of chloroform. Figure 2 shows the X-Ray crystal structure with a 3.3 Å Pt-Pt distance between two adjacent complexes. The complex units are helically distorted on top of each other, in agreement with our targeted nanowire superstructures.

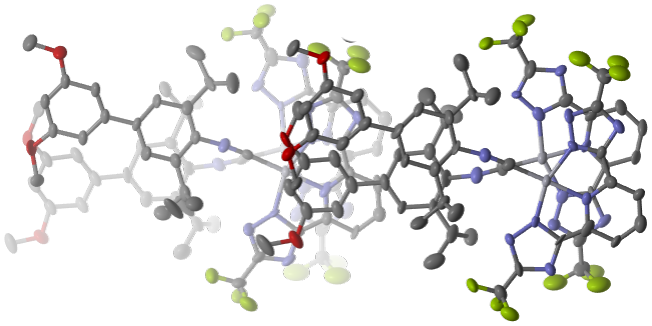

Fig. 2: X-ray crystal structure of (1). Solvent ($CHCl_3$) and hydrogen atoms are omitted for clarity. Color Code: C (gray), O (red), N (blue), Pt (light gray), and F (green).

Additionally, we started a collaboration with the Hevia group in Bern, who will study the mixed metal ate complexes from BB we use during our iterative oligo-naphthalene synthesis (Scheme 1a).

Besides, we started a second project, in which we investigate square planar Ni(II) complexes. One key goal is to reach long luminescence lifetimes with Ni(II), which is more abundant than Pt [8, 9]. These investigations establish the photo-physical characterization techniques and analysis.

Outlook

Following up on our preliminary studies, we now synthesize new chiral Pt complexes. Physical characterization will focus on UV-Vis absorbance, photoluminescence, circular dichroism, and circularly polarized luminescence. The complexes and final nanostructures will be studied by X-ray or electron diffraction. Finally, we will investigate changes of the aforementioned physical properties upon exposure to chiral VOC analytes. Our next step is the enantioselective VOC sensing by the new complex nanowire assemblies, the “chiral nose”-type nanomaterial.

References

[1] A. Prabodh, D. Bauer, S. Kubik, P. Rebmann, F. G. Klärner, T. Schrader, L. Delarue Bizzini, M. Mayor, F. Biedermann, Chirality Sensing of Terpenes, Steroids, Amino Acids, Peptides and Drugs with Acyclic Cucurbit[n]urils and Molecular Tweezers, Chem. Commun. 56, 4652-4655 (2020)

[2] Z. A. De los Santos, C. Wolf, Optical Terpene and Terpenoid Sensing: Chiral Recognition, Determination of Enantiomeric Composition and Total Concentration Analysis with Late Transition Metal Complexes, J. Am. Chem. Soc. 142, 4121–4125 (2020)

[3] O. S. Wenger, Vapochromism in Organometallic and Coordination Complexes: Chemical Sensors for Volatile Organic Compounds, Chem. Rev. 113, 3686-3733 (2013)

[4] W. B. Connick, R. E. Marsh, W. P. Schaefer, H. B. Gray, Linear-Chain Structures of Platinum(II) Diimine Complexes, Inorg. Chem. 36, 913-922 (1997)

[5] D. Lotter, M. Neuburger, M. Rickhaus, D. Häussinger, C. Sparr, StereoselectiveArene-Forming Aldol Condensation: Synthesis of Configurationally Stable Oligo-1,2-naphthylenes , Angew.Chem. Int. Ed. 55, 2920–2923 (2016)

[6] D. Lotter, A. Castrogiovanni, M. Neuburger, C. Sparr, Catalyst-Controlled Stereodivergent Synthesis of Atropisomeric Multiaxis Systems, ACS Cent. Sci. 4, 656–660 (2018)

[7] L. Büldt, X. Guo, A. Prescimone, O. S. Wenger, A Molybdenum(0) Isocyanide Analogue of Ru(2,2’-Bipyridine)32+: A Strong Reductant for Photoredox Catalysis, Angew. Chem. Int. Ed. 55, 11247-11250 (2016)

[8] Y. Wong, M. Tang, M. Ng, V. W. Yam, Toward the Design of Phosphorescent Emitters of Cyclometalated Earth-Abundant Nickel(II) and Their Supramolecular Study, J. Am. Chem. Soc. 142, 7638-7646 (2020)

[9] T. Ogawa, N. Sinha, B. Pfund, A. Prescimone, O. S. Wenger, Molecular Design Principles to Elongate the Metal-to-Ligand Charge Transfer Excited-State Lifetimes of Square-Planar Nickel(II) Complexes, J. Am. Chem. Soc. 144, 21948-21960 (2022)

Surface chemistry of hafnium oxide nanocrystals as X-ray computed tomography contrast agents

Project P2001: Imaging cardiovascular macro- and micro-structure using HfO_2 nanocrystals as X-ray tomography
Project Leader: J. De Roo and A. Bonnin
Collaborators: E. Maksimova (SNI PhD Student)

Introduction

In 2019, cardiovascular diseases were responsible for 32% of all global deaths [1]. Heart transplantation is nowadays a routine surgery to treat heart failure or coronary artery disease. The early stages of transplant rejection can be monitored by endo-myocardial biopsy (EMB).

2D histology (microscopic analysis of tissue) is the conventional technique to clinically assess the microstructure of removed cardiac tissue [2]. However, this analysis is mainly qualitative and time-consuming. On the other hand, Synchrotron Radiation X-ray Phase Contrast Imaging (SR X-PCI) is a non-destructive tomography technique, providing 3D information. Nevertheless, while SR X-PCI measurements can provide 3D virtual histology, it is currently difficult to automatically identify early stages of rejection. Furthermore, for clinical implementation, X-PCI should be compatible with laboratory-source X-rays that are usually less sensitive. Therefore, the development of contrast agents that target immune cells is essential to both improve cell differentiation and increase sensitivity [3].

In this project we aim to develop hafnium oxide nanocrystals as novel contrast agents and apply them in cell-targeted 3D histology. Hafnium oxide nanocrystals are chosen as a due to high X-ray density (Z = 72). Targeting the HfO_2 contrast agent to immune cells in cardiac tissue will enable future laboratory-source 3D histology, and the improved contrast could allow for semi-automatic segmentation by machine learning algorithms. Therefore, the clinical diagnosis will become more reliable, and automated, helping pathologists in their diagnosis.

Usually, HfO_2 nanocrystals are first synthesized in nonpolar solvents and stabilized by surfactants [4]. However, for biomedical application it is necessary to transfer them to aqueous environment without aggregation and, preferably, stabilize them at physiological pH.

Synthesis and characterization

Hafnium nanoparticles were synthesized via well-established solvothermal process [5]. Hafnium tert-butoxide and benzyl alcohol were heated at 220°C for 96 hours in muffle furnace (Fig. 1a). After synthesis, the nanocrystals are isolated, purified and stabilized with either 2-[2-(2-methoxyethoxy)ethoxy]acetic acid (MEEAA) to impart colloidal stability of nanoparticles (Fig. 1b). The average diameter of 2.6 ± 0.8 nm was confirmed by both TEM and DLS (Fig. 1c-d).

Ligand exchange

Initially synthesized nanocrystals capped by MEEAA are known to be stable in water but only until pH = 3 maximum. To provide good colloidal stability at higher pH, more relevant for use in biological applications, we conducted a li-

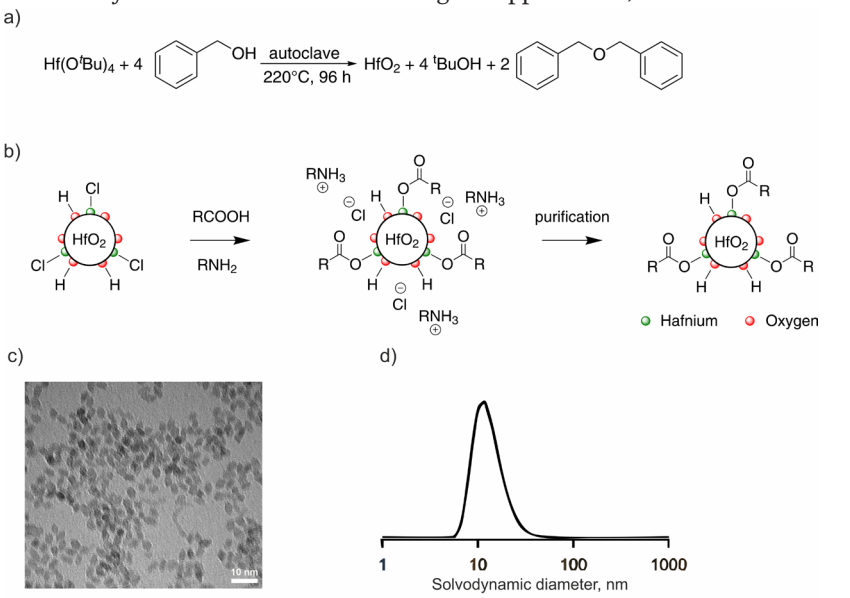

Fig. 1: a) Synthetic procedure of HfO_2 nanoparticles; b) stabilization of as-synthesized particles with carboxylic acid; c) TEM picture of nanocrystals; d) size distribution of nanocrystals obtained by DLS.

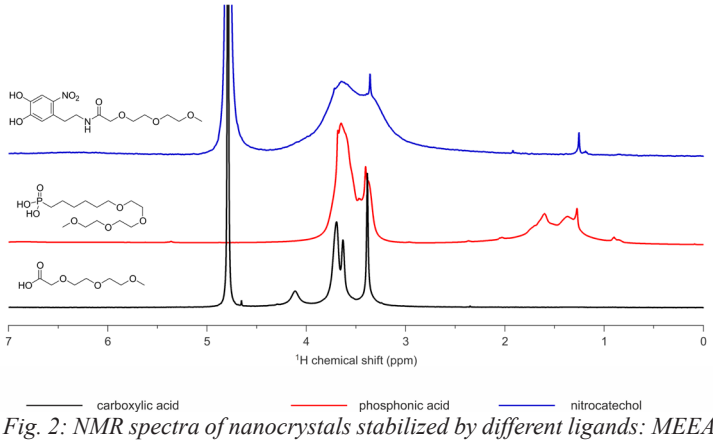

Fig. 2: NMR spectra of nanocrystals stabilized by different ligands: MEEAA as carboxylic acid, MEEEHPA as phosphonic acid, nitrodopamine-mPEG as catechol.

gand exchange of native carboxylic acid to phosphonic acid and catechol ligands, since they are known by their greater binding affinity to nanocrystal surface [5]. Ligand exchange was tracked by nuclear magnetic resonance (Fig. 2). Peaks broadening corresponds to moieties bound to the surface, while their sharpening indicates either dynamic or weak binding to the surface.

Phosphonic acids provide good stability until pH = 6 and still comparatively high stability over range of physiological pH. In their turn, catechols are tightly bound to nanocrystals surface in the range of pH = 6-10 due to fully non-protonated state of ligand at this range.

Preliminary data on CT contrast

Aqueous solution of hafnia nanocrystals with three types of ligands were prepared in different concentrations to prove that ligand does not have any influence on CT contrast.
CT measurements were conducted at 20 keV at the synchrothron in PSI (TOMCAT beamline). From figure 3 it is clear that CT contrast is independent on ligands, thus, opening a full freedom for further use of any of above-described organic compounds as stabilizers.

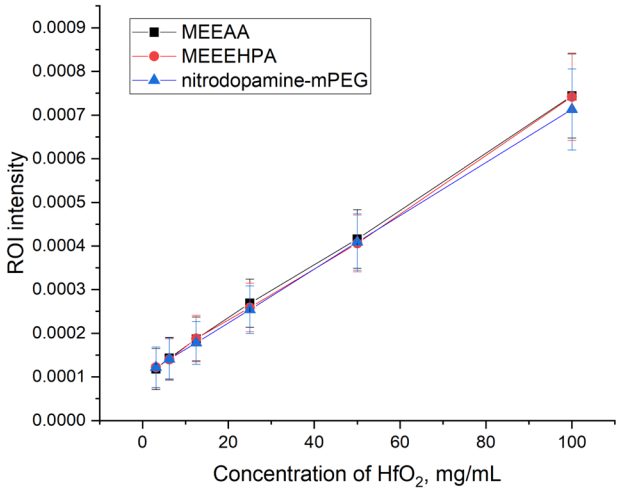

Fig. 3: Dependence of CT contrast depending on capping ligand and concentration of HfO_2.

Conclusion and outlook

We successfully synthesized hafnia nanocrystals in non-polar solvent and transferred them to aqueous media thanks to pegylation of the surface. Native ligand was further exchanged to phosphonic acid or to catechol to provide colloidal stability at physiological pH. We also confirmed that the type of ligand does not influence on CT contrast.
The next step of this work will be to provide functional groups capable of binding to antibodies for active targeting.

References

[1] Cardiovascular diseases. World Health Organization. 2022

[2] M. N. Gurcan, L. E. Boucheron, A. Can, A. Madabhushi, N. M. Rajpoot, B. Yener, Histopathological image analysis: a review. IEEE Rev Biomed Eng, 2, 147-171 (2009)

[3] H. Dejea, P. Garcia-Canadilla, A. C. Cook, E. Guasch, M. Zamora, F. Crispi, et al. Comprehensive analysis of animal models of cardiovascular disease using multiscale X-ray phase contrast tomography. Sci Rep, 9(1), 6996 (2019)

[4] J. De Roo, K. De Keukeleere, J. Feys, P. Lommens, Z. Hens, I. Van Driessche, Fast, microwave-assisted synthesis of monodisperse HfO2 nanoparticles. J Nanoparticle Res. 15(7) (2013)

[5] L. Deblock, E. Goossens, R. Pokratath, K. De Buysser, J. De Roo, Mapping out the Aqueous Surface Chemistry of Metal Oxide Nanocrystals: Carboxylate, Phosphonate, and Catecholate Ligands. JACS Au, 2(3), 711-722 (2022)

Mechanosensitive responses in live bacteria

Project P2002: A death-dealing nanomachine
Project Leader: R. H. Y. Lim and M. Basler
Collaborators: M. Brüderlin (SNI PhD Student), P. Cedro

Introduction

Bacterial cells respond to various signals from the environment and activate specific responses, such as assembly of extracellular appendages or activation of various signaling pathways. Interestingly, some of these pathways can be also activated during cell-cell interactions and thus contribute to defense mechanisms or virulence [1]. The mechanisms behind activation and the signals that allow bacteria to sense other cells or contact with surfaces are largely unknown. In this project, we investigate the reaction of bacteria to mechanical stress using atomic force microscopy (AFM) along with live-cell fluorescence microscopy (FM).

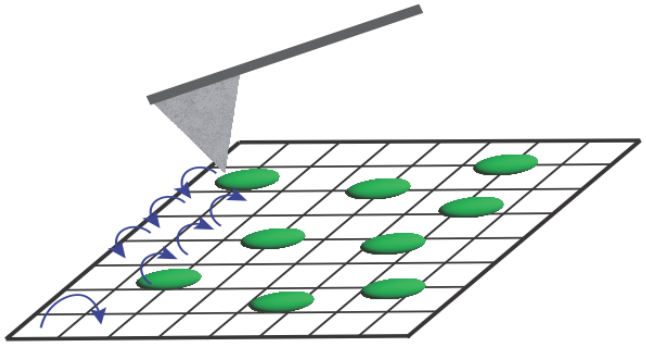

Fig. 1: Cartoon of the experimental set-up. The green rods indicate bacterial cells and the blue arrows show the path of the AFM cantilever during a force mapping experiment.

As seen in figure 1 we are using the fact that we can agitate the cells using the AFM while imaging their response in fluorescence. This allows us to simulate bacterial interaction with another object and quantify the response in a highly controlled matter [2].

Mechanosensitivity of bacterial cells

During the first part of the project, all experiments were performed as close to biological conditions as possible. For that the bacterial strains were largely kept as wild-type. In addition, we labeled certain proteins with the fluorescent protein mNeonGreen which allowed us tracking bacterial cells and their responses using fluorescence microscopy. Lastly, we also knocked-out the flagellar motility protein FliC which increased the attachment of bacteria to the Petri dish during imaging and reduced noise due to swimming bacteria.

With these mutations, the first force mapping experiment revealed a lot of information about the mechanosensitive responses in bacteria. As shown in figure 2, certain proteins localized to fluorescent foci upon triggering using the AFM cantilever. This allowed us to quantify the number of cells reacting to the mechanical force. Using the high time resolution of the fluorescence imaging it was also possible to measure the time needed for the bacteria to build up the fluorescent foci. After counting over 500 assembly events, we determined the response time to be 12.26 ± 0.55 s very consistently throughout all conditions. At the same time using different forces and force loading rates we were able to analyze the thresholds needed to trigger the responses. Our results show that increases in loading rate as well as increases in maximum force led to up to 8-fold increases in foci assembly rate when comparing the lowest to the higher conditions.

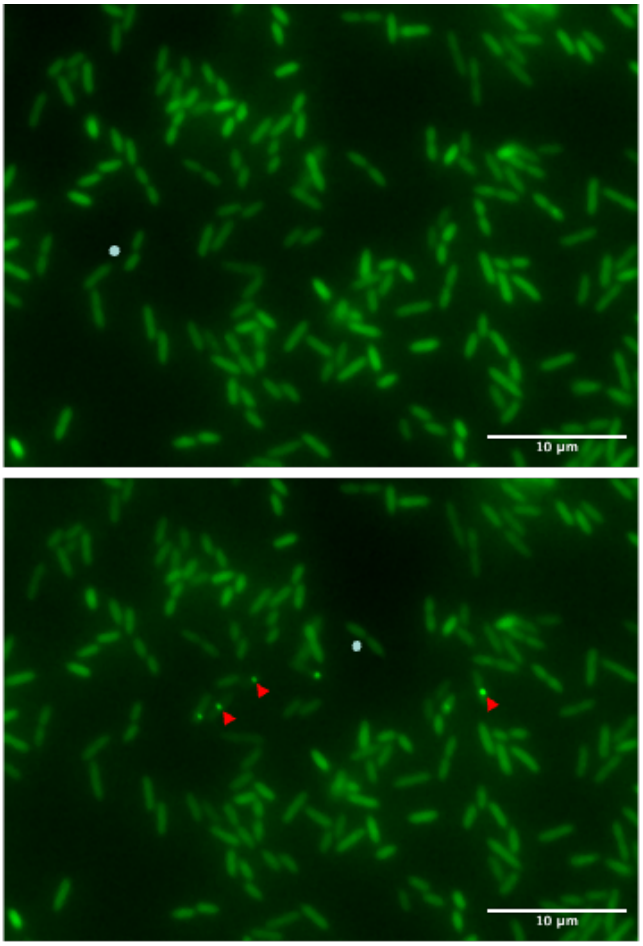

Fig. 2: Top: Fluorescence image of bacteria labeled with mNeonGreen protein. The image shows the cells before pressure application. Bottom: the same field of view after applying pressure. The cyan dots indicate the position of the cantilever tip while the red arrows show triggered assembly of protein foci by the AFM.

While this increase is significant there are still some questions left unanswered. First, while the number of triggered foci generation increases with larger forces and loading rates, after a threshold of about 25 nN of force this increase seems negligible. Additionally, though higher, even for the largest chosen forces, only about 20% of all cells respond to the AFM cantilever.

Force Curve analysis

To answer these questions, we did extensive analysis of the force curves obtained during the force mapping experiments. Important to note, of the 10'000 force curves recorded only about 10% show an expected indentation curve of a soft sample. The rest of the curves either showed curves corresponding to hitting the Petri dish or noisy data caused by the sample moving.

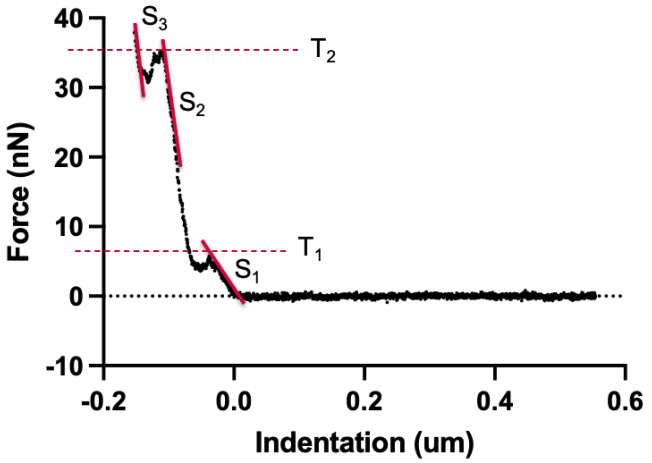

Fig. 3: Example force curve from a force mapping experiment. The continuous red lines show the slopes (stiffness) of different parts of the cell envelope when applying pressure. The dotted lines indicate membrane breaking thresholds. T_1 being the outer membrane and T_2 being the inner membrane.

Despite that, the viable curves reveal new insights in the mechanisms of bacterial response. As shown in the example curve in figure 3, there are two membrane breaking points seen in these curves. The first membrane break T_1 at 5.3 nN corresponds to breaking through the outer membrane and the second membrane break T_2 shows the threshold needed to break the peptidoglycan and inner membrane. At around 23.5 nN this break gives an indication how bacteria respond to mechanical stress.
Additionally, the force curves give us information about the stiffness of the individual parts of the bacterial cells. By using the slopes S_1, S_2 and S_3 and the formula for Young's Modulus:

$$E = \frac{\sqrt{\pi}}{2}(1-\upsilon^2)\frac{S}{\sqrt{A_c(h)}}$$

E being the Young's Modulus, υ being the Poisson ratio, S being the sample stiffness and $A_c(h)$ being the area of contact of the cantilever tip. We were able to determine the contact stiffness of bacteria at around 900 kPa by applying the Oliver-Pharr model for the area of contact.

Conclusion and Outlook

The first part of the project has allowed us for the first time to elucidate multiple biophysical characteristics behind bacterial responses to physical contact. By combining the fluorescent information with the force curves recorded by the AFM we propose that membrane damage is required to reliably cause a response of bacteria. This model is supported by the fact that for the higher forces and loading rates more membrane breaks can be seen in the force curves. It also explains why after applying more than 25 nN of force there is only negligible increase in firing rate, since the median membrane breaking threshold is 23.5 nN.

For the future, two main directions will be pursued. On the one hand, now that wild type bacteria have been investigated, we will be able to screen different mutants to directly elucidate which pathways are essential for bacterial response to mechanical stress. Additionally, more time will be invested into optimizing the cell fixation. This will allow us to do single cell experiments with the AFM where we can more fundamentally test how and where a cell needs to be stimulated in order to trigger a response. For that will be something that has never been done before and might result in profound insights into bacterial pathways that are unique in their complexity of responses to mechanical stimulation.

References

[1] B.-J. Laventie, and U. Jenal, Surface sensing and adaptation in Bacteria. An. Rev. Microbiol. 74, 735-760 (2020)

[2] C. D. Cox, N. Bavi, B. Martinic, Bacterial mechanosensors. Ann. Rev. Physiol. 80, 71-93 (2018)

Towards all-optical single-spin scanning magnetometry

Project P2003: Nanoscale quantum sensing of complex spin systems in extreme environments
Project Leader: P. Maletinsky and M. Poggio
Collaborators: J. Zuber (SNI PhD Student), M. Li, J. Happacher, M. Grimau, B. Shields

Introduction

This project aims at further advancing the field of quantum sensing by pushing the functionality and performance of a promising alternative to the nitrogen vacancy (NV) center in single spin magnetometry: the negatively charged silicon vacancy (SiV) center in diamond. While the NV center is widely established as a versatile magnetometer in the temperature range from 4 K - 300 K [1,2], ultra-low temperatures and strong magnetic fields have remained largely inaccessible due to various intrinsic limitations of NV centers under such conditions. This regime however is home to interesting and exotic physics such as fractional quantum Hall effects, which have attracted considerable recent attention. In addition to its exceptional optical properties, the SiV is inherently less susceptible to its charge environment [3] and all-optical coherent control has been demonstrated down to 40 mK [4], presenting it as a viable candidate for applications unsuitable for the NV center. The goal of this project is, therefore, to establish the SiV center as a novel quantum sensor in the reliable scanning probe geometry developed by the Basel Quantum Sensing Group over the last years.

Coherent single silicon vacancy centers in diamond

Our conventional approach to creating SiV centers in diamond micropillars consists of preparing a pristine diamond bulk sample, which is subsequently implanted with Si ions. In addition to introducing Si into the diamond lattice, this process also generates lattice vacancies.
During a high-temperature (>1200°C) vacuum anneal, these vacancies become mobile and may combine with Si atoms to form a stable defect complex – the SiV center. Upon confirmation that implantation and anneal have been successful (i.e., that SiV fluorescence can be detected) we fabricate parabolic diamond nanopillars by electron lithography and reactive ion etching. Such parabolic pillars enhance light-extraction efficiencies by at least one order of magnitude over the bulk, and we employ the resulting pillars as scanning probes for nanoscale magnetometry [5].

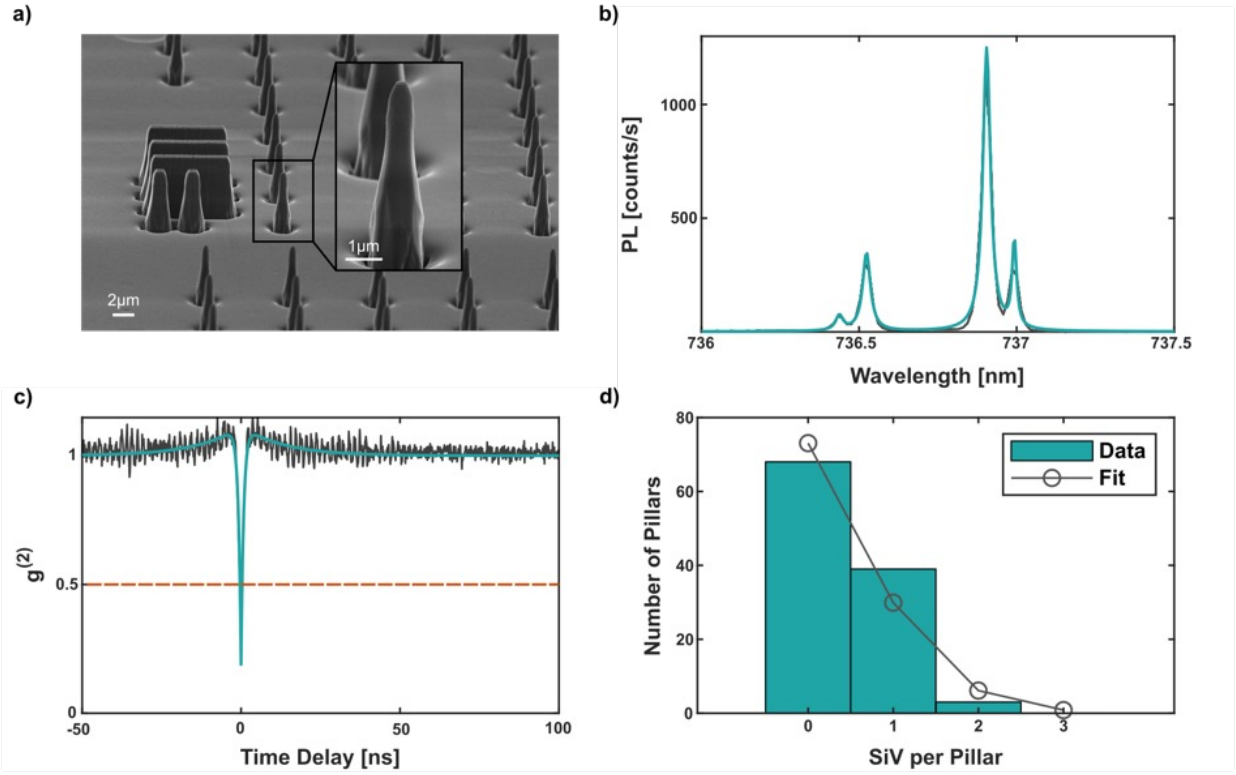

Fig. 1: a) SEM image of the parabolic pillar sample with a close-up of a pillar in the inset. b) Spectrum of a single SiV in a parabolic pillar, a four-peak Lorentzian is fitted in mint. c) Second order correlation function $g^{(2)}$ of a single SiV in a parabolic pillar, fit in mint. The dashed orange line is a guide to the eye, marking the single emitter regime. d) Bar plot of the emitter-per-pillar statistic, the grey line denotes a Poissonian distribution with mean 0.4.

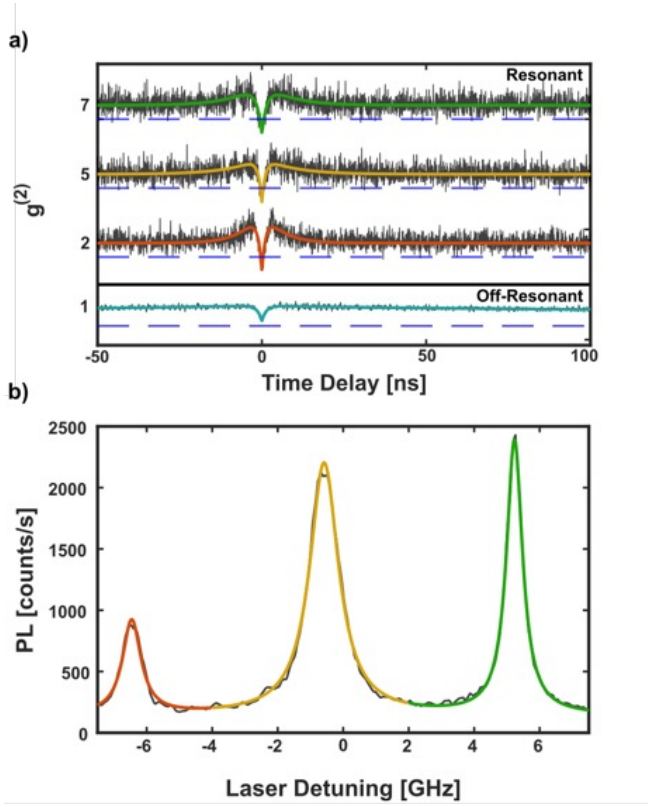

Fig. 2: a) Off-resonant (mint) and resonant (orange, yellow, green) second order correlation function $g^{(2)}$. On a pillar that contains three SiVs, the off-resonant $g^{(2)}$ is showing a dip above 0.5 (dashed blue line as a guide to the eye), confirming several emitters. However, when probing this pillar with PLE, three individual lines are exposed b). Performing $g^{(2)}$ measurements on these three individual lines produces a dip below 0.5, confirming that we address only one emitter.

This year, we have been able to reduce the number of emitters inside of our diamond microstructures, finally achieving a successful fabrication procedure to produce single SiV^- centers in individual parabolic pillars (Fig. 1). To this end, we produced a sample that was implanted with varying doses of Si^+, to assess the yield of single emitters in our samples as a function of number of implanted ions. This enabled us to fine tune implantation parameters and sample geometries even more accurately. On this sample, we fabricated our diamond parabolic reflectors (Fig. 1a) and, by automizing the characterization procedure, measured on hundreds of pillars, completely assessing their room-temperature optical properties, and producing statistics that confirm a Poissonian distribution with mean of 0.4 emitters per pillar (Fig. 1d). This specific sample marks a milestone in this project, producing single emitters in diamond nanopillars. The optical coherence of these SiV^- centers will be assessed as a next step, by cooling the sample to liquid helium temperatures and performing photoluminescence excitation (PLE).
At the same time, we have further investigated a second sample with several emitters per pillar and performed PLE measurements which consist of sweeping a resonant 737 nm laser across an SiV^- optical transition, while simultaneously collecting the phonon side band (PSB) emission. During this investigation, we have found a way to reduce the optical linewidth of the SiVs down to close to their lifetime limit. We achieve this using a new approach, illuminating the SiVs with blue laser light that has the effect of stabilizing the charge environment of the SiV in a semi-permanent way: After a single exposure of the SiVs, they remain charge stable (in SiV^-) and show little spectral diffusion over hours, without the need of any further optical manipulation. Additionally, we have performed second order correlation function $g^{(2)}$ measurements under resonant excitation on pillars that contain more than one SiV^-, showing that we can address individual emitters even when several are contained within one pillar. This experiment demonstrated that even if diamond nanopillars contain more than one SiV, the nature of our resonant optical excitation enables us to achieve single spin spatial resolution (Fig. 2a), all the while our charge stabilization method ensures that individual lines cannot be confused (Fig. 2b).

Summary

Project P2003 has reached significant milestones this year, including establishing a recipe to create single SiV centers in diamond parabolic reflectors, suitable for scanning probe magnetometry. Additionally, we have discovered a charge stabilization mechanism which makes even nanoscale scanning probes containing several emitters excellent candidates for nanoscale quantum sensing and magnetometry. Steps forward include bringing the emitters even closer to the surface to optimize spatial resolution as well as demonstrate coherent spin control, and therefore establishing and cementing our proposed sensor as a viable alternative to the NV center at ultra-low temperatures and Tesla-range magnetic fields.

References

[1] L. Thiel, Z. Wang, M. A. Tschudin, D. Rohner, I. Gutiérrez-Lezama, N. Ubrig, M. Gibertini, E. Giannini, A. F. Morpurgo, P. Maletinsky, Probing magnetism in 2D materials at the nanoscale with single-spin microscopy. Science, 364(6444), 973-976 (2019)

[2] N. Hedrich, K. Wagner, O. V. Pylypovskyi, B. J. Shields, T. Kosub, D. D. Sheka, D. Makarov, P. Maletinsky, Nanoscale mechanics of antiferromagnetic domain walls, Nature Physics, 17(5), 574-577 (2021)

[3] L. J. Rogers, K. D. Jahnke, M. W. Doherty, A. Dietrich, L. P. McGuinness, et al., Electronic structure of the negatively charged silicon-vacancy center in diamond, Phys. Rev. B, 89(23), 235101 (2014)

[4] J. N. Becker, B. Pingault, D. Groß, M. Gündoğan, N. Kukharchyk, M. Markham, A. Edmonds, M. Atatüre, P. Bushev, C. Becher, All-optical control of the silicon-vacancy spin in diamond at millikelvin temperatures, Phys. Rev. Let. 120(5), 053603 (2018)

[5] N. Hedrich, D. Rohner, M. Batzer, P. Maletinsky, B. J. Shields, Parabolic diamond scanning probes for single-spin magnetic field imaging, Phys. Rev. Appl., 14(6), 064007 (2020)

Atomic and electronic surface structure of multi-ferroic GeTe

Project P2004: Local manipulation of spin domains in a multiferroic Rashba semiconductor
Project Leader: M. Muntwiler and T. Jung
Collaborators: M. Heinrich (SNI PhD Student)

Introduction
To maintain the ongoing trend towards smaller and faster computation devices, non-traditional approaches of quantum state manipulation are required. One such option, also known as spintronics, would employ the electron spin as a carrier of information. Multiferroic materials can bridge the gap between traditional electronics and spintronics as they couple multiple ferroic orders, such as ferroelectricity, ferromagnetism and ferroelasticity in the same system [1]. This opens a path to spin control via electric fields (magnetoelectric coupling) rather than energy consuming high magnetic fields.

Project goals
Rhombohedral α-GeTe is a well known ferroelectric semiconductor with a large Rashba spin-splitting. Adding Mn into the crystal structure renders the resulting $Ge_{1-x}Mn_xTe$ ferromagnetic. Previous studies have shown that $Ge_{1-x}Mn_xTe$ is multiferroic and that it's indeed possible to switch its surface spin polarizations via external electric fields [2]. This project aims at understanding its detailed surface atomic, electronic and magnetic structure and their correlations on the local and large scale, the role of the surface layers as well as the importance of ferroic domains and domain walls.
We combine complementary approaches in synchrotron based, spatially averaging X-ray photoelectron diffraction (XPD, PhD) and spectroscopy (XPS, ARPES) and scanning tunneling microscopy (STM) and spectroscopy (STS) on a local, atomic scale. The experiments are mainly conducted at the PEARL beamline of the Paul Scherrer Institute [3]. To probe the ferroelastic coupling, we plan on polarizing the surface of Ge1-xMnxTe by applied voltages and to measure the change of surface structure via photoelectron diffraction. Moreover, we plan to probe the magnetoelectric coupling by measuring the spin resolved local density of states (LDOS) and spin polarization via spin-polarized scanning tunneling microscopy (SP-STM) and spectroscopy (SP-STS).

Results
The project started in July 2021. So far, we explored the preparation of GeTe and $Ge_{1-x}Mn_xTe$ films via molecular beam epitaxy in our lab and in the lab of our cooperation partner in Linz, Austria [4]. The samples were transported in an ultrahigh vacuum suitcase. We p
e electronic structure was investigated locally by point spectroscopy (Fig. 1d). Three distinct peaks can be seen. By comparison to (simulated) ARPES band maps, they can be attributed to the onsets of the surface states and a surface resonance coming from a bulk band. Using a lock-in technique to detect the dI/dV signal while superimposing a small bias modulation on the tip-sample bias during the STM scans, we record the spatial distribution of density of states (DOS) at a certain energy level above and below the Fermi energy.

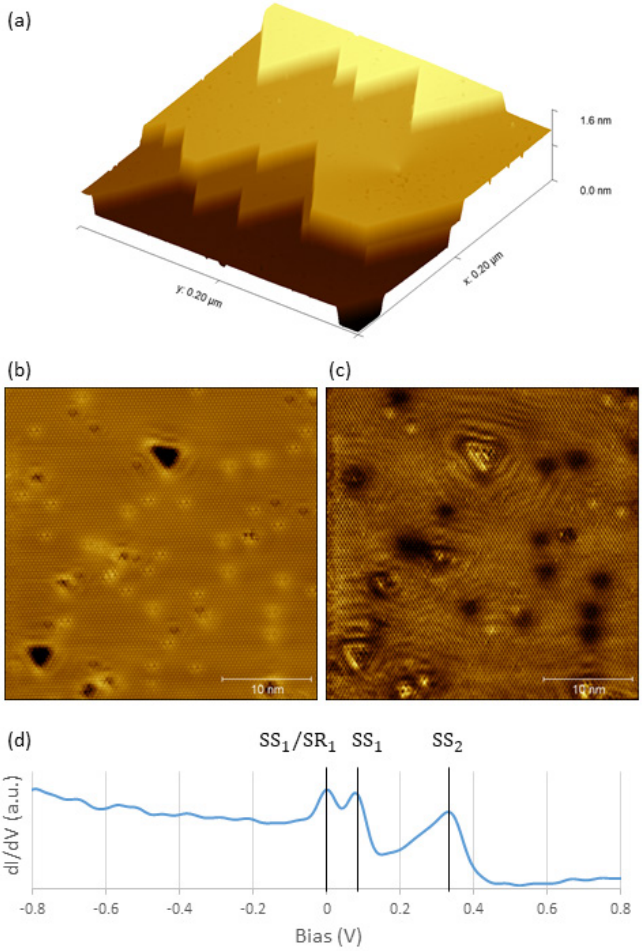

Friedel oscillations arising from the scattering of surface electrons at defect sites are clearly visible around dark and bright centers. By Fourier transform they can be mapped to points in momentum space [6] that is also accessible in ARPES measurements and band structure theory. In contrast to ARPES, Fourier transform STM (FT-STM) reveals not only occupied states but also unoccupied states above the Fermi level (positive bias in Fig. 1d).

Fig. 2: a),a') Experimental and b),b') simulated XPD patterns of the Ge 3s and Te 4s photoemission peaks. The simulated patterns are the result of an optimization process of variable surface layer distances.

In addition, we performed XPD measurements at different chemical peaks at different temperatures. Figure 2 shows two experimentally acquired XPD patterns of the Ge 3s and Te 4s peaks. Since a photoelectron can either go directly into the analyzer or first be scattered by surrounding atoms in

the atomic lattice, the result is an interference pattern. Recording this interference pattern from different angles results in the circular intensity modulation plots shown in figure 2a and a'. Using soft X-rays, the emitted photoelectrons have low kinetic energies (100-200 eV) and their diffraction patterns stem from only the first few surface layers. Figure 2b and b' show first results of simulated XPD patterns [5] of an optimized surface layer model matching closely the experimental patterns. This optimized model indicates a relaxation of the top layers from the bulk crystal structure.

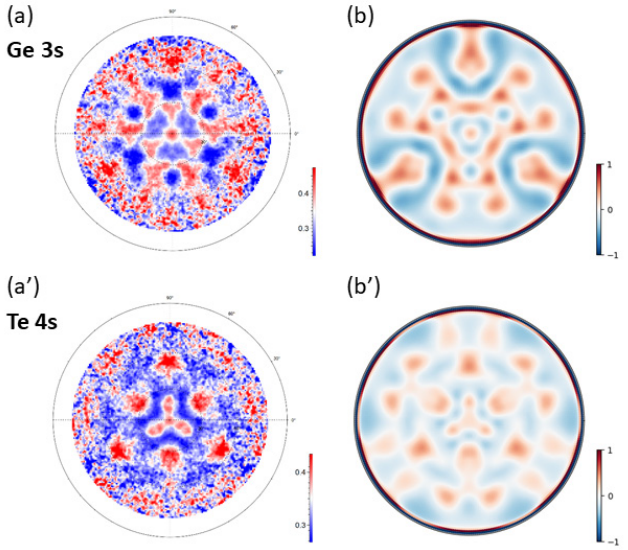

Outlook

Our focus will be on the characterization of the atomic, electronic and magnetic surface structure of $Ge_{0.85}Mn_{0.15}Te$.
An upgrade of our STM with a magnetic coil is planned for the end of the first quarter of 2023, which will be followed by first spin-resolved scanning tunneling microscopy (SP-STM) measurements. The preparation of magnetic tips and a reference sample will be important prerequisites for this type of measurement. As soon as spin-resolved STM is demonstrated, we will start to map the surface spin orientations of $Ge_{0.85}Mn_{0.15}Te$ on an atomic scale and to probe the magnetoelectric coupling by manipulating local spin orientations with tip bias pulses.

In addition we plan on measuring operando XPD, where we will probe the surface structure change of $Ge_{0.85}Mn_{0.15}Te$ under external applied voltages. Corresponding multiple scattering calculations compared to the unbiased, relaxed surface will give us a better understanding of the piezoelectric coupling involved at the surface.

References

[1] N. Spaldin, S. Cheong and R. Ramesh, Multiferroics: Past, present, and future, Physics Today 63, 38-43 (2010)

[2] J. Krempaský et al., Operando Imaging of All-Electric Spin Texture Manipulation in Ferroelectric and Multiferroic Rashba Semiconductors, Phys. Rev. X 8, 021067 (2018)

[3] M. Muntwiler, J. Zhang, R. Stania, F. Matsui, P. Oberta et al., Surface science at the PEARL beamline of the Swiss Light Source, J. Synchrotron Rad. 24, 354 (2017)

[4] M. Hassan, G. Springholz, R. T. Lechner, H. Groiss, R. Kirchschlager, G. Bauer, Molecular beam epitaxy of single phase GeMnTe with high ferromagnetic transition temperature, Journal of crystal growth 323(1), 363–367 (2011)

[5] J. García de Abajo, M. A. Van Hove, and C. S. Fadley, Multiple scattering of electrons in solids and molecules: A cluster-model approach, Phys. Rev. B 63, 075404 (2001)

[6] L. Petersen, P. T. Sprunger, Ph. Hofmann, E. Laegsgaard, B. G. Briner, M. Doering, H.-P. Rust, A. M. Bradshaw, F. Besenbacher, E. W. Plummer, Direct imaging of the two-dimensional Fermi contour: Fourier-transform STM, Phys. Rev. B 57, R6858(R) (1998)

[7] J. Krempaský, H. Volfova, S. Muff, N. Pilet, G. Landolt et al., Surface versus bulk contributions to the giant Rashba splitting in the ferroelectric α-GeTe semiconductor, arxiv:1503.05004 (2015)

Harnessing polymer compartments with bacterial toxins

Project P2005: Transmembrane protein-mediated loading of synthetic compartments
Project Leader: C. Palivan and R. A. Kammerer
Collaborators: P. Jaśko (SNI PhD Student)

Compartmentalization, a prerequisite for the spatiotemporal control of biochemical pathways in cells, is an emerging concept in designing new materials for medical and technological applications. Synthetic nano- and micro-compartments (NCs, MCs) with their chemical versatility and superior stability provide the basis for developing catalytic compartments, artificial organelles, or cell mimics that are furnished with specific biomolecules to drive desired reactions or deliver therapeutic payloads [1, 2]. However, limited compartment loading efficiency and transport across synthetic membranes remain hurdles that need to be overcome to increase the efficacy of in situ reactions.

Engineering bacterial toxins which inherently exert their cytotoxic activity through pore formation to deliver enzymes into cells, hold great potential to tackle these hurdles (Fig. 1). Despite three decades of extensive research in pore-forming proteins, little is known about the structural and molecular basis underlying toxin insertion into the membrane, a prerequisite for protein cargo release [3]. By improving our understanding of pore formation, we aim to confer the feature of protein-mediated cargo delivery on polymer compartments. In particular, we are interested to explore how the studied bacterial toxins retain their native function in such biohybrid systems.

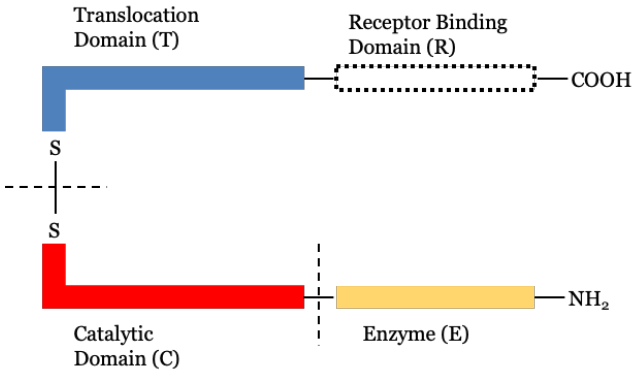

Fig. 1: Schematic representation of the architecture common to the toxins. Our recombinant toxins are devoid of the receptor-binding domain (R). An additional enzyme (E) can be fused to the catalytic domain or directly to the translocation domain.

This interdisciplinary project encompasses the design and production of recombinant pore-forming toxins and the development of compartments with synthetic membranes made of amphiphilic block copolymers. Purified recombinant proteins are used initially to scrutinize conditions that promote their interactions with the membrane, ultimately resulting in their integration with the polymeric compartment membranes. Furthermore, by exploring the structural and functional features of the pore-forming proteins, we plan to engineer the system such that protein cargo can translocate to the artificial polymeric compartment interior or that specific molecular flow across the membrane can occur (Fig. 2).

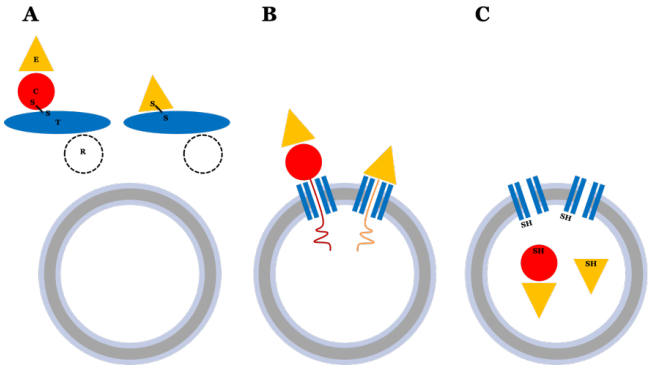

Fig. 2: Concept of the catalytic domain (C - red) and/or additional enzyme (E – yellow) delivery to the vesicle compartment by the translocation domain (T - blue) of studied protein toxins.

We applied molecular biology techniques that allowed us to establish the production of recombinant proteins. In order to study the interaction between the recombinant toxins and the synthetic membrane, we genetically engineered fluorescent proteins onto the amino- or carboxy terminus of bacterial toxins (referred to as toxins A and B) and produced 8 fusion variants in total (Fig. 3).

In addition, biophysical tools such as circular dichroism (CD) or nano-differential scanning fluorimetry (nanoDSF) were applied to characterize protein stability. The GFP variant fused to the translocation domain facilitated monitoring toxin binding to the membrane under neutral and acidic conditions. These pH conditions are crucial because bacterial toxins enter cells via endocytosis where the acidification promotes toxin insertion into the endosomal membrane [3]. As a preliminary step, we produced large lipid unilamellar vesicles (LUVs) to mimic cell membranes for in situ functionality assessment of protein variants (Fig. 4). In addition, we monitored the interaction of the purified TD-GFP with vesicle membranes and evaluated the stability of proteoliposomes by means of fluorescence correlation spectroscopy (FCS), light scattering techniques, and electron microscopy (EM). The results using lipidic compartments represent a first step to indicate the interaction of the recombinant toxins with lipid membranes. This will serve to indicate the properties the synthetic membranes should possess for func-

tional insertion Therefore it will allow selection of the suitable amphiphilic block copolymers, e.g., functionalized with specific end groups (negatively charged) that will cope with the toxin-membrane interaction.

Preliminary results suggest that the interaction of A and B toxins with lipidic LUV membranes depends on acidic pH and negatively charged groups on the membrane surface. In addition, studies carried out with polymersomes (polymeric LUVs) revealed that the toxin-membrane interaction could be tuned by ionic conditions, as well as curvature and thickness of the membrane. Owing to the chemical versatility and size tunability of amphiphilic block copolymers these parameters can be easily modified. We next plan to optimize the synthetic compartments such that they serve as platform for the insertion of recombinant toxins.

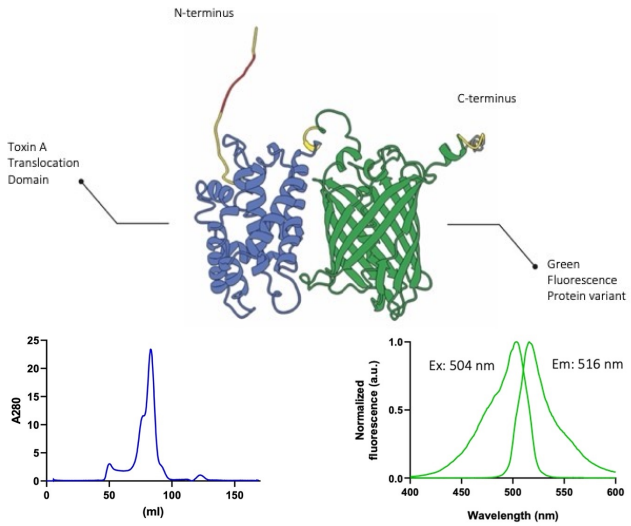

Fig. 3: Top panel: AlphaFold2 model of the Toxin A translocation domain - green fluorescence fusion protein (TD-GFP). Bottom panel: Left, size-exclusion chromatography (SEC) of Toxin A TD-GFP; right, absorption and emission spectra of Toxin A TD-GFP.

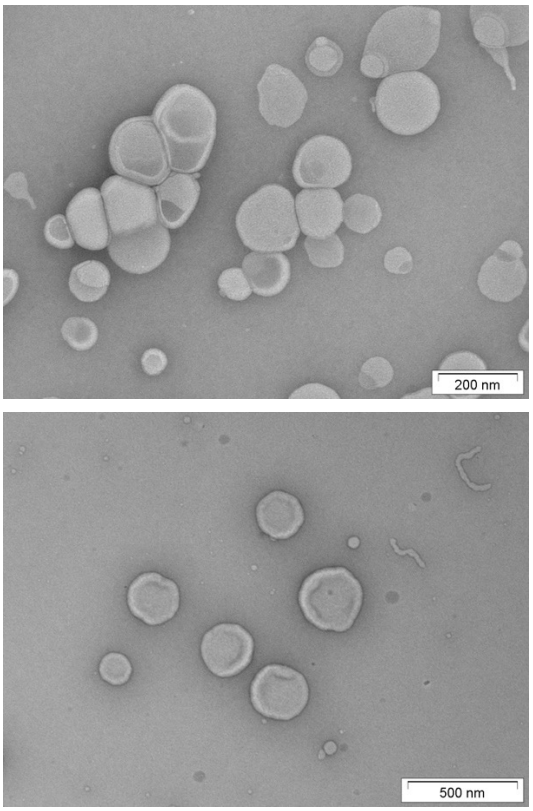

Fig. 4: TEM images of negatively stained vesicles without the toxins. Top, liposomes; bottom, polymersomes.

References

[1] E. C. Dos Santos, A. Belluati, D. Necula, D. Scherrer, C. E. Meyer, R. P. Wehr, E. Lörtscher, C. G. Palivan, W. Meier, Combinatorial Strategy for Studying Biochemical Pathways in Double Emulsion Templated Cell-Sized Compartments, Adv Mater. 32, 48 (2020)

[2] V. Maffeis, A. Belluati, I. Craciun. D. Wu, S. Novak, C. A. Schoenenberger, C. G. Palivan, Clustering of catalytic nanocompartments for enhancing an extracellular non-native cascade reaction, Chem Sci. 12, 37 (2021)

[3] R. A. Kammerer and R. M. Benoit, Botulinum neurotoxins: new questions arising from structural biology, Trends Biochem, Sci. 39, 11 (2014)

Self-assembly of group IV metal oxo clusters with amphiphiles at the air-water interface

Project P2006: RESTRAIN – Reticular chemistry at interfaces as a form of nanotechnology
Project Leader: P. Shahgaldian and J. De Roo
Collaborators: A. Roshan (SNI PhD Student)

Introduction

Metal-organic frameworks (MOFs) - coordination networks consisting of a regular array of metal ions or clusters with polytopic organic linkers are an interesting class of materials with several applications owing to their porous structure (e.g., catalysis, gas storage and separation)]1]. The choice of secondary building units (SBUs), organic linkers, modulators, temperature, reaction time, and the method of synthesis collectively control the shape, size, and morphology of the MOF crystals [2]. Despite their excellent physicochemical properties, implementing MOFs in practical applications is limited because of their relatively small size, typically in the micrometer range. RESTRAIN aims to address the challenge of producing large MOF crystals through interface-assisted methods and template effects.

Secondary building units and organic linkers

Group IV metal oxo clusters, the atomically precise smallest conceivable nanocrystal prototypes, are chosen as SBUs. To that end, we produced acetate-capped zirconium and hafnium oxo clusters (***1***) from their corresponding metal alkoxides under inert conditions [3]. The M_6O_8 (M = Zr/Hf) core of these clusters have been used to design MOFs such as UiO-66 and MOF-808.

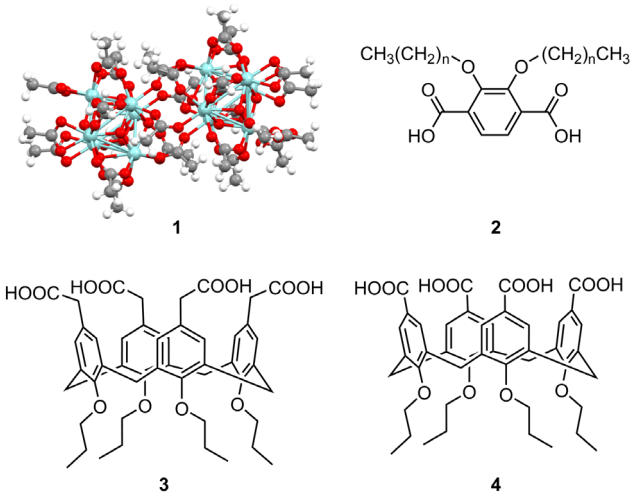

*Fig. 1: Structure of SBUs - metal oxo clusters (**1**, $[M_6O_4(OH)_4(CH_3COO)_{12}]_2$, M = Zr/Hf), and amphiphilic organic linkers - terephthalates (**2**, n = 2, 7, 11) and calix[4]arenes (**3** and **4**). In **1**, cyan atoms represent either zirconium or hafnium; all other atoms follow conventional CPK coloring.*

Langmuir monolayers of amphiphilic calix[4]arenes are known to favor the nucleation and surface-templated crystal growth of small organic molecules [4]. To exploit the same template effect at the air-water interface for MOF crystallization, we carefully chose amphiphilic molecules as organic building blocks. Two symmetric and rigid macrocyclic calix[4]arenes and three alkylated terephthalic acid derivatives were successfully synthesized through multi-step reactions. The amphiphilic calix[4]arenes **3** and **4** can form crystalline metal-organic coordination networks in the presence of metal ions such as Cu^{2+} and Ni^{2+}, which encouraged us to combine them with metal oxo clusters [5, 6]. On the other hand, terephthalates (***2***) are the most extensively studied organic linkers in MOF synthesis and are used to produce numerous MOFs with different transition metals, namely MOF-5(Zn), UiO-66(Zr), MIL-53(Al), MIL-101(Cr), etc. [7].

Langmuir monolayer and Brewster angle microscopy studies

RESTRAIN targets to produce 2D MOFs at the air-water interface and later extrapolate them into 3D through template effects. Similar to the reported amphiphile-based coordination network studies, we combined our organic linkers with metal oxo clusters on a Langmuir trough. Interestingly, the acetate-capped cluster was soluble in water, which enabled us to use its micromolar solution as the subphase. Amphiphiles were dissolved in a suitable volatile solvent and spread over the cluster solution. The interfacial properties of different cluster-amphiphile combinations were assessed through the Langmuir balance technique. The self-assembled monolayer formation upon barrier compression can be followed by the large surface pressures on Langmuir isotherms.

A representative surface pressure-area compression isotherm for the combination of 2,3-bis(octyloxy)terephthalic acid with zirconium acetate cluster is shown in figure 2. Although the terephthalate possesses both hydrophilic carboxylates and hydrophobic aliphatic chains, it can't form a monolayer on the water surface. However, when the subphase contained low concentrations of cluster (i.e., 10 µM), the terephthalate derivative studied formed a stable Langmuir monolayer with a collapse pressure as high as 40 mN/mm. This high collapse pressure value can be safely attributed to the ligand exchange of acetate clusters with terephthalate molecules. The limiting area (A_{lim}) of 92 Å^2/molecule measured is consistent with the cross-sectional area of UiO-66 MOF (107 Å^2/terephthalate molecule).

The monolayer produced was further imaged with Brewster-angle microscopy (BAM). Micrographs of terephthalate acquired on pure water confirm its inability to form monolayers at the interface. Remarkably, the presence of zirconium acetate cluster in the subphase resulted in the formation of a self-assembled monolayer even before barrier compression (Fig. 2D) with the presence of bright islands. Subsequent compression brought the monolayer islands closer to

eventually cover the whole interfacial area. To characterize further this system, the monomolecular layers produced at the air-water interface were transferred onto hydrophobic substrates (highly oriented pyrolytic graphite, HOPG), using the Langmuir-Schaefer (LS) technique at a surface pressure of 20 mN/mm. Contact angle measurements confirmed the successful transfer of monolayers onto the substrate.

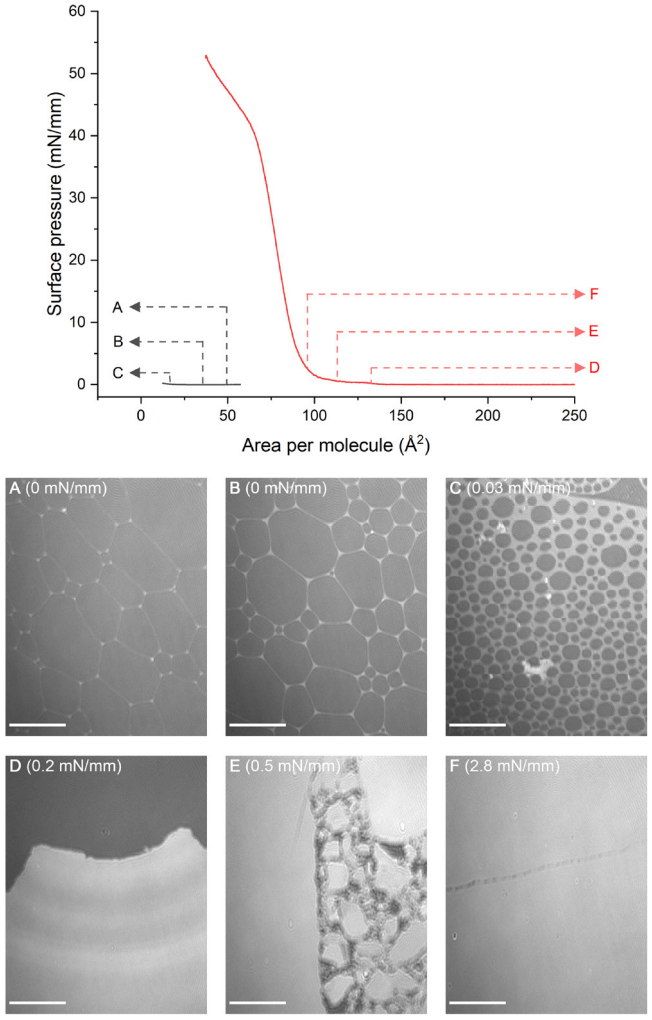

Fig. 2: Surface pressure - area compression isotherm of 2,3-bis(octyloxy)terephthalic acid on pure water (black) and 10 µM zirconium acetate cluster solution (red). Corresponding Brewster angle microscopy micrographs of monolayers on water (A-C) and cluster solution (D-F). Letter labels indicate the position on the isotherm where the corresponding BAM micrographs were acquired. Scale bar 100 µm.

Atomic force microscopy studies

High-resolution images of the transferred monolayer were obtained by means of atomic force microscopy. The average thickness of the monolayer was measured at 1.6 ± 0.5 nm; this is in good agreement with the theoretical values of the oxo cluster-amphiphilic terephthalate molecular model.

Conclusion and outlook

We successfully demonstrated the formation of self-assembled monolayers based on group IV metal oxo clusters and amphiphilic organic linkers at the air-water interface. Work is underway to induce crystallinity, characterize further and study the template effects to produce large MOF single crystals.

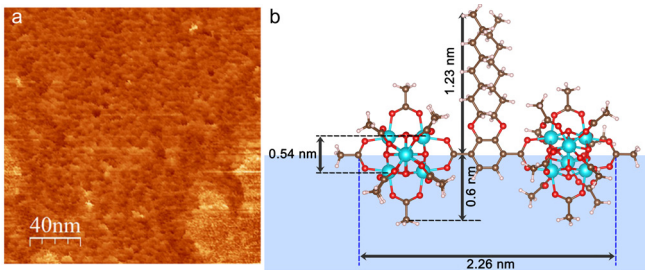

Fig. 3: a) High-resolution AFM micrographs of Zirconium acetate cluster-2,3-bis(octyloxy)terephthalic acid monolayer. b) Proposed schematic molecular model with dimensions.

References

[1] H. Furukawa, K. E. Cordova, M. O'Keeffe, O. M. Yaghi, The chemistry and applications of metal-organic frameworks, Science 341, 1230444-1230456 (2013)

[2] N. Stock, S. Biswas, Synthesis of metal-organic frameworks (MOFs): Routes to various MOF topologies, morphologies, and composites, Chem. Rev. 112, 933–969 (2012)

[3] D. Van den Eynden, R. Pokratath, J. Pulparayil Mathew, E. Goossens, K. De Buysser, J. De Roo, Fatty acid capped, metal oxo clusters as the smallest conceivable nanocrystal prototypes, Chem. Sci. (2023)

[4] N. Moridi, D. Elend, O. Danylyuk, K. Suwinska, P. Shahgaldian, Amidophenol-modified amphiphilic calixarenes: Synthesis, interfacial self-assembly, and acetaminophen crystal nucleation properties, Langmuir 27, 9116–9121 (2011)

[5] M. Moradi, L. G. Tulli, J. Nowakowski, M. Baljozovic, T. A. Jung, P. Shahgaldian, Two-Dimensional calix[4]arene-based metal-Organic coordination networks of tunable crystallinity, Angew. Chem. Int. Ed. 129, 14587–14591 (2017)

[6] M. Moradi, N. L. Lengweiler, C. E. Housecroft, L. G. Tulli, H. Stahlberg, T. A. Jung, P. Shahgaldian, Coordination-driven monolayer-to-bilayer transition in two-dimensional metal-organic networks, J. Phys. Chem. B 125, 4204–4211 (2021)

[7] P. Rocío-Bautista, I. Taima-Mancera, J. Pasán, V. Pino, Metal-Organic Frameworks in Green Analytical Chemistry, Separations 6, 33 (2019)

Size and shape dependent rotation characteristics of ultrasound-actuated thin film rotors

Project P2007: Development of nanoscale acoustic tweezers for mechanobiology application
Project Leader: S. Tsujino and R. H. Y. Lim
Collaborators: S. Jia (SNI PhD Student)

Introduction

In the annual report of year 2021, we briefly demonstrated the ultrasonic manipulation of lithography-defined rotors by acoustic levitator in air and by cone-shaped transducer in water, respectively. Thin film disks with short blades on their periphery have been utilized as sample holders in a room temperature x-ray crystallography experiment reported recently [1]. Nevertheless, the mechanisms of generating the acoustic torque and controlling the rotation direction remain obscure. This year, we have found a way to control the rotational direction of acoustically levitated rotors in air by engineering the shape and configuration of the short blades on their periphery. For the experiment in water, we have achieved the rotational manipulation of ultrasonic rotors of a size down to 25 µm. Our findings will pave the way for more elaborate thin film sample holders for airborne experiments and micrometer-scale ultrasonic rotors in liquid.

Airborne acoustic levitation of thin film ultrasonic rotors in air

Using UV lithography, we fabricated thin film rotors of different sizes (see Fig. 1 a-c) and different blades. We levitated them in a single-axis acoustic levitator with the ultrasonic frequency of 40.6 kHz (see Fig. 1e) and observe them by a high-speed camera overlooking the rotor at a degree of 15°. The measured acoustic pressure was normalized by the threshold pressure 1.35 kPa for levitating a small (< 0.5 mm) water droplet measured on the same setup [2]. As shown in figure 1d, the threshold pressure P_{th} for levitating R1-R3 increases with the reduction in the rotor size. As expected from the quadratic dependence of acoustic radiation pressure on the acoustic pressure amplitude P_{ac}, we observed a rapid rise in f_s as P increased for all the three rotors regardless of their dissimilar sizes. It is also noteworthy that the P_{th} for R1, 0.19, is significantly lower compared to the value 1.05 for R3, which can be ascribed to the larger disturbance of the acoustic field and the five-time enhancement of P_{ac} with R1 [1]. Whereas such enhancement is negligible for R3 due to a much smaller disk-diameter-to-λ ratio. Figure 1f shows the rotation characteristics of 4-mm-diameter rotors with different blade shape and configuration. The similar levitation threshold pressure P_{th} for the rotor with square and symmetric blades, R1, and the blade-less rotor R4 indicates the similar acoustic pressure distribution on their surfaces. No rotation seen for R4 in the pressure range shown here implies that the blades are critical to generating acoustic torque. Nevertheless, the rotation direction of R1 is rather incidental and is not suggested by its apparently symmetric shape. The key role played by the blades has thus led us to the design of R5, of which each blade is rounded on one side. R5 is found to always rotate in the direction from the rounded to the straight edge of its blades (as marked by the counterclockwise (CCW) blue arrows in figure 1b, with its rotation characteristic similar to that of R1. When R5 is flipped, it rotates clockwise (CW) with its rotation characteristic almost unchanged. In comparison, R6, with two of its rounded blades flipped compared to R5, its rotation direction became incidental as was observed with R1 and was even noticed to revert upon switching the acoustic pressure.

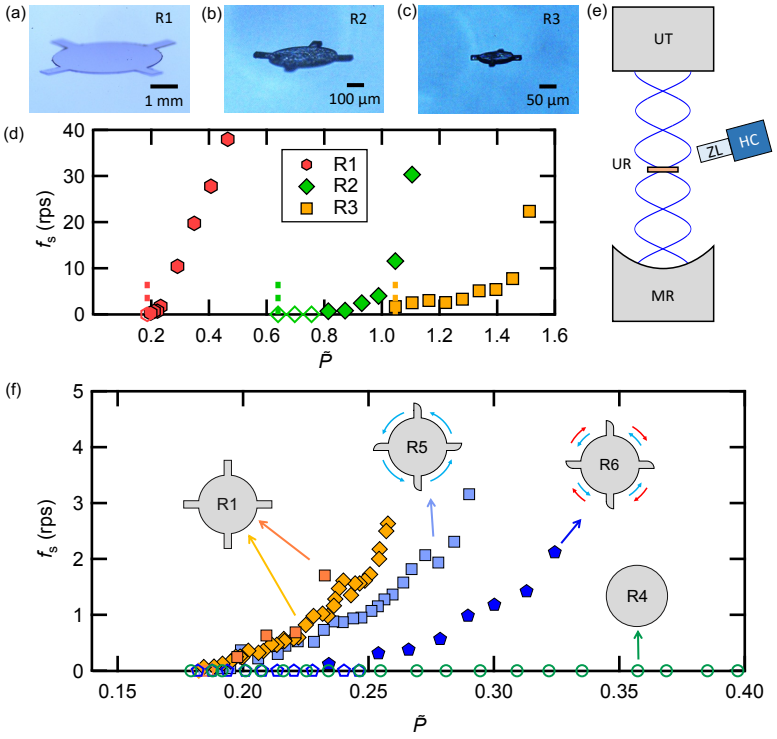

Fig. 1: a-c) Snapshots of the ultrasonic rotors R1-R3. d) Rotation characteristics of R1-R3. The vertical dashed lines mark the levitation threshold pressure for each sample. e) Schematic of the single-axis acoustic levitator. HC: high-speed camera, ZL: zoom lens, UR: ultrasonic rotor. f) Comparison of the rotation characteristics for R1, R4, R5, and R6. The unfilled markers show the points when the samples did not rotate but simply levitated.

The decisive role of the blades in controlling the rotation direction was reproduced by numerically calculating the acoustic pressure distribution around R5. Figure 2a shows the iso-surfaces of the time-average pressure in the acous-

tic cavity of the levitator, and figure 2b is the top-view of the instantaneous surface pressure distribution related to the ambient pressure when the pressure integrated over the rotor surface is maximum. As indicated by the blue arrows and dashed circles in figure 2b, the gathering of the flow in the downstream on the rounded edge of the blade leads to a higher pressure there than that on the straight edge at the same lateral coordinate, which produces the acoustic torque in CCW.

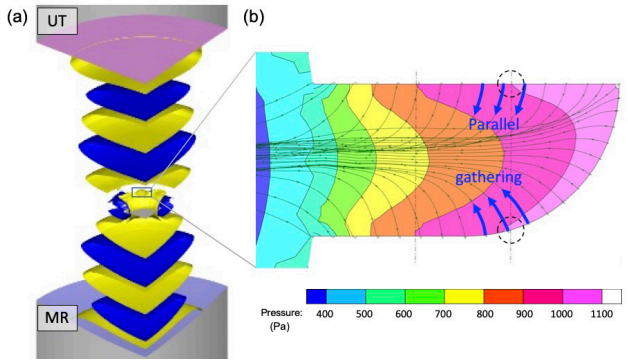

Fig. 2: a) Time-averaged acoustic field in the acoustic levitator in the presence of R5 by computational fluidic dynamics (CFD) simulation. b) Instantaneous acoustic pressure on the surface of the blade of R5, when the integral of acoustic pressure on the disk surface is positive maximum. The curves are streamlines.

Rotational manipulation of ultrasonic rotors in water

Using the same fabrication technique mentioned above, we made miniaturized ultrasonic rotors with a size down to 25 µm and observed their rotation characteristics in water. As shown in figure 3a, a cone-shaped transducer is immersed in a water bath, the bottom of which being a glass slide. The pulsed ultrasound emitting from the transducer produce on the plane of the glass slide circular pressure nodes with a nominal separation of approximately λ/2, which are visualized by the aggregation of ~3-µm-tracer particles (see Fig. 3b), where the separation if ~80 µm]. When the distance in between was adjusted to 1.9 mm and the rotor size is approximately equal to λ/2, the acoustic torque was observed to be enhanced, as implied by the highest rotation speed in the vicinity of the dashed lines in figure 3c. Due to the sinusoidal variation of the acoustic radiation force along the radial direction, the blades on the opposite sides can pick up the acoustic torque in the same direction. On each blade is exerted an azimuthal force which is produced by the difference of the acoustic radiation pressure by the different of the acoustic radiation pressure between the two sides of a blade. Using 13 MHz, we were able to rotate ultrasonic rotors of 50 and 25 µm in diameter (see Figs. 3 d – e), respectively.

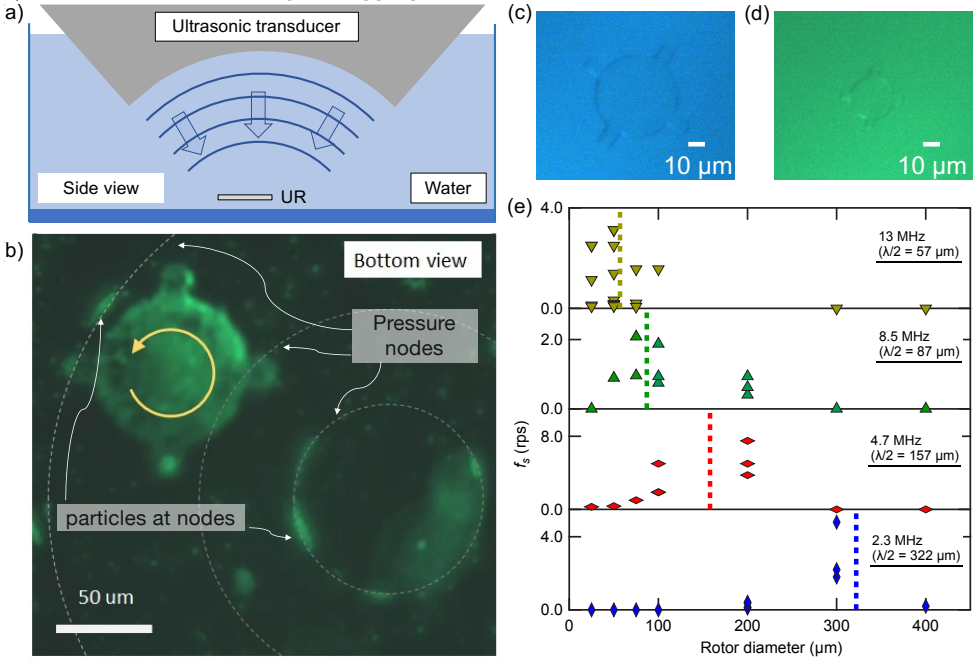

Fig. 3: a) Side-view schematic of the acoustic rotor experiment in- water. UR: ultrasonic rotor. b) Bottom-view snapshot of the rotation experiment of a 75-µm acoustic rotor under 13 MHz ultrasound. In-plane pressure nodes (dashed curves) are visualized by the aggregation of green fluorescent polyethylene tracer particles (~3-µm-diameter). c) Relationships between the rotor diameter and the rotation speed fs at four ultrasound frequencies, 2.3, 4.7, 8.5, and 13 MHz. Dashed lines mark the one-half wavelength at each frequency. d) and (e) show a 50-µm- and a 25-µm-diameter in water, respectively.

Summary

In the second year of the project, we have furthered our investigation on the airborne levitation and the in-water actuation of the thin-film ultrasonic rotors. As a result, we elucidate the mechanism of generating acoustic torque for our ultrasonic rotors by experiment and numerical simulation. We have consolidated our findings into a manuscript which has been recently accepted for publication in Applied Physics Letters [3]. Towards the application of ultrasonic manipulation for mechanobiology, we are currently using cone-shaped ultrasonic transducers to deform cellular samples. In the meantime, we are also developing surface acoustic wave (SAW) devices for the manipulation of samples at a higher spatial resolution.

References

[1] M. W. Kepa, T. Tomizaki, Y. Sato, D. Ozerov, H. Sekiguchi, N. Yasuda, K. Aoyama, P. Skopintsev, Jörg Standfuss, R. Cheng, M. Henning, and S. Tsujino, Acoustic levitation and rotation of thin films and their application for room temperature protein crystallography, Sci. Rep. 12, 5349 (2022)

[2] S. Tsujino, Y. Sato, Y. Takeda, and T. Tomizaki, Oscillation resonances and anisotropic damping of the motion of acoustically levitated droplets in single-axis acoustic levitators, Appl. Phys. Lett. 115, 053702 (2019)

[3] S. Jia, Y. Sato, and S. Tsujino, Size and shape dependent rotation characteristics of thin film ultrasonic rotors, Appl. Phys. Lett. 121, 254102 (2022)

Integrating a nanowire quantum dot on a scanning probe tip

Project P2008: Scanning nanowire quantum dot
Project Leader: D. Zumbühl and M. Poggio
Collaborators: L. Forrer (SNI PhD Student)

Introduction

We are developing a new kind of scanning probe microscope, which employs gated quantum dots (QDs) embedded in semiconductor nanowires (NWs), integrated on the tips of standard force microscopy cantilevers. These sensors will be sensitive scanning probes of charge and electronic density [1]. The sensors will be used to characterize the spatial profile of charge noise, quantum dots, and electric fields [2] in spin qubit devices, aiding the design of coherent quantum computation processors. This is particularly relevant here in the Department of Physics of the University of Basel, where the NCCR SPIN, aimed at producing scalable spin qubits in Si was established in the summer of 2020.

Our scanning probe method builds on previously developed scanning single-electron transistors (SETs) made from metallic islands [1] and scanning QDs defined in carbon nanotubes (CNTs) [2]. Research efforts using such devices have been extremely fruitful, due to the high sensitivity to electric field. Indeed, QD-based sensors are the preferred sensors of charge in applications in quantum computation with spins in QDs, where they are incorporated on the same substrate as the sample of interest. Such charge sensors make use of sharp spikes in the electrical conductance of the QDs (Coulomb peaks) and are capable of detecting a small fraction of an electronic charge at micron distance. Until now, however, both scanning SETs and scanning QDs in CNTs have been relatively cumbersome to use, extremely delicate, and limited in their design. These drawbacks are a result of the specialized processes involved in their fabrication.

Our approach addresses this shortcoming by using standard AFM cantilevers as the scanning probe combined with NWs as the QD hosts. By developing a scheme for patterning leads, gates, and contacts directly to the cantilever tip [3], we will have maximum flexibility for the design of our sensors. AFM levers allow easy tip-sample distance control, topographic contrast. NW QDs possess many qualities that make them suitable for use in scanning probes: they are small (~10-50 nm), need few gates because of the natural 1D confinement, and can due to the low-dimensional geometry of the NW be easily brought closer than 100 nm to a sample. Importantly, their strong confinement and tunable nature endows NW QDs with a higher sensitivity to electric fields and nearby charges than their SET counterparts. Moreover, NW crystals can be grown with an exceptional control over material composition. The specific NW material composition can pass on useful properties to the embedded probe QDs, such as a strong spin-orbit interaction, which may offer interesting new modalities of sensing.

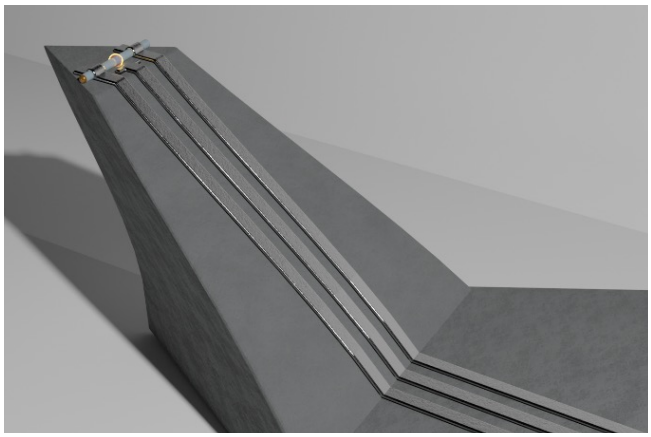

Fig. 1: A schematic representation of a patterned cantilever tip with a gate-controlled NW QD at its tip. Such a scanning probe would represent a new and highly sensitive tool for measuring small electric fields with nanometer-scale resolution.

Goals

The main goals of this project are to: 1) Fabricate scanning probe cantilevers hosting a NW with embedded gated QDs (T); 2) Image the electronic density of nanoscale samples with unprecedented sensitivity (F); 3) Implement high-bandwidth scanning probe imaging using microwave reflectometry techniques (T); 4) Image and study the dynamics of charge fluctuators in semiconducting devices (F).

Results

In this project, we have developed new methods to pattern scanning probe cantilevers with nanostructures such as gate electrodes and contacts, using electron-beam lithography [3]. Our process involves coating cantilevers with a floating resist layer, which is then patterned with nanometer resolution (see Fig. 2). We have tested the method for various kinds of cantilever shapes, which we pattern using focused-ion-beam milling. Summarizing, we are now able to make wide variety of gates, with dimensions down to 50 nm, and contacts suitable for QD control. This method gives us the opportunity to fabricate gates on the tip of our lever and contact NWs by evaporation of metal as done on conventional planar substrates [4, 5].

We have demonstrated QD formation on substrates using our fabrication techniques. We are currently optimizing NW transfer to the apex of the cantilevers through the use of contact mode atomic force microscopy. Furthermore, we have built a 4 K electronic transport probe, and are testing our low-temperature scanning probe setup. Finally, we have acquired all necessary instrumentation for implementing high-bandwidth microwave reflectometry read-out tech-

niques, and are in the process of testing these and integrating them with our scanning probe sensors.

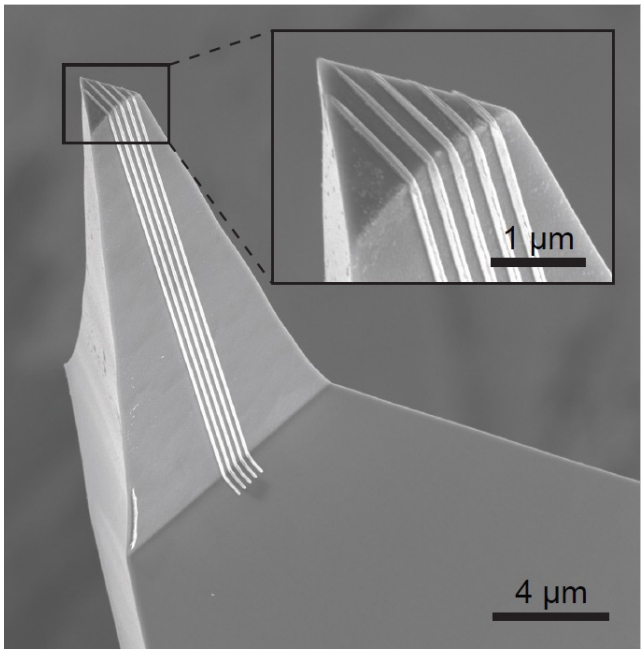

Fig. 2: Scanning electron micrograph of tipped end of cantilever, patterned with nanoscale gate array defined through etching process [3].

Outlook

We are currently working on reliable and non-invasive transfer of individual NWs to the patterned apex of the cantilevers. While we have demonstrated successful transfer using a nanomanipulator inside an SEM, our tests indicate that this process does not preserve good electronic transport properties of the NWs. We are now optimizing a direct pick-up method, where we use an atomic force microscopy setup with our cantilevers to pick up NWs directly from a substrate. Furthermore, we are finishing the construction and testing of our 4K scanning probe setup. First scanning probe experiments are planned to take place in January 2023, where we will use our unique cantilevers with multiple nanoscale gates to demonstrate multi-gate scanning probe microscopy.

This new technique will allow us to study defects and charge noise, which are main source of decoherence in spin and superconducting qubit devices. Once the NW QDs on-cantilever are functioning, we will perform these measurements with increased sensitivity. Furthermore, by combining our multi-gate cantilevers with microwave reflectometry readout techniques, we will be able to image QD formation and QD properties such as energy level splittings in pristine samples, such as ungated heterostructures, thin Si quantum wells, and NWs.

References

[1] M. J. Yoo, T. A. Fulton, H. F. Hess, R. L. Willett, L. N. Dunkleberger, R. J. Chichester, L. N. Pfeiffer, and K. W. West, Scanning Single-Electron Transistor Microscopy: Imaging Individual Charges, Science 276, 579 (1997)

[2] L. Ella, A. Rozen, J. Birkbeck, M. Ben-Shalom, D. Perello, J. Zultak, T. Taniguchi, K. Watanabe, A. K. Geim, S. Ilani, and J. A. Sulpizio, Simultaneous voltage and current density imaging of flowing electrons in two dimensions, Nat. Nanotechnol. 14, 480 (2019)

[3] L. Forrer, A. Kamber, A. Knoll, M. Poggio, and F. Braakman, Electron-beam lithography of nanostructures at the tips of scanning probe cantilevers, arXiv: 2209.11503 (2022)

[4] F. S. Thomas, A. Baumgartner, L. Gubser, C. Jünger, G. Fülöp, M. Nilsson, F. Rossi, V. Zannier, L. Sorba, C. Schönenberger, Highly symmetric and tunable tunnel couplings in InAs/InP nanowire heterostructure quantum dots, Nanotechnology. 31 (2020)

[5] F. N. M. Froning, M. Rehmann, J. Ridderbos, M. Brauns, F. A. Zwanenburg, A. Li, E. P. A. M. Bakkers, D. M. Zumbühl, F. R. Braakman, Single, double, and triple quantum dots in Ge/Si nanowires, APL. 113 (2018)

Hybrid Van der Waals heterostructures for vertical organic electronics

Project P2009: Hybrid Van der Waals heterostructures for vertical permeable-base organic transistors
Project Leader: M. Calame
Collaborators: J. Oswald (Associate SNI PhD Student), D. Beretta, M. Stiefel, R. Furrer, A. Romio, M.D. Mansour, D. Vuillaume

Introduction and state-of-the-art
The mechanical and electrical properties of organic thin films and 2D materials, such as graphene, enable the realization of flexible electronics operating at low-voltage and high frequency. In this project, we study the structural and electrical properties of vertical hetero-structures made of graphene and organic thin films. In such architecture, the charge transport occurs in very short vertical channels allowing for the realization of fast switching devices, e.g. vertical organic transistors and light emitting diodes [2-4].

Fabrication and material characterization
We fabricate graphene/organic interfaces by optical lithography in three steps: (i) Metallic bottom electrodes are patterned on a Si/SiO_2 substrate; (ii) A thin film of organic semiconductor (e.g. P3HT) is spin-coated and patterned by lift-off; (iii) CVD (Chemical Vapor Deposition) graphene is grown on a copper foil, wet transferred on the organic film (Fig. 1a), and subsequently structured by photolithography and reactive ion etching. The morphology and chemical composition of the devices are then investigated by atomic force microscopy (Fig. 1a-b.) and Raman spectroscopy (Fig. 1c.), respectively.

Measurement setup
The electrical characterization was carried out at room temperature in the setup shown in figure 2c, which include four probes and an annealing stage. A Keithley 236 sourcemeter and an Agilent 4294a impedance analyzer are used for the electrical measurements. Temperature dependent I-V traces were collected in a Lakeshore probe station.

Electrical characterization
Au/P3HT/Graphene junctions were characterized as shown in the inset of figure 2a. Electrical measurements at several different temperatures are shown in figure 3. The IV traces were fitted to a thermionic emission model. Using this model, we were able to extract the potential barriers and Richardson constants for both interfaces (i.e. Au/P3HT and P3HT/Graphene). The potential barriers at room temperature are roughly 0.3 eV and 0.25 eV for P3HT/Graphene and P3HT/Au (squares in Fig. 3b.), respectively.

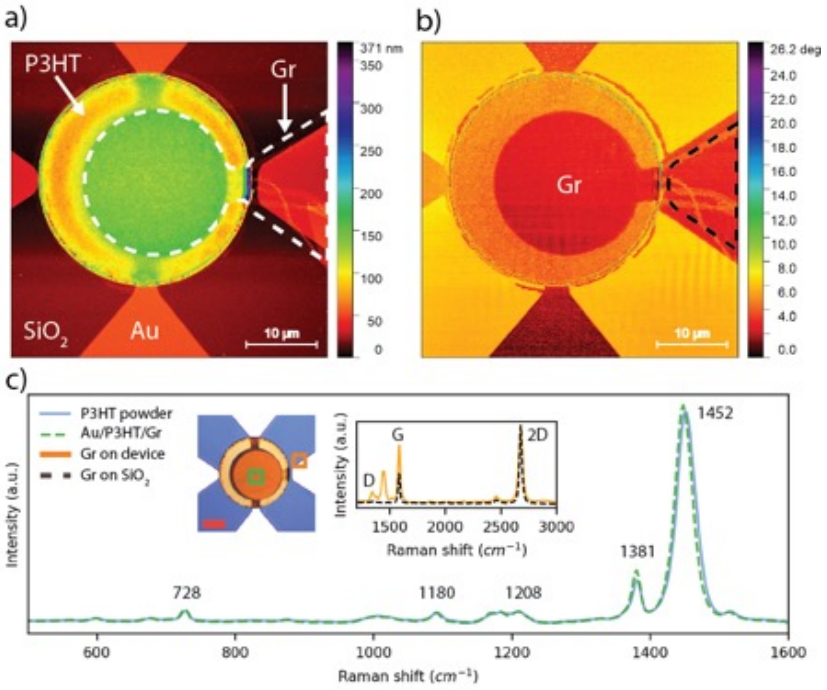

Fig. 1: Reproduced from [1].AFM (a) height and (b) phase aimages of a representative 20 µm device. c) Raman spectra of P3HT powder (blue line) and of a representative Au/P3HT/Gr device (dashed green line). The optical image shows the acquisition position of the spectra (the red scale bar is 10 µm). The inset shows the Raman spectra of a device graphene against the Raman spectrum of a representative CVD graphene on SiO_2.

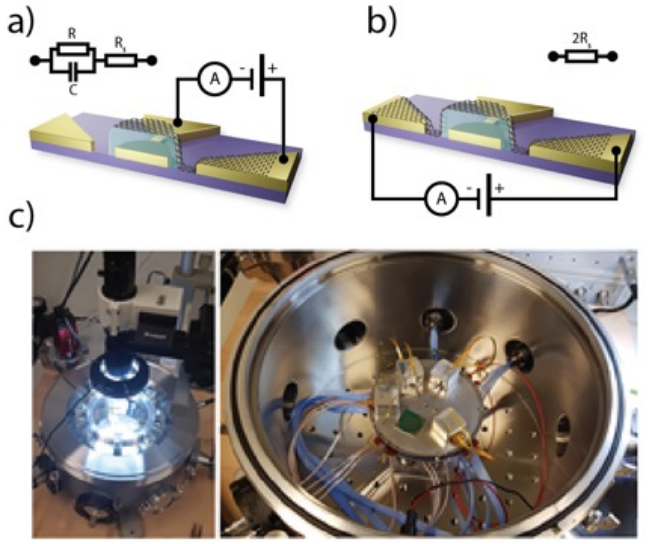

Fig. 2: Reproduced from [1]. Device schematics and electrical schemes of the a) Au/P3HT/Gr stack and of the b) graphene bridge devices. c) The measurement setup used for the electrical characterization of the devices. The devices are measured under high vacuum (p < 10-5 mbar).

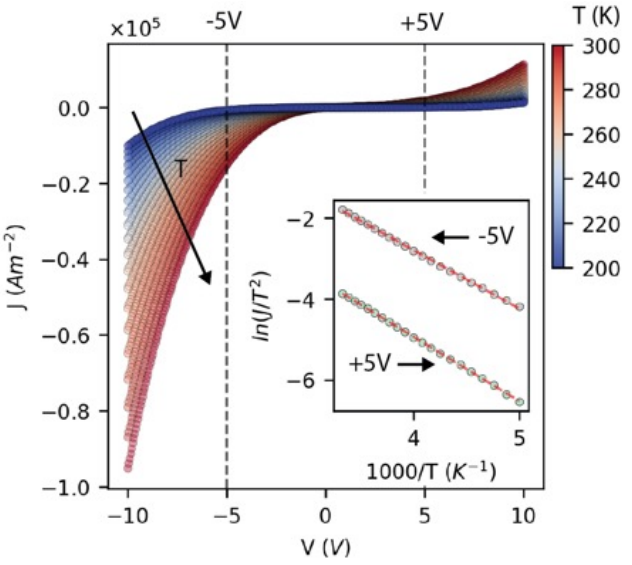

Fig. 3: Reproduced from [1]. Temperature-dependent J–V characteristic of a 5 µm device from 200 to 300 K in steps of 5 K. The inset shows the Richardson plot for 5 V and −5 V.

Conclusions and outlook

This study on the Au/P3HT/Graphene junction showed us the importance of achieving a low carrier injection barrier at the emitter electrode in order to develop high frequency devices. Therefore, quasi-Ohmic contact should be achieved by introducing a doped layer between the emitter and the organic semiconductor. For the graphene/P3HT interface, we observed a relatively high Schottky barrier at the interface. We expect that the resulting high interface resistance can be beneficial for the operation of vertical transistors as the base current is thus reduced.

References

[1] J. Oswald, D. Beretta, M. Stiefel, R. Furrer, A. Romio, M. Daher Mansour, D. Vuillaume, M. Calame, Charge Transport Across Au–P3HT–Graphene van der Waals Vertical Heterostructures, ACS Appl. Mater. Interfaces 14, 42, 48240–48249 (2022)

[2] B. Lüssem, A. Günther, A. Fischer, D. Kasemann, K. Leo, Vertical organic transistors, J. Phys. Condens. Matter 27, 443003 (2015)

[3] E. Guo, S. Xing, F. Dollinger, R. Hübner, S.-J. Wang, Z. Wu, K. Leo, H. Kleemann, Integrated complementary inverters and ring oscillators based on vertical-channel dual-base organic thin-film transistors, Nat Electron (2021)

[4] Z. Wu, Y. Liu, E. Guo, G. Darbandy, S.-J. Wang, R. Hübner, A. Kloes, H. Kleemann, K. Leo, Efficient and low-voltage vertical organic permeable base light-emitting transistors, Nat. Mater. 20, 1007–1014 (2021)

Building up the basic ingredients for Schrödinger-cat-qubit experiments

Project P2101: A planar nanofabrication process for coupled Schrödinger-cat qubits in parametrically-driven nonlinear superconducting resonators
Project Leader: A. Grimm and C. Bruder
Collaborators: A. Bruno (SNI PhD Student)

Introduction

Quantum two-level systems are routinely used to encode qubits but tend to be inherently fragile, leading to errors in the encoded information. Quantum error correction (QEC) addresses this challenge by encoding effective qubits into more complex quantum systems. Unfortunately, the hardware overhead associated with QEC can quickly become very large.

In contrast, a qubit that is intrinsically protected against a subset of quantum errors can be encoded into superpositions of two opposite-phase oscillations in a resonator, so-called Schrödinger-cat states. This "Schrödinger-cat qubit" has the potential to significantly reduce the complexity of QEC, because it can replace a large number of two-level-system qubits in a QEC code [1]. In a recent experiment, we have demonstrated the stabilization and operation of such a qubit through the interplay between Kerr nonlinearity and single-mode squeezing in a superconducting microwave resonator [2]. This type of Schrödinger-cat qubit is typically referred to as the "Kerr-cat qubit".

Previous implementations of Kerr-cat qubits relied on three-dimensional microwave cavities. This counteracts the reduction in hardware complexity achievable with this system and is not fundamentally required. In this project, we will develop a nanofabrication process for fully planar Kerr-cat qubits. This will result in an easily scalable platform enabling us to investigate interactions between several such qubits.

The first months of this SNI project were spent building up the basics required for the fabrication, measurement, and operation of Kerr-cat qubits in line with the ramping up of the research activities of the host group. In addition to experimental tasks, such as building a measurement and control setup, two important prerequisites for the implementation and measurement of Schrödinger-cat qubits were achieved and will be described in the following.

Implementation and testing of transmon qubits

While Schrödinger-cat qubits are intrinsically robust against certain errors, they are nevertheless dependent on the figures of merit of the underlying superconducting circuit. These figures of merit need to be benchmarked by fabricating and measuring standard two-level system qubits before progressing to the more complex circuits needed for cat qubits.

As a first step towards this goal, we have implemented a nano-fabrication process for Al-AlO_x-Al Josephson junctions, which are an essential ingredient for both Kerr-cat qubits and standard superconducting qubits.

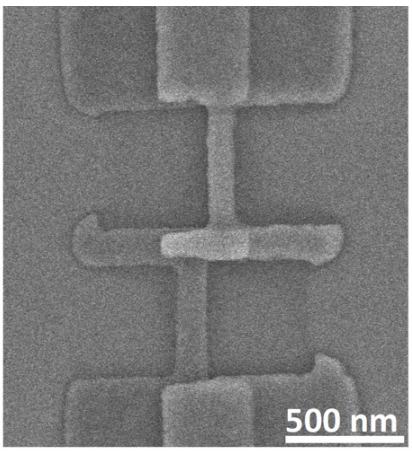

Fig. 1: Scanning-electron micrograph of a small-area Josephson junction fabricated with our process.

This process follows the so-called bridge-free technique [3]. It involves the following steps which are, with the exception of step 7, all carried out in the cleanroom facilities at the Paul Scherrer Institute: 1) cleaning of the sapphire substrate (sonication in NMP/Acetone/IPA) 2) Ebeam-resist spinning (double-layer: PMMA/MMA) 3) Discharge-layer sputtering (10nm Au) 4) Ebeam-lithography 5) Removal of the discharge layer (KI-etch) 6) resist development (2 min in IPA:water 3:1) 7) Shadow-angle evaporation of two Al layers with an interleaved oxidation step to define the junction (carried out in a Plassys MEB550SL3 evaporator in the IBM BRNC cleanroom) 8) liftoff and cleaning (2 hrs. in heated NMP, then Acetone and IPA) 9) chip dicing.

A scanning-electron micrograph of a small-area Josephson junction elaborated with our fabrication process in shown in figure 1. The two electrodes of the junction are entering the frame of the image from the top and bottom respectively. At the center of the image two overlapping layers of Al, separated by an AlO_x layer define the junction. Our junctions are fabricated with a yield >99% over several hundred tested devices.

We then fabricated superconducting transmon qubits [4], based on these elements. A transmon qubit consists of a Josephson junction shunted by a capacitance which is elaborated using the same fabrication process. The transmon is typically coupled to a microwave resonator in such a way that the latter changes its frequency based on the qubit state. To determine the qubit state, a microwave tone is reflected off that resonator and measured [4]. In this initial stage of the project, we are using microwave cavities as measurement resonators as shown in figure 2. This allows

us to independently test our qubit fabrication process before switching to a fully planar layout.

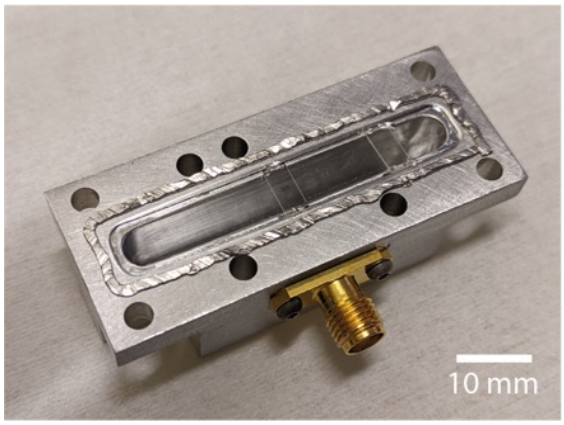

Fig. 2: Lower half of a microwave cavity with two sapphire chips holding transmon qubits. The capacitive pads of the qubits can be seen in the image. An indium seal is used to make the cavity light tight. Microwave signals are routed to and from the system via an antenna inside the cavity connected to the SMA connector visible in the image.

The majority of the qubits we measured had T_1 relaxation times and T_2 Ramsey coherence times on the order of several 10 µs with the best device reaching an intrinsic-loss-limited T_1 (after removing the avoidable limit coming from the coupling to the transmission line) of ~60 µs and a Ramsey T_2 of ~40 µs. These are encouraging first results just short of the state-of-the-art in the field for these devices and we expect further improvements by using more aggressive substrate-cleaning and lower-loss materials [5].

Near-quantum-limited amplifiers

Another essential ingredient for our research are near-quantum-limited amplifiers. These devices constitute the first stage of amplification inside the dilution refrigerator. Their low added noise (typically a few quanta) and large gain (~20 dB) ensure that the signal-to-noise ratio of our measurements degrades only minimally in subsequent parts of the measurement chain. We have implemented and tested so-called SNAIL-parametric amplifiers (SPAs) [6]. SPAs are based on more complex Josephson-junction circuits (see Fig. 3) fabricated with the Dolan-bridge recipe [7]. Our first test device (see Fig. 4) yielded gains above 20 dB at some frequency points. Further improvement will be required to cover the entire frequency range relevant to our samples.

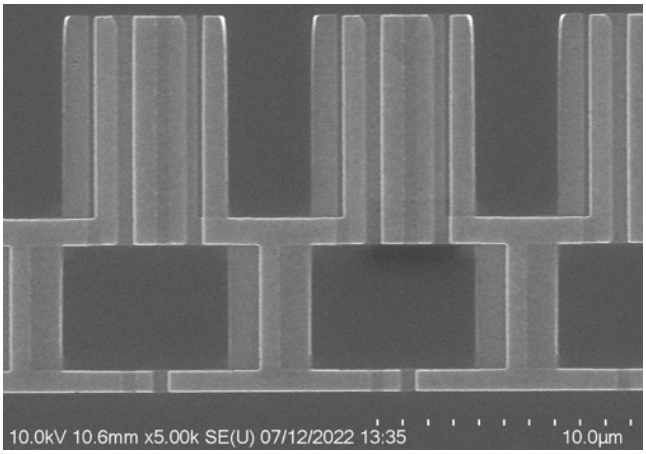

Fig. 3: Array of SNAILs [6] each consisting of three large series Josephson junctions (top) in parallel with one small junction (bottom).

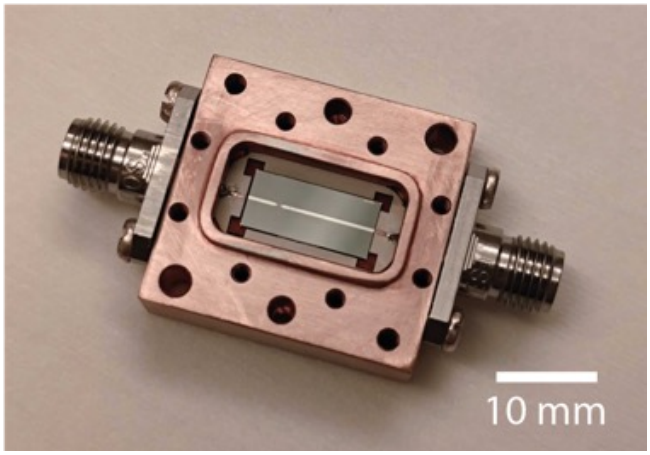

Fig. 4: A SNAIL-parametric amplifier (SPA). The SNAIL array is situated at the narrow part of the stripline visible on the chip. Signals are routed to and from the amplifier via the SMA connectors.

The next steps in this project will build upon these capabilities to implement and measure Schrödinger-cat qubits accompanied by a transition to a fully planar device layout.

References

[1] A. S. Darmawan, B. J. Brown, A. L. Grimsmo, D. K. Tuckett, S. Puri, Practical Quantum Error Correction with the XZZX Code and Kerr-Cat Qubits. PRX Quantum 2, 030345 (2021)

[2] A. Grimm, N. E. Frattini, et al. Stabilization and operation of a Kerr-cat qubit, Nature 584, 205–209 (2020)

[3] F. Lecocq, I. M. Pop, Z. Peng, I. Matei, T. Crozes, T. Fournier, C. Naud, W. Guichard, O. Buisson, Junction fabrication by shadow evaporation without a suspended bridge, Nanotechnology 22(31), 315302 (2011)

[4] A. Blais, A. L, Grimsmo, S. M. Girvin, A. Wallraff, Circuit quantum electrodynamics, Rev. Mod. Phys. 93, 025005 (2021)

[5] A. P. M. Place, et al. New material platform for superconducting transmon qubits with coherence times exceeding 0.3 milliseconds, Nat. Commun. 12, 1779 (2021)

[6] N. E. Frattini, U. Vool, S. Shankar, A. Narla, K. M. Sliwa, M. H. Devoret, 3-wave mixing Josephson dipole element, Appl. Phys. Lett. 110, 222603 (2017)

[7] G. J. Dolan, Offset masks for lift-off photoprocessing, Appl. Phys. Letters 31, 337–339 (1977)

Gold nanoparticle for Raman visualization of ovarian cancer cells

Project P2103: Gold nanoparticle assemblies for SERS based detection of EGFR expressing ovarian cancer cells in tumor xenografts
Project Leader: S. Saxer and V. Heinzelmann
Collaborators: A. Stumpo (SNI PhD Student)

Introduction

Ovarian cancer (OC) is the gynaecologic malignancy with the highest mortality. Several reports suggested that overexpression of the epidermal growth factor receptors (EGFR) family plays an important role in OC [1], leading to clinical trials of different EGFR inhibitors such as gefitinib and erlotinib [2]. Nevertheless, the most common OC treatment approach remains the debulking surgery followed by chemotherapy.
A precise pre-operative disease visualization is essential because patients with post-surgical residual tumors less than 1 cm have higher survival rates than those with more residual tumor masses [3]. Currently, the most common imaging methods include computed tomography, magnetic resonance, positron emission tomography, and fluorescence-guided surgery (the current gold standard for surgical guidance), each of them with one or more drawbacks [4].

Recently, Raman microscopy is emerging as a label-free, sensitive, and non-invasive imaging and diagnostic technique [5]. In particular, by combining Raman microscopy with properly functionalized gold nanoparticles (AuNPs), it is possible to reach a sensitive detection of specific cell types exploiting the so-called SERS measurement [6].
In the context of imaging and diagnosis, the SERS measurement needs the AuNPs surface to be functionalized with a proper mixture of inert and active targeting functionalities. In fact, a 100% surface coverage of Raman reporter achieves the strongest signal but result in non-specific binding. On the opposite, an excess surface coverage of PEG molecules would lead to the highest stability but loss of Raman signal. Therefore, in order to achieve a perfect balance between Raman signal sensitivity, binding specificity and AuNPs stability/biocompatibility, an appropriate mixture of Raman reporters, protective layer of PEG molecules and antibodies has to be obtained on AuNPs surface [7].
We have outlined 60 nm gold nanoparticles with SERS properties to selectively target EGFR+ ovarian cancer cells. First, 60 nm AuNPs were functionalized, and their physicochemical properties (PCCs) characterized after each step. Then, anti–human EGFR antibodies were attached on the AuNPs surface, and their functionality evaluated. Finally, once established their biocompatibility with ovarian cancer cells, AuNPs capability to distinguish EGFR+/EGFR- ovarian cancer cell lines is evaluated in vitro.

Results and discussions

Burgio et al. [7] defined the ideal ratio of surface chemistry between three molecules; Raman reporter, protective PEG layer and anti-EGFR antibodies in order to achieve a perfect balance between AuNPs properties and successfully target glioblastoma. Therefore, the same ratio was chosen for surface chemistry of our gold nanoparticles.

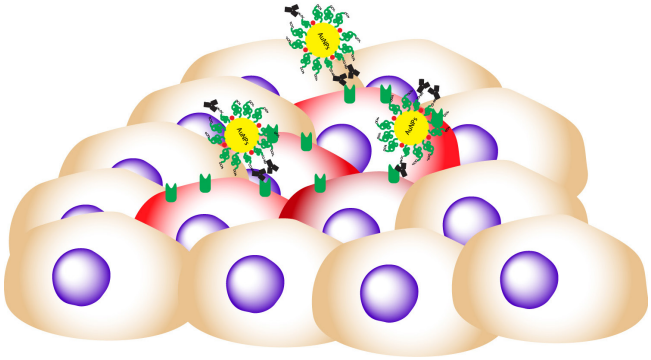

Fig. 1: Schematic illustration of AuNPs mechanism of action. AuNPs with proper mixture of inert and active targeting molecules recognize only ovarian cancer cells expressing EGFR.

Once AuNPs core size was confirmed, change in size after each functionalization step were detected (Fig. 2). Figure 2 clearly shows an insignificant increase in size after 1,4 Benzene-dithiol (1,4 BDT), carboxy-PEG (cPEG) and anti-EGFR antibodies (Ab) functionalization, used respectively as Raman active molecule, linker molecule and targeting protein. As expected, a significant increase in size is observed after methoxy-PEG functionalization (mPEG), due to a consistent increase in PEG molecules surface density [8]. The same result is observed with AuNPs surface charge (Fig. 3), with a noteworthy decrease of it after mPEG functionalization, purposefully chosen to reduce AuNPs surface charge and therefore increase their biocompatibility and specificity.

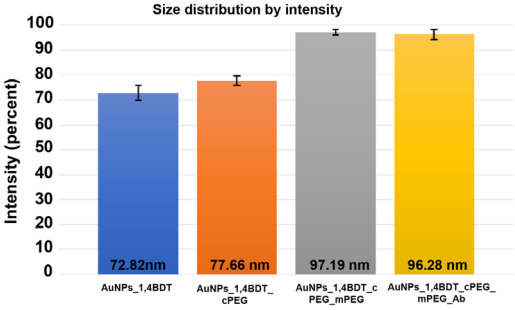

Fig. 2: AuNPs size distribution after each functionalization step. Measured with Zetasizer ZS instrument (Malvern Panalytical).

Since neither size nor surface charge changed after antibodies functionalization, Western blot was carried out to prove both antibody successful functionalization and functionality (Fig. 4). A clear band, corresponding to the extracellular domain of EGFR protein, is observed only when AuNPs are functionalized with antibodies. In the antibody's absence, AuNPs are not able to bind the protein and no band is visible.

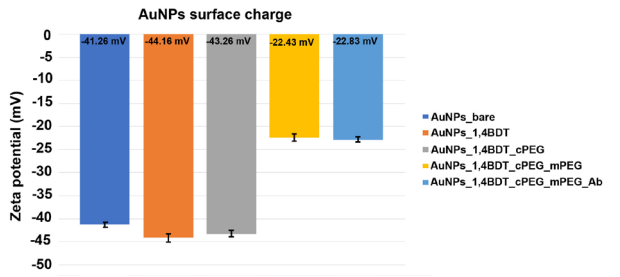

Fig. 3: AuNPs surface charge after each functionalization step. Measured with Zetasizer ZS instrument (Malvern Panalytical).

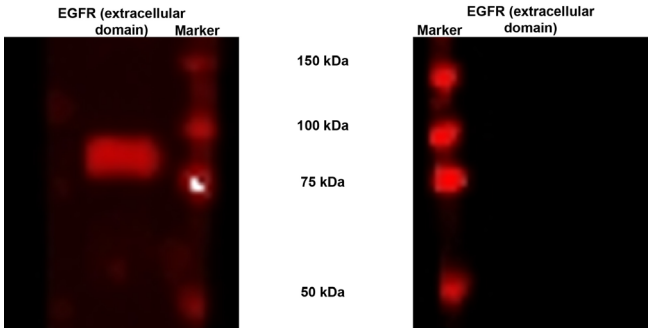

Fig. 4: Western blot. On the left: the membrane was incubated with AuNPs with anti-EGFR antibodies attached to their surface. On the right: the membrane was incubated with AuNPs without any antibodies on their surface.

Afterwards, 1,4 BDT presence and SERS effect on AuNPs surface was investigated, detecting Raman signal of 1,4 BDT free and attached on AuNPs (Fig. 5). With the exception of the peak at 2'556 cm^{-1}, all typical 1,4 BDT Raman peaks are shown following each functionalization step. Furthermore, typical 1,4 BDT peaks are slightly shifted and widened when the molecule is on the AuNPs surface. This is due complexes formation on nanoparticles surface.

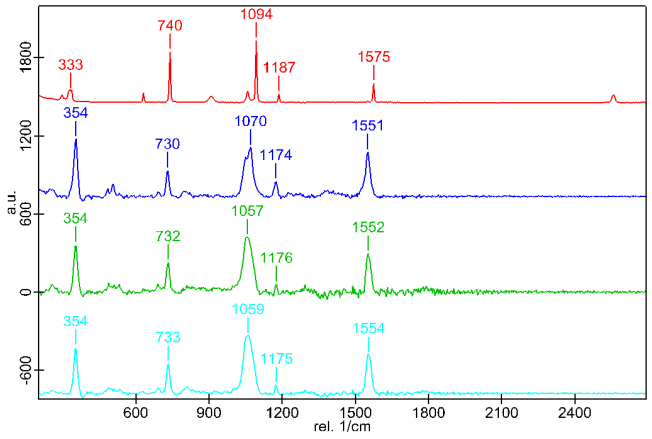

Fig. 5: Raman signal of 1,4 BDT. 1,4 BDT powder was chosen as reference spectrum. Measured with a WiTEC Alpha300R Raman Microscope. 785 nm laser wavelength; 60 mW laser power; 50x objective.

Eventually, fully functionalized AuNPs stability in cell culture media was evaluated over time (Fig. 6). AuNPs are perfectly stable up to 6 h, with a slight increase of size at 24 h.

Outlooks

Despite the promising prospects of dispersed AuNPs, we aim to transfer these knowledges on AuNPs assemblies. The novel assemblies will not only allow to distinguish healthy and malignant cells but also offer better signal than dispersed AuNPs, through the extraordinary intense SERS effect in the interparticle gaps. Furthermore, a different ratio between inert and active molecules will be evaluated, in order to improve AuNPs specificity and biocompatibility. Eventually, AuNPs assemblies will be tested in vitro on OC cell lines to prove their efficacy and in vivo to evaluate bio-durability and biodistribution.

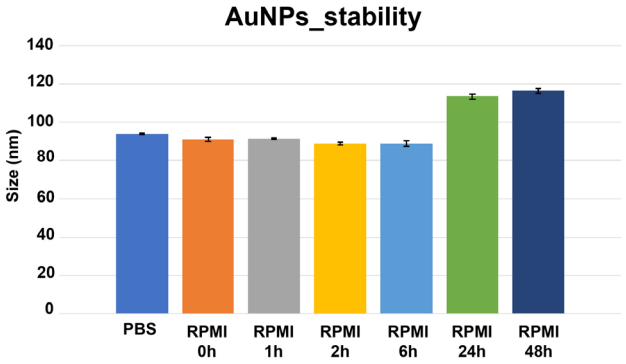

Fig. 6: AuNPs stability in RPMI cell culture media, implemented with 10% FCS and 1% P/S. Samples were kept at 37°C. AuNPs in PBS were taken as reference. Measured with Zetasizer ZS instrument (Malvern Panalytical).

References

[1] E. Teplinsky, F. Muggia, EGFR and HER2: Is there a role in ovarian cancer? Translational Cancer Research 4, 107–117 (2015)

[2] Q. Sheng, J. Liu, The therapeutic potential of targeting the EGFR family in epithelial ovarian cancer, British J. Cancer 104, 1241–1245 (2011)

[3] A. Musto, L. Rampin, C. Nanni, M. C. Marzola, S. Fanti, D. Rubello, Present and future of PET and PET/CT in gynaecologic malignancies. Eur. J. Radiol. 78, 12–20 (2011)

[4] B. Orr, R. P. Edwards, Diagnosis and treatment of ovarian cancer. Hematol. Oncol. Clin. North Am. 32, 943–964 (2018)

[5] I. P. Santos, et al. Raman spectroscopy for cancer detection and cancer surgery guidance: Translation to the clinics, Analyst 142, 3025–3047 (2017)

[6] H. Karabeber, R. Huang, P. Iacono, J. M. Samii, K. Pitter, E. C. Holland, M. F. Kircher, Guiding brain tumor resection using surface-enhanced Raman scattering nanoparticles and a hand-held Raman scanner. ACS Nano 8, 9755–9766 (2014)

[7] F. Burgio, D. Piffaretti, F. Schmidt, U. Pieles, M. Reinert, M.-F. Ritz, S. Saxer, Tuning the Surface Chemistry of Gold Nanoparticles to Specifically Image Glioblastoma Cells Using Surface-Enhanced Raman Spectroscopy, ACS Appl Nano Mater 3, 2447–2454 (2020)

[8] H. Chen, H. Paholak, M. Ito, et al. 'Living' PEGylation on gold nanoparticles to optimize cancer cell uptake by controlling targeting ligand and charge densities, Nanotechnology 24, (2013)

RT-Xray shows unusual O_2 binding to FGE

Project P2104: Methods to understand the role of ordered waters and disordered residues in enzyme catalysis using macromolecular crystallography at physiological temperatures
Project Leader: F. P. Seebeck and J. H. Beale
Collaborators: S. Bolotova (SNI PhD Student), F. Leisinger

Abstract
The objective of this project is to implement room temperature (RT) crystallography methods to determine enzyme structures that are physiologically more relevant that those emerging from standard measurements at cryogenic temperatures. In the past year we have applied a first version of this method in a study about the active site geometry of a copper-dependent enzyme.

Introduction
Reductive activation of O_2 to superoxide is the first catalytic step in O_2-utilization by mononuclear copper and iron enzymes [1, 2]. In their active sites this difficult electron transfer is driven by the thermodynamically favorable formation of a coordination complex between superoxide and Fe^{III} or Cu^{II}. A set of ligands arranged in a geometry that stabilizes the metal in the oxidized state relative to the reduced state, and allows binding of superoxide to the metal with minimal structural reorganization can further increase the efficiency of O_2 activation [2]. Numerous synthetic copper and iron complexes that fulfill these structural requirements do indeed activate O_2 and can oxidize a broad range of substrates. The literature also provides ample documentation that heme enzymes and mononuclear non-heme iron or copper enzymes exploit the same architectural features to expedite the activation of O_2.
The formylglycine generating enzyme (FGE, EC 1.8.3.7) seems to deviate from this paradigm. This copper-dependent enzyme catalyzes the posttranslational conversion of a specific cysteine residue in sulfatases and some phosphatases to formylglycine [3]. In the resting state FGE binds Cu^I via two cysteines, in a linear bis-thiolate arrangement (Fig. 1a) [4]. In the enzyme:substrat complex (FGE:Cu^I:S), the metal is surrounded by three thiolates in a planar trigonal geometry (Fig. 1b)[5]. A highly ordered water (H_2O_1) hovers 3.3 Å above the copper center without making any attractive interaction. This geometry does not provide a preformed coordination site for O_2. Consistently, the oxygenated complex (FGE:Cu^I:S:O_2) binds O_2 in the same position as H_2O_1, juxtaposed, but not coordinated, to the still trigonally coordinated copper center (Fig. 1c)[6]. All available observations support the idea that FGE accumulates as a pre-catalytic complex comprising all substrates but without forming a reactive copper-oxygen species. It is possible that the X-ray structures of observed at 100 K (which is the standard temperature at which X-ray diffraction data is usually collected) do not reflect the dominant species at room temperature, raising the question as to whether our mechanistic model is based on cryo-artefacts. Determination of the structures of FGE at physiological temperatures (293 K) would be an important step to answer this question.

With this goal in mind, we developed a user-friendly protocol for the collection of X-ray diffraction data at 293 K on a standard macromolecular crystallography synchrotron beamline.

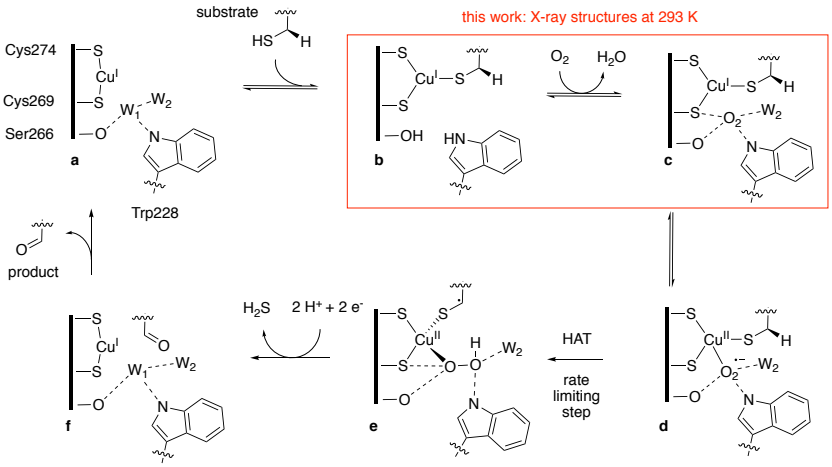

Fig. 1: Proposed mechanism of FGE: Hydrogen atom abstraction (HAT) from the substrate has been identified as the rate limiting and first irreversible step. No structural information is available for species d – f.

Results and Discussion
The detailed measurement protocol will be described in a manuscript that we plan to submit for publication early in 2023. Here are some of the key results:
The structure of FGE:Cu^I:S at 293 K. The active sites of FGE:Cu^I:S observed at 100 K and at 293 K adopt indistinguishable structures (Fig. 2, top left and bottom right). Specifically, the planar trigonal tris-thiolate Cu^I complex remains unchanged upon warming, and the crystallographic waters H_2O_1-4 occupy the same position. H_2O_1 is present at full occupancy 3.3 Å away from Cu^I. In this position H_2O_1 makes three hydrogen bonds H_2O_2, Ser266 and Trp228 arranged in a planar trigonal geometry. This environment is less stabilizing than the tetrahedral array of interactions that an average water in bulk solvent can establish [7]. Therefore, we suspect that H_2O_1 is a "high-energy" water that is easily replaced by another neutral small guest with less requirements for hydrogen bonding [5]. The 293 K structure of FGE:Cu^I:S shows that even under physiological conditions, this position is fully occupied by H_2O_1.

The structure of FGE:Cu^{I}:S:O_2 at 293 K. Consistent with the idea that H_2O_1 is easily replaced with an alternative ligand, we observed that O_2 or nitroxide at concentrations below 5 mM outcompete H_2O (55 M) for this binding pocket (Fig. 1c)[6]. However, the idea that O_2 would maintain van der Waals distance to Cu^{I} in an accumulating species proved to be a controversial idea. Maybe, the counterargument goes, FGE:Cu:S holds O_2 without coordination (as in c) because the copper-superoxide species (for example d) is destabilized at low temperatures, whereas at room temperature it may dominate the ensemble. With the possibility to measure crystal structures at 293 K within less than 10 s and with low radiation doses, we now have the proper tool available to resolve this controversy directly. From previous experiments we knew that oxygenating FGE:Cu:S crystals by soaking in O_2 solutions ($[O_2] \leq 5$ mM, t = 10 – 20 s) starts substrate turnover in crystallo. This activity changes the crystal symmetry (space group P 2_1 2_1 2_1 to P 2 2 2), and reduces the overall resolution by at least 0.2 – 0.5 Å. These negative effects increase with time to the extent that crystals decompose and seize to diffract after 120 s. It was therefore essential to minimize the data collection time. Optimized experimental parameters as described above (method 2) allowed us the collect diffraction data sets of FGE:Cu:S:O_2 crystals with total exposure times of less than 10 s. Three data sets could be solved to resolutions of 1.6 Å and 1.8 Å. The active sites in these structures observed at 293 K are again very similar to those of FGE:Cu:S:O_2 at 100 K. On top of the planar trigonal Cu^{I} site residual electron density with an ellipsoid shape indicates that H_2O_1 has been replaced by a molecule with two heavy atoms. This density could be modeled with O^1 and O_2 of molecular oxygen present at an occupancy of 100%. O^1 makes the closest contact to Cu^{I} (3.0 Å) and O_2 makes closest contact with H_2O_2 (2.6 Å). The slightly increased B-factor of the substrate peptide residues Pro5 to Pro9 in the active site of FGE:Cu:S:O_2 of ~31 $Å^2$ compared to the same residues of the substrate in FGE:Cu:S (22 $Å^2$) is an indicator for the exponential decay of the enzyme:substrate complex to the enzyme:product complex.

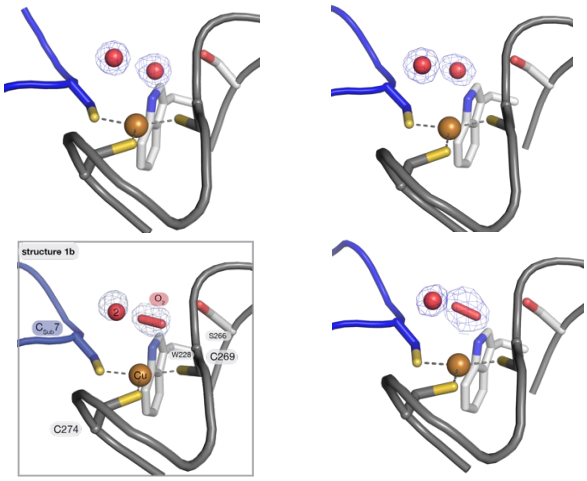

Fig. 2: Active site of FGE observed by crystallography. 2mFo-DFc map contoured at sigma-level 1.2 as blue mesh. Top left) FGE:Cu^{I}:S, 100 K resolution: 1.4 Å; top right): FGE:Cu^{I}:S, 293 K, 1.5 Å; bottom left) FGE:Cu^{I}:S:O_2, 100 K resolution: 1.4 Å;6 bottom right) FGE:Cu^{I}:S:O_2, 293 K, 1.8 Å

The alternative interpretation that the ellipsoid electron density is caused by a disordered water is inconsistent with the observation that - without exception - all anaerobic structures show H_2O_1 as a spherical electron density immobilized at one invariant position. The B-factor of this single heavy atom matches those of all surrounding waters H_2O_1-4 at 100 K (B-factors: 16, 16, 14, 19 $Å^2$) and at 293 K (B-factors: 18, 25, 19, 27 $Å^2$). To cause an ellipsoid electron density, H_2O_1 would have to be much more disordered than H_2O_2-4. Furthermore, a fourth data set collected from an oxygenated crystal (resolution: 1.4 Å) revealed a structure with a sharply defined spherical electron density in position of H_2O_1. Apparently, this crystal did not bind enough O_2 to dominate the observed structure. This sample corroborates that the ellipsoid electron density in the other three structures in not a result of disorder induced by O_2-soaking or by the protocol followed for measurements at 293 K.

Conclusion

We have developed a user-friendly methodology to determine the crystal structure of O_2-bound Michaelis-Menten complexes of active enzymes at physiological temperatures.

References

[1] E. I. Solomon, S. Goudarzi, K. D. Sutherlin, O_2 Activation by Non-Heme Iron Enzymes. Biochemistry, 55(46), 6363 - 6374 (2016)

[2] E. I. Solomon, D. E. Heppner, E. M. Johnston, J. W. Ginsbach, J. Cirera, M. Qayyum et al. Copper Active Sites in Biology, Chem Rev, 114(7), 3659 - 3853 (2014)

[3] T. Dierks, B. Schmidt, L. V. Borissenko, J. H. Peng, A. Preusser, M. Mariappan et al. Multiple Sulfatase Deficiency Is Caused by Mutations in the Gene Encoding the Human C -Formylglycine Generating Enzyme, Cell, 113(4), 435-444 (2003)

[4] M. Meury, M. Knop, F. P. Seebeck, Structural Basis for Copper-Oxygen Mediated C-H Bond Activation by the Formylglycine-Generating Enzyme. Angew Chem Int Ed Engl, 56(27): 8115 - 8119 (2017)

[5] D. A. Miarzlou, F. Leisinger, D. Joss, D. Häussinger F. P. Seebeck, Structure of formylglycine-generating enzyme in complex with copper and a substrate reveals an acidic pocket for binding and activation of molecular oxygen, Chem Sci, 10(29), 7049 - 7058 (2019)

[6] F. Leisinger, D. A. Miarzlou, F. P. Seebeck, Non-Coordinative Binding of O_2 at the Active Center of a Copper-Dependent Enzyme, Angew Chem Int Ed Engl, 60(11), 6154 - 6159 (2021)

[7] T. Urbic, K. A. Dill, Water is a cagey liquid, J Am Chem Soc, 140, 17106 – 171 (2018)

Magnetic torque transducer in a phononic band-gap structure

Project P2107: High-sensitive torque magnetometry for 2D materials
Project Leader: I. Zardo and M. Poggio
Collaborators: M. Claus (SNI PhD Student)

Introduction

Progress in fabrication and development of nanomechanical resonators now allows measurement of mass, force, and torque with exquisite sensitivity. These improvements are mostly due to the dramatic reduction in the size of mechanical transducers over the last 30 years, which now even include individual carbon nanotubes. Decreasing size and defect density reduces mechanical losses and therefore improves transducer sensitivity [1]. Recently, phonon engineering has also been exploited to diminish mechanical losses [2] via patterned mechanical supports engineered to have a phononic band-gap around a transducer's mechanical resonance frequency. In addition, the supports have been designed to optimally clamp the resonator, further reducing loss. These techniques have been used to make high-Q optomechanical devices [2] and are beginning to be applied in the design of ultra-sensitive force sensors. So far, however, no one has applied them to sensitive torque sensing.

Here, we intend to apply these techniques to fabricate ultra-sensitive mechanical torque sensors and to design these sensors especially for the investigation of 2D materials – including 2D magnets and van der Waals (vdW) heterostructures. In addition to being sensitive enough to measure ultrathin magnetic materials, our sensors will incorporate the possibility of making electrical contact to the sample, something which has been practically challenging in the most sensitive cantilever-based torque sensors. A sketch of the envisioned device is shown in figure 1.

Torque magnetometry is an established and highly sensitive technique for studying nanomagnets, correlated metals, and superconductors [3]. Dynamic torque (frequency shift), which is proportional to the curvature of the magnetic free energy with respect to rotations, is a particularly useful observable for identifying magnetic phase transitions [4], because – just like the magnetic susceptibility – it is discontinuous for both first and second order phase transitions. Torque magnetometry is broadband and capable of measuring both magnetostatic effects and magnetization dynamics, including spin resonance and relaxation processes [5]. The improved sensitivity of our planned torque sensors and the ability to integrate electrical leads and contacts to the sample will enable a whole series of experiments: e.g. detecting superconducting and magnetic phase transitions in twisted bi-layer graphene [5], vdW heterostructures, and other 2D materials, including the reported magnetic phase transition in gated monolayer MoS_2 [6]. Determining the magnetic state of 2D materials is especially challenging due to their tiny magnetic moment, making conventional methods such as SQUID magnetometry, neutron diffraction, and X-ray techniques ineffective. Our vision is to create and apply a new experimental platform for the investigation of magnetic and superconducting phase transitions in 2D systems.

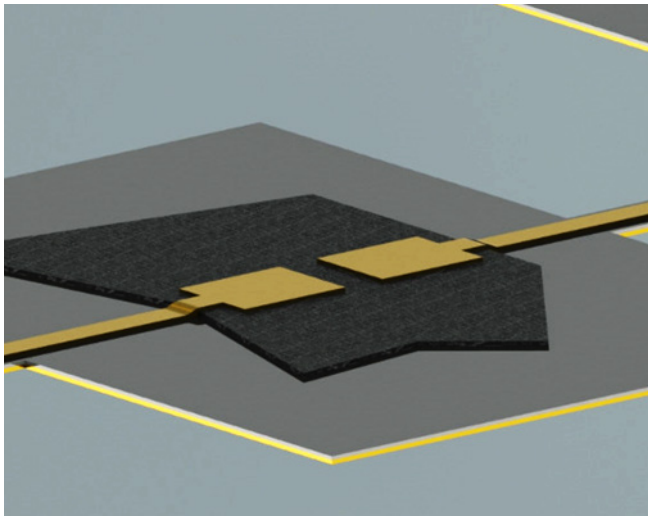

Fig. 1: Schematic diagram of a torque sensor with 2D sample, bottom back gate, and top contacts.

Goals

Sensitive torque magnetometry has been used to determine the magnetic behavior of very small magnets [7], persistent currents in normal metal nano-rings [8], and tiny superconducting structures [9]. So far, however, its sensitivity has not been leveraged to measure any of the emerging class of 2D vdW materials and their heterostructures, which are far too thin for conventional SQUID or torque magnetometers. Recently discovered correlated states in these systems range from superconductivity, to highly insulating states, to magnetism. In some cases, transitions between these states can even be induced by electrostatic gates. Our specially designed torque sensors will allow us to measure these phase transitions, yielding the associated phase diagrams and giving new insight into these poorly understood condensed matter phenomena.

Accordingly, the goals of this project are to:

1) Fabricate torsional resonators allowing for electrical contact to the sample and integrate them within a phononic band-gap support with optimal clamping;
2) Demonstrate state-of-the-art torque sensitivity on samples with electrical contacts;
3) Use the transducers to measure magnetic and superconducting phase transitions in 2D materials as a function of applied gate voltage, magnetic field, and temperature.

Results

In the first year, we have developed fabrication techniques for making torsional beams inside a phononic band-gap structure made from SiN. First, a 100 nm thin SiN film is

deposited to both faces of a silicon substrate, which is then patterned with direct laser lithography and reactive ion etching. Once the mechanical resonator and phononic band-gap structure have been patterned in the SiN film, devices are suspended by removing the silicon substrate with a final wet-etch step to yield an acoustically isolated mechanical torque transducer. Subsequently, a nanosized magnetic test sample is attached to the sensor for proof of principle measurements.
An optical image of one of the torque transducers and its frequency response spectrum are shown in figure 2. The latter shows a band gap between 450 and 700 kHz, and a torsional resonance of the transducer at 523 kHz, well within the band-gap. With this phonon escape from the resonantor into the substrate should be suppressed strongly by the band-gap.

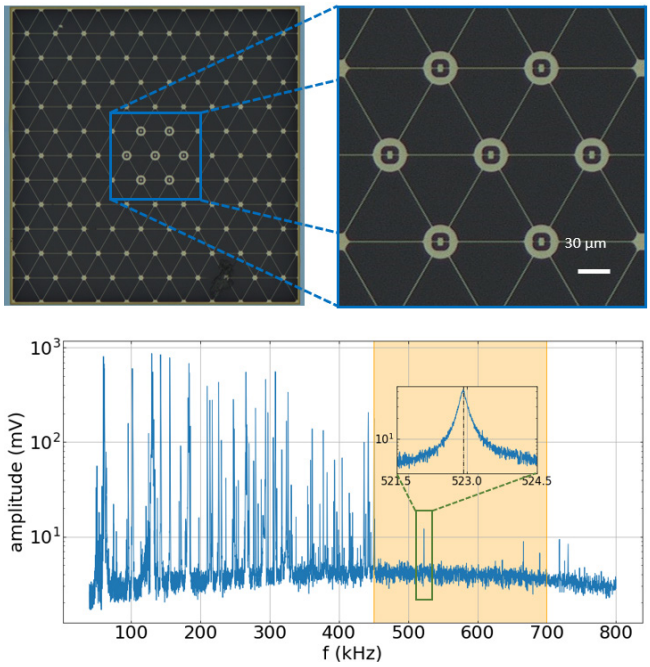

Fig. 2: Torque transducers inside a phononic band-gap structure and measured frequency response spectrum of one torsional resonator with the band-gap colored orange. The inset shows the fundamental torsional resonance peak.

In spite of successful fabrication of such a band-gapped torsional transducer, we did not observe a substantial improvement in the Q-factor compared to transducers without band-gap. This indicates that mechanical dissipation of our torsional resonator is dominated by bending and/or surface losses, demanding for optimization of the device on other premises.

Outlook

With the acquired expertise in producing suspended SiN microresonators, we are able to design and fabricate high-sensitive torque transducers with high precision and good yield. In a next step, the dominant loss mechanisms will be addressed. For this, doubly clamped flexural beams will be used as transducers integrated in the bandgap structures, which benefit from dissipation dilution, a well established technique to drastically reduce such losses [10]. At the same time, 2D material exfoliation, stacking, stamping techniques will be explored, and a first torque magnetometry measurement on a 2D magnetic specimen is expected to take place in the weeks to come.

References

[1] F. R. Braakman and M. Poggio, Force sensing with nanowire cantilevers, Nanotechnol. 30, 332001 (2019)

[2] Y. Tsaturyan, A. Barg, E. S. Polzik, A. Schliesser, Ultra-coherent nanomechanical resonators via soft-clamping and dissipation dilution, Nat. Nanotechnol. 12, 776 (2017)

[3] A. Mehlin, F. Xue, D. Liang, H. F. Du, M. J. Stolt, S. Jin, M. L. Tian, M. Poggio, Stabilized Skyrmion phase detection in MnSi Nanowires by Dynamic Cantilever Magnetometry, Nano Lett. 15, 4839 (2015)

[4] J. E. Losby, et al., Torque-mixing magnetic resonance spectroscopy, Science 350, 798 (2015)

[5] U. Zondiner, et al., Cascade of phase transitions and Dirac revivals in magic-angle graphene, Nature 582, 203 (2020)

[6] J. G. Roch, D. Miserev, G. Froehlicher, N. Leisgang, L. Sponfeldner, K. Watanabe, T. Taniguchi, J. Klinovaja, D. Loss, R. J. Warburton, First-order magnetic phase transition of mobile electrons in monolayer MoS2, Phys. Rev. Lett. 124, 187602 (2020)

[7] A. Mehlin, B. Gross, M. Wyss, T. Schefer, G. Tütüncüoglu, F. Heimbach, A. Fontcuberta i Morral, D. Grundler, M. Poggio, Observation of end-vortex nucleation in individual ferromagnetic nanotubes, Phys. Rev. B 97, 134422 (2018)

[8] A. C. Bleszynski-Jayich, W. E. Shanks, B. Peaudecerf, E. Ginossar, F. von Oppen, L. Glazman, J. G. E. Harris, Persistent currents in normal metal rings, Science 326, 272 (2009)

[9] J. Jang, D. G. Ferguson, V. Vakaryuk, R. Budakian, S. B. Chung, P. M. Goldbart, Y. Maeno, Phase-locked cantilever magnetometry, Science 331, 186 (2011)

[10] S. Schmid, L. G. Villanueva, M. L. Roukes, Fundamentals of Nanomechanical Resonators, 77-87 (Springer, 2016)

Achromatic & Apochromatic X-ray focusing

Project A16.01: ACHROMATIX (Paul Scherrer Institut, University of Basel, Biomaterials Science Center, XRnanotech GmbH, Villigen)
Project Leader: J. Vila Comamala
Collaborators: G. Schulz, G. Rodgers, U. T. Sanli, P. Qi, A. Kubec, F. Döring, B. Müller, C. David

Introduction

Diffractive and refractive X-ray optics are essential elements for X-ray analysis techniques with many applications in biology, energy and materials science. However, diffractive and refractive lenses suffer from chromatic aberration, that is, only X-rays with a narrow energy range are focused at the same position along the optical axis. This particularly hinders the development of full-field transmission X-ray microscopy using laboratory X-ray tube sources, since broad-bandwidth radiation cannot be efficiently used. On the other hand, using a monochromator severely cuts down the photon flux to inoperable X-ray intensities. In the past two years, we started the development of achromatic X-ray lenses by combining a diffractive and refractive element [1, 2], as shown in figure 1a. After developing the calculation tools for designing the right combination of optical components that are able to cancel out the chromatic aberration, we have also developed the fabrication methods to produce the required refractive and diffractive elements. The X-ray diffractive lenses have been produced using state-of-the-art electron beam lithography and electro deposition methods available at the cleanroom facilities of the Paul Scherrer Institut. The refractive part of the achromatic X-ray lens was produced by two-photon polymerization 3D printing. Using scanning transmission X-ray microscopy and ptychography at a synchrotron experimental station, the first ever demonstration of an achromatic X-ray lens was realized during the first year of the project [3]. During the second year of the project, the development of achromatic X-ray lenses have progressed in several ways. On the one hand, we have developed the methods to produce the refractive and diffractive element on the same substrate. In this approach the refractive and diffractive parts of the achromat are aligned during the production steps. Thus, such a monolithic achromatic X-ray lens extremely simplifies the alignment required during its implementation in the experimental setup and paves the way for a broader use of such a concept. In synchrotron experiments, a monolithic achromatic X-ray lens was shown to deliver a 250 nm focal spot, that is a factor of two improvement compared to the previous published result [3]. On the other hand, we have also explored the possibility of realizing apochromatic X-ray focusing [2] by introducing the right separation distance between the diffractive and refractive elements, as schematically shown in figure 1b. As in the case for visible light lenses, the apochromatic focusing allows to use an even wider range of photon energies. This concept has been experimentally tested in a synchrotron experimental station. A publication has been submitted and it is currently under review. Finally, we realized several synchrotron experiments to demonstrate the applications of achromatic X-ray lenses for full-field and scanning transmission X-ray microscopy.

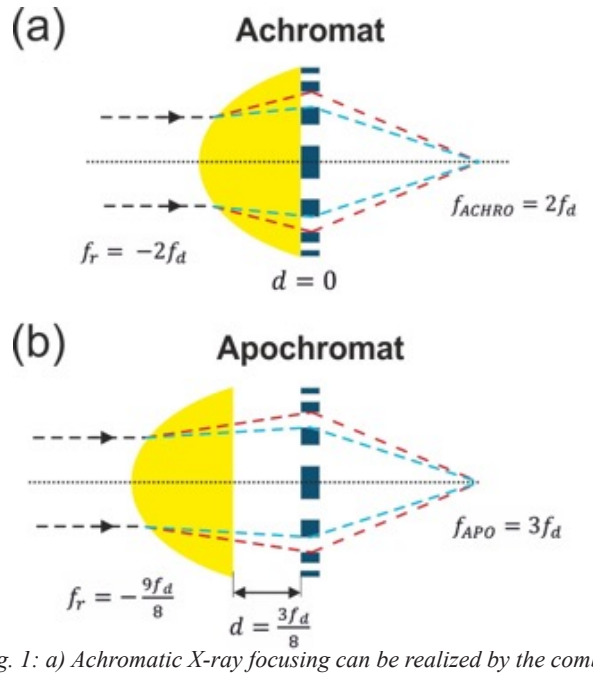

Fig. 1: a) Achromatic X-ray focusing can be realized by the combination of a refractive and diffractive lens. b) Apochromatic X-ray focusing can be obtained by combining a refractive and diffractive lens separated by the right distance.

Development of monolithic X-ray achromat

The first implementation of an achromatic X-ray lens was realized by two elements produced in separate substrates. During its installation at the X-ray experimental setup, two separate sets of motorized stages were required. The alignment of the two elements was demanding and time consuming. Thus, we explored the possibility of producing the two elements on a single substrate. For that, the fabrication steps of the diffractive and refractive element had to be made compatible. The fabrication of the monolithic X-ray achromat started with the production of the gold Fresnel zone plate. The main challenge to be tackled was to enable the two-photon polymerization 3D printing on the gold seed layer for electroplating, which caused bubbling on the silicon nitride membrane during the first production attempts. The solution was to use a silicon nitride membrane just slightly larger than the Fresnel zone plate and produce the supports of the refractive structure on the bulk region of the silicon chip. A scanning electron microscopy picture of a monolithic achromat is shown in figure 2a. Such an optical element was able to deliver a focal spot of 250 nm, as shown in the ptychographic reconstruction of figure 2b. This is a factor of two improvement in terms of spot size compared to previously achieved results.

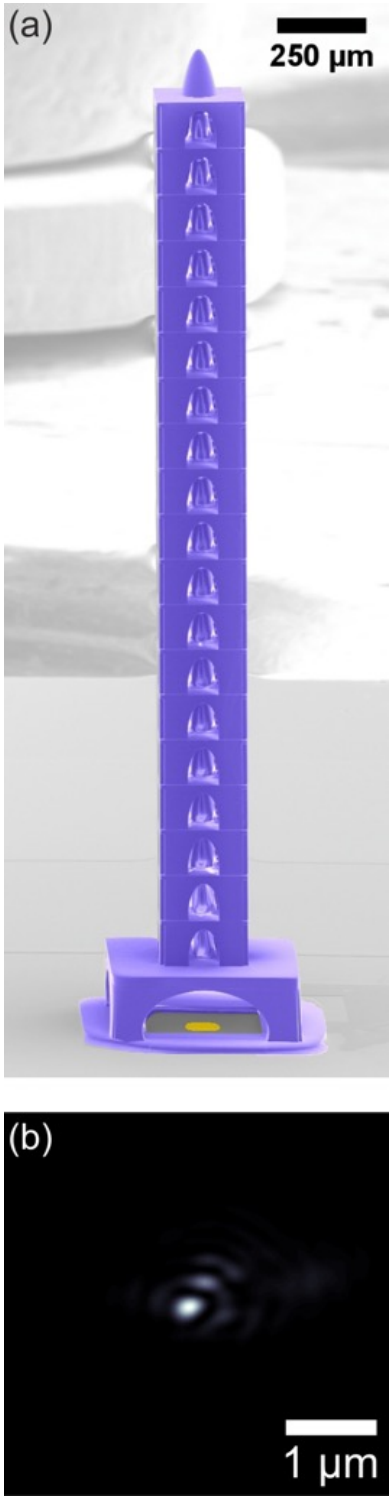

Fig. 2: a) Monolithic X-ray achromat (false color was added for visulatization purposes). b) X-ray focal spot of 250 nm delivered by the monolithic X-ray achromat.

Development of apochromatic X-ray focusing

Like for visible light optics, the achromatic X-ray concept can be extended to the apochromatic case. In particular, it can be realized by tuning the separation distance between the refractive and diffractive elements. To date, such a concept has been only theoretically proposed [2]. Using the same fabrication principles, we produced the required elements to implement the apochromatic X-ray focusing in synchrotron beamline. The focusing capabilities of the apochromat combination were then characterized by ptychography and scanning transmission X-ray microscopy. Figure 3 demonstrate the apochromatic behavior of assembled lens by showing the measured focal spot position (dots) in comparison with the expected curves (lines).

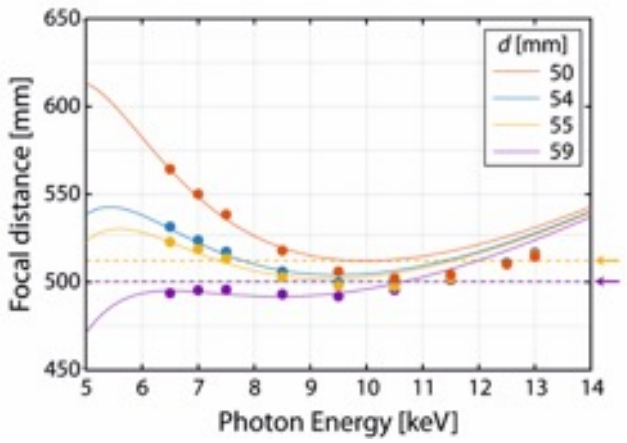

Fig. 3: Demonstration of apochromatic X-ray focusing. The experimentally measured position of the focus (dots) matches the theoretically expected position (curves).

Further developments of applications using an achromatic X-ray lenses

In further synchrotron experiments, we successfully demonstrated the use of an achromatic X-ray lens for full-field transmission X-ray microscopy. Several images of test samples were acquired at 7.5 keV photon energy. In addition, we also tested the feasibility of performing X-ray absorption spectroscopy using a monolithic X-ray achromat, which enables the acquisition of images at different energies without requiring a refocusing of the X-ray setup. Photon energies between 7.1 and 8.5 keV were used, covering the edges of iron, cobalt and nickel.

References

[1] Y. Wang, W. Yun and C. Jacobsen, Achromatic Fresnel optics for wideband extreme-ultraviolet and X-ray imaging, Nature 424, 50 (2003)

[2] H. N. Chapman and S. Bajt, High-resolution achromatic X-ray optical systems for broad-band imaging and for focusing attosecond pulses, Proc. R. Soc. A 477, 20210334 (2021)

[3] A. Kubec, M-C. Zdora, U. T. Sanli, A. Diaz, J. Vila-Comamala, C. David, An achromatic X-ray lens, Nat. Commun. 13, 1305 (2022)

Detectors to look inside cells

Project A16.04: HPDET-EM (University of Basel, Biozentrum, Paul Scherrer Institut, Dectris Ltd., Baden-Dättwil)
Project Leader: T. Maier
Collaborators: M. Er-Rafik, M. Chami, M. Steinmetz, H. Remigy, C. Schulze-Briese

Resolution breakthrough in electron microscopy

Electron microscopy is a well-established technique for the visualization of cryopreserved or metal-stained biological materials and has long been capable of delivering atomic resolution for radiation hard non-biological samples. However, when visualizing cryo-preserved biomolecules the resolution of visualization has typically remained at around 8 Å until the 2010s, even when combining information from hundred-thousands of individual regular particles in single particle analysis. Such limited resolution did not allow for deriving or refining atomic structural models and thus precluded obtaining detailed mechanistic insights into the biological process.

A series of technological advances then led to a breakthrough "resolution revolution" in biological cryo-electron microscopy [1]. Direct electron detectors allow recording movies at low-dose exposures with sub-second frame duration instead of still images. Such movies revealed strong electron beam-induced motions of the vitrified water layer and allowed for in silico motion tracking and correction. Novel refinement procedures for particle orientations based on Bayesian statistics provide better information extraction from noisy data. Altogether, over the past decade, cryo-electron microscopic single-particle analysis has developed into an efficient and favored method for high-resolution structure determination for larger proteins or protein complexes. Resolutions around 2.5-3.5 Å are now commonly achieved for non-symmetric biological macromolecules and are sufficient for deriving and refining atomic models of proteins, while record resolutions for symmetric assemblies are even approaching true atomic resolution at around 1 Å.

Electron Tomography for in situ cellular studies

To obtain high-resolution visualization of regular particles in single particle analysis identical particles are embedded in random orientations in a very thin layer of a vitrified aqueous solution. The particles are imaged by recording individual transmission electron microscopy projection images (or time-resolved movies) of different sample areas, each containing multiple individual particles, by horizontally scanning a flat sample. Three-dimensional information is reconstructed by back-projection from many individual particles.
Cellular structures require a different imaging approach for two reasons. First, cells and subcellular regions are non-regular and non-repetitive objects. Thus, combining information from different areas is not feasible and all information for three-dimensional reconstruction has to be collected for each sample volume. Second, most cells, and certainly more complex tissue samples, are too thick for imaging by transmission electron microscopy. Cells are typically in the micrometer size range, where limited transmission and secondary scattering of electrons degrade image quality.

Thin sectioning of cells and tissues is thus required for high-resolution in situ imaging of biomolecules [2]. Thin sections have traditionally been generated by ultramicrotome cutting but are most effectively generated in a controlled state with minimal artefacts and contamination by dual-beam microscopy for focused ion beam milling. Data collection is carried out in tomographic mode by taking a series of images for a single location of a vitrified thin section or milled lamella ad different tilt angles (Fig. 1).

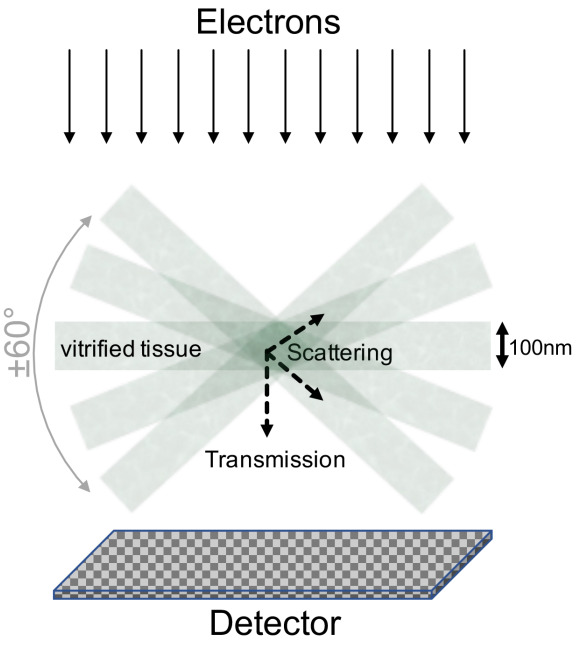

Fig. 1: Biological cryo electron tomography data are acquired by tilt-series imaging of thin sections of vitrified cells or tissue.

Collecting the highest quality tomographic tilt-series data is challenging as radiation damage over the entire data sets massively limits the total electron dose. For collecting optimal tilt series, this available total dose must be distributed over many images, resulting in a much lower electron dose per area per image as compared to single particle analysis. Additionally, tilting of the sample causes substantial variations in sample thickness and errors in sample alignment across the tilt series have to be corrected for. High-energy electrons accelerated at above 200 kV with sufficient transmission through the sample are required to image lamellae. As a consequence, optimal detector performance for noise-free data acquisition at 200 kV or above is crucial for biological cryo-electron tomography.

Novel detector technology for tomography

Replacing radiation sensitive film or charge-coupled device (CCD) cameras with direct electron detectors was a major contributor to the resolution revolution in cryo-electron microscopy. The detectors currently used in biological electron microscopy studies are direct electron detectors based on CMOS monolithic active pixel sensor (MAPS) technology, that detects partial energy loss of electrons passing through the sensor layer. They are characterized by small pixels large pixel numbers, up to 24 MPixels, and medium to high read-out and tolerated dose rates, and are optimized for measurements at high electron energy between 200 kV and 300 kV.
DECTRIS has developed hybrid-pixel detectors 3, based on a semiconductor pixelated sensor layer connected via bump-bonds to a layer of application-specific-integrated circuits (ASIC). Incoming electrons deposit their entire energy in the sensor layer, and the resulting electrical signal is transduced via the bump bonds to the ASIC. Hybrid-pixel detectors are currently the leading solution for biological X-ray crystallography. However, substantial adaptations are required for their efficient use in electron microscopy and in biological cryo-electron tomography in particular.

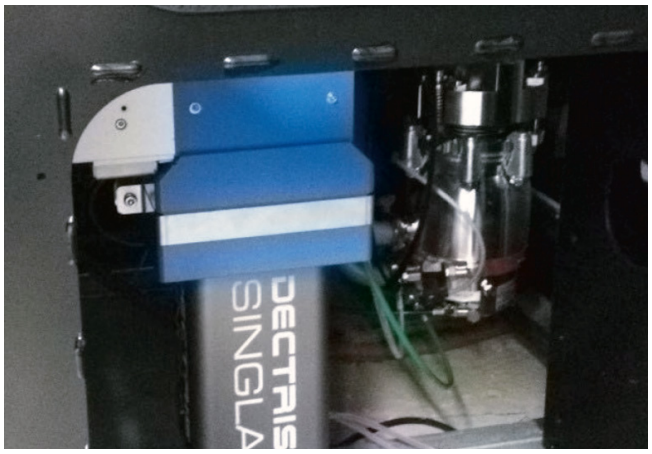

Fig. 2: DECTRIS detector mounted on a 200 kV cryo-electron microscope at the BioEM lab of Biozentrum.

Here, we aimed at testing a detector prototype and strategies for future application of hybrid-pixel detector technology to cryo-electron tomography of biological samples. The detector prototype uses the same bump-bond technology as in hybrid-pixel X-ray detectors, but has been specifically adapted for the challenges of cryo-electron tomography.
Key steps in this project were to develop samples for detector testing, to mount and connect the detector to a 200 kV electron microscope, to establish software control for successful data collection, to determine principal detector characteristics, to collect data on biological test samples and to evaluate these data by tomographic reconstruction. A particular emphasis is on analyzing the effects of the modular detector design with inter-module gaps.
The detector and related read-out electronics and computer have been installed on the Talos F200C microscope of the BioEM lab of University of Basel (Fig. 2) and instrument control and read-out were successfully established.

Cryo-electron tomographic data series have been collected for plunge-frozen biological samples with added gold nanoparticle fiducial markers (Fig. 3) and a workflow for data processing and tomographic reconstruction has successfully been established. We now continue to test the exploitation of the unique detector properties across different data collection schemes.

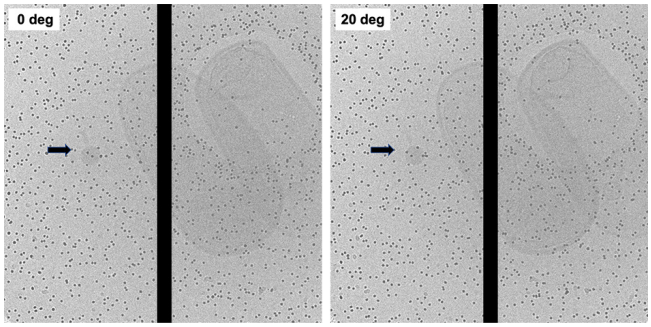

Fig. 3: Tomographic data collection. Slices of cryo-electron tomographic data collection at 0° (left) and 20° tilt (right) of E. coli and bacteriophage T4 (indicated by arrow) with gold nanoparticles.

The HPDET-EM project has now after a cost-neutral project extension, reached all central milestones. The results of this project now provide a first perspective on applications of hybrid-pixel detectors to biological cryo-electron tomography based on a detector prototype and they contribute to advancing novel technology for visualizing life at the molecular level in situ, as it happens inside cells and organisms.

References

[1] W. Kühlbrandt, The Resolution Revolution, Science 343, 1443 (2014)

[2] M. Turk and W. Baumeister, The promise and the challenges of cryo-electron tomography, FEBS Letters 594, 3243 (2020)

[3] A. Förster, S. Brandstetter and C. Schulze-Briese, Transforming X-ray detection with hybrid photon counting detectors, Philos. Trans. Royal. Soc. A 377, 20180241 (2019)

Peptide-hydrogel-patch for lesion coverage on oral mucosa

Project A16.05: Hydrogel-Patch (FHNW Muttenz, University of Basel, Universitäres Zentrum für Zahnmedizin Basel, credentis AG – vVardis, Windisch)
Project Leader: L. Kind
Collaborators: M. Bornstein, F. Schlottig, O. Germershaus, A. Venturato

Oral wounds in soft tissue can have various causes. They arise, for example, because of injuries, infections, or reduced immune reactions. In any case, the wounds cause pain when eating or speaking and thus impair the patients' normal oral function. Until now, the primary focus of therapy was on treatment of symptoms, which in most of the cases comprises the topical application of pain-reliving oral gels that are mixed with an anesthetic and/or with anti-inflammatory drugs. These gels only stick to the mucous membrane until the anesthetic has penetrated the wound area and then detach from the oral mucosa within minutes. If the anesthetics wear off, the gel must be applied to the affected area again. It is therefore a recurring process of only a short effective duration.

The elaborated hydrogels in this project, will protect the sensitive wound-area by adhesion as a patch for a longer time, still flexible enough to adapt smoothly to the mucosa surface, supporting the healing process, and being able to act as a drug delivery system.

In this work we considered to apply, a self-assembling synthetic peptide (derived from P11-family), that has already been established in other areas of oral medicine (guided enamel regeneration[1], desensitization, protection of natural teeth [2], bone regeneration [3], periodontal treatment [4] and periimplantitis treatment).

Peptides from P11-family served as a base hydrogel compound, which is either crosslinked or stabilized by a secondary hydrogel network, resulting in a hybrid material. For the sake of simplicity, the established hydrogels in this project, can be allocated to 3 representative groups (group A, B and C) and any addition to the P11-peptides are called modifiers (Fig. 1).

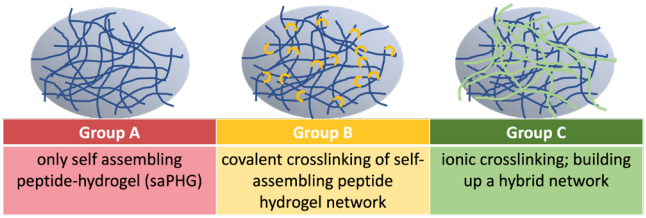

Fig. 1: Classification of the different hydrogel candidates.

These generated biocompatible hybrid hydrogels (Fig. 1), can vary in net-surface charge, have different assembling conditions, and can be combined with each other. Additionally, they can be physico-chemically modified to achieve and fine-tune the desired beneficial properties (Fig. 2). Potential candidates were tested with the specially optimized analytical methods in terms of the most important factors, like mechanical strength, adhesion performance, biocompatibility, and antimicrobial properties (Fig. 2).

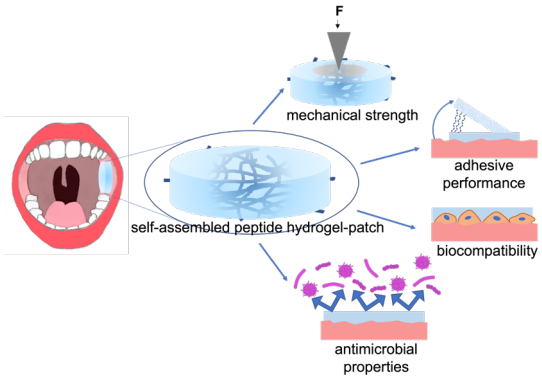

Fig. 2: Key requirements of a hydrogel for use as an oral mucosa patch.

Procedure, Results and Discussions

Within the first part of this project, we established hydrogels assigned to the previously mentioned groups based on their structure and composition (Fig. 1). Based on these groups, the analytical methods for characterization were optimized and evaluated (rheology, swelling ratio, biocompatibility and adhesion tests, and scratch tests). The results served as baseline, to determine trends about the influence of the physico-chemical modifications made to the established system.

Besides to the numerous advantages of unmodified hydrogels from group A (control), in terms of self-assembling conditions, biocompatibility, adhesion and drug-delivery potential, this hydrogel type suffers from the distinctive disadvantage of being liquified during application and handling and requiring a regeneration time for reassembly. This property should be improved by physico-chemical modification. Therefore, adjustments were made by changing modifier, adjusting concentrations (of modifier or peptide), or by applying new combinations of hydrogels (co-hydrogel mix). With the analytic set-up, the changed properties could be screened and could be placed in context with the desired properties.

Based on the rheological data (Fig. 3), a higher modifier concentration strengthens the hydrogel in texture, but it could be observed that the transition to the liquid system (break down of gel-like structure represented by the flow point (Fig. 3A) takes place already at lower shear stress with increasing modifier concentration (values of crossover of G` and G`` decreases (Fig. 3B)).

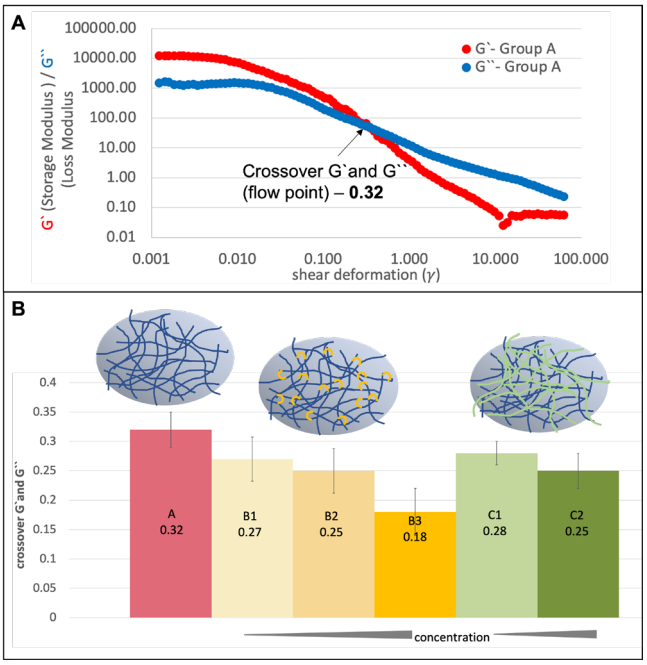

Fig. 3: A) Example of rheology data from group A to determine the crossover G`and G``(flow point). B) Comparison of crossover of the different groups (A, B, C) depending on the modifier-concentration within the group (B1<B2<B3 and C1<C2).

In addition, more ridged gels showed poorer adhesion to soft tissue (Fig. 4).

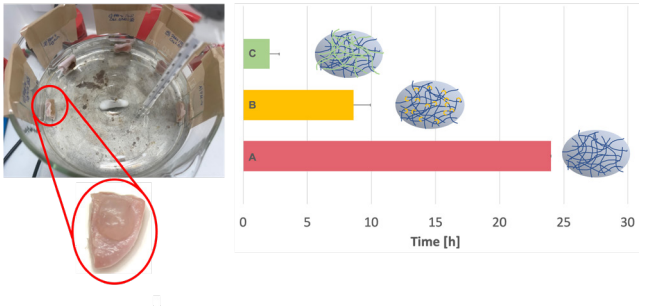

Fig. 4: Adhesion tests on pig tongue specimens. Left: pig tongue specimens with applied hydrogel are mounted to glass slides and attached to the glass bowl rim and immersed in PBS-buffer; stirring speed: 450 rpm; incubation time: 24 h. Right: The graph shows the time until detachment of hydrogels.

Conclusion was, to establish a hydrogel that has a stable texture, high crossover point, and good adhesion to soft tissue. Lignin-based hydrogels were expected to play an important role in biomaterials for tissue engineering and gene therapy [5] Since the positive properties of lignin [6] can be a suitable complement to our P11-peptides, promising lignin-co-P11-peptide hydrogels were produced and characterized.

Figure 5 shows the achieved shift to higher crossover points by lignin and the texture also met the requirements (homogeneous, soft, and flexible). Some optimizations and characterization still must be carried out here, but lignin-based co-hydrogels are already giving promising results.

Summary

It has been shown that the P11-peptide hydrogels without modifier already have very advantaged properties for use as a hydrogel-patch system. However, this type of hydrogel suffers from the major disadvantage of being liquified during application and handling and requires a recovery time for reassembling. With the appropriate modification, it is possible to avoid this disadvantage. The construction of a co-hydrogel network with lignin hydrogels in a biocompatible formulation shows immense progress in relation to the parameters mentioned for use as an oral hydrogel patch. Further analysis must be carried out for optimization and confirmation.

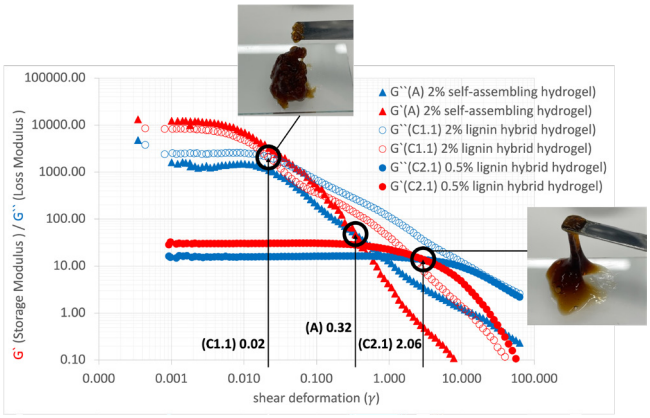

Fig. 5: Amplitude sweeps presented with shear stress plotted on the x-axis and storage modulus G' and loss modulus G'' plotted on the y-axis; bullets representing the crossover point of G`and G``. Triangle: self-assembling peptide (control); Bullets not filled: lignin biocomposite hydrogel with P11-peptide (2%); Bullets filled: lignin biocomposite hydrogel with P11-peptide (0.5%). The small inset images show the texture of the respective hydrogels.

References

[1] L. Kind, S. Stevanovic, S. Wuttig, S. Wimberger, J. Hofer, B. Müller, U. Pieles, Biomimetic Remineralization of Carious Lesions by Self-Assembling Peptide, J. Dent. Res. 96, 790 (2017)

[2] M. Schlee, F. Rathe, C. Bommer, F. Bröseler, L. Kind, Self-assembling peptide matrix for treatment of dentin hypersensitivity: A randomized controlled clinical trial, J. Periodontol. 89, 653 (2018)

[3] S. Saha, X. B. Yang, N. Wijayathunga, S. Harris, G. A. Feichtinger, R. P. W. Davies, J. Kirkham, A biomimetic self-assembling peptide promotes bone regeneration in vivo: A rat cranical defect study, Bone 127, 602 (2019)

[4] F. Koch, A. Wolff, S. Mathes, U. Pieles, S. S. Saxer, B. Kreikemeyer, K. Peters, Amino acid composition of nanofibrillar self-assembling peptide hydrogels affects responses of periodontal tissue cells in vitro, Int. J. Nanomedicine 13, 6717 (2018)

[5] E. Fortunati, W. Yang, F. Luzi, J. Kenny, L. Torre, Lignocellulosic nanostructures as reinforcement in extruded and solvent casted polymeric nano-composites, Euro. Polym J. 80, 295-316 (2016)

[6] S. Huang, S. Shuyi, H. Gan, W. Linjun, Facile fabrication and characterization of highly stretchable lignin-based hydroxyethyl cellulose self-healing hydrogel, Carbohydrate Polymers 223, 115080 (2019)

Microstructured degradable hydrogel-based periodontal LIGAment RE-COnstitution device

Project A16.07: LIGARECO (FHNW Muttenz, University of Basel, Klinik für Oral Health & Medicine, NovoNexile AG, Füllinsdorf)
Project Leader: J. Köser
Collaborators: K. Mukaddam, S. Kühl, S. Tugulu

Introduction

Peri-implant infections of osseointegrated implants represent a major concern in contemporary dentistry. The weak adhesion of soft tissue at the coronal part of the implant has been proposed as a potential risk factor for peri-implant infections [1]. Micro- and nanostructured implant collars have been tested as potential candidates to improve soft tissue adhesion. Despite encouraging preclinical results, none of the presented approaches has yielded a mechanically robust soft tissue organization with radially oriented collagenous periodontal ligament fibers found around natural teeth.
Within the presented project, we develop a regenerative device that mediates and guides the formation of radially oriented periodontal ligament bundles around the collar of dental implants. Radial channels within the device aim to orient fiber-producing periodontal ligament cells and guide collagen fiber production in a perpendicular and mechanically stable orientation around the implant surface. This arrangement may significantly improve the soft tissue strength and sealing around dental implants and render it comparable to healthy gingival tissues around natural teeth. The regenerative device is designed to be used as part of dental implant treatment (Fig. 1). While scientists ultimately aim to develop reconstituted periodontal ligaments for the bone-dental implant interaction [2], our approach aims to improve conventionally and commercially available osseointegrated dental implants by an improved ligament reinforced soft tissue attachment.

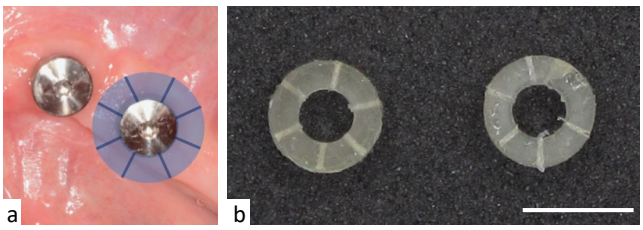

Fig. 1: a) Scheme of the location of the proposed device, which is placed around the upper part of the implant before wound closing, and b) sample devices prepared during the project. Scale bar: 8 mm.

Cell alignment in micro-channels has been investigated worldwide for basic research, and specific tissue engineering approaches like, e.g., neuronal lesion repair, tissue vascularization, or tendon regeneration. Cell colonization of such micro-channels in cell culture conditions is supported by using a cell adhesive biomaterial or coating the channel walls with adhesion molecules.

Within the presented project, we use an in-situ cross-linkable and biodegradable PEG-hydrogel for device fabrication. Multi-functional PEG precursors are combined and formulated to provide specific viscosities and polymerization kinetics that allow the fabrication of form-stable, patterned hydrogel templates with biological functionalities and degradation times that are specifically adjusted to the requirements of the targeted biological indication.

Cell colonization of micro-channels

Cells readily attached to biofunctionalized channeled hydrogels and, over time, colonized the micro-channels. There was no obvious preference for channel invasion versus cell growth on the outer hydrogel surface, and we assume colonization resulted from cell proliferation and expansion. In the previous reporting period, we analyzed channel diameters between 200 µm and 600 µm. We found that all microchannel invading cells formed monolayers on the channel sidewalls, resulting in a central lumen in the micro-channels (Fig. 2a). Although this lumen can be considered essential for transporting nutrients and factors from the surroundings to the cells, a massive ligament composed of ECM deposited by cells will most likely depend on additional cells spanning the central lumen. By decreasing the channel diameter towards 0.1 mm, although channel colonization was slowed down, we regularly observed cells spanning the central channel lumen (Fig. 2b). Alternatively, cells can potentially colonize the channel center if filled with a cell adhesive and cell-degradable biomaterial. The deposition of such material will be the focus during the project's final phase.

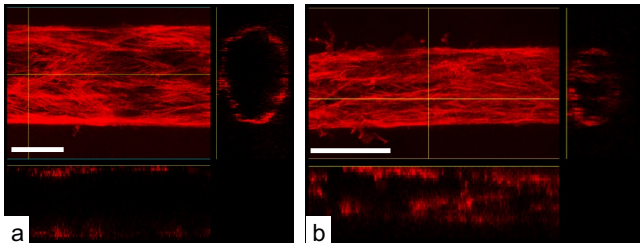

Fig. 2: Effect of micro-channel diameter on PDL cell colonization. Fluorescence micrographs of actin-stained PDL cells in microchannels of different diameters (top view and cross sections). PDL cells cover the walls of larger channels (0.2 mm, a), whereas in smaller channels (0.1 mm, b), additional micro-channel volume spanning cells are found. Scale bar: 100 um.

Cell alignment in patterned hydrogel channels

When cell orientation in structured micro-channels with templated line patterns was investigated, it turned out that fibroblast cells of different origins exhibited different sensitivity towards these guiding cues. Templates with relatively deeper lines (Rc = 1.45 +/- 0.27 µm) resulted in the alignment of immortalized rat2 fibroblasts as well as primary gingival fibroblasts and periodontal ligament (PDL) cells, whereas templates with less pronounced line features (Rc = 0.57 +/- 0.11 µm)

only induced orientation in the gingival fibroblasts and PDL cells (see also Fig. 3).

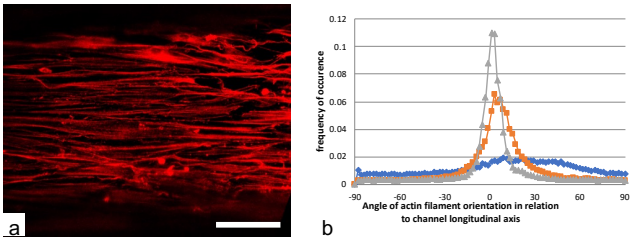

Fig. 3: Orientation of fibroblast cells in 0.4 mm channels. PDL cells align in micro-channels with minimal instructive line features (a, fluorescence micrograph of actin-stained PDL cells; and grey data in b) while rat2 fibroblasts require larger feature dimensions to induce cell orientation (b, blue graph minimal features, orange graph deeper features). Scale bar: 100 µm.

ECM deposition of primary cells

ECM deposition in cultured cells is generally very low compared to living tissues. The low deposition has been partly attributed to the high dilution of the synthesized ECM constituents in cell culture medium. It has been demonstrated in certain cell systems to increase by synthetic and natural polymers, which induce molecular crowding. When culturing the cell systems used within the project, the ECM deposition of PDL cells and gingival fibroblasts could be increased by a factor of 2-3 by adding ascorbic acid and the molecular crowder carrageenan. In contrast, the ECM deposition of rat2 fibroblasts was not responsive towards these two effector molecules (Fig. 4).

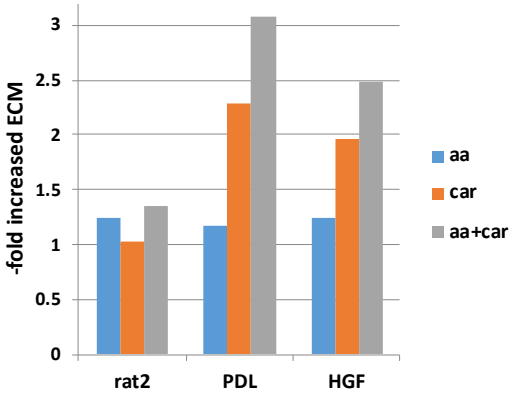

Fig. 4: Effect of ascorbic acid and carrageenan on ECM production of cultured rat2, PDL and gingival fibroblast cells. Cells were cultured under standard conditions or in the presence of ascorbic acid (aa) and carrageenan (car). Subsequently, cell cultures were decellularized, and the ECM deposits were quantified compared to standard culture conditions.

Alternative device fabrication by micro-molding

The final project phase will address alternative and upscalable micro-channel fabrication methodologies using optimized biofunctionalization strategies to enhance cell invasion of the periodontal ligament reconstituting device. Micro-molding is applied to manufacture channel templates embedded in PEG-hydrogels – produced from sacrificial or biodegradable materials that allow cell invasion in the templated micro-channels. Preliminary results from the first experiments with microgrooves templated within PEG-hydrogels appear to confirm this assumption.

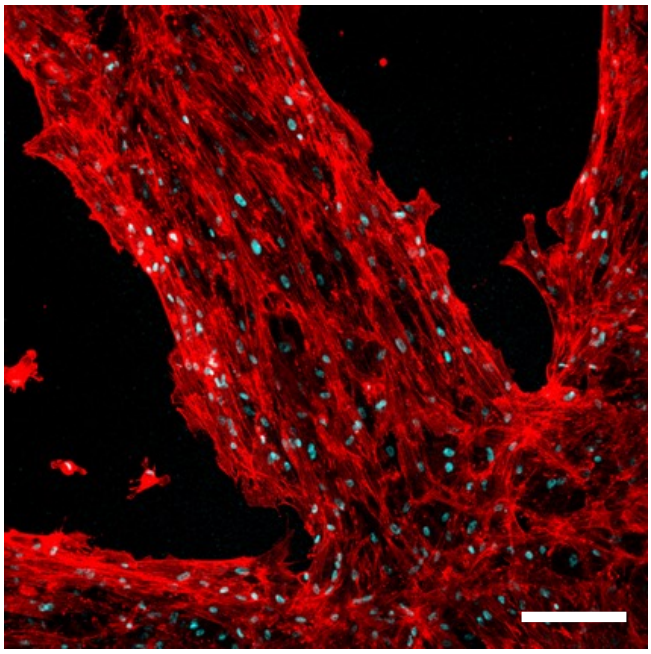

Fig. 5: Primary periodontal ligament cells cultured on PEG hydrogels templated with a micro-molded pattern. Cells were stained with rhodamine-phalloidin and DAPI to detect the actin cytoskeleton and nuclei. Scale bar: 200 µm.

Summary and outlook

In the LIGARECO project, we developed a micro-channeled and biodegradable PEG-hydrogel-based device to reconstitute periodontal ligament fibres following dental implant placement. Biofunctionalization strategies were introduced, which enabled cell invasion of templated micro-channels and the orientation of the cells along the longitudinal channel axis. ECM deposition of the relevant cell population was determined, and alternative, upscalable fabrication strategies were investigated. Future experiments applying animal models shall determine cell invasion timelines in vivo and allow for selecting degradation time-optimized PEG-hydrogel precursors. The methods developed within the project lay the basis for further applications of biodegradable PEG-hydrogels in tissue engineering and regeneration.

References

[1] I. Atsuta, Y. Ayukawa, R. Kondo, W. Oshiro, Y. Matsuura, A. Furuhashi, Y. Tsukiyama, K. Koyano, Soft tissue sealing around dental implants based on histological interpretation. JPR 60, 3–11 (2016)

[2] M. Gulati, V. Anand, V. Govila,N. Jain, P. Rastogi, R. Bahuguna, B. Anand, Periodontio-integrated implants: A revolutionary concept. Dent Res J (Isfahan) 11, 154–162 (2014)

Acknowledgement: The help of the SNI Nano Imaging Lab with the characterization of the structured channel templates is gratefully acknowledged.

Nanocompass: A nanoscale magnetometer

Project A16.10: Nanocompass (FHNW Muttenz, FHNW Windisch, Camille Bauer Metrawatt AG, Wohlen)
Project Leader: J. Pascal
Collaborators: H. Nicolas, A. Inderbitzin, J-B. Kammerer, R. Sousa, S. Gorenflo, M. Ulrich

Introduction

Magnetic sensors are ubiquitous in consumer, automotive, industrial, and medical electronics. Among the very popular types, we find Hall effect sensors and magnetoresistive sensors, which are both available as low-cost integrated circuits. Whereas Hall sensors exhibit high dynamic ranges, magnetoresistive sensors exhibit high magnetic resolution. In parallel, the development of magnetic random-access memories (MRAMs) massively progressed over the past decades and benefits from a strong interest from major semiconductor companies (e.g. Samsung, Intel, TSMC, IBM). MRAMs are mainly based on nanometric devices called spin transfer torque magnetic tunnel junctions (STT-MTJs). In this context, this project aims to divert STT-MTJs and use them as magnetic sensors resulting in sensor's dimensions smaller than anything ever reported, while offering low cost and high resolution.

Magnetic Tunnel Junctions (MTJs)

The devices used in this project are cylindrical structures with both diameter and height of 50 to 100 nm. They are made of multiple layers to achieve the key properties of MTJs. The core layers of such junctions consist in two ferromagnetic layers (FeCoB) of 1 to 2 nm thickness. These layers are separated by a thin layer of oxidized magnesium (MgO) with a thickness of 1 to 2 nm. This results in a pillar where several quantum effects can be observed such as tunnel magnetoresistance (TMR), quantum tunneling or the spin transfer torque (STT). As an overall result, the MTJ can be seen as a magnetoresistance with two different values only, depending on the relative orientation of the magnetization of the two ferromagnetic layers. In the same direction, parallel (P), the resistance is low whereas in the opposite direction, antiparallel (AP), the resistance is high. The ratio between the two states is called the TMR ratio and typically ranges from 50% to 120%.

Sensor principle

To change the state of a MTJ between P and AP, a specific voltage should be applied across the device, called the critical voltage (AP→P and P→AP). The polarity of the voltage defines the state (AP or P) in which the MTJ will be set. However, the critical voltage is not only related to the stack of the junction but also to external parameters such as the external magnetic field. Hence, by tracking the evolution of the critical voltage, one can directly track the evolution of the external magnetic field (Fig. 1).

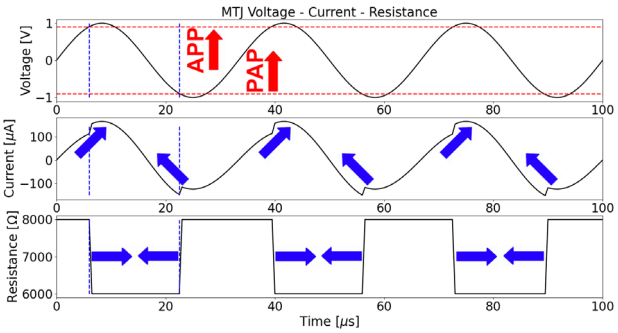

Fig. 1: Sensor principle, showing the voltage, current and resistance of the MTJ. The red and blue arrows indicate how the signals are changing for an increasing external magnetic field.

To achieve this, a 200 kHz triangular signal with an amplitude of ± 1.6 V is applied across the MTJ. When the voltage reaches the critical voltage, the resistance of the junction suddenly changes. To detect the changes, the current through the MTJ is continuously measured using a simple shunt resistor. The resulting signal exhibits discontinuities that can be detected by applying this signal through a high-pass filter. At the output, one can obtain short pulses corresponding to the reversal events. At this point, the magnetic field information is stored in the time between each pulse. We then reconstruct a pulse width modulated (PWM) signal that can be filtered into a dc signal using a low pass filter. The average value of this dc signal therefore follows linearly the variations of the external magnetic field. Finally, an analog-to-digital converter is used to digitize the voltage signal (Fig. 2).

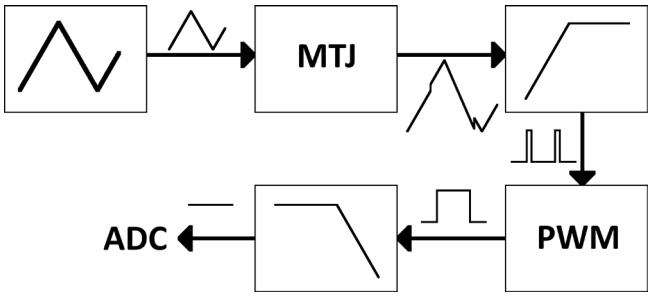

Fig. 2: Signal processing schematic.

Experimental results

The MTJs used in this project were fabricated on standard 4" wafers which contain up to 20,000 MTJs. Each junction is accessed using a custom probe to connect the top and bottom

electrodes of the MTJ to the signal processing electronics, which is currently implemented in a discrete version on a printed circuit board (PCB). The wafer is then placed within a Helmholtz coil that generates a vertical magnetic field along the sensing axis of the MTJs, that is perpendicular to the wafer. With the present setup, the field strength can reach up to ± 8 mT (Fig. 3).

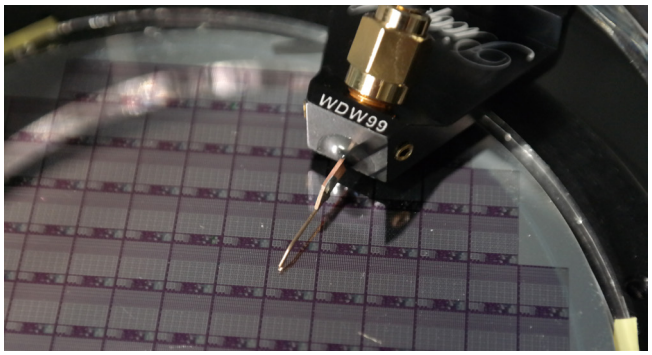

Fig. 3: Wafer (i.e., MTJs) under test

Using the detailed sensor architecture, test setup and the presented MTJs, we could extract the key properties of the sensor [1]. We report a sensitivity of 11.59 mV/mT (Fig. 4) with an integral nonlinearity error of 2.06% FS (full scale). A rms (root mean square) noise of 145 µT is achieved with a sampling rate of 400 Hz (Fig. 5). The measured noise power spectral density is 13.7 µT/√Hz. The dynamic range of these MTJs can be as high as ± 46 mT.

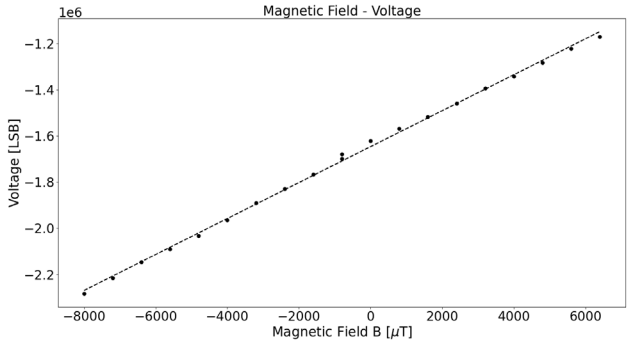

Fig. 4: Measured output sensitivity [1]

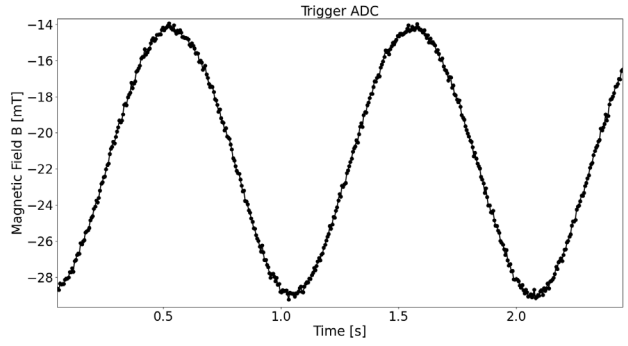

Fig. 5: Measured 1 Hz, 16 mT sine wave magnetic field [1]

Discussion

While the reported performances of the sensor are comparable with published magnetoresistive sensors of similar dimensions, the measured noise level is still higher than commercial sensors. This difference is due to both the intrinsic stochasticity of the junction and the large sensing element sizes implemented in the commercial chips and which reduce their noise. This unavoidable probabilistic property of MTJs creates a white noise in the measurements, which needs to be averaged to be reduced. In addition, different studies [2] show that the noise of MTJs increases with the reduction of the size. Therefore, the development of dedicated MTJs and an in-depth analysis of the stochasticity of the junctions are still required to reduce the noise level and to establish a complete model of the sensing unit.

Conclusion

With this project, we successfully demonstrated the implementation of a nanoscale spin transfer torque magnetic tunnel junction as a magnetic sensor. We report sensing element sizes as low as 50 nm, making them among the smallest ever reported. The tested MTJs were originally designed for MRAM applications, making them fully compatible with monolithic integration. In addition, the electronics required to operate the MTJ as a sensing unit is compact, simple and uses only CMOS components. This makes the complete system fully compatible with CMOS integration. With the improvements of the electronics, as well as the optimization of the stack for sensing applications, the performances of the sensor should be improved. This sensor can have applications in different domains ranging from medical systems to physics experiments and industrial applications.

References

[1] H. Nicolas, R. C. Sousa, A. Mora-Hernández, I.-L. Prejbeanu, L. Hebrard, J.-B. Kammerer, and J. Pascal, A Magnetic Sensor Based on a Nanometric Spin Transfer Torque Magnetic Tunnel Junction Suitable for Monolithic Integration, 2022 IEEE Sensors (2022)

[2] Z. Q. Lei, G. J. Li, W. F. Egelhoff, P. T. Lai, and P. W. T. Pong, Review of Noise Sources in Magnetic Tunnel Junction Sensors, IEEE Transactions on Magnetics (2011)

Blue laser diode pumped Ti:Sapphire sub-100 fs laser amplifier for nanomachining

Project A16.11: NanoLase (FHNW Windisch, Paul Scherrer Institut, TLD Photonics AG, Wettingen)
Project Leader: B. Resan
Collaborators: D. Hug, A. Trisorio, A. Dax, R. Carreto

Introduction
The workhorse for most of demanding laser applications are femtosecond lasers based on Titanium doped Sapphire (Ti:Sa) gain medium. The main drawback up to now is the absence of direct diode pumping scheme enforcing the use of Q-switched, nanosecond solid-state laser (e.g. Nd:YAG) as pump laser source. This leads to very inefficient optical pumping and a large purchasing and maintenance cost for such systems, the later prohibiting the spread of Ti:Sa lasers in wider industrial applications. In this project, we aim to develop a high average power, 100-µJ energy level, sub-100 fs Ti:Sa laser amplifier, based first, on recently available high power blue diodes at 450 nm, and second, on a novel Single Crystal Fiber (SCF) geometry. The SCF geometry will increase couple of times the laser average power, due to superior cooling capability. The direct diode pumping will increase wall-plug efficiency by ~10 times (wall-plug efficiency ~5% versus typical ~0.5%). It will also make the laser much more compact and reliable. In addition, we will design a wavelength conversion stage (second harmonic generation - SHG) to obtain blue fs pulse at 400 nm. We will perform first material processing tests with this novel laser with blue beam suitable for metal nanomachining and IR for polymers. Couple of times shorter pulses, compared to currently commercially available, and high-power blue lasers, should enable us to make a breakthrough in laser materials processing and move from micro to nanomachining, with high throughput.

Experimental Setup
The regenerative amplifier is pumped by a pulsed, fiber-coupled laser diode, emitting 20 W at 450 nm. The pump beam (Fig. 1, (1)) is focused through a dichroic mirror (2) into the Ti:Sa crystal (3) at a diameter of 70 µm. The horizontally polarized seed pulse (4) is entering the regenerative amplifier cavity through a thin film polarizer (5). The polarization of the seed pulse is rotated by 90 degrees, using a quarter-wave plate (6) and Pockels cell (7). Now, the vertically polarized seed pulse is locked inside the cavity between the end mirrors (8, 9) and is amplified each time it passes through the pumped Ti:Sa crystal. Two curved mirrors with a focal length of 100 mm (10, 11) are used to achieve the cavity stability and a proper size of seed and pump beams inside the Ti:Sa crystal. In order to reach enough amplification, the seed pulse has to pass the Ti:Sa crystal several times before its polarization is rotated by 90 degrees again and is coupled out via the thin film polarizer.

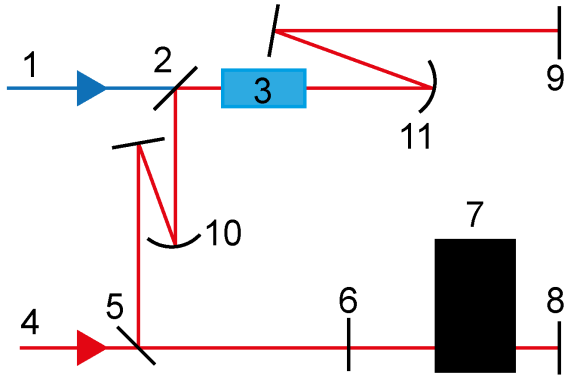

Fig. 1: Schematic setup of the regenerative amplifier.

Small Signal Gain Measurement
A single pass of the seed laser through the pumped Ti:Sa Crystal is used to measure the small signal gain (SSG) of the regenerative amplifier. The SSG is detected with a photodiode and verified by a high sensitivity power meter. By optimizing the overlap of seed and pump laser as well as the pump pulse duration, SSG reaches over 30% (Fig. 2), which is sufficient to compensate the losses of approximate 10 % inside the cavity and amplify the seed pulse in a few ten passes through the pumped crystal.

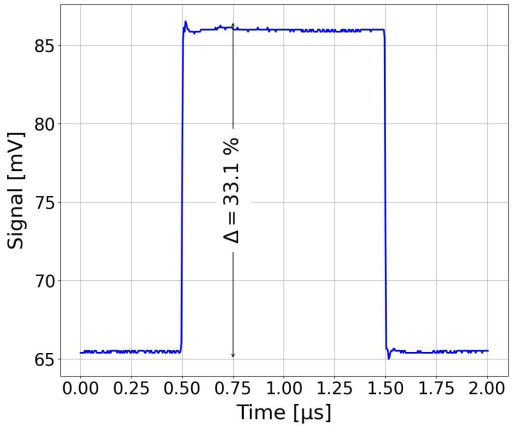

Fig. 2: Averaged SSG signal @ 1 µs pump pulse width.

Thermal Management
To keep the thermal load (Fig. 3) inside the crystal at a minimum, the shortest possible pump pulse width is used. This pulse duration is defined by the number of passes of the pulse through the crystal or the time the pulse remains in the cavity.

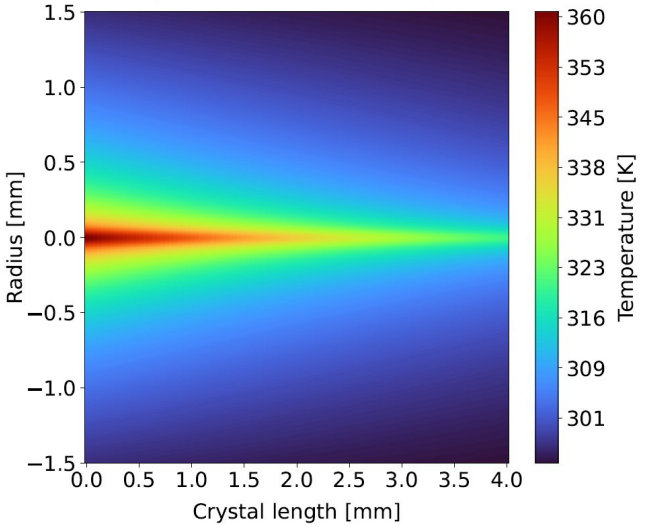

Fig. 3: Temperature distribution through pumped Ti:Sa crystal.

Stability Simulations

To ensure minimal losses and stable regenerative amplifier cavity, Gaussian mode stability simulations were run (Fig. 4). The simulations are used to optimize beam diameters inside the Ti:Sa crystal and Pockels cell. It was also made sure that no modes higher than the fundamental mode were excited.

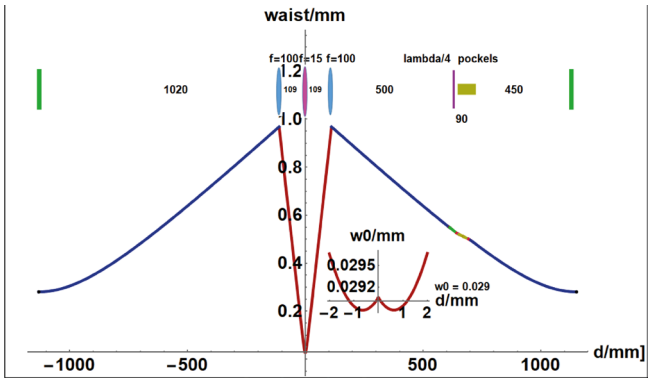

Fig. 4: Stability simulation of regenerative amplifier cavity.

Results

We could show that a direct blue laser diode pumped Ti:Sa regenerative amplifier is feasible. By optimizing the overlap of the seed and pump beam, a small signal gain of over 30% could be demonstrated. The measurement of the average power with a high sensitivity power meter showing an increase of 40-50 µW correlate very well with the measured small signal gain at the photo diode and the modulated pump laser with a pulse width of 1 µs at 1 kHz. With the modulation of the fiber coupled blue laser diode, the overall thermal load inside the crystal was minimized which leads to a more stable and more efficient operation of the regenerative amplifier. We finished design the regenerative amplifier cavity and acquired all needed components to build it.

Outlook

With the completion of the feasibility measurements, we are ready to assemble and operate the already fully designed regenerative laser amplifier (Fig. 5) starting at kHz and move towards MHz regime. Subsequently, with this blue diode pumped Ti:Sa amplifier, we will perform the material processing trials, first micro-machining, and then nano-machining.

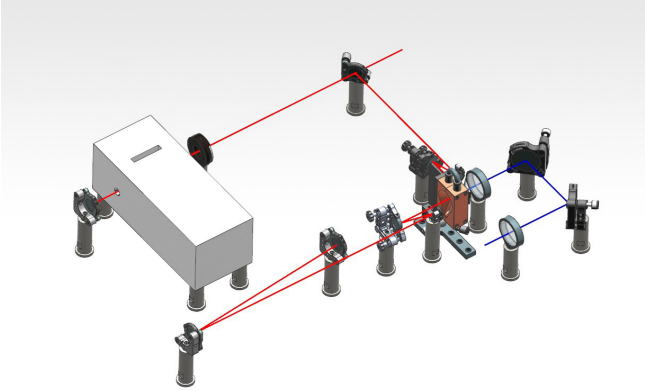

Fig. 5: Regenerative amplifier setup

References

[1] A. Rohrbacher, O. E. Olarte, V. Villamaina, P. Loza-Alvarez and B. Resan, Multiphoton imaging with blue-diode-pumped SESAM-modelocked Ti:sapphire oscillator generating 5 nJ 82 fs pulses, Opt. Express 25, 10677 (2017)

[2] S. Backus, M. Kirchner, R. Lemons, D. Schmidt, C. Durfee, M. Murnane, and H. Kapteyn, Direct diode pumped Ti:sapphire ultrafast regenerative amplifier system, Opt. Express 25, 3666 (2017)

Combinatorial nanoparticle design for therapeutic drug delivery across the blood brain barrier

Project A16.12: NANOthruBBB (FHNW Muttenz, University of Basel, Pharmaceutical Technology, Perseo Pharma AG, Muttenz)
Project Leader: P. Shahgaldian
Collaborators: C. Wu, N. Santacroce, L. Suter-Dick, N. J. Roos, J. Huwyler, E. Laprevotte, Y. Dudal

Introduction

Therapeutic biomacromolecule delivery to the brain is hindered by the blood-brain barrier (BBB), a complex cellular filter protecting the central nervous system from blood-borne pathogens. Despite the benefits biological drugs (i.e., biologics) have achieved in treating a wide range of diseases including cancer and autoimmune diseases, they have thus far minor impact on pathologies where the therapeutic target is in the brain [1]. This is for example the case for lysosomal storage diseases (LSDs) that arise from inherited lysosomal dysfunctions caused by deficient enzymes and/or membrane proteins. While enzyme replacement therapies (ERTs) are currently frontline treatments of LSDs, they fall short when it comes to deliver therapeutic lysosomal enzymes through the BBB. Consequently, more than two-thirds of LSD patients treated with ERTs suffer from progressive and severe central nervous system dysfunctions [3]. In order to overcome the major stumbling block that the BBB represents for the delivery of biologics to the brain, a variety of nanoparticulate drug carrier systems have been designed and several targeting moieties that favor their transport through the BBB have been identified [2]. The foremost objective of Nano-thru-BBB was to apply a novel surface combinatorial chemistry approach to produce a large range of nanoparticulate systems and to systematically study their ability to cross the blood brain barrier in vitro (cultured brain endothelial cells) and in vivo (zebrafish embryos). The results gathered in the frame of this project represent a solid basis for Perseo Pharma to develop a novel class of nanomedicines capable of safely delivering enzymatic activity to the brain for the treatment of LSDs.

Combinatorial nanoparticle surface modification

A combinatorial surface modification method was developed and applied to produce a series of NP systems with varying surface functionalities. We used both simple ligands containing carboxy-, hydroxyl- and amino-functions, to modulate the surface chemistry of the NPs, as well as more complex ligands containing glucose, transferrin, transferrin receptor-targeting peptide (T7 peptide) or a cell-penetrating peptide (HIV TAT peptide). A series of 30 different types of NPs were produced and microscopically characterized.

In vitro screening of BBB transport properties of surface-modified NPs

To study the capability of the combinatorially modified NPs to cross the BBB, we first worked with an in vitro model system. Human brain endothelial cells (hCMEC/D3) were cultured on tissue culture plastic or onto semipermeable membranes in transwell inserts, to test cytotoxicity, cell uptake and transcytosis of NPs. Cytotoxicity assessment (Fig. 1A) showed that cells remain viable with a minor (< 20%) loss of viability after incubation with all tested NPs at concentrations up to 200 µg/ml. The screening of cellular uptake and NP permeance was performed with NP concentrations of 100 µg/ml. As shown in figure 2B, NPs modified with glucose, transferrin and carboxy-, amino-functions exhibited a statistically significant enhanced internalization. Similarly, these NPs showed better transcytosis through the BBB, based on their ability to cross the cell barrier (permeance).

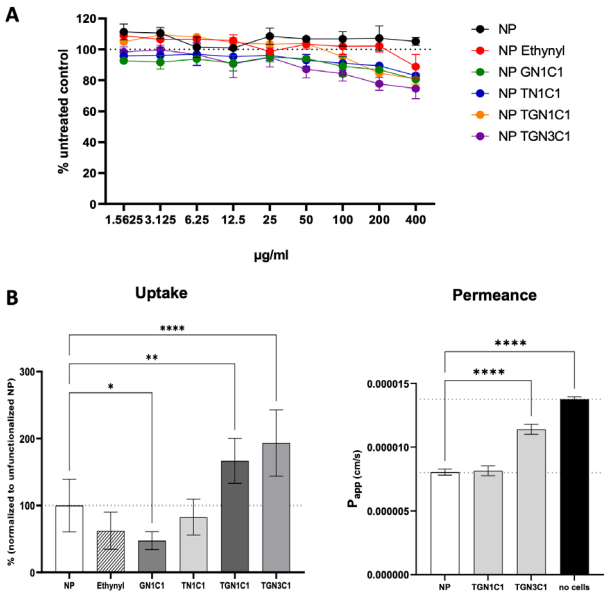

Fig. 1: A) Cytotoxicity assay. Cells were treated for 24 h with a NP concentration between 0 - 400 µg/ml. Cell viability was evaluated with the detection of intracellular ATP (n=3). B) Uptake and permeance of different surface-modified NP constructs (T, G, N and C refer to modification with transferrin, glucose, amino- and carboxy-functions; numbers indicate the molar ratio between amino- and carboxy-functions) applied to D3 cells. Uptake was quantified on 96-well plates after 1 h incubation at 37°C with 100 µg/ml NPs. Permeance of NP was tested on a transwells supporting a tight endothelial (D3) monolayer that hindered the passage of Dextran Texas Red (5 µg/mL, 3 h) co-administered with 100 µg/ml NPs.

Mechanisms of cellular uptake and processing

To further investigate the effects of chemical functionalities at the NPs surface on targeted delivery, the internalization of NPs was analyzed after D3 cells were treated with competitors to the transferrin receptor (recombinant transferrin) or the glucose transporter GLUT1 (BAY 876) (Fig. 2). Our results show that only the internalization of NPs bearing transferrin functional moieties decreased after competition with transferrin. In the same manner, only the internalization ratio of NPs bearing glucose moieties decreased after pre-treatment

with BAY867. This set of data confirms that chemical functionalities at NPs surface mediate receptor-dependent endocytosis.

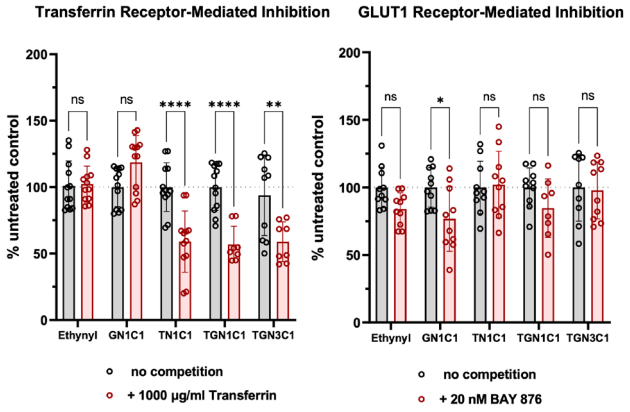

Fig. 2: Cellular uptake of surface-modified NPs in the presence or absence of competitors. For competition experiments, cells were treated for 1 h with 20 µg/mL NPs in the presence or absence of unlabeled transferrin, or GLUT1 ligand (BAY 876). The quantification of internalized NPs was determined with image analysis (NP area per cell). Plotted data are normalized to condition without competitor (N=10).

Further, the lysosomal escape ability of NPs exhibiting enhanced cellular internalization was investigated as this is required for successful transcytosis. After incubation with the surface-modified NPs, the colocalization of NPs and lysosomes within the cells was analyzed and expressed as Manders' overlapp coefficient (MOC). The results depicted in figure 3 reveal that NPs without functionalization remained trapped into the lysosomes. Glucose and amine functional groups facilitate lysosomal escape, whereas transferrin modifications were less efficient (higher MOC).

In vivo experiments carried out on a zebrafish model have confirmed the possibility to track fluorescently labeled SNPs in the fish embryo. This model will be used for further testing of Perseo nanomedicines targeting the central nervous system.

Conclusion and outlook

In Nano-thru-BBB, we developed a novel method allowing a combinatorial modification of NPs. This method has been applied to produce NPs displaying different chemical moieties at their surface in a stoichiometric manner. In vitro testing of surface modified NPs on human brain endothelial cell model (D3) demonstrated that NPs, up to 200 µg/ml, do not induce relevant cytotoxic effects.

The formulations with specific modifications (transferrin, glucose, and amine) on NPs significantly enhanced the internalization (endocytosis) and permeance (transcytosis) of NPs. In addition, investigations on the internalization of the NPs with specific chemical functionalities demonstrated that specific functionalization led to receptor-dependent endocytosis. Although the underlying mechanisms of endocytosis and transcytosis require further investigations, our data demonstrate that chemical functionalization of NPs promotes BBB transcytosis by facilitating lysosomal escape. Moreover, the developed methods can be applied for the screening of additional modified NPs.

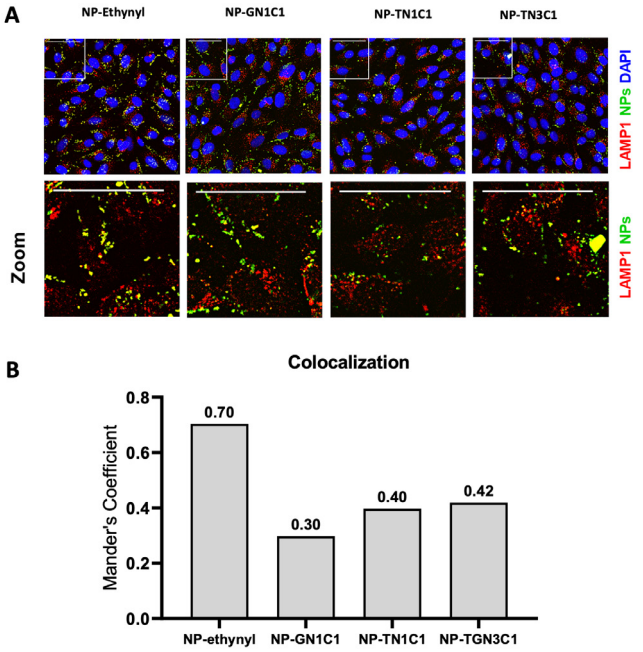

Fig. 3: A) Immunofluorescence detection of nuclei (blue), lysosomes (LAMP1, red) and NPs (green). For the detection of NPs and lysosomes (LAMP1), cells were fixed and stained using immunofluorescence (Alexa 488 (NPs), Alexa 647 (LAMP1)). Images were taken with a laser scanning confocal microscope using the 40x objective. B) Manders' Overlapp Coefficient (MOC), of different NP constructs. A factor of 1 means 100% overlap.

References

[1] A. Villabona-Rueda, C. Erice, C. A. Pardo, M. F. Stins, The evolving concept of the blood brain barrier (BBB): from a single static barrier to a heterogeneous and dynamic relay center, Front. Cell. Neurosci. 13, 405 (2019)

[2] S. Ding, A. I. Khan, X. Cai, Y. Song, Z. Lyu, D. Du, P. Dutta, Y. Lin, Overcoming blood–brain barrier transport: advances in nanoparticle-based drug delivery strategies, Mater. Today 37, 112–125 (2020)

[3] F. M. Platt, A. d'Azzo, B. L. Davidson, E. F. Neufeld, C. J. Tifft, Lysosomal storage diseases, Nat. Rev. Dis. Primers 4, 27 (2018)

[4] M. R. Correro, N. Moridi, H. Schützinger, S. Sykora, E. M. Amman, E. H. Peters, P. F.-X. Corvini, P. Shahgaldian, Enzyme shielding in an enzyme-thin and soft organosilica layer, Angew. Chem. Int. Ed. 55, 6285 (2016)

PEPS: Printed Electrochemical Protein Sensor

Project A16.13: PEPS (CSEM Allschwil, CSEM Landquart, FHNW Muttenz, MOMM Diagnostics GmbH, Basel)
Project Leader: F. Kurth and M. Zinggeler
Collaborators: S. Generelli, L. Burr, D. Meinel, M. Wipf

Introduction
The PEPS project aims at the development of an electrochemical protein sensor for the ultra-sensitive quantification of proteins of relevance for the diagnosis of preeclampsia in a point-of-care (POC) system. The target protein to be quantified electrochemically is the placental growth factor (PlGF) present in whole blood. For this, the electrodes do not only need to measure specifically a single protein within a solution containing high concentrations of a plethora of other proteins but at the same time have to overcome surface fouling limiting the electrochemical measurement. Optimally, the developed electrodes are incorporated into a system, which allows a non-user biased operation including sample preparation, very similar to a lateral flow assay. In addition to PlGF, the detection of another protein (s-Flt1) reflecting the disease progression of preeclampsia is required, which will in the future need to be quantified simultaneous to PlGF for an accurate diagnosis.

Nanocomposite electrode immunoassay
In 2021, first achievements could be accomplished regarding the development of electrodes with an anti-fouling surface functionalization that at the same time allows for excellent charge transfer [1]. This could be achieved by the incorporation of carbon nanotubes into a photoreactive copolymer. The coated electrodes could withstand protein adsorption for at least 1 hour while preserving the electroactive surface charge compared to blank electrodes measured in protein-free solution.

This year, we continued the characterization of those functionalized electrodes, and developed a highly sensitive immunoassay electrode system [2]. For this, the previously designed anti-fouling but conductive coating was only partially cured and capture antibodies targeting c-reactive protein (CRP) were deposited onto this functional layer. After complete photocuring, the functional electrodes could be employed for a CRP immunoassay in blood serum (Fig. 1). The test results achieved a high sensitivity with a limit of detection (LOD) of 3.1 ng/mL and a limit of quantification (LOQ) of 11.9 ng/mL, thereby substantiating the great potential of the developed system for protein quantification in complex samples for the clinics. Despite their high sensitivity and selectivity, the developed electrodes are cheap in production due to a combination of screen-printing and liquid deposition, both highly scalable in production.

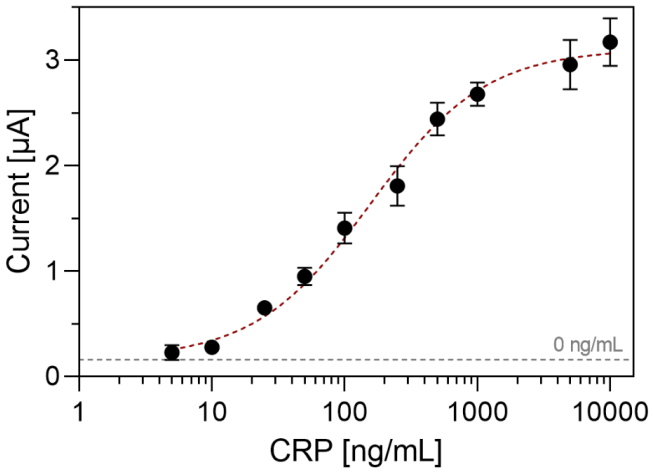

Fig. 1: Calibration curve of the electrochemical immunoassay for CRP measured for pure CRP-free serum samples spiked with increasing CRP concentrations. The grey dashed line marks the current measured in CRP-free serum samples (negative control). The figure is taken from Zinggeler et al. with permission [2].

Protein assay development for PlGF and sFlt-1
FHNW and MOMM have developed Enzyme-Linked Lateral Flow ImmunoAssays (ELLIFAs) for the preeclampsia biomarkers PlGF and sFlt-1. Using enzymatic amplification, we could demonstrate an improvement in analytical sensitivity of more than 60-fold compared to conventional Lateral Flow Assay (LFA) technology (Fig. 2). The ELLFIA assays were then transferred to the electrochemical sensor development by CSEM.

The electrochemical determination of PlGF was performed using a solution made by premixing the PlGF with biotinylated polyclonal detection antibody (dAb-biot) and the horseradish peroxidase-streptavidin conjugate (HRP-strep) in buffer. The solution was quickly mixed, successively left quiescent for 10 min, and then dispensed onto the working electrode (WE). The immunoreaction between the WE-immobilized capture antibody (cAb) and the PlGF occurred for 10 min. After this incubation time, the solution was dried by gently applying a cellulose absorbent pad to the sensor. Finally, the 3,3',5,5'-Tetramethylbenzidine (TMB) and hydrogen peroxide (H_2O_2) enzymatic substrate solution was dropped onto the sensor surface, and the amplification reaction occurred. The electrochemical readout is obtained by applying a potential difference for 1 min between the WE and an Ag/AgCl pseudo-reference electrode, and the current value was taken at 59 seconds.

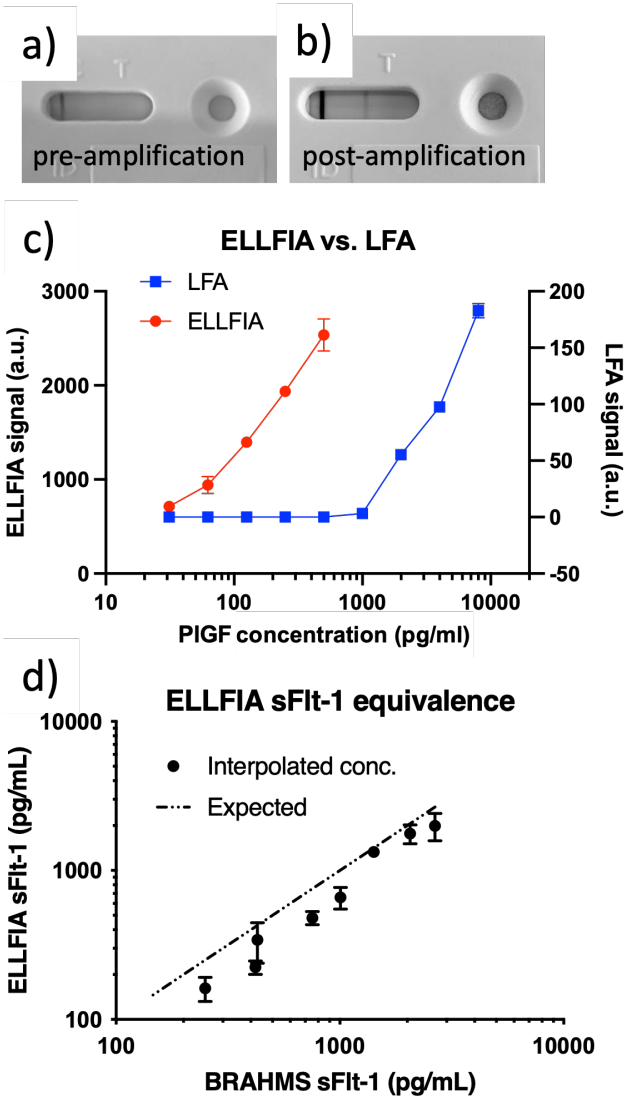

Fig. 2: Enzyme-Linked Lateral Flow ImmunoAssay (ELLFIA) significantly improves the analytical sensitivity of a rapid test. The limit of detection of conventional LFA technology using gold nanoparticle labels and a) pre-amplification versus b) enzymatic amplification. c)The pre-amplified signal (blue data) is improved by two orders of magnitude using enzymatic amplification (red data). d) Equivalence of ELLFIA sFlt-1 assay vs. central laboratory assay from ThermoFisher (BRAHMS sFlt-1 Kryptor).

Electrochemical Vertical Flow Assay (eVFA)

The electrochemical vertical flow assay (eVFA) is essentially made from the building blocks of a conventional lateral flow assay strip, just that the different components in the assembly are aligned on top of each other and a functionalized electrode is serving as the target analyte capture area. The eVFA is based on the assay developments for the electrochemical detection as well as on a two-chamber approach to improve the sensitivity of the immunoassay (Fig. 3, top). In the first chamber, the sample is dropped from the top and it flows through the same layers as in the lateral flows: sample, conjugation, and wicking pads. A laser perforated WE is implemented in the eVFA as a running pad, where the solution continues to flow. Once the immunoreaction occurred, the sensor is slid to the detection chamber, where the enzymatic amplification is started by the addition of the substrate. This setup allows minimizing the background signal and therefore improving the assay sensitivity, also reducing the incubation and washing steps to a total number of two (compared to a ten-step reaction on a bare working electrode). The assay was optimized with the C-reactive protein (CRP) as a model system in human serum, reaching a limit of detection of 33 ng/mL as proof of concept (Fig. 3, bottom). The principle of the eVFA has also been filed as a patent [3].

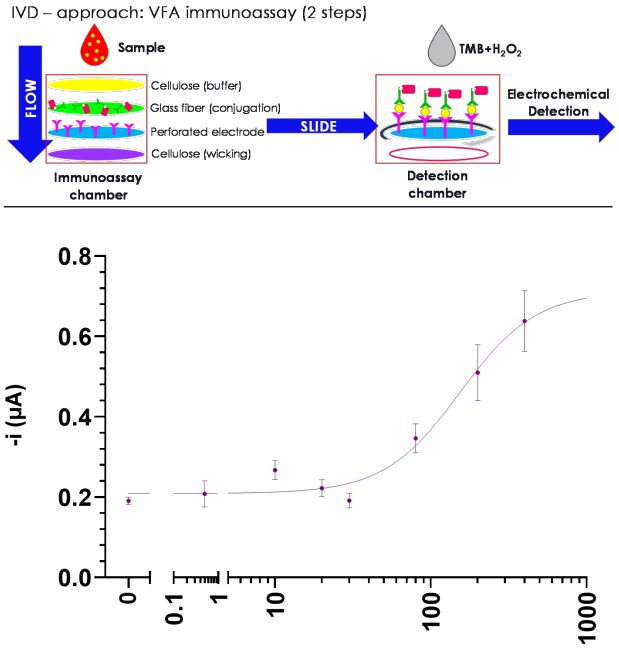

Fig. 3: (Top) Schematic principle of the eVFA. The sliding mechanism strongly improves the signal-to-background ratio and thus improves the sensitivity of the immunoassay. (Bottom) Calibration curve for the quantification of CRP in human serum using the eVFA.

References

[1] M. Zinggeler, S. Generelli, D. Gygax, D. Meinel and M. Wipf, PEPS: Printed Electrochemical Protein Sensor, SNI annual report 2021 (2021)

[2] M. Zinggeler, S. Schär and F. Kurth, Printed anti-fouling electrodes for biosensing applications, ACS Appl. Mater. Interfaces, 14, 51, 56578–56584 (2022)

[3] M. Zinggeler and S. Schär, Sensing device with improved detection sensitivity for detecting the presence of a predefined chemical, biological or biochemical entity in a fluid sample, patent filed

Development of theragnostic nanobody-polymer-conjugates targeting B7H3

Project A17.10: B7H3 Nanobody PC (CIS Pharma AG, Bubendorf, FHNW Muttenz, Paul Scherrer Institut, Universitäts-Kinderspital Zürich)
Project Leader: Ch. Geraths
Collaborators: M. Behe, T. Villiger, O. Germershaus, J. Nazarian

Background and Concept

Conventional tumor chemotherapy or radiotherapy are efficient at eradication of tumor cells but often lack target cell specificity, resulting in significant side effects. Theragnostics are modalities which may be used for both diagnosis and treatment, facilitating improved disease management, and reducing risks and costs of cancer therapy.

B7H3 is a transmembrane protein, acting as a suppressor of T-cell activation and proliferation as well as a potential checkpoint inhibitor ligand, which is overexpressed in different tumors, e.g. non-small cell lung cancer and prostate cancer [1].

Nanobodies are derived from heavy-chain antibodies from Camelidae and are characterized by low molecular weight, high stability, low immunogenicity, excellent affinity and specificity and high solubility. [2] Therefore, nanobodies represent ideal targeting moieties in the development of immunoconjugates.

The aim of this project is the development of a nanobody-polymer conjugate targeting B7H3 and allowing attachment of either diagnostic tracers such as radionuclides and/or therapeutic agents such as cytotoxic drugs (Fig. 1). By employing suitable polymeric carriers, the blood half life of the conjugate may be tailored according to diagnostic or therapeutic requirements, off-target effects may be reduced and ultimately penetration of the blood-brain barrier may be achieved.

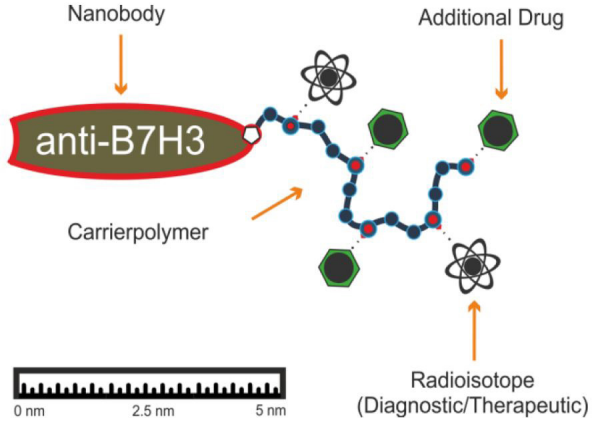

Fig. 1: Concept of B7H3-nanobody-polymer conjugate.

Nanobody Design and Expression

The nanobodies against B7H3 were designed using a humanized synthetic single domain antibody library coding for 3 x 10^9 VHH nanobodies in a two-stage approach. The first selection round was performed in a phage display using purified B7H3 antigen and subsequent enrichment of candidates in glioblastoma and HEK293 cells expressing the antigen using a FACS display. Non-specific binding was verified using KO cells.

The screening led to 84 nanobody candidates of which 10 were selected for further screening. The top two candidates of this screening were selected for expression.

Several expression and cultivation strategies were tested for the lead candidate nanobodies. As the initial cloning and expression approach did not lead to satisfactory yields and titers, an updated and simplified expression strategy was established. All constructs contained a SUMO-tag for cleavage of the hexahistidine site by the SUMOylase His-SENP1 and were expressed with a C-terminal cysteine for polymer linking. From the crystal structure of the nanobody, the C-terminus appeared not to be involved in secondary structures. Therefore, the C-terminal linkers were simplified, one version with direct coupling of cysteine to the nanobody (Fig. 2b and d) and another version with a simple GSGS-linker upstream of the cysteine (Fig. 2a and c).

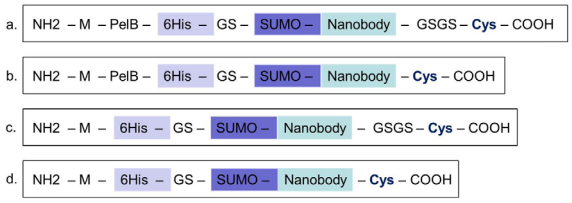

Fig. 2: Updated cloning strategy for nanobody expression.

Furthermore, expression in the cytoplasm and periplasm of E. coli were compared by expressing the construct with a PelB leader sequence for periplasmic transport (Fig. 2a and b) and without a signalling sequence for cytoplasmic expression (Fig. 2c and d). All constructs were be cloned in the plasmid pNHD and expressed in the E. coli SHuffle (DE3) strain. After cultivation and cell lysis, purification was performed by nickel affinity chromatography.

SDS-PAGE analysis of the different constructs showed that all variants can be expressed in the used setup. Overall, cytoplasmic expression (constructs c and d) displays higher expression levels compared to periplasmic expression. Subsequently, it was decided to continue with construct c (cytoplasmic expression including a C-terminal GSGS linker between the nanobody and the terminal cysteine) for further production steps of both top nanobody candidates.

Both nanobody candidates were efficiently expressed in E. coli Shuffle and purified by nickel affinity chromatography, allowing high yields and titers as displayed in figure 3 and table 1.

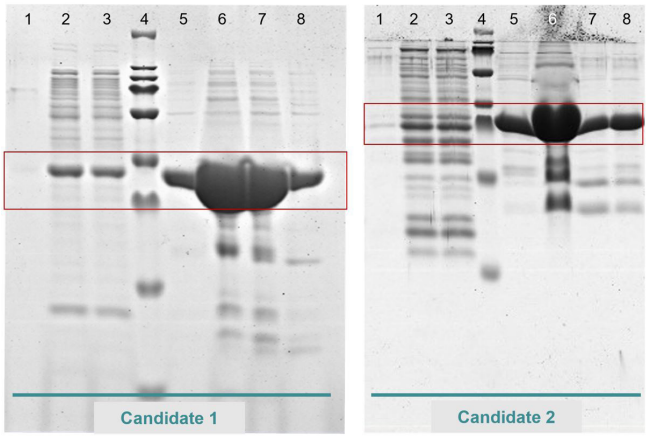

Fig. 3: Gradient SDS-Page of the production and purification of the two nanobody candidates (red boxes indicate expected molecular weight of nanobodies). Left: Candidate 1; 1. Supernatant; 2. Lysate; 3. Supernatant Lysate; 4. Ladder; 5-8. Elution fraction 1 to 4. Right: Candidate 2; 1. Supernatant; 2. Lysate; 3. Supernatant Lysate; 4. Ladder; 5-8. Elution fraction 1 to 4.

Table 1: Production titers and yields of the nanobodies candidates 1 and 2.

	Cand. 1	Cand. 2
Protein pooled (mg/ml)	1.75	2.63
Volume pooled (ml)	18	12
Total protein (mg)	31.50	31.54
Production yield (mg/L)	52.5	52.57

After successful production of both nanobodies, the functional cleavage of the His-SUMO tag on the N-terminus was confirmed. The presence of nanobodies after purification was successfully confirmed by SDS-PAGE and mass spectrometry.

Polymeric Carrier Design and Characterization

Polymeric carriers comprising various amino acid derivatives in their sidechains have been designed and synthesized. The respective acrylic monomers differ in their charge and hydrophobic balance and their primary amino-groups are later intended to be functionalized with amine-reactive payloads. The biocompatibility of monomers was assessed by Alamar Blue Assay on L929 mouse fibroblasts. Cytotoxic compounds in this assay reduce metabolic activity and reduce or inhibit the reduction of Resazurin. Typically, acrylic monomers are characterized by high toxicities but monomer design achieved very low toxicity (Fig. 4).

Monomer B comprising a hydrophobic lauric acid sidechain and monomer C having an aromatic side chain showed some degree of toxicity at concentrations substantially above 600 µM. Monomer A and D showed no cytotoxic effects even at 1000 µmol top concentration. LC50 values were calculated to be: A (not possible); B (718.5 µM); C (619.9 µM); D (not possible). The residual monomer content of the polymer carriers after purification lies below a detection limit of 10 ppm. Common purification methods will therefore be sufficient to remove residual monomers after polymerization to values of no concern.

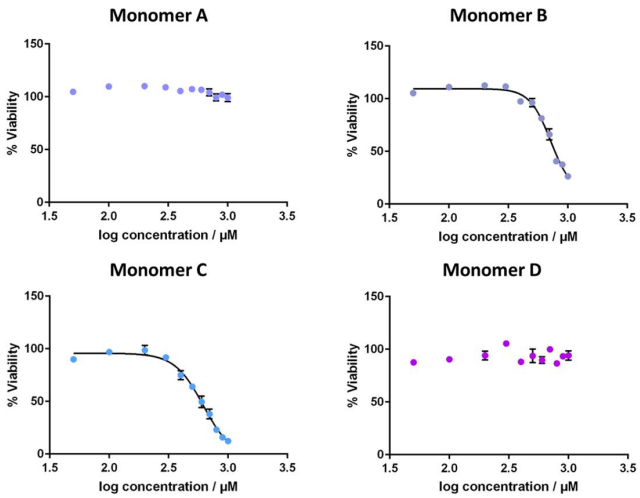

Fig. 4: Results of evaluation of biocompatibility of different acrylic monomers design for polymeric carrier synthesis.

Summary

The development and expression of anti-B7H3 nanobodies was anticipated to be a challenging task. After successful optimization of the expression strategy, both nanobody candidates selected for expression could be produced with good titers and production yields. The design and synthesis of suitable acrylic monomers with high biocompatibility was successfully achieved, allowing efficient synthesis of polymeric carriers with common purification methods.

References

[1] S. Yang, W. Wei, Q. Zhao, B7-H3, a checkpoint molecule, as a target for cancer immunotherapy, Int. J. Biol. Sci. 16, 1767 (2020)

[2] S. Sun, Z. Ding, X. Yang, et al., Nanobody: A Small Antibody with Big Implications for Tumor Therapeutic Strategy, Int. J. Nanomedicine 16, 2337 (2021)

Cosmic-ray reliability of nanoscale oxide layers in power semiconductors

Project A17.2: CRONOS (FHNW Windisch, ANAXAM, SwissSEM GmbH, Lenzburg)
Project Leader: R. Minamisawa
Collaborators: S. Rehm, A. Kopta, V. Novak, B. Ammann, P. Würsch, N. Schulz, L. Spejo

Motiviation

Power semiconductors enable the efficient usage of electricity in various application from eBikes up to power transmission between countries. To keep the losses of such power semiconductors low, the material properties are exhausted as much es possible, which means boundaries are bumped into. One such boundary is cosmic ray failures: due to the high fields within a power semiconductor it becomes susceptible to failures due to cosmic rays. This is usually tested with the gate (control input) shortened to the emitter (negative power connection). This however results in no field across the gate oxide. In applications, the gate is usually charged to +-15 V with respect to the emitter. Since the gate oxide is very thin (<100 nm) the result is a very high field strength of > 150 kV/mm. The goal of this work is to test the effects of cosmic rays on the reliability of this nano-scale gate oxide with a gate voltage applied.

Sample simulation and preparation

For the experimental investigations, 1200 V / 250 A trench-gate IGBTs from SwissSEM (product number SIS0250C120i20) have been selected as test vehicles. Figure 1 shows the upper part of the IGBT structure simulated under the same conditions as during the cosmic ray tests at PSI.

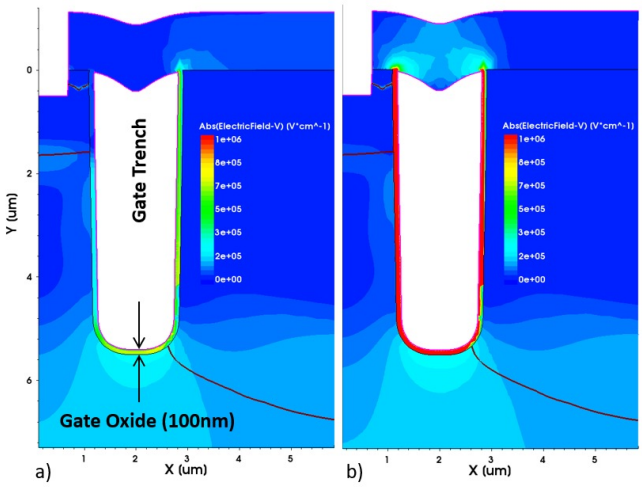

Fig. 1: Electric field in the IGBT during blocking. V_{CE}=850 V. a) V_{GE}=0 V, b) V_{GE}=-15 V

The figure shows the absolute value of the electric field when a voltage of 850 V is applied between the collector and emitter terminals of the device (V_{CE}). In figure 1a), a gate-emitter voltage (V_{GE}) of 0 V has been simulated, whereas figure 1b) shows the result when using V_{GE}= -15 V. At V_{GE}= 0 V, the electric field in the gate-oxide reaches a value of about 20 kV/mm, whereas it at V_{GE}= -15 V goes up to 150 kV/mm. These two simulation cases correspond to the conditions during the measurements as shown in figure 5. The investigated IGBTs are commercially available devices in mass production in a foundry in Asia. For this test, an arbitrary production lot was selected and assembled in the SwissSEM module line in Jiashan (China).

The assembly was done on a PCB specially designed by FHNW for this test. The completed PCB can be seen in figure 2 below. The assembly process consisted of the following steps:
1. Soldering of the IGBT chips to the PCB
2. Acoustic scan to check for solder voids
3. Wire bonding
4. Frame gluing and potting with silicone gel

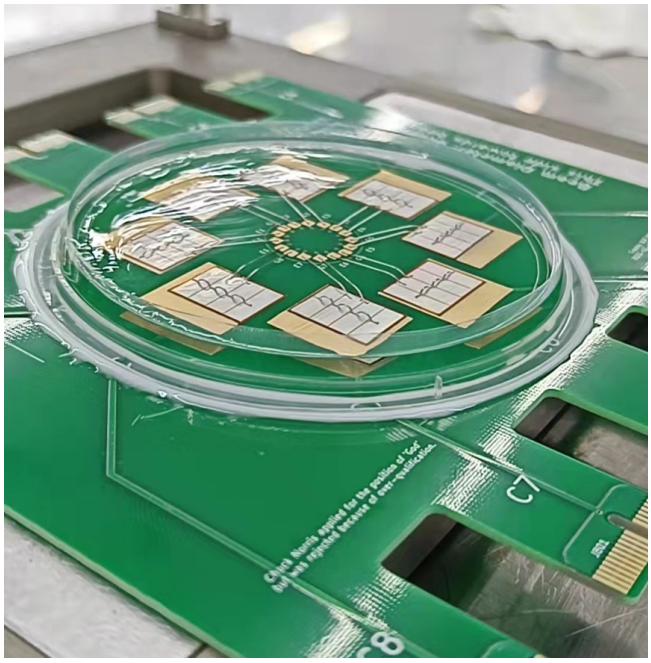

Fig. 2: 1200 V IGBTs assembled on a PCB, ready for the beam.

The samples were then shipped to FHNW for a pre-stress characterization.

Cosmic Ray Test System

During cosmic ray tests the samples are bombarded with high energy protons (200 MeV) while simultaneously blocking high voltage (~60% of max. voltage). The voltage is increased stepwise, which increases the sensitivity of the samples to interactions with the protons. If a proton interaction occurs in a critical area the sample will fail. Each sample has its own electronic fuse which detects the increase in current

and shuts down the failed sample. Eight electronic fuses are on each master PCB (seen on a drawer in Fig. 3). There are six master PCBs, thus the number of samples is 48.

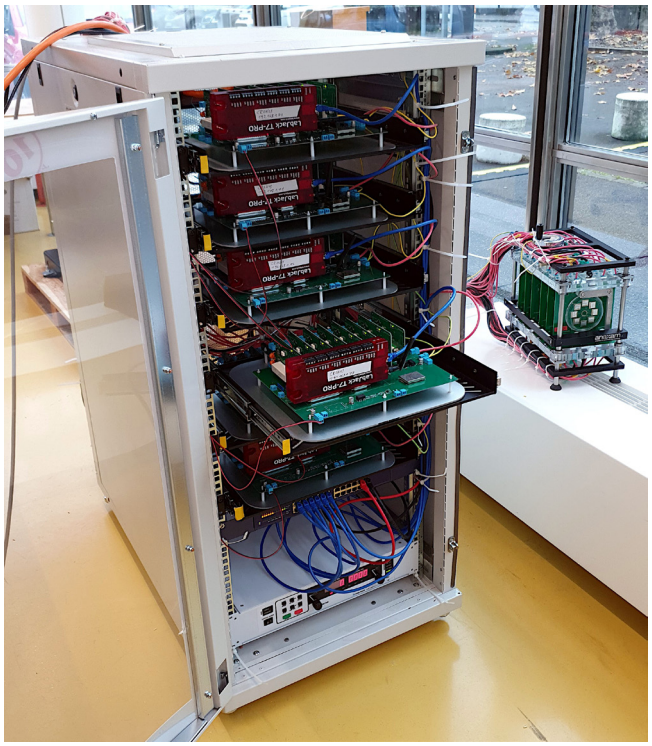

Fig. 3: CRONOS test system with 48 channels and the sample holder (right).

Sample holder for irradiation tests

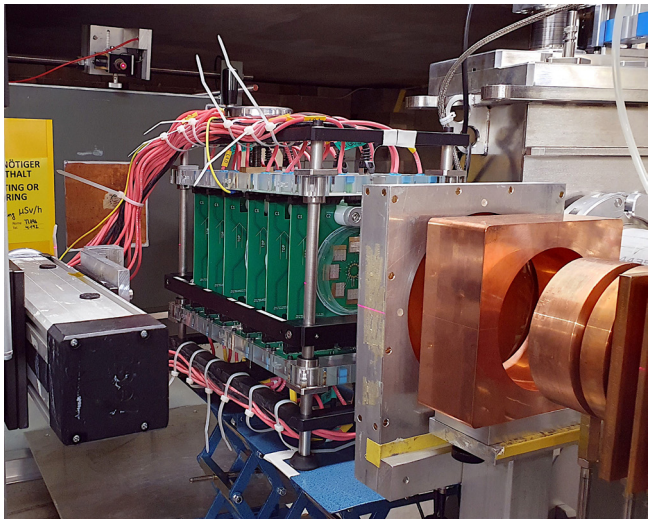

Fig. 4: Prepared IGBTs in the PIF beamline at PSI.

The device under Test (DUT) holder was fully customized for the target experiment, complying with the constraints on the number of devices as well as the beamline dimensions, see figure 4. The holder can accommodate up to 6 PCBs, where the IGBTs are in turn bonded, featuring a total of 48 DUTs. The arrangement and dimension of the holder is such that both neutron and proton particles can penetrate over the whole PCB stack.

The DUT holder was designed in order to provide quick and simple replacement of PCBs during the test to achieve a high throughput rate. To mount the samples, the frame is slid into the test holder, between the circuit boards. A wheel connected to a screw drive is mechanically closing the holder. By spinning the wheel, the lower plexiglas moves up and the upper plexiglas moves down until the test samples are well connected.

Proton irradiation tests and first results

The tests at the proton irradiation facility (PIF) were successfully conducted. Figure 5 shows the failure in time (FIT) rate of 1200V IGBTs with two different gate voltages. As can be seen, the negative gate voltage leads to a lower FIT rate.

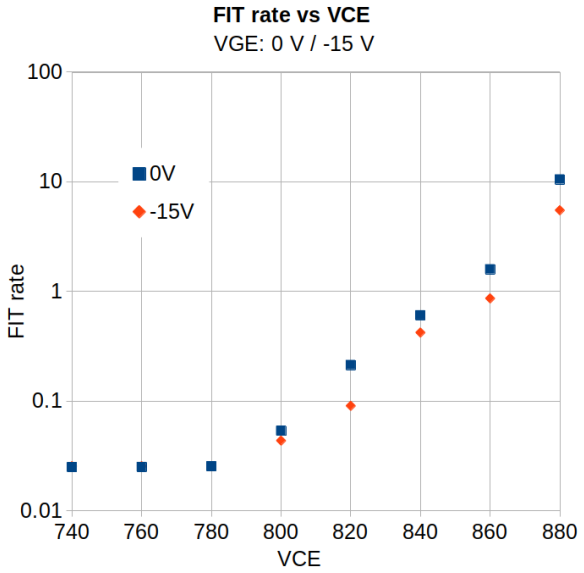

Fig. 5: Measured FIT rate of 1200 V IGBTs with different gate voltages (0 V and -15 V).

Two batches of samples for later oxide reliability tests were also pre-stressed, one batch with 0 V and another with -15 V on the gate.

Oxide reliability tests

Thirty batches with 240 IGBTs have been characterized with a Keysight B1505A Power Device Analyzer. The measurements were performed at room temperature (22°C), and the transfer curves were obtained for all samples. Capacitance characterizations between gate and emitter have also been carried out using a LCR Impedance Analyzer at constant frequency and variable gate voltage with forward and backward voltage sweep. Both analyses aim to investigate the gate oxide degradation after cosmic ray exposure and gate oxide reliability testing. The transfer curves provide variation in the device's threshold voltage being directly related to the gate charges. The CV characterization provides an additional measurement of the gate oxide integrity, which added gate charges and defects can also be characterized.

After cosmic ray exposure and gate oxide reliability testing, these characterizations will be performed in the surviving samples. Thus, the effects of each procedure can be investigated individually and compared to the initial characterization of the samples.

Functional cryo-EM sample preparation

Project A17.3: FuncEM (University of Basel, Biozentrum, Paul Scherrer Institut, cryoWrite AG, Basel)
Project Leader: T. Braun
Collaborators: I. Takashi, N. Zimmermann, A. Fränkl, M. Mohammadi, L. Rima, N. Candia, A. Lorca, A. Engel

Introduction

Cryogenic electron microscopy (cryo-EM) radically changed structural investigations in biomedical and fundamental research. But unfortunately, sample preparation is still a significant bottleneck in the workflow. Notably, the classical process uses a lot of sample and tends to damage the specimen by the paper blotting step and the exposure to the harsh air-water interface. The cryoWrite system [1-3] minimizes sample consumption and loss, eliminates the paper blotting step, and allows unprecedented control over the preparation process.

In this project, we aim to improve the microfluidic preparation process further by (i) protecting the specimen better from the aggressive air-water interface, (ii) gently controlling the thickness of the sample, and (iii) developing a real-time system to monitor the sample activity immediately before vitrification. The latter enables performing functional assays in situ in the sample layer, establishing a correlative link between biological function and the studied structures (Fig. 1).

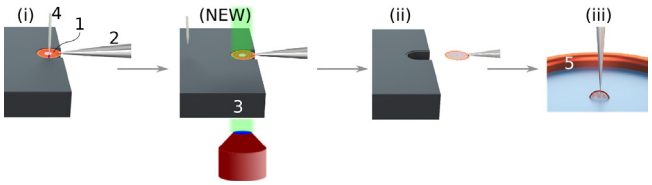

Fig. 1: Working principle of nL sized cryo-EM grid preparation. (i) A standard holey carbon film EM grid (1) is mounted between the tips of tweezers (2) and positioned flat (horizontal) in a slot in a temperature-controlled stage (3). The stage temperature is set at or close to the dew point temperature and can be regulated using a PID controller. The dew point stage (3) is mounted on a motorized XY axis to move the grid relative to a microcapillary (4), which can be lowered to a few µm above the grid. This microcapillary deposits a few nL of the sample by a high precision pump system while moving, covering an area of about 0.5 mm^2. (ii-iii) After a settling time, the automatic plunge-freezing is initiated. Then, the tweezers and grid are rapidly withdrawn from the stage, flipped by 90 degrees into the vertical position, and plunged into a cryogen (5). (NEW) In this project, we propose to image the specimen immediately before the sample is vitrified.

As a benchmark project, we analyze the 3D structure of motile cilia (or eukaryotic flagella in synonym) by cryo electron-tomography. The classical specimen preparation involves hefty paper blotting, which tentatively disturbs cilia structure and function. Therefore we optimize the vitrified layer for thickness to avoid squeezing the cilia's structure and aim to perform an in situ activity test before vitrification. Additionally, we developed a method to establish a protecting molecular layer (coverslip) to passivate the air-water interface.

Coverslip injector for the cryoWriter

The specimen is exposed to physical and chemical harsh air-water interfaces during the preparation for cryo-EM. For an average protein, the diffusion times are in the low microsecond range and an outrunning of protein diffusion to the air-water interface is impossible. Therefore we developed a climate jet, controlling the micro-environment of the grid. The jet provides an oxygen-depleted environment of precisely controlled temperature and relative humidity (Fig. 2). Finally, a nozzle directs the gas stream over the cryo-EM grid. Notably, this nozzle also allows the injection of surface active modulators into the gas stream as short pulses. This enables the creation of a protecting layer at the air-water interface of the thin sample [4].

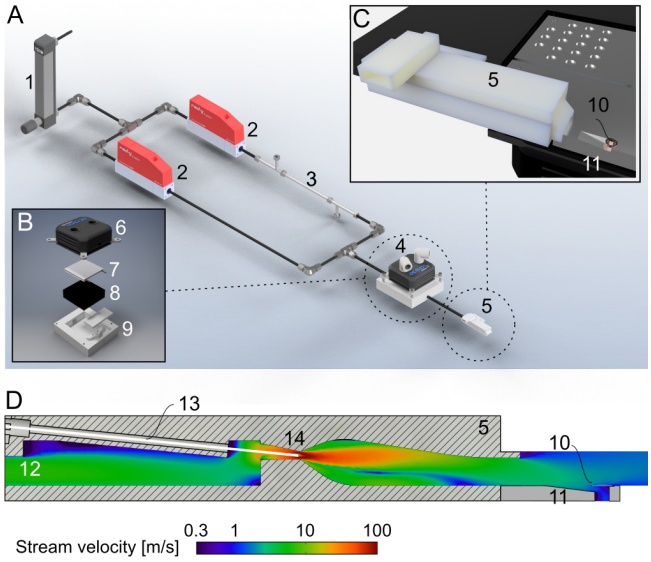

Fig. 2: Climate jet and coverslip injector. A) The climate jet system controls the temperature and humidity of a N_2-stream. After a pressure reducer (1), the stream is split into two lines which are individually controlled by flow controllers (2). One line is humidified by a humidifying column (3). The two streams are combined and enter a conditioner (4), which adjusts the temperature of the two combined N_2-streams before entering the nozzle (5), forming a jet stream flowing over the cryo-EM grid. B) Temperature conditioner. A water-cooled (6) Peltier element (7) efficiently heats or cools the gas stream, which flows between a metal grill (8) and plastic cap (9) for efficient heat transfer. C) The nozzle (5) points toward the cryo-EM grid, placed with good thermal contact on top of an indentation in the temperature-controlled dew-point stage (11). D) Outlet

nozzle cross-section: The conditioned N_2-stream enters a chamber (12) with humidity and temperature sensors. A microcapillary (13), filled with a solution of effector molecules, points to the middle of a narrow restriction (14) with maximal gas stream velocity. A pump system injects effector molecules into the gas stream, which are nebulized and streamed towards the cryo-EM sample holder (grid, 10).

Our results show (Fig. 2) that the cover-slip injector improves sample quality with decreased background noise, reduced number of damaged protein particles, and less preferential orientation. The spray also improves the sample spreading on the cryo-EM grid, increasing the usable sample area for imaging.

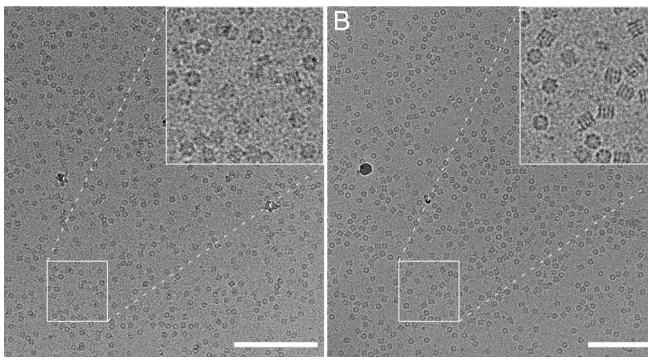

Fig. 3: Effect of the coverslip injector with Chaperonin 60 as the sample. The grids were prepared without injection A) or active spray B). A pulse of a OG solution was applied simultaneously with reaspiration of the sample. In the negative control A) >50% of the particles are damaged, whereas only <25% are damaged suing the coverslip injection. Scale bars: 200 nm [1].

Preparation of cilia for cryo-EM tomography

Eukaryotic, demembranized flagella axonemes are fragile structures challenging to prepare – particularly classical preparation methods involving intense paper blotting damage these organelles. We present the initial results in the project's P1901 report.

The mechanical instabilities of the test stand currently used in the Biozentrum restrict the sample area which can be prepared. Therefore, access and use of the new cryoWriter developed by cryoWriter AG is of utmost importance for the project.

Improved commercial cryoWriter

The new cryowriter system of cryoWrite AG is a vastly improved instrument compared to the current test stand in the Biozentrum. In particular, the mechanical design and the new high-precision pump system enable the direct writing of large thin sample areas. This achievement is essential for the functional tests we plan in the second half of the project. Furthermore, the new instrument allows complete automatization (Fig. 4). A critical aspect here is the clamping and flattening of the cryo-EM grid.

Outlook: In situ monitoring of thin sample layer

We are developing a new optical system for monitoring the thin layer in situ immediately before vitrification. The new optics allows characterization by fluorescence microscopy and interferometry. Together with subsequent cryo-EM, this allows correlative function-structure investigations.

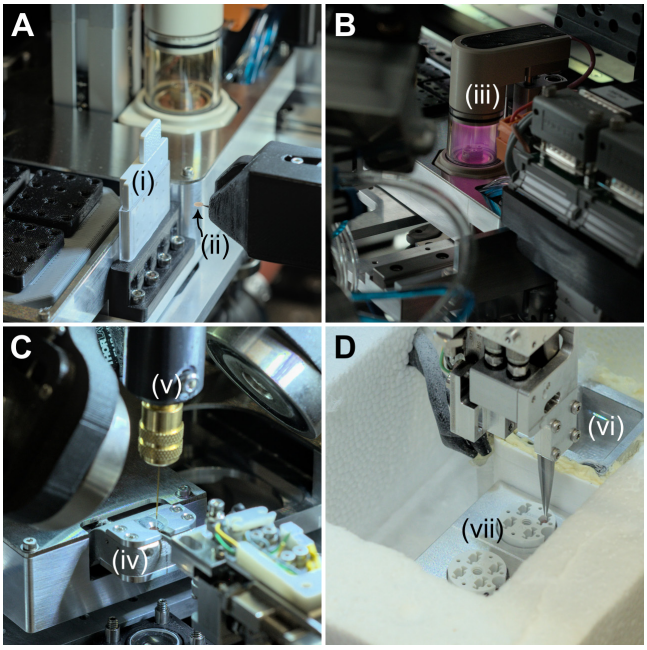

Fig. 4: CryoWriter prototype developed by cryoWrite AG. The system is fully automated. A) Pickup of grid, B) automated glow-discharging, C) Sample writing in concentric rings, D) Vitrification by plunge-freezing and storage of grid in transfer cartridges for cryo-EM under liquid nitrogen. Note that particularly the writing step (C) is significantly improved, thanks to the automated grid-clamping mechanism and newly developed high-precision pump. (i): Grid storage container for new grids; (ii) Grid, taken out by the automated tweezers from the storage box; (iii) Glow-discharger in operation; (iv) Dew-point stage with grid clamping mechanism; (v) Mounting mechanism for microcapillary writing the sample onto the grid; (vi) Temperature controlled liquified ethane for vitrification; (vii) Transfer containers for prepared samples under liquid nitrogen.

References

[1] S. A. Arnold, S. Albiez, N. Opara, M. Chami, C. Schmidli, A. Bieri, C. Padeste, H. Stahlberg, T. Braun, Total sample conditioning and preparation of nanoliter volumes for electron microscopy. ACS Nano, 10, 4981-4988 (2016)

[2] S. A. Arnold, S. Albiez, A. Bieri, A. Syntychaki, R. Adaixo, R. A. McLeod, K. N. Goldie, H. Stahlberg, T. Braun, Blotting-free and lossless cryo-electron microscopy grid preparation from nanoliter-sized protein samples and single-cell extracts, J. Struct. Biol. 197 (3), (2017)

[3] C. Schmidli, S. Albiez, L. Rima, R. Righetto, I. Mohammed, P. Oliva, L. Kovacik, H. Stahlberg, T. Braun, Microfluidic protein isolation and sample preparation for high-resolution cryo-EM. PNAS U.S.A. 116 (30) (2019)

[4] L. Rima, M. Zimmermann, A. Fränkl, T. Clairfeuille, M. Lauer, A. Engel, H-A. Engel, T. Braun, cryoWriter: a blotting free cryo-EM preparation system with a climate jet and cover-slip injector, Faraday Discuss. 240, (2022)

Nanoimprinted metasurfaces for foldable and rollable displays

Project A17.4: META-DISPLAY (CSEM Allschwil, Paul Scherrer Institut, Rolic Technologies Ltd., Allschwil)
Project Leader: B. Gallinet
Collaborators: C. Eggenspiller, F. Federspiel, R. Frantz, I. Giannopoulos, J. Heidler, D. Kazazis, M. Kraus, D. Pires

Introduction

Future displays in devices such as tablets or smartphones will be foldable or rollable to simplify consumer use and storage. These displays must be extremely thin to have the flexibility of a foil. Reduction of back reflection from ambient light is crucial to maximize the display contrast.

The minimization of ambient light reflection is performed with a polarizer and a quarter waveplate (Fig. 1). The ambient light incident on the display is transmitted through the stack and acquires a circular polarization. After reflection on the OLED/TFT backplane, the circularly polarized light is transmitted back through the quarter-waveplate and acquires the orthogonal linear polarization. The reflected light is therefore not transmitted through the polarizer. There are additional challenges related to optical performance. The suppression of ambient light reflection must be minimized for a broad range of angles so that contrast is maximized at any viewer position. The quarter waveplate retarder must have high transmission in order to maximize brightness of the OLED display.

Standard phase retarding materials based on liquid crystals have typical thicknesses of a few microns. In foldable and rollable displays, a minimization of the device thickness is sought for better flexibility. Metasurfaces have the potential to overcome the thickness the limitations of phase retarding materials, as they can strongly alter the phase of the electromagnetic field within a single micron [1].

In this project, dielectric metasurfaces are designed, fabricated and integrated as colorless and highly transmissive quarter waveplate. The nanostructures are patterned with electron beam lithography and replicated using nanoimprint lithography (NIL), which is widely used to replicate nanostructures cost-efficiently and at large scale.

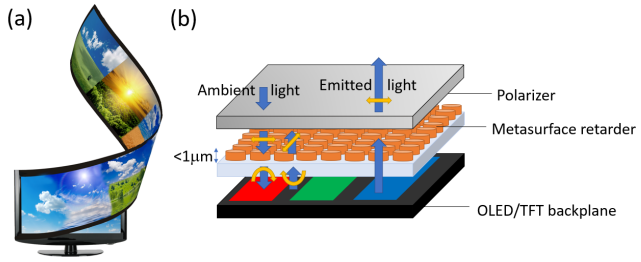

Fig. 1: a) Rollable display concept. b) Metasurface retarder for minimization of reflected ambient light and maximization of contrast.

Design

To maximize phase delay, the nanostructure aspect ratio and refractive index are maximized. Two approaches based on nanoimprint lithography are investigated (Fig. 2).

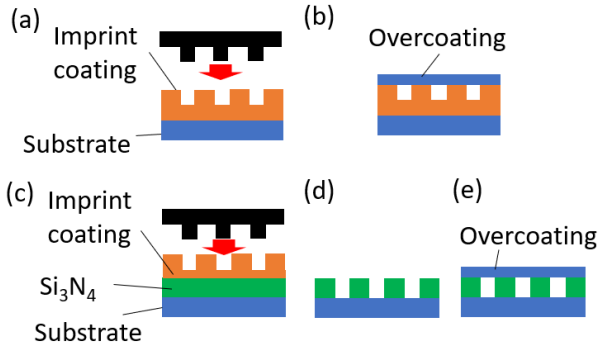

Fig. 2: Two fabrication approaches investigated in the project. a) Direct nanoimprint. b) Nanoimprint and etching into a silicon nitride thin film.

The first approach uses direct nanoimprint lithography adapted to high aspect ratios [2]. The nanoimprint material has a refractive index larger than 1.9. The second approach is based on nanoimprint on a thin film of silicon nitride, followed by pattern-transfer etching. It requires more process steps but allows for larger aspect ratios. After patterning, a low refractive index material is overcoated, which will make the link with the top polarizer. The pitch of the nanostructures is well below the visible light wavelength in order to minimize diffraction, which would be a source of disturbance for the user.

Figure 3 shows electromagnetic simulations of optical retardation for both approaches. The required retardation is 0.25 ± 0.05 waves over the visible range, corresponding to a quarter wave. The required retardation over the visible spectra comply with requirements over incidence angles up to 50°. The design based on nanoimprint and etching shows a more stable retardation as a function of wavelength and angle. Above 50°, some features appear in the low wavelength range for both transmission and phase retardation. They originate from first order diffraction. Both designs have an overall thickness below a micrometer. Simulated transmission is above 95% in average.

Fabrication

The nanoimprint master is realized with electron beam lithography and etching into a silicon wafer (Fig. 4a). The process parameters of the two key fabrication steps, namely lithography and pattern transfer, must be optimized to get the

desired result. PMMA is spincoated on a clean Si wafer and patterned by e-beam lithography. Subsequently, the PMMA pattern is transferred to silicon by dry etching using inductively coupled plasma (ICP). Despite the pattern's sub-100nm critical dimension, a highly anisotropic etching down to the desired depth can be achieved by using low pressure and low temperature conditions. Finally, the remaining PMMA layer is stripped by oxygen plasma and the pure Si master with the high aspect ratio structures is then ready to be used for nanoimprint lithography. Top view and cross section images of masters are shown in figure 4b and 4c, respectively.

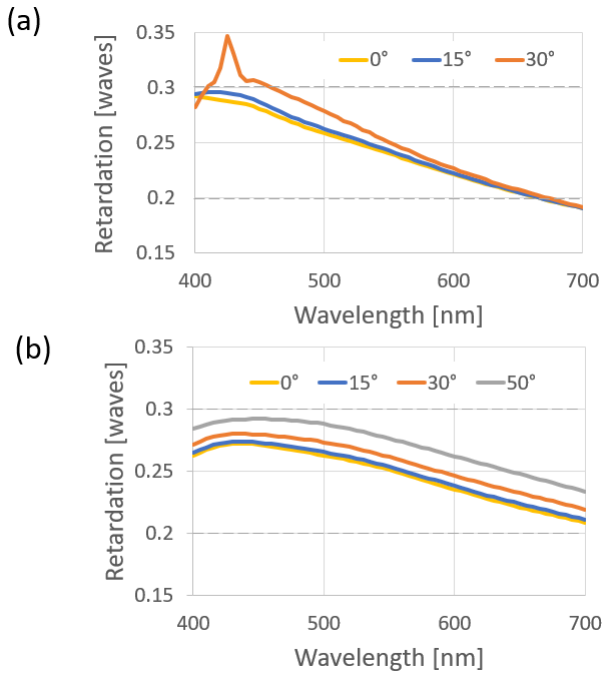

Fig. 3: Simulations of optical retardation from two fabrication approaches. a) Direct nanoimprint of index above 1.9. b) Nanoimprint and etching into a previously pattern silicon nitride thin film.

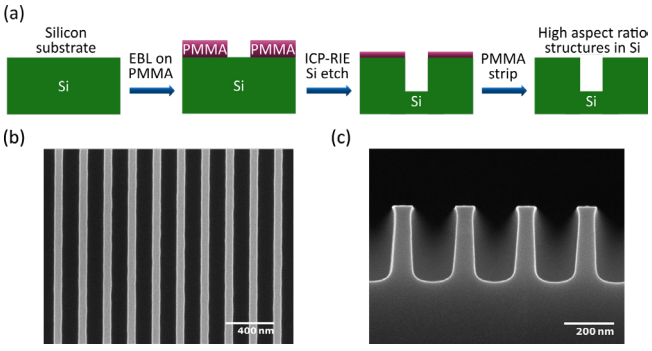

Fig. 4: a) Process flow of the nanoimprint master fabrication and SEM inspection of top- b) and cross-section c) views.

Direct UV nanoimprint with the IOC-133 material from Inkron (index 1.95) has been performed to replicate the master. A roll-to-plate approach has been used: the master is flexible and placed on a roll while the substrate is planar (Fig. 5a). Roll-to-plate UV nanoimprinting technology is used for the direct replication on thin foil, which enables industrial scale production. It is also compatible with coatings of thickness below 1um. A soft PDMS copy has been made from the silicon master, from which the roll-to-plate stamp has been created. First tests show successful replication of the desired nanostructure in a high refractive index imprint material (Fig. 5b).

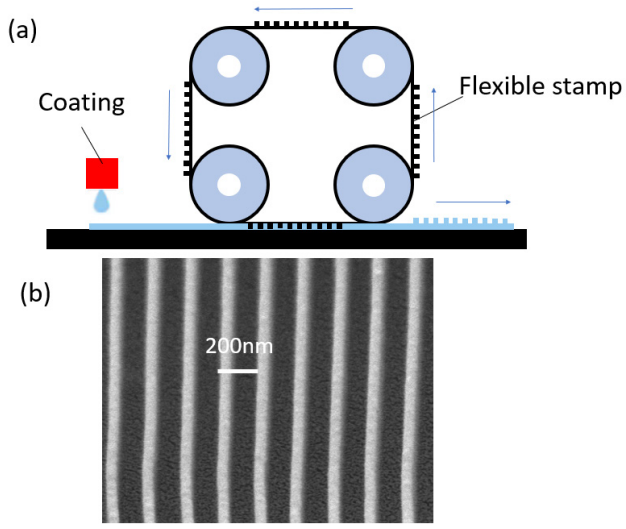

Fig. 5: a) Roll-to-plate nanoimprint process. b) Scanning electron micrograph of the silicon nanoimprint master. c) Atomic force microscopy image of a nanoimprinted structure into a high refractive index material.

Conclusion

In this project, the design and first fabrication process developments of an ultra-thin optical phase retarder based on metasurfaces have been carried out. These metasurfaces are foreseen to maximize contrast of foldable and rollable displays. Further work will include fabrication process development and optical measurements of phase retardation, as well as integration in a demonstrator. This metasurface technology can also be applied in other segments of the consumer electronics market, for example as flat imaging elements.

References

[1] A. Arbabi, Y. Horie, M. Bagheri, A. Faraon, Dielectric metasurfaces for complete control of phase and polarization with subwavelength spatial resolution and high transmission, Nat. Nanotechnol. 10, 937- 943 (2015)

[2] F. Lütolf, F. Friebel, I. Kuznetsov, B. Rudin, F. Emaury, B. Gallinet, R. Ferrini, G. Basset, B. Resan, Wafer-scale replicated gratings for compressing ultrafast laser pulses at telecom wavelengths, Opt. Continuum 1, 1051-1059 (2022)

Publications

A. Ahsan, L. Buimaga-Iarinca, T. Nijs, S. Nowakowska, R. Sk, et al., Induced fit and mobility of cycloalkanes within nanometer-sized confinements at 5 K, J. Phys. Chem. Lett., 13(32), 7504–7513 (2022) https://doi.org/10.1021/acs.jpclett.2c01592

S. J. An, M-H. Bae, M-J. Lee, M. S. Song, M. H. Madsen, J. Nygard, C. Schönenberger, A. Baumgartner, J. Seo, M. Juing, Impact of the gate geometry on adiabatic charge pumping in InAs double quantum dots, Nanoscale Adv. 4, 3816-3823 (2022) https://doi.org/10.1039/D2NA00372D

A. Bordoloi, V. Zannier, L. Sorba, C. Schönenberger, A. Baumgartner, Spin cross-correlation experiments in an electron entangler, Nature (2022) https://doi.org/10.1038/s41586-022-05436-z

L. C. Camenzind, S. Geyer, A. Fuhrer, R. J. Warburton, D. M. Zumbühl, and A. V. Kuhlmann, A hole spin qubit in a fin field-effect transistor above 4 kelvin, Nat. Electron. 5, 178-183 (2022) https://doi.org/10.1038/s41928-022-00722-0

L. Diez, L. E. Kapinos, J. Hochmair, S. Huebschmann, A. Dominquez-Baquero, A. Vogt, M. Rankovic, M. Zweckstetter, R. Y. H. Lim, S. Wegmann, Phosphorylation but not oligomerization drives the accumulation of Tau with Nucleoporin Nup98, Int. J. Mol. Sci. 23, 3495 (2022) https://doi.org/10.3390/ijms23073495

S. Di Leone, M. Kyropolou, J. Köchlin, R. Wehr, W. Meier, C. G. Palivan, Tailoring a solvent-assisted method for solid-supported hybrid lipid-polymer membranes, Langmuir, 38(21), 6561-6570 (2022) https://doi.org/10.1021/acs.langmuir.2c00204

L. Driencourt and B. Gallinet, Design guidelines for enhanced activity of water splitting photoelectrodes with plasmonic nanoparticles, J. Phys. Chem. C 126(4), 1701–1710 (2022) https://doi.org/10.1021/acs.jpcc.1c09246

M. Endres, A. Kononov, M. Stiefel, M. Wyss, H. S. Arachchige, J. Yan, D. Mandrus, K. Watanabe, T. Taniguchi, C. Schönenberger, Transparent Josephson junctions in higher-order topological insulator WTe2 via Pd diffusion, Phys. Rev. Mat. 6, L081201 (2022) https://doi.org/10.1103/PhysRevMaterials.6.L081201

M. Ernzer, M. Bosch Aguilera, M. Brunelli, G.-L. Schmid, C. Bruder, P. P. Potts, and P. Treutlein, Optical coherent feedback control of a mechanical oscillator, arXiv:2210.07674 (2022), https://doi.org/10.48550/arXiv.2210.07674

S. Flågan, P. Maletinsky, R. J. Warburton, and D. Riedel, Microcavity platform for widely tunable optical double resonance, Optica 9(10), 1197 (2022) https://doi.org/10.1364/OPTICA.466003

S. Flågan, D. Riedel, A. Javadi, T. Jakubczyk, P. Maletinsky, et al., High quality-factor diamond-confined open microcavity, Journal of Applied Physics 131, 113102 (2022) https://doi.org/10.1063/5.0081577

L. Forrer, A. Kamber, A. Knoll, M. Poggio, and F. Braakman, Electron-beam lithography of nanostructures at the tips of scanning probe cantilevers, arXiv: 2209.11503 (2022) https://doi.org/10.48550/arXiv.2209.11503

C. I. Giunta, S. A. Nazemi, M. Olesinska, P. Shahgaldian, Plasmonic photothermal activation of an organosilica shielded cold-adapted lipase co-immobilised with gold nanoparticles on silica particles, Nanoscale Adv. 5 , 81-87 (2023) https://doi.org/10.1039/D2NA00605G

F. Huber, H-P. Lang, S. Heller, J. A. Bielicki, C. Gerber, E. Meyer, A. Egli, Rapid bacteria detection from patients' blood bypassing classical bacterial culturing, Biosensors, 12(11) 994 (2022) https://doi.org/10.3390/bios12110994

R. Haller, G. Fülöp, D. Indolese, J. Ridderbos, R. Kraft, et al. Phase-dependent microwave response of a graphene Josephson junction, Phys. Rev. Research 4, 13198 (2022); https://doi.org/10.1103/PhysRevResearch.4.013198

J. Happacher, D. A. Broadway, P. Reiser, A. Jiménez, M. A. Tschudin, et al., Low Temperature photo-physics of single NV centers in diamond, Phys. Rev. Lett. 128, 177401, https://doi.org/10.1103/PhysRevLett.128.177401

I. C.-Y. Hou, A. Hinaut, S. Scherb, E. Meyer, A. Narita, K. Müllen, Synthesis of giant dendritic polyphenylenes with 366 and 546 Carbon atoms and their high-vacuum electrospray deposition, Chem. Asian J., 17(11), e202200220 (2022) https://doi.org/10.1002/asia.202200220

S. Jia, Y. Sato, and S. Tsujino, Size and shape dependent rotation characteristics of thin film ultrasonic rotors, Appl. Phys. Lett. 121, 254102 (2022) https://doi.org/10.1063/5.0126000

J. Kalita, L. E. Kapinos, T. Zheng, C. Rencurel, A. Zilman, R. Y. H. Lim, Karyopherin enrichment and compensation fortifies the nuclear pore complex against nucleocytoplasmic leakage, J. Cell Biol. 221(3) e202108107 (2022) https://doi.org/10.1083/jcb.202108107

A. Kubec, M.-C. Zdora, U. T. Sanli, A. Diaz, J. Vila-Comamala, C. David, An achromatic X-ray lens. Nat. Commun. 13, 1305 (2022) https://doi.org/10.1038/s41467-022-28902-8

C. Lotter, C. L. Alter, J. S. Bolten, P. Detampel, C. G. Palivan, T. Einfalt, J. Huwyler, Incorporation of phosphatidylserine improves efficiency of lipid based gene delivery systems. Eur. J. Pharm. Biopharm. 172, 134–143 (2022) https://doi.org/10.1016/j.ejpb.2022.02.007

F. Lütolf, F. Friebel, I. Kuznetsov, B. Rudin, F. Emaury, B. Gallinet, R. Ferrini, G. Basset, B. Resan, Wafer-scale replicated gratings for compressing ultrafast laser pulses at telecom wavelengths, Optics Continuum 1(5), 1051- 1059 (2022) https://doi.org/10.1364/OPTCON.456059

E. Marchiori, L. Ceccarelli, N. Rossi, L. Lorenzelli, C. L. Degen, M. Poggio, Nanoscale magnetic field imaging for 2D materials, Nat. Rev. Phys., 4, 49-60 (2022) https://doi.

org/10.1038/s42254-021-00380-9

E. Marchiori, L. Ceccarelli, N. Rossi, G. Romagnoli, J. Hermann, J.-C. Besse, S. Krinner, A. Wallraff, M. Poggio, Magnetic imaging of superconducting qubit devices with scanning SQUID-on-tip, Appl. Phys. Lett. 121, 052601 (2022) https://doi.org/10.1063/5.0103597

T. Mortelmans, D. Kazazis, C. Padeste, P. Berger, X. Li, Y. Ekinci, Poly(methyl methacrylate)-based nanofluidic device for rapid and multiplexed serological antibody detection of SARS-CoV-2, ACS Appl. Nano Mater. 2022, 5, 517–526, https://doi.org/10.1021/acsanm.1c03309

T. Mortelmans, D. Kazazis, J. Werder, P. M. Kristiansen, Y. Ekinci, Injection Molding of Thermoplastics for Low-Cost Nanofluidic Devices, ACS Appl. Nano Mater, 5(12), 17758–17766 (2022) https://doi.org/10.1021/acsanm.2c03731

J. Oswald, D. Beretta, M. Stiefel, R. Furrer, A. Romio, M. Daher Mansour, D. Vuillaume, M. Calame, Charge transport across Au–P3HT–graphene van der Waals vertical heterostructures, ACS Appl. Mater. Interfaces 2022, 14(42), 48240–48249 (2022) https://doi.org/10.1021/acsami.2c13148

P. Pip, S. Treves, J. R. Massey, S. Finizio, Z. Luo, et al., X-ray imaging of the magnetic configuration of a three-dimensional artificial spin ice building block, Appl. Phys. Letters Mat. 10, 101101 (2022) https://doi.org/10.1063/5.0101797

S. Flågan, P. Maletinsky, R. J. Warburton, D. Riedel, Microcavity platform for widely tunable optical double resonance, Optica 9, 1197-1209 (2022) https://doi.org/10.1364/OPTICA.466003

L. Rima, M. Zimmermann, A. Fränkl, T. Clairfeuille, M. Lauer, A. Engel, H.-A. Engel, T. Braun, CryoWriter: A blotting free cryo-EM preparation system with a climate jet and cover-slip injector, Faraday Discuss. 240, 55-66 (2022) https://doi.org/10.1039/D2FD00066K

T. Ruelle, D. Jaeger, F. Fogliano, F. R. Braakman, M. Poggio, A tunable fiber Fabry-Perot cavity for hybrid optomechanics stabilized at 4 K, Rev. Sci. Instrum. 93, 095003 (2022) https://doi.org/10.1063/5.0098140

M. Samani, C. P. Scheller, O. S. Sedeh, D. M. Zumbühl, N. Yurttagül, et al. Microkelvin electronics on a pulse-tube cryostat with a gate Coulomb-blockade thermometer, Phys. Rev. Research 4, 033225 (2022) https://doi.org/10.1103/PhysRevResearch.4.033225

S. Scherb, A. Hinaut, X. Yao, A. Götz, S. H. Al-Hilfi et al., Solution-synthesized extended graphene nanoribbons deposited by high-vacuum electrospray deposition, ACS Nano 2023, 17, 1, 597–605 (2022) https://doi.org/10.1021/acsnano.2c09748

Z. Scherübl, G. Fülöp, J. Gramich, A. Pályi, C. Schönenberger, J. Nygard, S. Csonka. From Cooper pair splitting to the non-local spectroscopy of a Shiba state, Phys. Rev. Research 4, 23143 (2022) https://doi.org/10.1103/PhysRevResearch.4.023143

G.-L. Schmid, C. T. Ngai, M. Ernzer, M. Bosch Aguilera, T. Karg, P. Treutlein, Coherent feedback cooling of a nanomechanical membrane with atomic spins, Phys. Rev. X, 12, 011020 (2022) https://doi.org/10.1103/PhysRevX.12.011020

C. Schönenberger, 2D materials shrink superconducting qubits, Nat. Mater. 21, 381 (2022) https://doi.org/10.1038/s41563-022-01220-6

Y. Song, X. Gao, A. Hinaut, S. Scherb, S. Huang, T. Glatzel, O. Hod, M. Urbakh, E. Meyer, Velocity dependence of Moiré friction, Nano Lett., 22, 23, 9529–9536 (2022), https://doi.org/10.1021/acs.nanolett.2c03667

L. Sponfeldner, N. Leisgang, S. Shree, I. Paradisanos, K. Watanabe, et al., Capacitively and inductively coupled excitons in bilayer MoS2, Phys. Rev. Lett. 129, 107401 (2022) https://doi.org/10.1103/PhysRevLett.129.107401

S. Tarvirdipour, M. Skowicki, C-A. Schoenenberger, L. E. Kapinos, R. Y. H. Lim, Y. Benenson, C. G. Palivan, A self-assembling peptidic platform to boost the cellular uptake and nuclear delivery of oligonucleotides. Biomater. Sci. 10(15), 4309-4323 (2022) https://doi.org/10.1039/D2BM00826B

M. Wyss, K. Bagani, D. Jetter, E. Marchiori, A. Vervelaki, B. Gross, J. Ridderbos, S. Gliga, C. Schönenberger, M. Poggio, Magnetic, thermal, and topographic imaging with a nanometer-scale SQUID-on-lever scanning probe, Phys. Rev. Appl. 17, 034002 (2022) https://doi.org/10.1103/PhysRevApplied.17.034002

V. Yurgens, A. Corazza, J. A. Zuber, M. Gruet, M. Kasperczyk, et al., Spectrally stable nitrogen-vacancy centers in diamond formed by carbon implantation into thin microstructures, Appl. Phys. Lett. 121, 234001, https://doi.org/10.1063/5.0126669

L. Zhai, G. N. Nguyen, Clemens Spinnler, J. Ritzmann, M. C. Löbl, A. D. Wieck, A. Ludwig, A. Javadi, R. J. Warburton, Quantum interference of identical photons from remote GaAs quantum dots, Nat. Nanotechnol. 17, 829-833 (2022) https://doi.org/10.1038/s41565-022-01131-2

M. Zinggeler, S. Schär and F. Kurth, Printed anti-fouling electrodes for biosensing applications, ACS Appl. Mater. Interfaces 2022, 14, 51, 56578–56584 (2022) https://doi.org/10.1021/acsami.2c17557

F. Züger, A. Marsano, M. Poggio, M. R. Gullo, Nanocomposites in 3D bioprinting for engineering conductive and stimuli-responsive constructs mimicking electrically sensitive tissue, Adv. NanoBiomed Res. 2, 2100108 (2022) https://doi.org/10.1002/anbr.202100108

Educating
Talents
since 1460.

University of Basel
Petersplatz 1
P.O. Box
4001 Basel
Switzerland

www.unibas.ch

Swiss Nanoscience Institute

University of Basel
Klingelbergstrasse 82 4056
Basel
Switzerland

www.nanoscience.ch